Stony Brook University

Stony Brook University

Structural and Electrochemical Study of Positive Electrode Materials for Rechargeable Lithium Ion Batteries

A Dissertation Presented

by

Meng Jiang

to

The Graduate School

in Partial Fulfillment of the

Requirements

for the Degree of

Doctor of Philosophy

in

Chemistry

Stony Brook University

December 2008

Stony Brook University

The Graduate School

Meng Jiang

We, the dissertation committee for the above candidate for the **Doctor of Philosophy** degree, hereby recommend acceptance of this dissertation.

Clare P. Grey, D. Phil., Advisor
Professor, Department of Chemistry, SUNY at Stony Brook

Stanislaus S. Wong, Ph. D, Chairperson of Defense
Professor, Department of Chemistry, SUNY at Stony Brook

Andreas Mayr, Ph. D, Third member
Professor, Department of Chemistry, SUNY at Stony Brook

Christian Masquelier, Ph. D, Outside member
Professor, Laboratoire de Reactivite et de Chimie des Solides,
Université de Picardie Jules Verne

This dissertation is accepted by the Graduate School

Lawrence Martin
Dean of the Graduate School

Abstract of the Dissertation

Structural and Electrochemical Study of Positive Electrode Materials for Rechargeable Lithium Ion Batteries

by

Meng Jiang

Doctor of Philosophy

in

Chemistry

Stony Brook University

2008

The research presented in this dissertation focuses on a combined study of the electrochemistry and the structure of positive electrode materials for Li ion batteries. Li ion batteries are one of the most advanced energy storage systems and have been the subject of numerous scientific studies in recent decades. They have been widely used for various mobile devices such as cell phones, laptop computers and power tools. They are also promising candidates as power sources for automotive applications. Although

intensive research has been done to improve the performance of Li ion batteries, there are still many remaining challenges to overcome so that they can be used in a wider range of applications. In particular, cheaper and safer electrodes are required with much higher reversible capacity.

The series of layered nickel manganese oxides $[Ni_xLi_{1/3-2x/3}Mn_{2/3-x/3}]O_2$ ($0 < x < 1/2$) are promising alternatives for Li_2CoO_2, the commercial positive electrode materials in Li ion batteries, because of their lower cost and higher safety and abuse tolerance, when lithium is removed from their structure. Compounds with $x<1/2$, in which the total Li content is higher than transition metal content, are referred as "Li-excess" materials. The "Li_2MnO_3-like" region is always present in this type of materials, and the overcapacity is obtained in the first charge process, which is not reversible in the following cycles. A combined X-ray diffraction, solid state nuclear magnetic resonance and X-ray absorption spectroscopy study is performed to investigate the effect of synthetic methods on the structure, to probe the structural change of the materials during cycling and to understand the electrochemical reaction mechanism.

The conversion compounds are also investigated because of their high capacities. Since the various compounds have different voltage windows, they can have potential applications as both cathodes and anodes. Solid state nuclear magnetic resonance is used to study the change in the local environment of the structure during the cycling process. Two systems are included in this work, including iron fluorides and Cu-containing materials. A comparison study has been performed on FeF_3 and FeF_2. Different discharge reaction mechanisms are clarified for each compound, and possible phase transitions are proposed as well. As for the Cu-containing systems, three compounds were chosen with

different anions: CuS, CuO and CuF_2. The reaction mechanisms are studied by ^{63}Cu, ^{7}Li and ^{19}F NMR and supported by powder X-ray diffraction.

Table of Contents

Chapter 2

Structural Analysis of Layered Lithium Nickel Manganese Oxide and the Processing Effect on the Structure

Chapter 3

High-resolution X-ray diffraction, DIFFaX, NMR and first principles study of disorder in the Li_2MnO_3–$Li[Ni_{1/2}Mn_{1/2}]O_2$ solid solution

Chapter 4

$LiNi_{0.5+\delta}Mn_{0.5-\delta}O_2$ – A high-rate, high-capacity cathode for lithium rechargeable batteries

Chapter 5

Electrochemical and Structural Study of Li-excess Material $Li[Li_{1/9}Ni_{1/3}Mn_{5/9}]O_2$

Chapter 7

An Investigation of the Conversion Reaction Mechanisms for Cu compounds by Using Solid State NMR Spectroscopy

Chapter 8

Conclusions

List of Figures

Chapter1

Chapter 2

Chapter 3

Chapter 4

Chapter 5

Chapter 6

Chapter 7

List of Abbreviations

CMFNs	carbon metal fluoride nanocomposites
DFT	density functional theory
DMC	dimethyl carbonate
EC	ethylene carbonate
EXAFS	extended X-ray absorption fine structure
FWHM	full width at half maximum
GGA	generalized gradient approximation
HEV	hybrid electric vehicle
IP	image plate
LiB	Li-ion rechargeable battery
MAS	magic angle spinning
NMP	N-methyl pyrrolidone
NMR	nuclear magnetic resonance
OCV	open circuit voltage
PDF	pair distribution function
PVDF	poly-vinylidene fluoride
SEI	solid state interface
TM	transition metal
XAS	X-ray absorption spectroscopy
XANES	X-ray absorption near edge structure
XRD	X-ray diffraction

List of Symbols

β, γ	unit cell angles
γ_N	gyromagnetic ratio
δ	isotropic chemical shift
λ	radiation wavelength
μ_B	Bohr magneton
$\vec{\mu}_e$	magnetic moment of the unpaired electron
μ_e	value of the electron magnetic moment
μ_N	value of the nuclear magnetic moment
ν_r	rotor (sample) spinning frequency, s-1
ω_0	Larmor frequency, rad.s^{-1}
$\rho(r = 0)$	electron spin density at the observed nucleus
χ_M	magnetic molar susceptibility
θ	diffraction angle
τ_p	pulse width (radiofrequency duration)
a, b, c	unit cell parameters
A/h	hyperfine coupling constant
B_0	external applied magnetic field strength
C/h	charge or discharge rate
C	theoretical specific capacity
$\vec{D}_{en}$	dipolar coupling tensor between the nucleus and the unpaired electrons
d_{hkl}	interplanar spacing

F_{hkl}	structure factor of *hkl* reflection
H_F	Hamiltonian operator for Fermi-contact interaction
H_{en}	Hamiltonian operator for electron-nucleus dipolar coupling
h, k ,l	Miller indices
I	nuclear spin number
I_{hkl}	intensity of the *hkl* reflection
I_Z	*z*-component angular momentum operator, spin *I*
M	molecular weight
N_0	Avogadro's number
r_{IS}	distance between spin *I* and *S*
S	electronic spin
S(Q)	normalized scattering intensity
S_z	*z*-component of the electron spin *S*
$<S_z>$	time-averaged value of the paramagnetic electron spin
T_{1e}	lifetime of an electronic spin state
T_1	spin-lattice relaxation time
T_2	spin-spin relaxation time
U, V, W	Gaussian profile parameters
X, Y	Lorentzian profile parameters
x, y, z	atomic coordinates
yi	*i*th data point

Acknowledgements

First and foremost, I would like to thank my advisor, Professor Clare P. Grey, for her scientific creativity, her patience, her guidance, her support and availability from the beginning to the end. I am forever grateful to her for being my advisor. Her dedication to science and her enthusiasm will always inspire me to go through all the difficulties in doing research.

I wish to acknowledge my committee members: Professors Stanislaus S. Wong, Andreas Mayr and Michael G. White for their encouragement and advices. Professor Christian Masquelier is thanked for being the outside member for my defense.

Prof. Gerbrand Ceder, and Prof. Yang Shao-Horn from Massachusetts Institute of Technology are acknowledged for fruitful discussions and collaborations. Special thank goes to Naoko Yamakawa from SONY for bringing in the wonderful projects and ideas, and spending time with me fixing probes and spectrometers in the basement. Thank Prof. Ying S. Meng from University of Florida for collecting the TEM data. I am thankful for the assistance from the beam line scientists: Thomas Proffen and Pete Encinias (Los Alamos National Laboratory), Winfried Kockelmann (ISIS), Jim Richardson, Joseph S. Fieramosca and Ryoji Kiyanagi (Intense Pulse Neutron Source), Jonathan Hanson, Peter W. Stephens, Kevin Stone, Xiaoqing Yang, Kyung-Wan Nam and Won-Sub Yoon (Brookhaven National Laboratory), Peter L. Lee, Peter J. Chupas, Christopher S. Johnson and Michael M. Thackeray (Argonne National Laboratory). Dr. Boris Itin at New York Structural Biology Center (NYSBC) is acknowledged for his help in running the experiments at NYSBC.

I would like to thank all the past and present group members: Nicolas Dupré, Won-Sub Yoon, Jordi Cabana Jiménez, Ulla Gro Nielsen, Sylvio Indris, Benjamin Meyer, Rangeet Bhattacharyya, Fred Blanc, Derek Middlemiss, Peter J. Chupas, Younkee Paik, Namjun Kim, Santanu Chaudhuri, Luming Peng, John Palumbo, Julien Breger, Paul Sideris, Stephen Boyd, Hailong Chen, Nicole Leifer, Lesley Holmes, Hua Huo, Jongsik Kim, Dongli Zeng, Baris Key, Fulya Dogan, Kellie Morgan, Lucienne Buannic, Ken Rosina, Yunxu Zhu, Riza Dervisoglu, and Nargis Naqvi. I learned a lot from everyone both scientifically and personally, and shared so many unforgettable moments with you. Lauretta Passanant is also thanked for her kindness and her always-filled stock of candies.

Many thanks to my friends in Stony Brook: Dandan Huang,Yao Li, Xin Chen, Chen Ji, Lili Zhou, Pranav Nawani, Hyunsoo Park, Xiaojie Zhou and David Sporled, for their patience and support, always being around with me, and listening to me when I face hard time in my life.

Very special thanks to my husband, Li Li, who is always very supportive and understanding, and sharing all the happy and sad moments with me.

Last but not the least, I want to thank my parents, for their support and inspiration. I could never have accomplished this without their endless love.

List of Publications

1. "Cation Ordering in Layered O3 $Li[Ni_xLi_{1/3-2x/3}Mn_{2/3-x/3}]O_2$ ($0<x<1/2$) Compounds", Meng, Y. S.; Ceder, G.; Grey, C. P.; Yoon, W.-S.; Jiang, M.; Bréger, J.; Shao-Horn, Y. *Chem. Mater.* **2005**, *17*, 2386-2394.

---Chapter 2

2. "High Resolution X-ray Diffraction, DIFFaX and NMR study of Stacking Faults in the Li_2MnO_3-$Li(NiMn)_{1/2}O_2$ Solid Solution", Bréger, J.; Jiang, M; Dupré, N.; Meng, Y. S.; Shao-Horn, Y.; Ceder, G.; Grey, C. P. *J. Solid State Chem.* **2005**, *178*, 2575-2585.

--- Chapter 3

3. "$LiNi_{0.5+\delta}Mn_{0.5+\delta}O_2$ – A High-rate, High Capacity Cathode for Lithium Rechargeable Batteries", Schougaard, S. B.; Bréger, J.; Jiang, M.; Grey, C. P.; Goodenough, J. B. *Adv. Mater.* **2006**, *18*, 905-909.

--- Chapter 4

4. "Electrochemical and Structural Study of Li-excess Material $Li[Li_{1/9}Ni_{1/3}Mn_{5/9}]O_2$", Jiang, M.; Key B.; Meng Y. S.; Grey, C. P.; in preparation.

--- Chapter 5

5. “A study of the lithium conversion mechanism of iron fluoride in a Li ion battery, by using solid state NMR, XRD and PDF analysis studies”, Yamakawa, N.; Jiang, M.; Grey, C. P.; in preparation.

---Chapter 6

6. “An Investigation of the Conversion Reaction Mechanisms for Cu compounds by Using Solid State NMR Spectroscopy”, Yamakawa, N.; Jiang, M.; Grey, C. P.; in preparation.

---Chapter 7

7. “High Voltage Study of Li-Excess Material as a Cathode Material for Li-Ion Batteries”, Jiang, M.; Grey, C. P. *Electrochem. Soc. Interface* **2006**, ASAP.

---Chapter 5

8. “Processing-Structure-Property Relation in Layered O3 $Li(NiMn)_{0.5}O_2$”, Meng, Y. S.; Kang, K.; Bréger, J.; Jiang, M.; Shao-Horn, Y.; Ceder, G.; Grey, C. P. in preparation.

Chapter 1

Introduction

1.1 Research motivations

In the recent decades, the shortage of fossil fuels has led to increased efforts in finding suitable alternative energy sources. Carbon dioxide, one of the major by-products from the combustion of fossil fuels has been proven to be one of the main causes of global warming. Previous studies have shown that most of this carbon dioxide comes from vehicle emissions. Electricity is a good substitution for powering vehicles for the following reasons. First, it can be obtained in variety of ways such as solar cells, nuclear power, and wind. Second, the use of electricity does not generate any side products, making it environmentally friendly. In order for electricity to be a viable alternative in vehicles, an energy storage system is needed. Among different rechargeable batteries, Li ion batteries have highest power density in both weight and volume (Fig.1.1).

In the 1990s, SONY commercialized the first rechargeable Lithium batteries using layered lithium cobalt oxide ($LiCoO_2$). This material was first demonstrated to reversibly intercalate/de-intercalate lithium during the electrochemical process by Goodenough and coworkers. $LiCoO_2$ (space group $R\bar{3}m$) can deliver a theoretical capacity of 130mAh/g with an operation voltage of about 3.6V and moderate cycling

kinetics. However, $LiCoO_2$ is toxic and expensive. In addition, there is a serious reversibility problem due to the formation of phases involving shearing of layers in the charged Li_xCoO_2 ($x < 0.5$).[1] Therefore, intensive studies have been performed in solid-state chemistry and electrochemistry to develop new intercalation compounds as an alternative to $LiCoO_2$ for positive electrodes for Li-ion batteries.

Previous studies have shown that the structure of the electrode material in Li ion batteries is strongly related to their electrochemical performance. Understanding the structure and reaction mechanism in these materials will help us to know how to modify the structure and to design new materials so as to improve battery performance.

In the current work, two types of positive electrode materials associated with different reaction mechanisms were examined from various aspects. They were investigated for short and long range ordering in the crystal structures under different synthesis conditions, the structural changes of the materials during cycling, and the reaction mechanisms at different stages of the charge and discharge. By obtaining the above information, we were able to understand some fundamental questions behind the battery performance. This chapter introduces basic information about how a Li ion battery works, the structures of the studied materials, and the techniques used for their characterization.

1.2 Rechargeable Li ion batteries

1.2.1 The electrochemical cell

Electrochemical cells are classified as primary (non-rechargeable, such as alkaline batteries) or secondary (rechargeable), based on their ability to be recharged. Primary batteries can only be discharged once, but secondary batteries can be recycled many times. Secondary batteries (such as Ni-Cd, Ni-MH and Li-ion) present high power densities and good temperature performances, but their energy densities are poor compared to primary battery systems, with the exception of Li ion batteries (LiBs). As shown in Figure 1.1,[2] LiBs can store more than twice the energy of other cells of the same mass and size, so they have been considered one of the most advanced energy storage systems.

A battery cell consists of three parts: a positive electrode (cathode), a negative electrode (anode) and an electrolyte. The negative electrode is oxidized and supplies electrons to the circuit during electrochemical reaction. The mobile ions are incorporated into the host structure of the positive electrode while transition metal ions in the material are reduced by accepting electrons from the external circuit to keep the charge balance. The electrolyte is an ionic conductor which acts as a medium for the ions traveling between the positive electrode and the negative electrode.

The secondary battery has two working processes: charging and discharging (Figure 1.2). During charging, the battery is connected with an external power supply. The cathode material is oxidized and the electrons flow to the anode through the external circuit. The anode is reduced by accepting the electrons. At the same time, anions

(negative ions) and cations (positive ions) travel through the electrolyte to the anode and cathode respectively. The potential difference between these two electrodes gets bigger, which results in an increase of the battery voltage. During discharging, the process is reversed, and oxidation and reduction reaction take place on the negative electrode and the positive electrode respectively. Thus, the battery is, in this case, referred to as "rechargeable" because this process is reversible and the chemical energy can be restored by supplying electric power upon charge.

The choice of electrode materials is crucial since the performance of the cell is mainly determined by their properties. There are several criteria for good electrode materials[3, 4]. These include a high gravimetric energy density, high volumetric energy density, high rate capability (power density), and high cycle life.

The gravimetric (or volumetric) energy density is defined as the energy per unit mass in Wh/kg (or per unit volume in Wh/L). The energy of the material is equal to the cell voltage timed by the specific capacity. To achieve a high value on this factor, high voltage, high specific capacity and low formula mass and/or formula volume are required. The cell voltage is determined by the potential difference of Li in the two electrodes. Usually, transition metal oxides, which are used as intercalation compounds for the positive electrode, possess an open circuit voltage (or OCV) of around 3.5 V, when Li metal is used as negative electrode. But the operating voltage of different electrode materials can be varied from 3.5~4.6V depending on the structural and electronic properties of the materials.[5-8]

The theoretical specific capacity (in mAh/g), noted as C_{th}, represents the number of Li ions (or electrons) involved in the electrochemical process in an hour. It is given by the following equation:

$$C_{th} = \frac{96500 \times \Delta x}{3.6 \times M} \qquad (1.1)$$

where Δx is the number of moles of Li that participate in the reversible electrochemical reaction, 96500 is the Faraday constant, and M is the molecular weight of the electrode compound.

The power density of a cell is defined as the battery power per unit mass (W/kg). The power of a battery is defined as the gravimetric energy density divided by the discharge time. This demonstrates the rate capability of the Li cell. The charge/discharge rate of a cell can be described by using the theoretical specific capacity, noted as C/h, meaning that it takes h hours to complete a theoretical charge or discharge. For example, a $2C$ (or $C/2$) rate will theoretically lead to a charge or discharge in 30 minutes (or 2 hours). When the power density is fixed for a certain material, it relies on the factors of the cells impedance, which is strongly correlated to the Li diffusion and electrical resistance of the electrode materials. These factors are inherent to the property of the materials and the cell design. Li diffusion in positive electrode materials in particular, is believed to be a critical factor in the rate capability of a cell.

The cycle life is defined as the number of charge/discharge cycles that can be performed while delivering a desired capacity. It mostly depends on the structural stability of the electrode materials, but will also be affected by the side reactions of

materials with the electrolyte and the formation of the solid electrolyte interface (SEI), the passivation layer that forms on the surface of electrode materials.

There are two types of reactions involved in the electrode materials during the electrochemical reaction: intercalation and conversion (Figure 1.3). These reactions can take place on both the positive and negative electrodes. The materials involved in the intercalation reaction usually have layered structures. For example, the materials used as positive electrode usually contain alternating layers of lithium, transition metal, and oxygen. During discharge, the transition metal ions are reduced with the Li intercalation into the layers without changing the whole frameworks. During charge, the transition metal ions are oxidized and the Li is removed from the layers leaving the layered transition metal oxide layered structure behind. The materials for negative electrodes are graphite and carbonaceous materials which also have carbon layers in the structure.[4, 9] Similarly, Li could go in and out of the layers during charge/discharge process.

The conversion reaction is mostly associated 3-d transition metal binary compounds M_xX_y (M= Co, Fe, Ni, Cu etc.; X=F, O, S, N etc.). These types of compounds have been intensively investigated in recent years due to their potential application as electrode materials in Li ion batteries. Because of their large range of working voltage associated with the variety of compounds, these materials can be used either as positive or negative electrodes. Tarascon *et al*.[10] demonstrate that specific capacities as high as 600～1000 mAh/g can be achieved in these systems, along with excellent cycling reversibility. Unlike the layered compounds, these materials react via a "conversion reaction" of the form:

$$M_xX_y + nyLi \Leftrightarrow yLi_nX + xM$$

In this reaction, the micron-sized M_xX_y (eg. M= Fe, Co, Ni, Cu etc. X=F, O, S, N etc.) decomposes to form a 1~10nm metallic particle/Li_nX nano-composite in the first reduction reaction (discharge). This is followed by repetitive redox reactions in which the size of the particles remain unchanged. The electrochemically driven nano-size confinement of the metal particles by the lithium salt Li_nX is believed to enhance their electrochemical activity, providing better reversibility to the Li_nX-M nanocomposite.

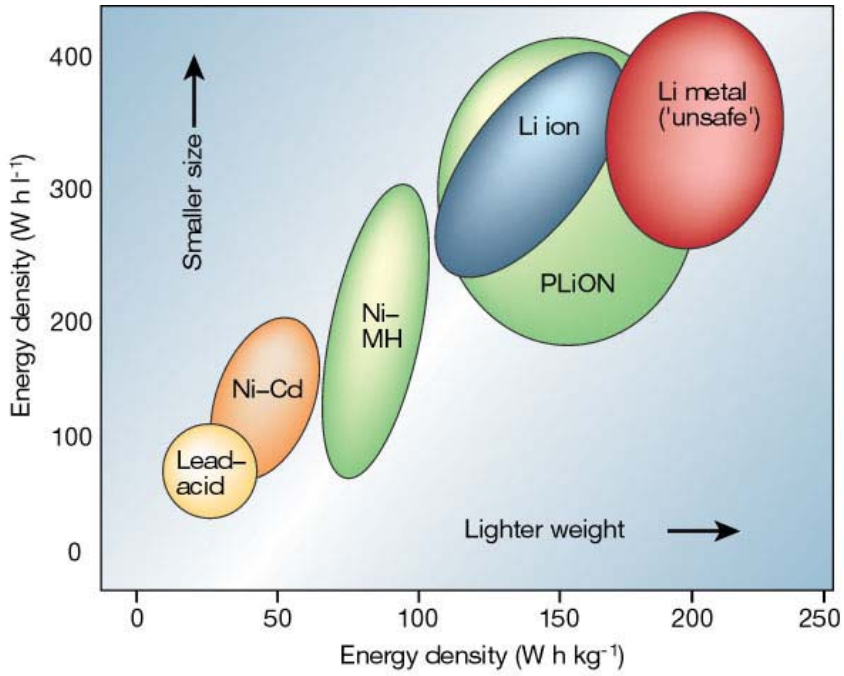

Figure 1.1: Comparison of the different rechargeable batteries in terms of volumetric and gravimetric energy density.[10]

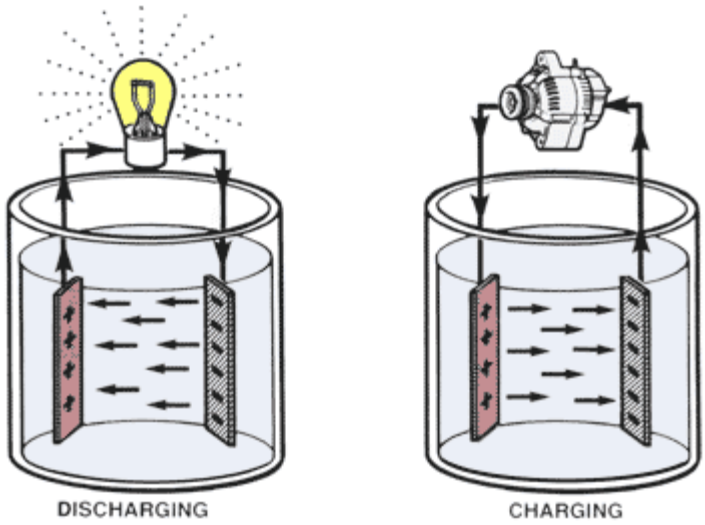

Figure 1.2: Charging and discharging process in secondary batteries.

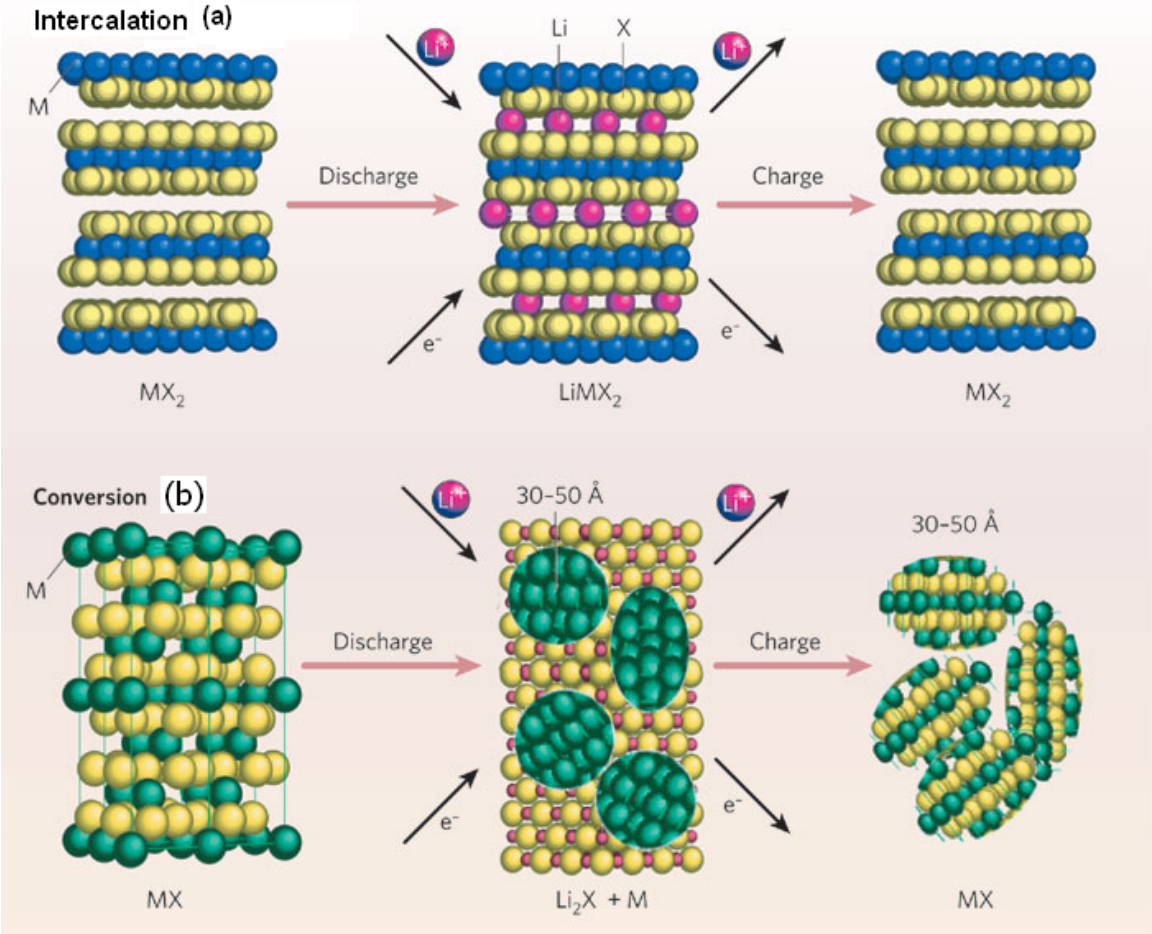

Figure 1.3: Schematic illustration of the two types of reactions in electrode materials: (a) intercalation and (b) conversion. [11]

1.2.2 Intercalation compounds: layered nickel manganese oxides

Currently, $LiCoO_2$ is the material that is most commonly used as the positive electrode material in commercial Li ion batteries. Layered lithium nickel manganese oxides have attracted interest as possible alternatives to $LiCoO_2$, because they are lower in cost, safer and more abuse tolerant when lithium is removed from their structure. The $Li[Li_{1/3-2x/3}Ni_xMn_{2/3-x/3}]O_2$ series of compounds were first reported by Dahn et al. and Ohzuku et al. in 2001.[12, 13] They all adopt $R\bar{3}m$ space group and have an ideal layered structure, like $LiCoO_2$, with lithium layers, transition metal layers and oxygen layers. Ni^{2+}/Ni^{4+} acts as the active redox couple that compensates the intercalation (deintercalation) of Li ions to (from) the layers.[14-25] The composition $Li(Ni_xLi_{1/3-2x/3}Mn_{2/3-x/3})O_2$ can be viewed as a continuous solid solution between the two end members, Li_2MnO_3 ($x = 0$), and $Li(Ni_{1/2}Mn_{1/2})O_2$ ($x = 1/2$), as shown in Figure 1.4.[22] Li_2MnO_3 adopts the *C2/m* space group and may be rewritten as $Li(Li_{1/3}Mn_{2/3})O_2$ in the notation used to describe many of these layered materials. The transition metal layer in Li_2MnO_3 comprises Li and Mn ions in an atomic ratio for Li:Mn of 1:2, arranged to form a "honey comb" ordering scheme in the *ab* plane (Figure 1.5),[22, 26] where each Li in the transition metal layers is surrounded by 6 Mn of the same layer.

The phases with $x<1/2$, in which the amount of lithium ions is higher than the amount of electrons that can be produced through the Ni^{2+}/Ni^{4+} reaction, are called Li-excess compounds.[15, 27-30] In this type of compound, some of the lithium ions stay in the transition metal layers in the pristine materials. During cycling, capacity values that are higher than those expected theoretically from the redox reaction are obtained when the

battery is charged for the first time. However, this extra capacity is neither recovered in the subsequent discharge nor generated again in the following cycles. In addition, a plateau-like region starting from 4.4V (Figure 1.6) is observed during the first charge and never comes back in the following cycles. Continuous efforts have been devoted to explain where this overcapacity comes from. Dahn et al.[15] proposed an oxygen loss mechanism (removal of Li_2O) to balance the charge, that seemed to be supported by Bruce *et al*'s observations of oxygen gas using *in situ* electrochemical mass spectroscopy measurements.[27] Unfortunately, quantification of the amount of oxygen gas produced was not possible, so it is not possible to address whether the evolution of oxygen can account for all the extra capacity. The proposed mechanism raised more issues than they addressed, e.g., if ideal layered structure is formed, why does it not accommodate more Li on deintercalation? And why can't Mn^{4+} be reduced as well as Ni^{4+} during discharge? Additionally, the structure changes associated with this hypothetical removal of oxygen are not quite clear.

In order to investigate what happened to the structure during the first cycle of charge-discharge in this series of compounds, $Li[Li_{1/9}Ni_{1/3}Mn_{5/9}]O_2$ is chosen as a model compound in this work. In this material, one-ninth of the Li ions reside in the transition metal layers originally and these materials deliver 200mAh/g theoretical capacity based on the redox reaction from Ni^{2+}/Ni^{4+}, and 331mAh/g capacity based on the total Li content in the compound.

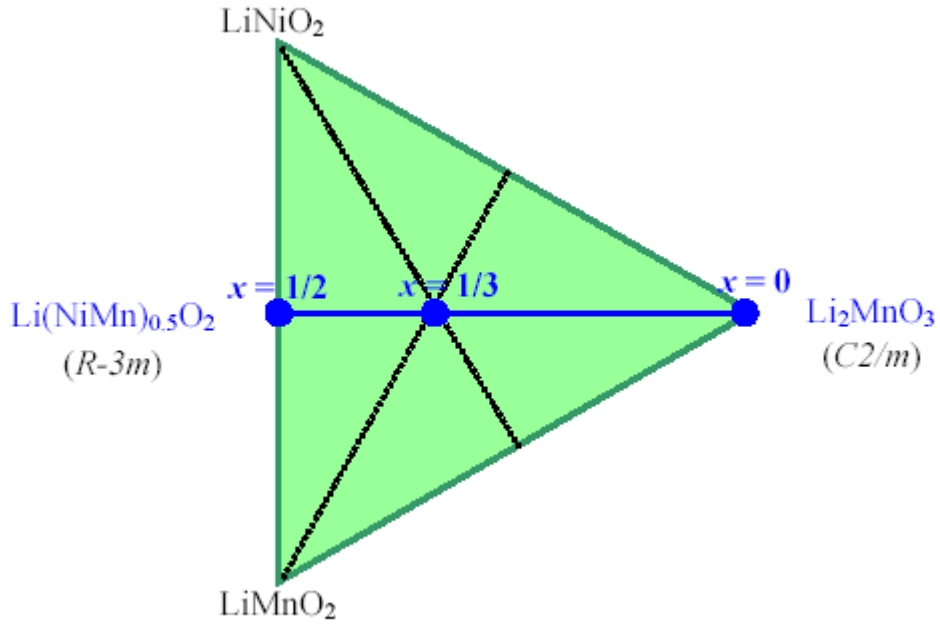

Figure 1.4: Ternary phase diagram of $LiNiO_2$-$LiMnO_2$-Li_2MnO_3. The solid blue line represents the solid solution $Li(Ni_xLi_{1/3-2x/3}Mn_{2/3-x/3})O_2$ ($0 \leq x \leq 1/2$).

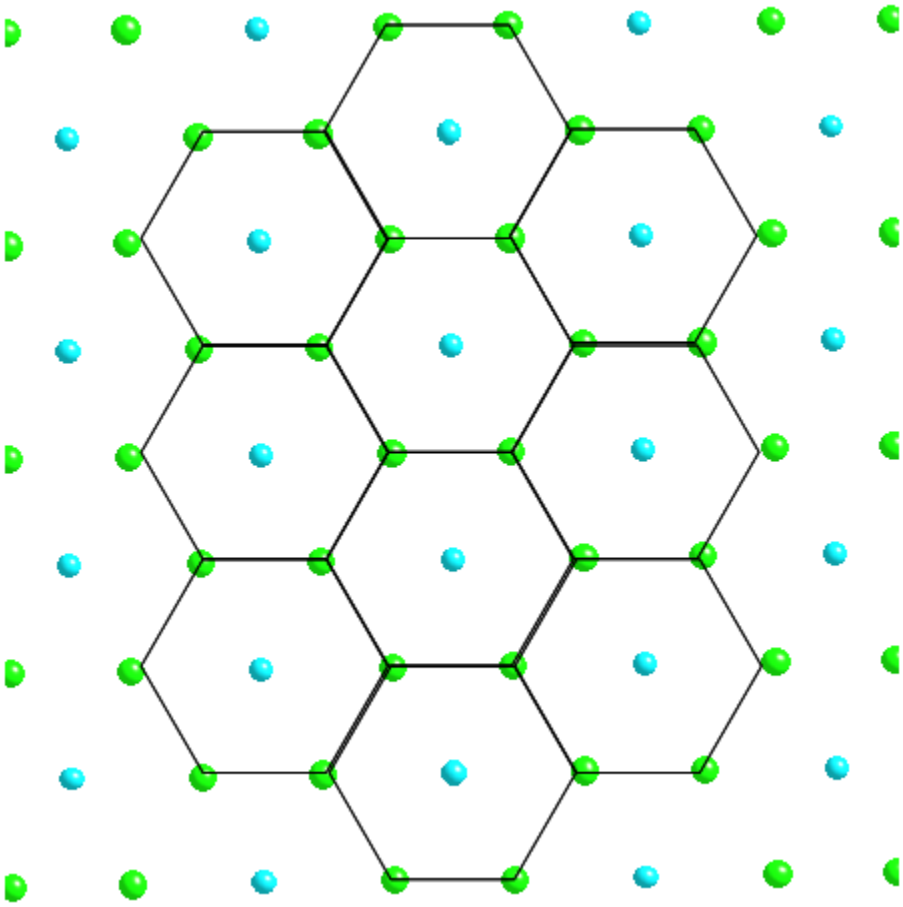

Figure 1.5: Illustration of the honey comb ordering in the transition metal layer of Li_2MnO_3. The blue and green spheres represent Li and Mn respectively.

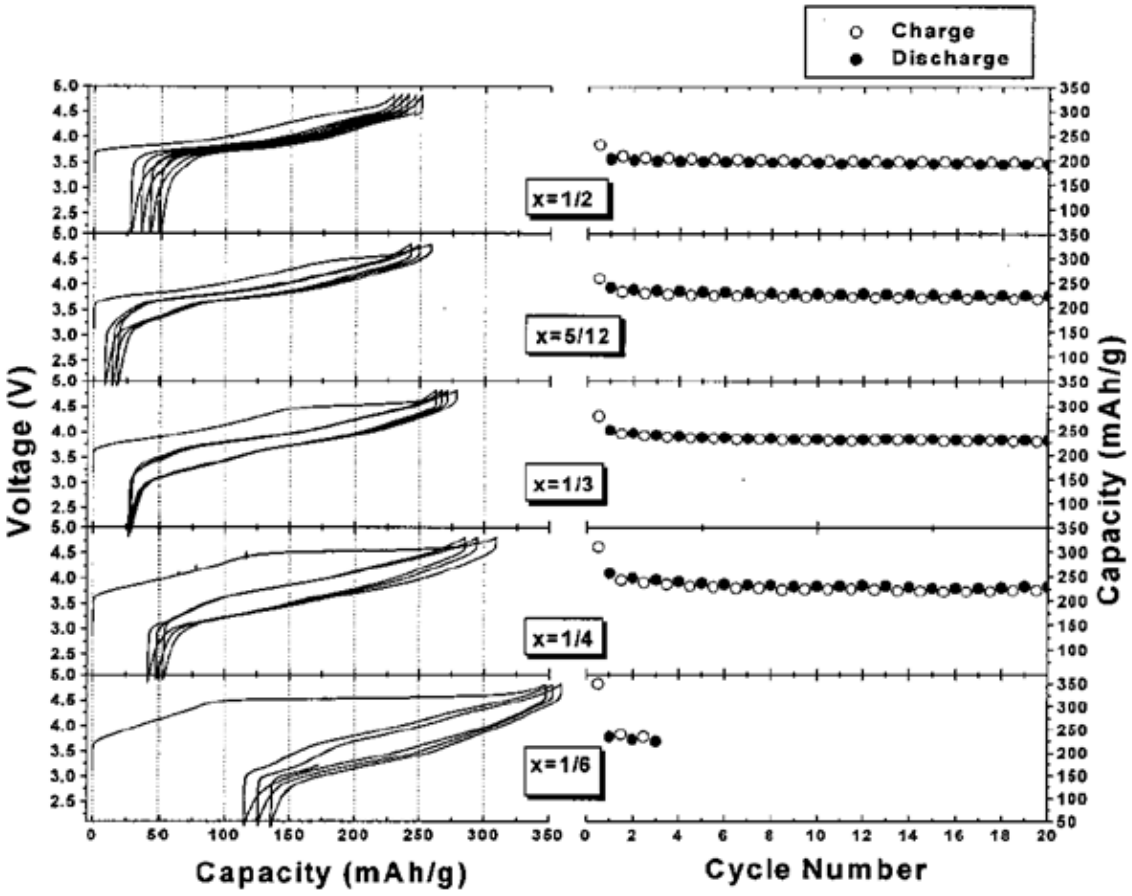

Figure 1.6: The cycling performance of a series of Li excess materials with a cut-off voltage window of 4.8-2.5V. [15]

1.2.3 Conversion compounds

Power density of the positive electrode materials is one of the most crucial problems limiting the application of Li ion batteries for use in electric vehicles. This is largely due to the limitation of the layered structure of the current materials and the valence changes of the transition metal ions. Conversion reactions open a door to a new type of reaction for the electrochemical process, and involve the redox couple M^{n+}/M^0 which could possibly give more theoretical capacity compared to intercalation reaction. However, the reaction mechanisms of the conversion reaction in different compounds vary significantly, and very little work has been done to understand these reaction processes. In this dissertation, two of these systems have been studied by solid state magnetic resonance (NMR) and X-ray diffraction (XRD).

Metal fluorides have been largely ignored as reversible positive electrodes for rechargeable lithium batteries. This is due to their insulative nature brought about by their characteristicly large bandgap.[31, 32] However, Amatucci *et al*.[33-37] have demonstrated the use of carbon metal fluoride nanocomposites (CMFNs) enables the electrochemical activity of metal fluorides. The concept was based on the fact that nano-sized crystals have a high total material volume on the surface. This surface contains a number of defects which can contribute substantially to the enhanced electronic and ionic activity. In addition, the highly conducting carbon is used to connect each grain electrically. With this method, 99% of the FeF_3 theoretical capacity can be recovered in the 4.5-2.5V region, as compared to 30% recovery without the CMFNs method.

The electrochemical processes in FeF_3 system are rather complicated. Several processes are observed in the electrochemical profile, and the phase transition mechanism of each step is still not very clear due to the limitation of the analytical techniques which have been used in the previous study. Since nano-sized particles are formed at the end of first discharge, and the same morphology remains throughout the rest of the cycling process, conventional diffraction methods are not sufficient to investigate the structure of the intermediate phase and the final products of the discharge and charge. Speculations about the phase transition have been proposed by Amatucci,[33, 34] and some calculations have been performed to understand the electrochemical process by Ceder et al.[38] However, no direct experimental data have been shown to either support or oppose these speculations. Solid state nuclear NMR is a powerful tool for the detection of short range ordering and is not limited by crystal size. It has been used to understand the electrochemical mechanism in this system (Chapter 6). Even though Fe metal formed at the end of first discharge is supposed to be ferromagnetic which could cause severe problems in an NMR experiment, the particle size of Fe metal is so small that it shows a superparamagnetic behavior. The superparamagnetism results in a huge broadening of the NMR spectra, but does not affect the spinning and tunning during the NMR experiment set up.

Another conversion reaction system studied in this dissertation is Cu compounds (Chapter 7). This system was chosen as a model in the facilitation of NMR experiments as Cu metal is not ferromagnetic like other metals commonly used in these systems i.e. Co and Ni. Three Cu compounds with different anions were chosen: CuF_2, CuS and CuO. A comprehensive study was performed on these compounds to understand their

electrochemistry, structural characterization of the intermediate phases, and the interactions between the copper metal particles and lithium compounds. A direct comparison between these copper compounds was made to understand the correlation between the interaction between particles and electrochemical behavior.

1.3 Solid state nuclear magnetic resonance

1.3.1 General introduction

Nuclear Magnetic Resonance (NMR) spectroscopy is an invaluable probe for the investigation of local structure. Different from diffraction techniques which tell us about the long range ordering in a structure, NMR can provide information about short range ordering. The NMR technique is element specific, such that the local environment of each crystallographic site can be distinguished. Another advantage of NMR is that it can be used to probe low molecular weight elements such as Li directly since the NMR peak intensity does not depend on atomic mass in the way that x-ray diffraction does. Thus, NMR can be used to probe the local environment of Li. This is extremely useful as Li is always involved in the electrochemical process.[39-45] The integrated intensity of a particular NMR resonance is proportional to the number of equivalent nuclei contributing to it. Therefore, quantitative analysis of the spectra can provide information about lithium content in the materials. Also, the location of lithium ions in the structure and the change of the local environment of Li during the electrochemical process can be monitored by performing ^{6,7}Li isotope experiments on the cycled electrode materials.

1.3.2 Magic Angle Spinning (MAS) NMR

Fast molecular motion can effectively remove all anisotropic interactions for molecules in solution, resulting in narrow resonances in the NMR spectra. However, molecular motion is much less rapid in solids compared to solution, which leads to the broadening of NMR resonances. The resolution of the spectra can be largely affected by this broadening of the peaks. Therefore, efforts have been made to develop techniques to acquire high resolution NMR spectra.

Magic Angle Spinning (MAS), which involves rotating the sample at a "magic angle" β of 54.736° with respect to the external magnetic field (Figure 1.7), was introduced by E. R. Andrew to eliminate anisotropic interactions such as chemical shielding interaction, heteronuclear dipolar coupling and first-order quadrupole coupling (for nuclei with spin I > ½).[46] There is an angular dependence of $(3\cos^2\beta\text{-}1)$ in the anisotropic interactions. When β is set to 54.736°, the term $(3\cos^2\beta\text{-}1)$ vanishes and high resolution NMR spectra can be obtained. When the spinning frequency v_r is faster than the size of the anisotropic interaction, only the isotropic resonance is observed; otherwise, the powder pattern is split into relatively narrow lines spaced at integer multiples of the sample rotation frequency (or MAS speed). These are referred to spinning sidebands. In practice, the spinning frequency is limited by the outer diameter of the spinner.

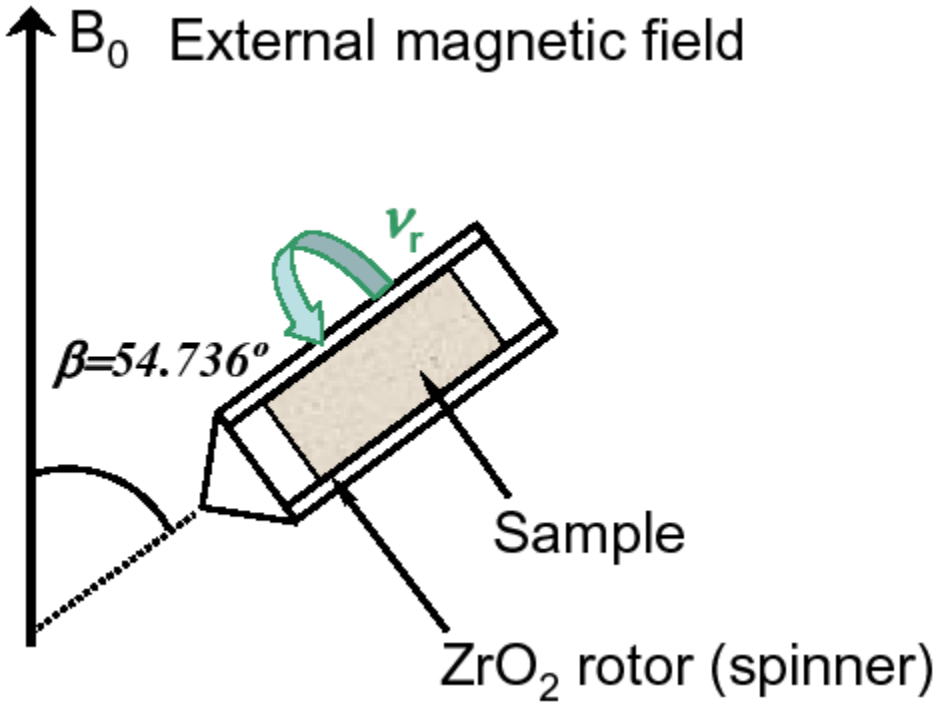

Figure 1.7: The schematic representation of magic angle spinning. The magic angle "β" is the angle between the spinner and the external magnetic field, and ν_r is the spinning speed.

1.3.3 Interaction in paramagnetic materials

Paramagnetic materials are defined by the presence of unpaired electrons. In most positive electrode materials, like layered nickel manganese oxide, paramagnetic ions such as Mn^{4+} are present in either the discharged or the charged state or both. The NMR spectra of paramagnetic materials are strongly affected by the interactions of nuclei with the unpaired electrons. These are referred to as "hyperfine" interactions, and are characterized by large shifts in the resonant frequencies.[47] Hyperfine shifts are typically temperature-dependent, and consist of two types of interactions that govern the isotropic and anisotropic shifts in the NMR spectra of paramagnetic materials: one involving a through-bond interaction (or *Fermi-contact* interaction), and another involving a through-space interaction (or *dipolar* interaction). These interactions and their effects on the materials studied will be discussed in more detail in the following sections.

1.3.3.1 Electron spins

In the presence of an external field $\vec{B}_0$, typically defined to be the *z*-direction, the magnetic moment ($\vec{\mu}_e$) of the electrons in paramagnetic ions interacts with the external field and align with $\vec{B}_0$. For the electrons with spin quantum number, S, (e,g., $S = 1$ for d^8 ion Ni^{2+} and $S = 3/2$ for d^3 ion Mn^{4+}), the energy levels are split into $2S + 1$ energy states, as shown in Figure 1.8.a for the case of $S = 1/2$. This is referred to the Zeeman term, and the Hamiltonian H_z corresponding to this interaction can be described as:[48-50]

$$H_Z = -\vec{\mu}_e \cdot \vec{B}_0 = g_e \mu_B \vec{S} \cdot \vec{B}_0 \qquad (1.2)$$

where the electron g-value, g_e, is 2.002322 for a free electron, and μ_B is the Bohr magneton. It should be noted that the coupling to the electrons and to the nucleus are different. The energy splitting and the magnetic moment associated with electrons are much larger than those of nucleus. Since the magnetic moment of the electron $\vec{\mu}_e$ is opposite in sign in comparison to the nuclear magnetic moment $\vec{\mu}_N$ the orientation of the two aligned spins is different from the nuclear case. In the case of $S = 1/2$, the electronic spin state with $Sz = -1/2$ (Sz represents the component of the spin along the z-direction) will lie at lower energies while the spin with $Sz = 1/2$ will lie at higher energies (Figure 1.8.a). In this case, two broad resonances may be expected in the NMR spectrum of the I-S spin system, one corresponding to nuclear I spins coupled to the S down-spins and the other to the S up-spins. The separation of the doublet will be given by A/h, the hyperfine coupling constant. In reality, a single line is obtained due to the fast relaxation of the electron ($< 10^{-8}$s) compared to the timescale of the NMR experiment. The lifetime of an ion in a particular electronic state (noted as T_{1e}) is so fast that nucleus cannot respond to each electronic state. Instead, as illustrated in Figure 1.8.b, the nucleus will interact with an average of the two electronic spin states $\overline{\mu}_e$, and only a single resonance at the average frequency is observed in the NMR spectrum. This average $\overline{\mu}_e$ is proportional to the time (or thermally) averaged value of the paramagnetic electron spin along the z axis, $\langle S_z \rangle$, and is given by:

$$\overline{\mu}_e = g_e \mu_B \langle S_z \rangle = -\frac{B_0}{\mu_0 N_0} \chi_M \qquad (1.3)$$

where N_0 is Avogadro's number, μ_0 is the permeability, and χ_M is the magnetic molar susceptibility in m^3mol^{-1}. A lifetime of the electron spin state ranging 10^{-9}-10^{-13} second is necessary to yield observable NMR spectra. Even in systems with long T_{1e}, the expected two resonances are difficult to obtain since the NMR signal is very broad.

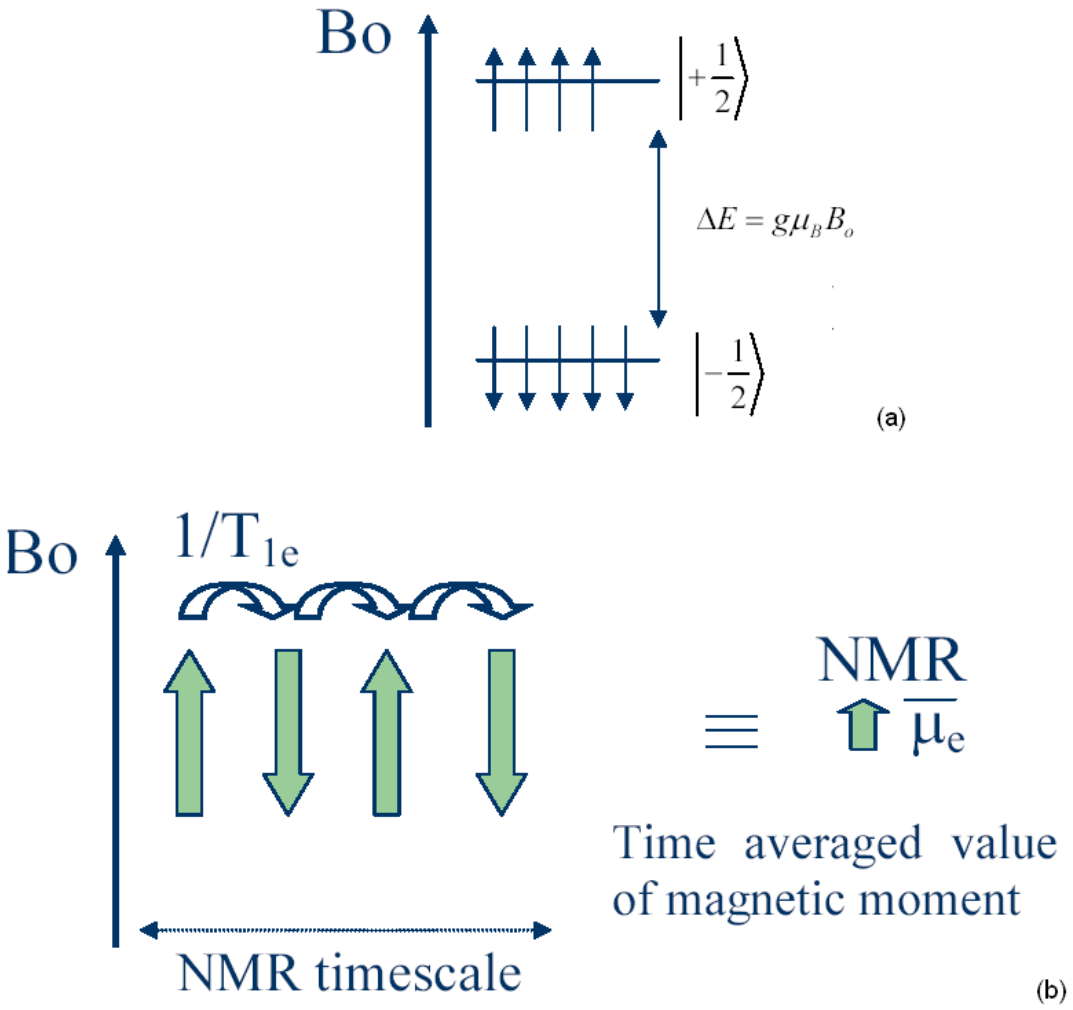

Figure 1.8: Effect of a static magnetic field on a paramagnet with electron magnetic moment μ_e and electronic spin S = ½. Note that the lowest energy level is the -1/2 state due to the negative charge of the electron. b) The relaxation rate ($1/T_{1e}$) of these spin states is faster than the NMR timescale, causing NMR experiments to be only sensitive to the time-averaged value of the magnetic moment.

1.3.3.2 Fermi contact interactions

The Fermi-contact interaction was first derived by Fermi by using relativistic quantum mechanics.[51] The unpaired electron at the nucleus can be represented by the circulating current, which produces a magnetic field with which the nucleus can interact. Thus, the Fermi contact term involves the interaction between the nuclear magnetic moment and the electron magnetic moment, and is proportional to the electron density at the nucleus. The Fermi-contact shift is a measure of the unpaired electron density from the paramagnet which is transferred to the nucleus with the NMR active spin. This occurs via the occupation of the s orbital and is related to the degree of covalency. Since the electron spin relaxation is very rapid, the Hamiltonian for the Fermi contact term H_F can be written as:[52]

$$H_F = I_z A_F \langle S_z \rangle \tag{1.4}$$

where I_z is the z-component of the observed nuclear spin, $\langle S_z \rangle$ is the time (or thermally) averaged value of the paramagnetic electron spin as described in Equation 1.3, and A_F/h is the isotropic electron-nuclear hyperfine coupling constant.

The NMR shift δ, due to the Fermi-contact interaction can be represented by: [53, 54]

$$\delta = \frac{\Delta\omega}{\omega_0} = -\frac{A_F}{h\omega_0}\langle S_z \rangle \tag{1.5}$$

where ω_0 is the observed Larmor frequency, and $\Delta\omega = \omega - \omega_0$.

The size and direction of the shift is determined by the hyperfine coupling constant A_F/h:

$$\frac{A_F}{h} = \frac{g_e \mu_B \gamma_N \rho(r=0)\mu_0}{3S} \qquad (1.6)$$

where $\rho(r = 0)$ is the electron spin density (from the paramagnet ion) at the observed nucleus and γ_N is the gyromagnetic ratio of the observed isotope. $\rho(r = 0)$ depends on the nature and the connectivity of the orbitals of the paramagnet and the observed nucleus, which is determined by bond lengths and angles.

In the layered nickel manganese oxide system, the hyperfine shift is due to the Fermi-contact interaction between the paramagnet ions (Mn^{4+} and Ni^{2+}) and the observed nucleus (Li^+) through oxygen. The interaction will be different in sign with different ions at different angles. For example, in an environment where Li, O and Mn atoms form a 90° bond angle, the overlap between the half-filled t_{2g} orbital of a Mn^{4+} (d^3) ion and an empty 2s Li^+ orbital in the 90° environment may occur either directly or by transfer via a bridging 2p orbital on an oxygen atom. In the case of the transferred hyperfine interaction, an interaction with the t_{2g} electron and the filled oxygen 2p orbital can only occur via a transfer of spin density of the opposite sign to the one already present in the half-filled t_{2g} orbital, as shown in Figure 1.9.a. This results in a transfer of positive spin density to the empty Li 2s orbital and will lead to a positive shift of around 120-150 ppm per Li-O-Mn 90° environment in the ^{6}Li NMR spectrum. In the case of the Li-O-Mn 180° environment (Figure 1.9.b), since there is no direct overlap mechanism available for the t_{2g} orbitals, the hyperfine interaction needs to occur via the empty e_g orbitals. Thus, the exchange coupling between the e_g and t_{2g} orbitals on the same atom favors the transfer of spin

density with the same sign of spin polarization as that in the t_{2g} orbitals to the e_g orbitals. This results in a net transfer of negative spin polarization from Mn^{4+} to the empty 2s Li orbital and consequently, a negative shift. Similarly, the Li-O-Ni^{2+} 90° environment will result in a negative shift as well.

The shift due to Fermi contact interaction is additive. For example, one local environment for Li in Li_2MnO_3 contains 12 sets of Li-O-Mn^{4+} bonds, each with a bond angle of close to 90° (Figure 1.10). This environment is associated with a hyperfine shift of 1500 ppm or a shift of 125 ppm per Li-O-Mn^{4+} interaction. Grey *et al.* explored various model compounds to develop an understanding of the hyperfine interaction mechanism and a database for Li NMR resonances. Thus, the information obtained from the model compounds can be extended to more complicated systems and to rationalize the size of the Li NMR shift, the bond angle of Li-O-M (transition metal ions) and the oxidation state of the transition metals.

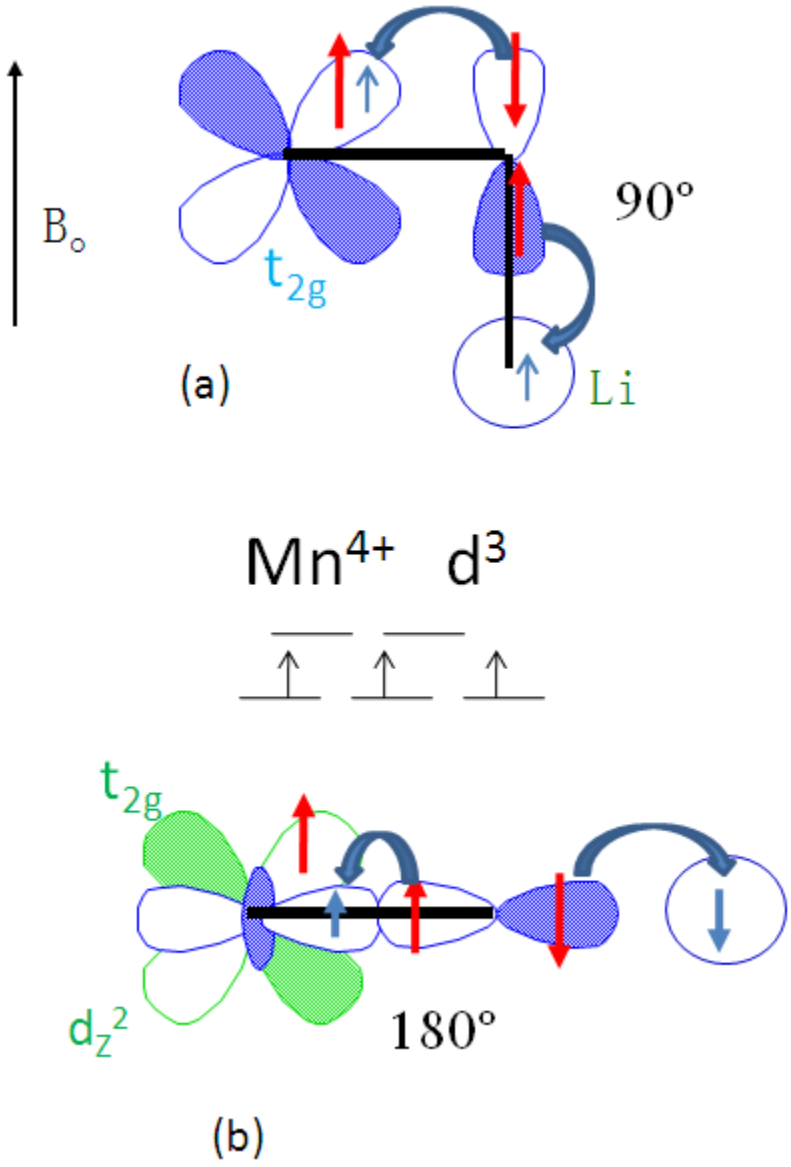

Figure 1.9: Schematic representations of the transfer of spin density from the paramagnet to the lithium nucleus in a) a Li-O-Mn 90º environment and b) a Li-O-Mn 180º environment. Blue arrows denote transferred electron spins to empty orbitals.

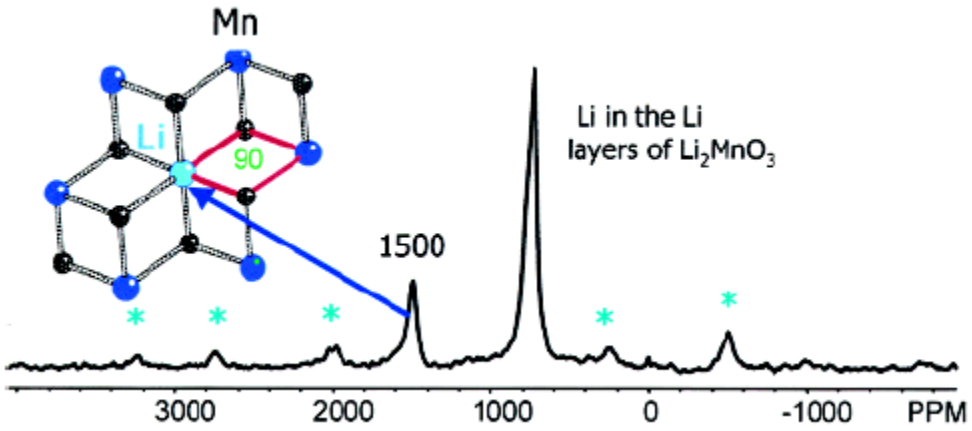

Figure 1.10: ^{6}Li MAS NMR spectrum of the layered compound Li_2MnO_3 acquired at a MAS frequency, ν_r, of 35 kHz. Spinning sidebands are marked with asterisks. The local environment in the Mn^{4+}/Li^{+} layers that gives rise to the isotropic resonance at 1500 ppm is shown. [47]

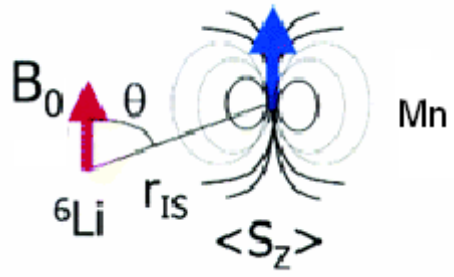

Figure 1.11: Schematic representation of the dipolar coupling between a ^{6}Li nuclear magnetic moment and the net electric magnetic moment due to a nearby paramagnet Mn ion. The spinning sidebands shown in Figure 1.10 mainly result from this interaction and cannot be completely removed by MAS.

1.3.3.3 Paramagnetic dipolar interactions

The dipolar interaction is a through-space interaction between the nuclear and electron magnetic moments, and is similar to the dipolar interaction between nuclear spins. The nuclear spins (*I*) are effected by local magnetic fields of the nearby electronic spins (*S)*, as illustrated in Figure 1.11 and the Hamiltonian for this electron-nucleus interaction, H_{en}, is given by:[47, 55]

$$H_{en} = \frac{\mu_0}{4\pi} \vec{\bar{\mu}}_e \cdot \tilde{D}_{en} \cdot \vec{\mu}_N \qquad (1.7)$$

where $\vec{\mu}_N$ is the nuclear magnetic moment ($=\gamma_N(h/2\pi)I_z$), $\bar{\mu}_e$ is the time (or thermally) averaged magnetic moment of the unpaired electrons, which has been described previously in Equation 1.3, and $\tilde{D}_{en}$ is the dipolar coupling tensor between the nucleus and the unpaired electrons, which is defined by its matrix elements as follows:[56, 57]

$$D_{ij} = \frac{1}{r_{IS}^{3}}(\delta_{ij} - 3e_i e_j) \qquad (1.8)$$

where r_{IS} is the distance between the observed nucleus and the unpaired electron, δij is the Kronecker delta ($\delta ij = 1$ if $i = j$ and 0 if $i \neq j$), *ei* and *ej* are the *x*, *y*, *z* components of a unit vector pointing from the nuclear spin to the electron spin in a chosen coordinate system.

When the electron magnetic moment $\bar{\mu}_e$ is isotropic, and this interaction will result in a line broadening but not a shift.[58] However, for anisotropic electron magnetic moment, a small shift will occur which is usually called the "pseudocontact" shift.[59] In

many battery materials, the size of the pseudocontact shift is presumed to be small and this pseudocontact interaction is generally ignored. Therefore, only the isotropic component of the dipolar interaction is usually considered. The broadening of the NMR spectra due to dipolar coupling can be averaged by using magic angle spinning (MAS) as discussed previously. Generally, the size of the interaction is larger than the magic angle spinning frequency resulting in large spinning sideband manifolds as observed in lithium manganates.

1.4 Powder diffraction

X-ray Powder diffraction is one the most powerful tools used to characterize the structure of crystalline compounds. It can be used to determine the structure of an unknown compound, and it can also be used as a fingerprint technique for detecting and quantifying a known compound or phase in a solid-state solution. The long-range structural information, such as cell parameters and site occupancies, can be obtained by performing a Rietveld refinement. Most of the positive electrode materials used for rechargeable Li ion batteries are crystalline powders and X-ray powder diffraction techniques have been used extensively in this dissertation to characterize them.

Rietveld refinement analysis is a whole diffraction pattern fitting method. It is used to simulate the pattern using a crystallographic model and various functions to account for experimental effects.[60-62] It is a powerful tool to determine the average structure of a material, including the atomic positions and site occupancy. To start the Rietveld refinement, initial information is required, including the cell parameters, space

group and experimental parameters (eg. the wavelength of the light source). There are three important factors to consider during the simulation: the position, the intensity and the profile of all the reflections.

The reflection position depends on the unit cell parameters *a, b*, and *c*. It can be represented by spacing or diffraction angle. The spacing is fixed for certain compounds, but the diffraction angle can vary according to wavelength, which is determined by Bragg's law, which expresses the condition for the constructive interference of the diffracted beams. The Bragg equation is given as:

$$2d\sin\theta = n\lambda \qquad (1.9)$$

where *h, k, l* are the Miller indices, *d* is the interplanar spacing, θ is the diffraction angle, and λ is the wavelength of the beam. The wavelength can be constant or varied depending on the set up of the beam line.

The intensity I_{hkl} of a reflection is determined by the structure factor F_{hkl}^2, which depends on atomic information, such as site occupancy, atomic coordinates, atomic motion, and atomic scattering factor. The structure factor F_{hkl} is given by the following equation: [61]

$$F_{hkl} = \sum_j O_j f_j \exp[2\pi i(hx_j + ky_j + lz_j)]\exp[-M_j] \qquad (1.10)$$

where x_j, y_j, and z_j are the atomic coordinates of the *j*th atom in the unit cell, f_j is the scattering factor of *j*th atom, and O_j is the site occupancy multiplier, which is the actual site occupancy divided by the site multiplicity. The component *Mj* represents the atomic motion and is given by:[61]

$$M_j = 8\pi^2 u_j^2 \sin^2(\theta/\lambda^2) \qquad (1.11)$$

where u_j^2 is the root mean square thermal/static displacement (or 'temperature factor') of the *j*th atom parallel to the scattering vector.

The Rietveld analysis depends on the calculation of the structure factor expected from a model structure. This method consists of a least-square refinement, which is to minimize the difference between the calculated profile and the experimental pattern, given by the following term S_y:

$$S_y = \sum_i w_i (y_i(obs) - y_i(calc))^2 \qquad (1.12)$$

where w_i is the weighting factor ($1/y_i$) of the *ith* data point, *yi(obs)* is the total observed intensity at *ith* the point. The total calculated intensity *yi(calc)* at the *ith* the point is given by:

$$y_i(calc) = B + s.A.p.\xi \sum_{hkl} L_{hkl} P_{hkl} F_{hkl}^2 . profile(2\theta_{hkl} - 2\theta_i) \qquad (1.13)$$

where *B*, *s*, *A*, *p* and ξ are the parameters associated with background, scale factor, absorption, polarization and extinction of the experiment, respectively. L_{hkl} and P_{hkl} are the geometry and preferred orientation parameters.

The *profile* of each reflection is determined by the profile function *profile* ($2\theta_{hkl}$-$2\theta_i$) (Equation 1.13). In powder diffraction, the reflection profiles are typically a pseudo-Voigt function, which is a convolution of a Gaussian and a Lorentzian function.[61, 63-67] The pseudo-Voigt function has been widely used to model peak shapes in powder diffraction, and is typically used with angle dependent functions. One of the main profile parameters is the Full Width at Half Maximum (*FWHM)*, which is represented by:

$$FWHM_G^2 = U\tan^2\theta + V\tan\theta + W \quad (1.14)$$

$$FWHM_L^2 = X\tan\theta + Y/\cos\theta \quad (1.15)$$

U, *V*, *W*, *X*, and *Y* are usually the parameters that can be refined. *V* must be negative, and all the others must be positive. At low scattering angle, the peak asymmetry is more severe, which results from the measurement geometry. Some parameters accounting for asymmetry can be refined or calibrated from reference compounds.

In the powder diffraction, the position of the reflection can be used for indexing and determination of structure using Rietveld methods. As well, the broadening of the reflection is related to the crystallite size, according to the Debye-Scherrer equation:[68]

$$B(2\theta) = \frac{\alpha\lambda}{L\cos\theta} \quad (1.16)$$

where *B(2θ)* is the full width in radians of a given *hkl* reflection measured at half its maximum intensity, λ is the wavelength of the x-rays, α is a constant which usually equals to 0.9, and *L* is the crystallite size in the direction perpendicular to the reflecting planes.

1.5 X-ray absorption spectroscopy (XAS)

X-ray absorption spectroscopy is a powerful technique to analyze the oxidation state and the local environment of center atoms. It utilizes the x-ray photoelectric and wave nature of the electron to determine local structure around selected atomic species in materials.[69, 70] Unlike x-ray diffraction, it does not require long range translational order- it works equally well in amorphous materials, liquids, (poly) crystalline solids, and molecular gases.

The experimental set up of XAS is simple and straightforward as illustrated in Figure 12. The monochromatic x-ray beam hits on a thin homogeneous sample of the investigated materials, and the intensities of the incident (I_0) and the transmitted x-ray beam (I or I_f, "f" for the fluorescence mode) are recorded in the stepwise progression of the incident photon energy. Then relationship between I_0 and I can be represented as flows:[71-73]

$$I = I_0 e^{-\mu(E)d} \qquad (1.17)$$

where $\mu(E)$ is the absorption coefficient, and d is the thickness of the sample. Then the absorption coefficient at a given photon energy E can be obtained by measuring I and I_0. The energy dependence of the absorption coefficient is collected by a stepwise scan of the photon energy in the monochromatic beam with the Bragg monochromator.

X-ray absorption spectra are produced over the range of 200 – 35,000 eV. The dominant physical process is one where the absorbed photon ejects a core photoelectron from the absorbing atom, leaving behind a core hole. The atom with the core hole is now

excited. The ejected photoelectron's energy will be equal to that of the absorbed photon minus the binding energy of the initial core state. The ejected photoelectron then interacts with electrons in the surrounding non-excited atoms.

Typical XAS spectra show a steep rise at the core-level binding energy of x-ray absorbing atoms and attenuate gradually with the X-ray energy as shown in Figure 12. They are usually divided into three parts: the edge region, the X-ray Absorption Near Edge Structure (XANES)[74, 75] and the extended X-ray absorption fine structure (EXAFS) (Figure 13).[76, 77] The absorption peaks at the absorption edges in a range of about 5 eV is due to electronic transitions to first unoccupied molecular levels above the chemical potential. It can give the information of the oxidation state of the absorbing atoms. The near-edge structure in an absorption spectrum covers the range between the threshold and the point at which the EXAFS begins. One normally thinks of the XANES as extending to an energy of the order 50 eV above the edge. The XANES is determined by the atomic geometrical arrangements in a local cluster around the absorbing atom via the multiple scattering of the excited photoelectron, so the shape of XANES is strongly correlated to the local structure of the absorbing atoms. Usually the first two parts of the XAS spectra, the edge region and the XANES part, are used to determine the oxidation states of the center atoms in the investigated materials. Model compounds containing the studied atom with similar local structure to the investigated material are used to set as a reference, then the spectra of the investigated material can be compared with the model compounds to derive the oxidation states of the absorbing atoms. The oscillatory structure extending for hundreds of electron volts past the edges was called the EXAFS, which is assigned to the single scattering of the excited photoelectron by neighboring atoms. As shown in Figure

14, the photo-electronic waves emitted from the central atom hit neighboring atoms which in turn backscatter. This backscattered wave either constructively or destructively interferes, giving rise to oscillation in the amplitude. By analyzing the oscillating spectrum at energies just above the absorption edge, it is possible to obtain information relating to the coordination environment of the central excited atom.

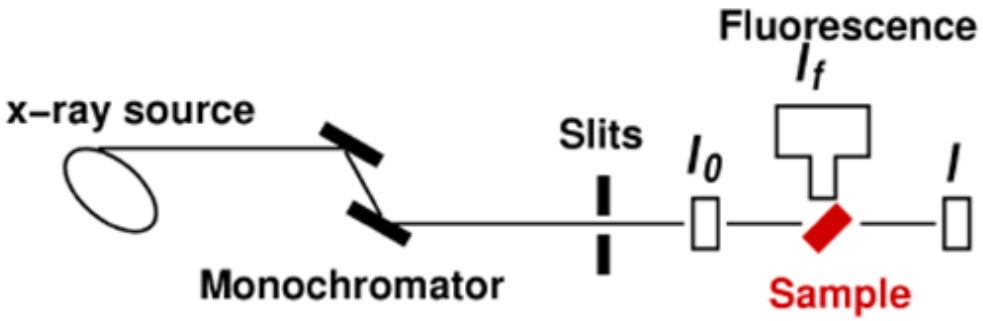

Figure 1.12: The experimental set up of X-ray spectroscopy. As shown in the figure, when the detector is on the same side as I_0, it is in fluorescence mode; when the detector is on the other side of sample, it is in transmission mode. The set up of the mode is determined by the concentration of the absorbing atom in the sample. If the concentration is high, transmission mode needs to be used. The fluorescence mode is for low concentration samples.

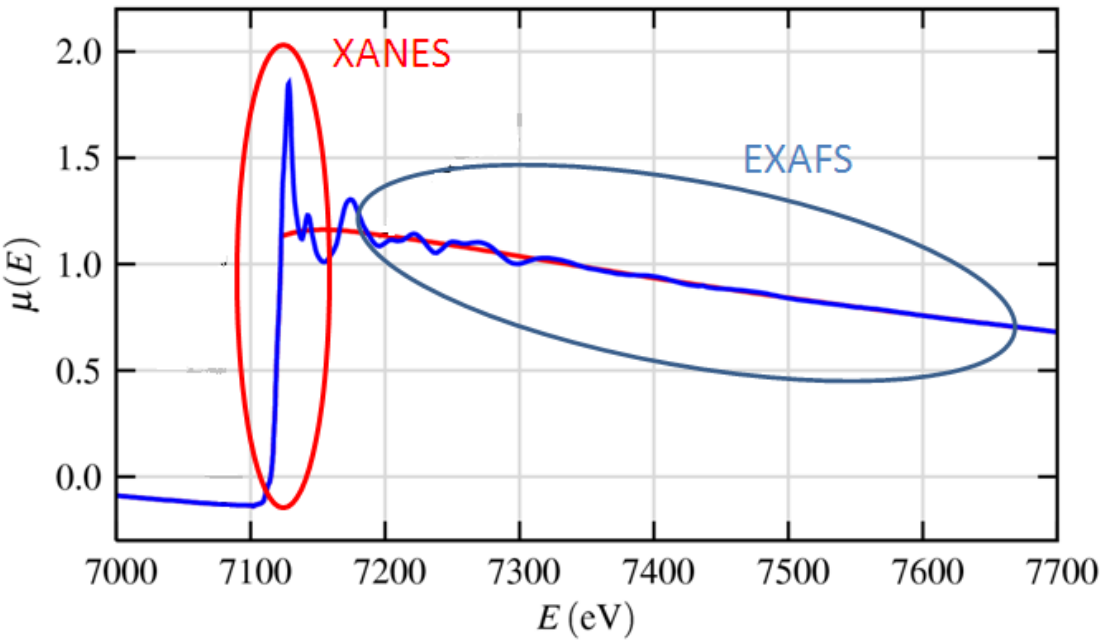

Figure 1.13: An example of the XAS spectrum.

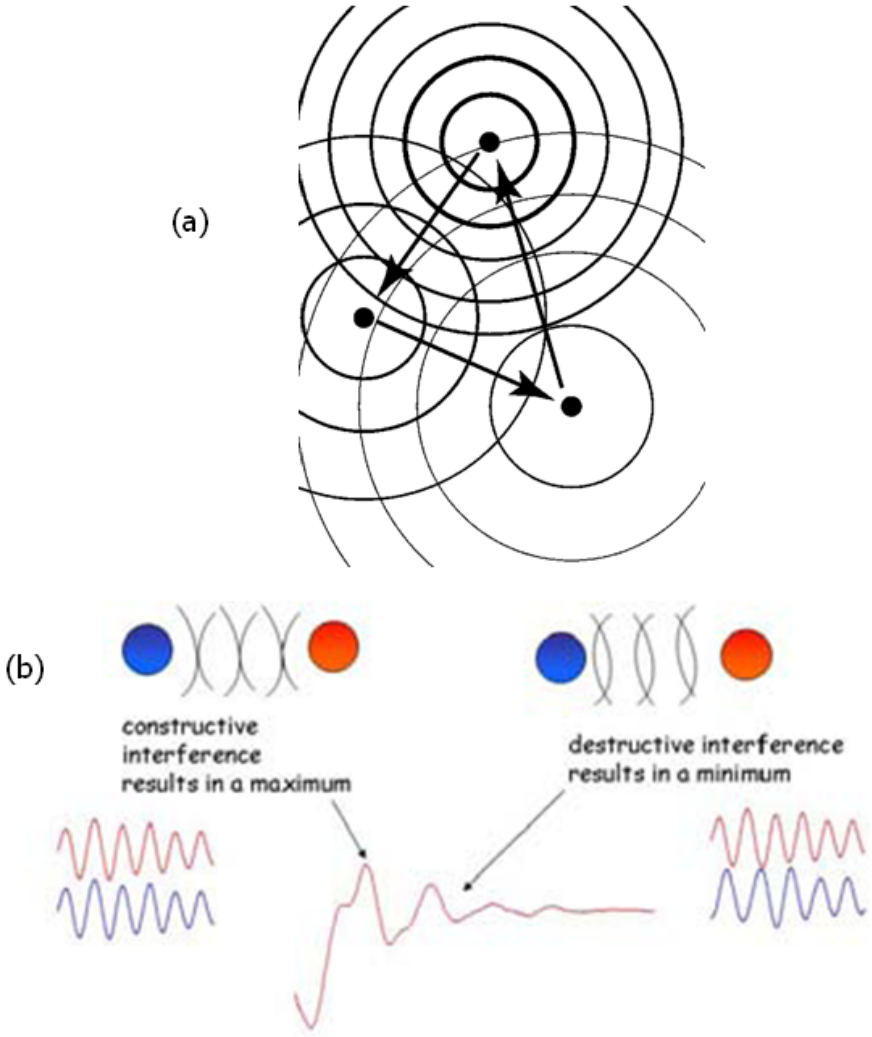

Figure 1.14: The illustration of (a) the Photo-electronic waves emitted from the central atom interference with neighboring atoms and (b) the reason for the oscillation of EXAFS.

1.6 References

1. Armstrong, A. R.; Robertson, A. D.; Gitzendanner, R.; Bruce, P. G. 1999; Academic Press Inc: 1999; pp 549-556.

2. Tarascon, J. M.; Armand, M., *Nature* **2001,** 414, (6861), 359-367.

3. Bruce, P. G., *Chemical Communications* **1997**, (19), 1817-1824.

4. Megahed, S.; Scrosati, B., *Journal of Power Sources* **1994,** 51, (1-2), 79-104.

5. Markovsky, B.; Talyossef, Y.; Salitra, G.; Aurbach, D.; Kim, H. J.; Choi, S., *Electrochemistry Communications* **2004,** 6, (8), 821-826.

6. Ein-Eli, Y.; Howard, W. F.; Lu, S. H.; Mukerjee, S.; McBreen, J.; Vaughey, J. T.; Thackeray, M. M., *Journal of the Electrochemical Society* **1998,** 145, (4), 1238-1244.

7. Ohzuku, T.; Takeda, S.; Iwanaga, M. 1999; 1999; pp 90-94.

8. Kawai, H.; Nagata, M.; Kageyama, H.; Tukamoto, H.; West, A. R., *Electrochimica Acta* **1999,** 45, (1-2), 315-327.

9. Dahn, J. R.; Zheng, T.; Liu, Y. H.; Xue, J. S., *Science* **1995,** 270, (5236), 590-593.

10. Poizot, P.; Laruelle, S.; Grugeon, S.; Dupont, L.; Tarascon, J. M., *Nature* **2000,** 407, (6803), 496-499.

11. Armand, M.; Tarascon, J. M., *Nature* **2008,** 451, (7179), 652-657.

12. Lu, Z. H.; MacNeil, D. D.; Dahn, J. R., *Electrochemical and Solid State Letters* **2001,** 4, (12), A200-A203.

13. Ohzuku, T.; Makimura, Y., *Chemistry Letters* **2001**, (8), 744-745.

14. Makimura, Y.; Ohzuku, T. 2003; 2003; pp 156-160.

15. Lu, Z. H.; Dahn, J. R., *Journal of the Electrochemical Society* **2002,** 149, (7), A815-A822.

16. Lu, Z. H.; Beaulieu, L. Y.; Donaberger, R. A.; Thomas, C. L.; Dahn, J. R., *Journal of the Electrochemical Society* **2002,** 149, (6), A778-A791.

17. Johnson, C. S.; Kim, J. S.; Kropf, A. J.; Kahaian, A. J.; Vaughey, J. T.; Fransson, L. M. L.; Edstrom, K.; Thackeray, M. M., *Chemistry of Materials* **2003,** 15, (12), 2313-2322.

18. Yoon, W. S.; Paik, Y.; Yang, X. Q.; Balasubramanian, M.; McBreen, J.; Grey, C. P., *Electrochemical and Solid State Letters* **2002,** 5, (11), A263-A266.

19. Yoon, W. S.; Grey, C. P.; Balasubramanian, M.; Yang, X. Q.; McBreen, J., *Chemistry of Materials* **2003,** 15, (16), 3161-3169.

20. Grey, C. P.; Yoon, W. S.; Reed, J.; Ceder, G., *Electrochemical and Solid State Letters* **2004,** 7, (9), A290-A293.

21. Meng, Y. S.; Ceder, G.; Grey, C. P.; Yoon, W. S.; Shao-Horn, Y., *Electrochemical and Solid State Letters* **2004,** 7, (6), A155-A158.

22. Meng, Y. S.; Ceder, G.; Grey, C. P.; Yoon, W. S.; Jiang, M.; Breger, J.; Shao-Horn, Y., *Chemistry of Materials* **2005,** 17, (9), 2386-2394.

23. Kim, J. S.; Johnson, C. S.; Vaughey, J. T.; Thackeray, M. M.; Hackney, S. A., *Chemistry of Materials* **2004,** 16, (10), 1996-2006.

24. Johnson, C. S.; Kim, J. S.; Lefief, C.; Li, N.; Vaughey, J. T.; Thackeray, M. M., *Electrochemistry Communications* **2004,** 6, (10), 1085-1091.

25. Reed, J.; Ceder, G., *Electrochemical and Solid State Letters* **2002,** 5, (7), A145-A148.

26. Yoon, W. S.; Kim, N.; Yang, X. Q.; McBreen, J.; Grey, C. P., *Journal of Power Sources* **2003,** 119, 649-653.

27. Armstrong, A. R.; Holzapfel, M.; Novak, P.; Johnson, C. S.; Kang, S. H.; Thackeray, M. M.; Bruce, P. G., *Journal of the American Chemical Society* **2006,** 128, (26), 8694-8698.

28. Robertson, A. D.; Bruce, P. G., *Electrochemical and Solid State Letters* **2004,** 7, (9), A294-A298.

29. Robertson, A. D.; Bruce, P. G., *Chemical Communications* **2002**, (23), 2790-2791.

30. Robertson, A. D.; Bruce, P. G., *Chemistry of Materials* **2003,** 15, (10), 1984-1992.

31. Thackeray, M. M.; David, W. I. F.; Goodenough, J. B., *Materials Research Bulletin* **1982,** 17, (6), 785-793.

32. H. Arai, S. O., Y. Sakurai, J. Yamaki, *Journal of Power Sources* **1997,** 68.

33. Badway, F.; Pereira, N.; Cosandey, F.; Amatucci, G. G., *Journal of the Electrochemical Society* **2003,** 150, (9), A1209-A1218.

34. Badway, F.; Cosandey, F.; Pereira, N.; Amatucci, G. G., *Journal of the Electrochemical Society* **2003,** 150, (10), A1318-A1327.

35. Bervas, M.; Badway, F.; Klein, L. C.; Amatucci, G. G., *Electrochemical and Solid State Letters* **2005,** 8, (4), A179-A183.

36. Badway, F.; Mansour, A. N.; Pereira, N.; Al-Sharab, J. F.; Cosandey, F.; Plitz, I.; Amatucci, G. G., *Chemistry of Materials* **2007,** 19, (17), 4129-4141.

37. Plitz, I.; Badway, F.; Al-Sharab, J.; DuPasquier, A.; Cosandey, F.; Amatucci, G. G., *Journal of the Electrochemical Society* **2005,** 152, (2), A307-A315.

38. Roert E. Doe, K. A. P., Y. Shirley Meng, Gerbrand Ceder, *in preparation* **2008**.

39. Pan, C. J.; Lee, Y. J.; Ammundsen, B.; Grey, C. P., *Chemistry of Materials* **2002,** 14, (5), 2289-2299.

40. Lee, Y. J.; Grey, C. P., *Chemistry of Materials* **2000,** 12, (12), 3871-3878.

41. Lee, Y. J.; Grey, C. P., *Journal of the Electrochemical Society* **2002,** 149, (2), A103-A114.

42. Lee, Y. J.; Wang, F.; Grey, C. P., *Journal of the American Chemical Society* **1998,** 120, (48), 12601-12613.

43. Lee, Y. J.; Wang, F.; Mukerjee, S.; McBreen, J.; Grey, C. P., *Journal of the Electrochemical Society* **2000,** 147, (3), 803-812.

44. Lee, Y. J.; Grey, C. P., *Journal of Physical Chemistry B* **2002,** 106, (14), 3576-3582.

45. Lee, Y. J.; Park, S. H.; Eng, C.; Parise, J. B.; Grey, C. P., *Chemistry of Materials* **2002,** 14, (1), 194-205.

46. Andrew, E. R.; Bradbury, A.; Eades, R. G., *Nature* **1958,** 182, (4650), 1659-1659.

47. Grey, C. P.; Dupre, N., *Chemical Reviews* **2004,** 104, (10), 4493-4512.

48. Drago, R. S.; Zink, J. I.; Richman, R. M.; Perry, W. D., *Journal of Chemical Education* **1974,** 51, (6), 371-376.

49. Drago, R. S.; Zink, J. I.; Richman, R. M.; Perry, W. D., *Journal of Chemical Education* **1974,** 51, (7), 464-467.

50. Kittel, C., *Introduction to Solid State Physics*. John Wiley & Sons: New York, 1986.

51. Fermi, E. Z. Z., *Phys.* **1930,** 60, 320.

52. Jesson, J. P., *NMR of Paramagnetic molecules: Principles and Applications* Academic Press: New York, 1973.

53. McConnell, H. M.; Berger, S. B., *Journal of Chemical Physics* **1957,** 27, (1), 230-234.

54. McConnell, H. M.; Robertson, R. E., *Journal of Chemical Physics* **1958,** 29, (6), 1361-1365.

55. Nayeem, A.; Yesinowski, J. P., *Journal of Chemical Physics* **1988,** 89, (8), 4600-4608.

56. Mehring, M., *Principle of High Resolution NMR in Solids*. Springer-Verlag: New York, 1983.

57. Haeberlen, U., *High-Resolution NMR in Solids*. Springer-Verlag: New York, 1983.

58. Bertini, I. L., C.; Parigi, G., *Solution NMR of Paramagnetic Molecules*. Elsevier: Amsterdam, 2001.

59. Kurland, R. M., B.R., *J. Mag. Reson.* **1970,** 2, 286.

60. Rietveld, H. M., *Journal of Applied Crystallography* **1969,** 2, 65-&.

61. Young, R. A., *The Rietveld Method*. Oxford Univeristy Press: 1993.

62. Young, R. A.; Wiles, D. B., *Journal of Applied Crystallography* **1982,** 15, (AUG), 430-438.

63. Caglioti, G.; Paoletti, A.; Ricci, F. P., *Nuclear Instruments & Methods* **1958,** 3, (4), 223-228.

64. Thompson, P.; Cox, D. E.; Hastings, J. B., *Journal of Applied Crystallography* **1987,** 20, 79-83.

65. Howard, C. J., *Journal of Applied Crystallography* **1982,** 15, (DEC), 615-620.

66. Stephens, P. W., *Journal of Applied Crystallography* **1999,** 32, 281-289.

67. McCusker, L. B.; Von Dreele, R. B.; Cox, D. E.; Louer, D.; Scardi, P., *Journal of Applied Crystallography* **1999,** 32, 36-50.

68. West, A. R., *Solid State Chemistry and it's Application*. John Wiley & Son: New York: 1992.

69. W., J. R., *The optical properties of the diffraction of x-rays*. Ox Bow press: Woodbridge, 1962.

70. J., B., *Neutron and synchrotron radiation for condensed matter studies* Springer Verlag: Berlin, 1993.

71. E., K. E., *Handbook on Synchrotron Radiation*. Northolland Publishing Company: Amsterdam, 1983.

72. J., S., *NEXAFS Sepctroscopy* Springer Verlag: Berlin, 1992.

73. Konningsberger, R., *X-ray absorption, principles, applications, techniques of EXAFS SEXAFS and XANES*. John-Wiley & Sons: New York, 1988.

74. Bianconi, A., *Applied Surface Science* **1980,** 6, (3-4), 392-418.

75. Williams, A. R.; Lang, N. D., *Physical Review Letters* **1978,** 40, (14), 954-957.

76. B., R. B., *Z. Phys.* **1929,** 55, 119.

77. A., K. B. L. G., *Phys. Rev.* **1930,** 36, 648.

Chapter 2

Structural Analysis of Layered Lithium Nickel Manganese Oxide and the Processing Effect on the Structure

Abstract

Two layered compounds, $Li[Li_{1/9}Ni_{1/3}Mn_{5/9}]O_2$ (x =1/3) and Li_2MnO_3 (x =0) of the $Li[Ni_xLi_{1/3-2x/3}Mn_{2/3-x/3}]O_2$ series were studied by synchrotron X-ray powder diffraction (XRD) analyses and solid state magnetic nuclear resonance (NMR). The XRD pattern of Li_2MnO_3 can be indexed with the *C2/m* space group, and the pattern of $Li[Li_{1/9}Ni_{1/3}Mn_{5/9}]O_2$ can be indexed with $R\bar{3}m$ space group. These two samples were processed differently. No obvious difference is observed in the XRD patterns of Li_2MnO_3 synthesized at different conditions, but the structure of the $Li[Li_{1/9}Ni_{1/3}Mn_{5/9}]O_2$ samples synthesized at 1000°C for 72 hours show more honey comb ordering in the transition metal layers.

Part of this chapter is based on the paper: "Cation Ordering in Layered O3 $Li[Ni_xLi_{1/3-2x/3}Mn_{2/3-x/3}]O_2$ ($0 < x < 1/2$) Compounds", Y. S. Meng, G. Ceder, C. P. Grey, W.-S. Yoon, M. Jiang, J. Breger, and Y. Shao-Horn., *Chem. Mater.* **2005,** *17,* 2386-2394. The Rietveld refinements were performed by Y. S. Meng, and Y. Shao-Horn.

2.1 Introduction

Layered compounds of the $Li[Ni_xLi_{1/3-2x/3}Mn_{2/3-x/3}]O_2$ ($0 < x < 1/2$) series, with alternating lithium layers and transition metal rich layers separated by close-packed oxygen arrays, have been studied extensively as potential positive electrode materials to replace $LiCoO_2$ for lithium rechargeable batteries in recent years.[1-12] The nickel content in the nominal compositions of these materials increases from $x = 0$ in Li_2MnO_3 $\{Li[Li_{1/3}Mn_{2/3}]O_2\}$ to $x = 1/2$ in $Li[Ni_{1/2}Mn_{1/2}]O_2$ upon substitution of lithium and manganese ions in the layered structure, as shown in Figure 1.4. These materials with $x \geq 1/3$ not only have excellent reversible capacities but also improved thermal stability.[1, 13, 14] It has been shown that upon lithium removal Ni^{2+} is oxidized to Ni^{4+} and Mn^{4+} remains unchanged above an average oxidation state of 3.5 necessary for a stable MnO_6 coordination,[3, 7, 15] which is associated with the structural stability of the layered structure of $Li[Ni_xLi_{1/3-2x/3}Mn_{2/3-x/3}]O_2$ during electrochemical cycling relative to the spinel form, unlike layered $LiMnO_2$.[16-18] The electrochemical behavior of these electrode materials is sensitive to nickel content, synthesis precursors, synthesis temperature, heat-treatment time, and cooling rates, which could be attributed to different cation arrangements in the layered structure.[12, 14]

A small fraction of nickel ions has been shown to reside in the lithium layers. This fraction is the highest in $Li[Ni_{1/2}Mn_{1/2}]O_2$ (around 9-12%) as the degree of nickel and lithium interlayer mixing (exchange) decreases and the nickel content x in $Li[Ni_xLi_{1/3-2x/3}Mn_{2/3-x/3}]O_2$ is reduced.[1, 2, 19] In addition, the extent of the mixing has been reported to decrease as the synthesis temperature increases from 900 to 1000 °C.

Given the charge difference between Li^+ and Mn^{4+}, one expects a strong ordering tendency between these ions. In-plane ordering of lithium and transition metal ions for compositions between $Li[Li_{1/9}Ni_{1/3}Mn_{5/9}]O_2$ (x = 1/3, denoted as Ni1/3) and Li_2MnO_3 {$Li[Li_{1/3}Mn_{2/3}]O_2$} (x = 0) has been evidenced by X-ray diffraction,[12, 20, 21] solid-state nuclear magnetic resonance (NMR),[5] and extended X-ray absorption fine structure (EXAFS) studies.[6] In the $Li[Li_{1/3}Mn_{2/3}]O_2$ structure, the ordering of Li^+ and Mn^{4+} with a ratio (1:2) on the trigonal lattice leads to the formation of two distinct crystallographic α and β, sites and thus a $\sqrt{3}\boldsymbol{a}_{hex} \times \sqrt{3}\boldsymbol{a}_{hex}$ supercell as reported in $Li_{0.33}CoO_2$[22, 23] and $Li_{0.33}NiO_2$[24] associated with lithium and vacancy ordering, as shown in Figure 2.1a. It should be noted that the conventional cell definition of Li_2MnO_3 is monoclinic having space group $C2/m$,[20] with $\boldsymbol{a}_{mon.}$ = 5.011 Å ($\approx\sqrt{3}\boldsymbol{a}_{hex.}$), $\boldsymbol{b}_{mon.}$=8.679 Å ($\approx\sqrt{3}\boldsymbol{a}_{hex.}$), and $\boldsymbol{c}_{mon.}$= 5.105 Å, $\beta_{mon.}$=109.46°, as shown in Figure 2.1b. With the addition of nickel to the transition metal layer that now has a nominal composition of $Ni_xLi_{1/3-2x/3}Mn_{2/3-x/3}$, the $\sqrt{3}\boldsymbol{a}_{hex} \times \sqrt{3}\boldsymbol{a}_{hex}$ supercell having lithium and nickel on α, and nickel and manganese on β sites remains evident from X-ray powder diffraction analyses until x value reaches 1/3. However, the space group for the compounds with nickel is changed from $C2/m$ to $R\bar{3}m$, with keeping the same layered structure (Figure 2.2).

In this chapter, we studied two members in the $Li[Ni_xLi_{1/3-2x/3}Mn_{2/3-x/3}]O_2$ ($0 < x < 1/2$) series: Li_2MnO_3 and $Li[Li_{1/9}Ni_{1/3}Mn_{5/9}]O_2$ by X-ray diffraction (XRD) and solid state nuclear magnetic resonance (NMR). The combination of these two techniques will give insight into both short and long range ordering. The correlation between synthesis conditions and structure will be discussed as well. The stacking faults presented in the materials synthesized at different conditions are discussed in Chapter 4.

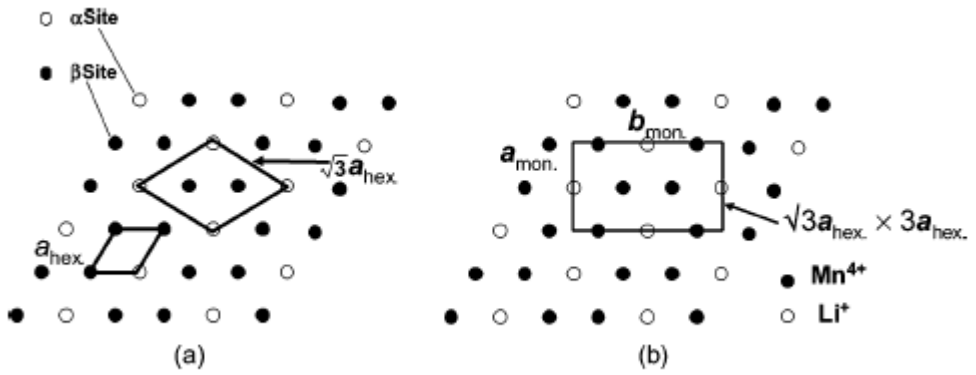

Figure 2.1: In-plane ordering of two different types of sites with a ratio of 1:2 (α sites in open circles and β sites in solid circles) on the trigonal lattice leads to the definition of (a) a $\sqrt{3}\boldsymbol{a}_{hex.}\times\sqrt{3}\boldsymbol{a}_{hex.}$ supercell (marked by lines) as reported in $Li_{0.33}CoO_2$ and $Li_{0.33}NiO_2$ or (b) an $\boldsymbol{a}_{mon.}$ ($\sim\sqrt{3}\boldsymbol{a}_{hex.}$) $\times$ $\boldsymbol{b}_{mon.}$ ($\sim 3\boldsymbol{a}_{hex}$) supercell (marked by lines) as observed in Li_2MnO_3.

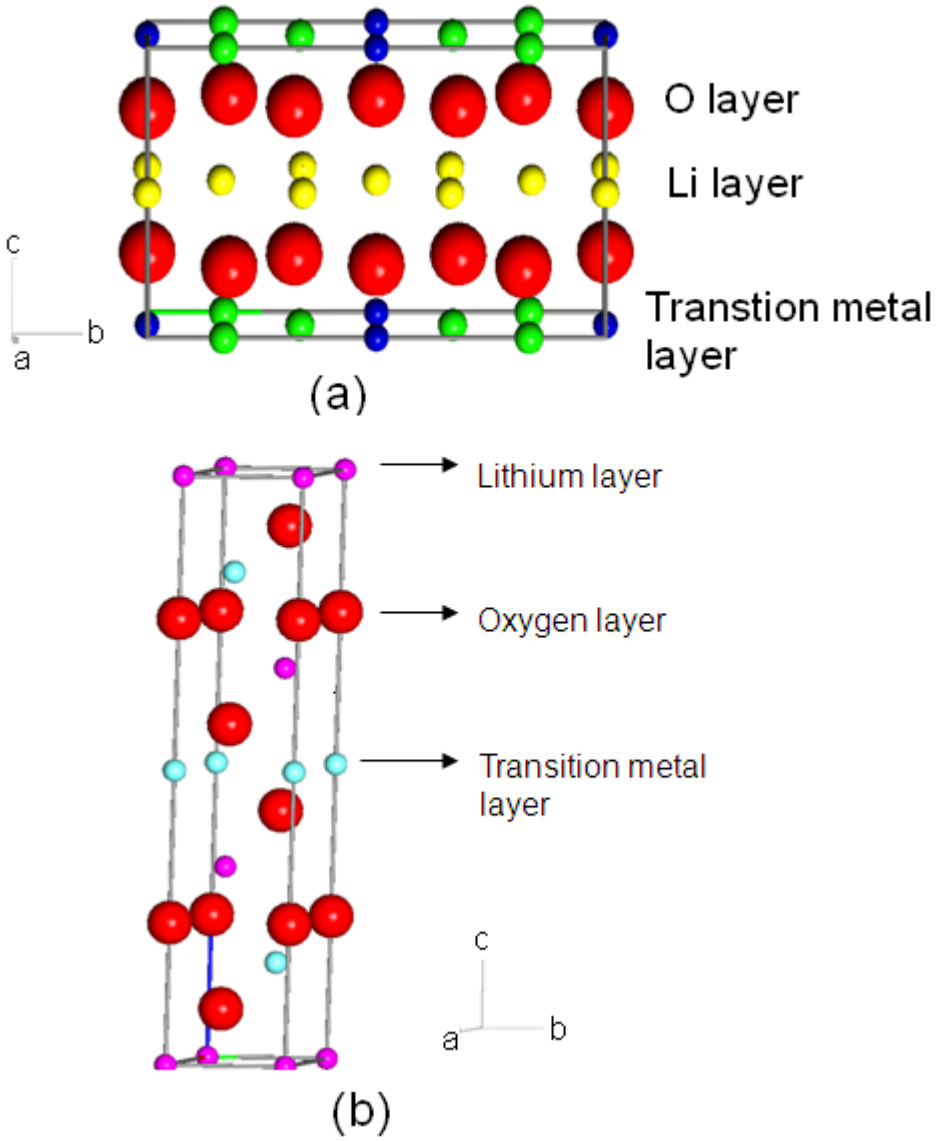

Figure 2.2: The illustration of the layered structures of (a) Li_2MnO_3 with C/2m space group and (b) $Li[Li_{1/9}Ni_{1/3}Mn_{5/9}]O_2$ with $R\bar{3}m$ space group.

2.2 Experimental

2.2.1 Synthesis

Stoichiometric amounts of Li_2CO_3 and Mn_2O_3 were mixed and fired at 650 °C for 12 h to remove the CO_2. Two different heating temperatures were used for the next step of synthesis, 850°C and 1000°C. Under each temperature, heating time was varied between 24 hours and 5 days, and the samples were either cooled slowly at a rate of 1 °C/min or quenched with liquid nitrogen. These samples are denoted to as the following format: Li_2MnO_3-heating temperature-heating time-cooling method. For example, the sample heated at 850°C for 24 hours with slow cooled method is referred as: Li_2MnO_3-850°C-24hrs-sc ("q" for quenched sample). $Li[Li_{1/9}Ni_{1/3}Mn_{5/9}]O_2$ powders were prepared by the double-mixed hydroxide method. An aqueous solution of stoichiometric amounts of transition metal nitrates was prepared and slowly dripped (1–2 h) into 400mL of a stirred solution of LiOH using a burette, yielding a precipitate of $M(OH)_2$, where M=Mn and Ni, with a homogeneous cation distribution. The dried precipitate was mixed with $Li(OH)\bullet H_2O$ in stoichiometric proportions. The mixture was then heated in air at 480°C for 12 h followed by a second heating at 900°C or 1000 °C for 12 hours or 72 hours. After the second heating, materials were cooled at a rate of 1 °C/min or quenched with liquid nitrogen. These samples are referred to with the same notation as used for Li_2MnO_3, according to their processing procedures. The stacking faults in the samples Li_2MnO_3-850-1d-sc, Li_2MnO_3-1000-1m-sc, and Ni1/3-1000-3d –sc are investigated in Chapter 3.

2.2.2 X-ray diffraction

Laboratory type X-ray diffraction (XRD) was performed on a Scintag powder X-ray diffractometer equipped with a Cu target X-ray tube (Cu $K\alpha_1$:λ=1.54 Å). A range of 2θ values from 10° to 90° with a scanning rate of 2° per minute and a step size of 0.02° was used. For the data used for Rietveld refinement, high resolution (HR)-XRD was collected at beam line 32-ID at the Advanced Photon Source (APS) in Argonne National Laboratory (λ=0.4958 Å) or at the X7B beam line at National Synchrotron Light Source (NSLS) at Brookhaven National Laboratory (λ=0.9220 Å).

2.2.3 Solid state nuclear magnetic resonance

^{6}Li MAS NMR spectroscopy was performed on discharged and charged CCN-FeF_3 samples with a 1.8 mm probe on a CMX-200 spectrometer using a magnetic field of 4.7 T. A spinning speed of 38 kHz and a rotor-synchronized spin-echo sequence (π/2–τ–π–τ–acq) were used to acquire the spectra. The spectra were collected at an operating frequency of 29.46 MHz with π/2 pulses of 3.5 μs and a delay time of 0.2 s. The spectrum was referenced to 1 M ^{6}LiCl (in H_2O) at 0 ppm.

2.3 Results and Discussions

2.3.1 Synchrotron X-ray diffraction analysis

Synchrotron X-ray diffraction data of the Li_2MnO_3-850°C-24hrs-q sample is shown in Figure 2.3. Both samples were found to be phase pure. Major diffraction peaks

of the sample Li_2MnO_3 are indexed according to the conventional monoclinic cell with space group $C2/m$. Profile matching of the synchrotron Li_2MnO_3 data showed that the structural parameters of the conventional monoclinic cell with space group $C2/m$ were $\boldsymbol{a}_{mon.}$= 4.926 Å, $\boldsymbol{b}_{mon.}$ = 8.527 Å, $\boldsymbol{c}_{mon.}$ = 5.028 Å, and β=109.22°. It should be noted that these parameters obtained in this study are slightly different from the values of previous single-crystal X-ray diffraction analyses ($\boldsymbol{a}_{mon.}$ = 4.937 Å, $\boldsymbol{b}_{mon.}$ = 8.532 Å, $\boldsymbol{c}_{mon.}$ =5.030 Å, and β=109.46°). In-plane ordering of Li^+ and Mn^{4+} (1:2) leads to deviation in the a/b ratio of the rhombohedral layered structure as the electrostatic interactions of Li^+ and Mn^{4+} ions differ along the $\boldsymbol{a}$ and $\boldsymbol{b}$ directions. The deviation in this ratio from the ideal value (1.732) decreases the crystal symmetry from rhombohedral to monoclinic, where the crystal structure can be modified by varying the a/b ratio and/or β. It is important to point out that the $a_{mon.}/b_{mon.}$ and β values of the Li_2MnO_3 sample in this study are 1.731 and 109.22°, which are closer to the ideal value (1.732 and 109.14° for the rhombohedral symmetry) than those of Li_2MnO_3 reported in the literature (single-crystal Li_2MnO_3, 1.728 and 109.46°; and Li_2MnO_3 powder, 1.730 and 109.39°). It is speculated that the difference in structural parameters could be attributed to the fact that the Li_2MnO_3 powder sample used in this study had slightly higher strains than the single-crystal and powder samples reported previously, as evidenced by the broadening of selective superlattice peaks (Figure 2.3).

Rietveld refinements of the synchrotron data of the Li_2MnO_3 sample were attempted but the superstructure peaks associated with the ordering of Li^+ and Mn^{4+} in the $Li_{1/3}Mn_{2/3}$ layer in the range of $6° \leq 2\theta \leq 11°$ with selective, pronounced peak broadening and asymmetry could not be modeled successfully, as shown in the insert of

Figure 2.3. Therefore, atomic positions and occupancies could not be refined with reasonable reliability factors. NMR analysis of this Li_2MnO_3 sample revealed that there was no or little evidence of in-plane Li^+ and Mn^{4+} mixing in the $Li_{1/3}Mn_{2/3}$ layer. It is proposed here that the selective broadening of these superlattice peaks is attributed to disorder in the stacking sequence of in-plane ordered $Li_{1/3}Mn_{2/3}$ layers (deviation from the normal stacking sequence, *acac*..., perpendicular to the layers) in the Li_2MnO_3 powder sample, which will be further explained in chapter 3.

Synchrotron X-ray diffraction data of the $Li[Ni_{1/3}Li_{1/9}Mn_{5/9}]O_2$ (Ni1/3-900°C-12hrs-q) sample are shown in Figure 2.4. The lattice parameters of the parent layered structure with space group $R\bar{3}m$ were found, $\boldsymbol{a}_{hex.}$= 2.863 Å and $\boldsymbol{c}_{hex.}$ =14.26 Å, which are consistent with previous studies of materials prepared under similar synthesis conditions ($\boldsymbol{a}_{hex.}$= 2.875 Å and $\boldsymbol{c}_{hex.}$=14.279 Å). In addition, our refinement showed that 5% of nickel was present in the lithium layer, which is in good agreement with previous neutron diffraction analyses of interlayer mixing of lithium and nickel ions (6-7%). Having more lithium in the transition metal layer and smaller values of *x*, the interlayer mixing (exchange) of Ni^{2+} and Li^+ is reduced. Therefore, the composition in the transition metal layer of $Li[Ni_{1/3}Li_{1/9}Mn_{5/9}]O_2$ can be written as $[Li_{0.17}Ni_{0.28}Mn_{0.55}]$.

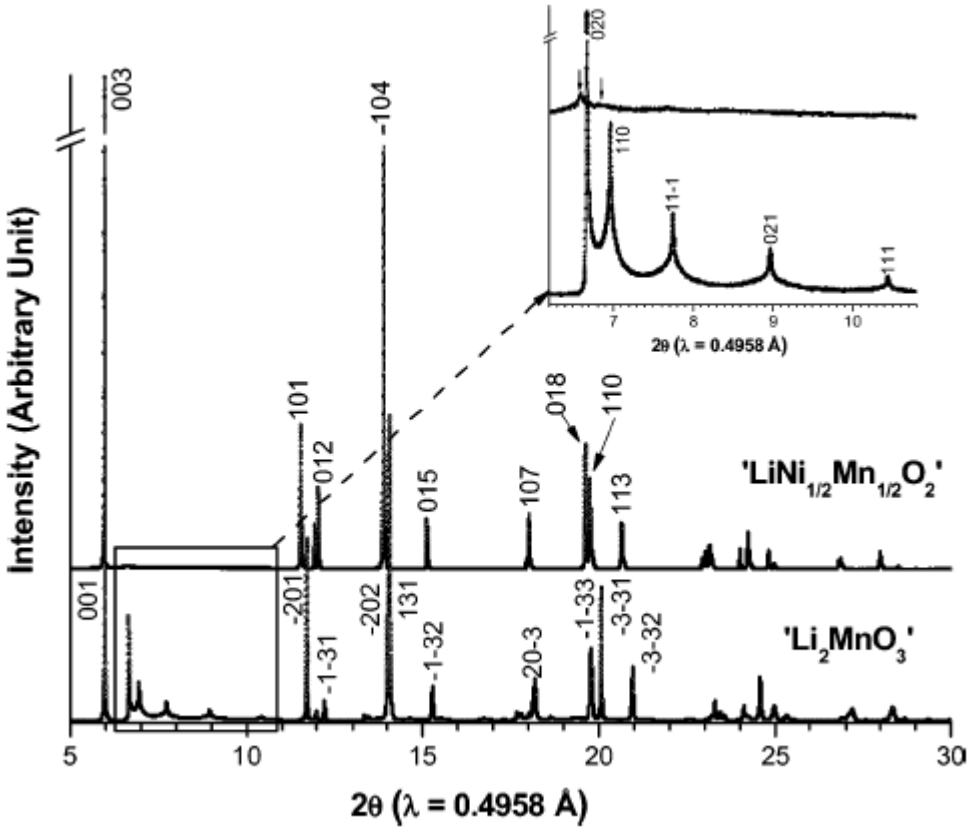

Figure 2.3: Synchrotron X-ray powder diffraction spectra of $Li[Ni_{1/2}Mn_{1/2}]O_2$ and Li_2MnO_3 samples. The XRD data of $Li[Ni_{1/2}Mn_{1/2}]O_2$ is not discussed in this chapter.

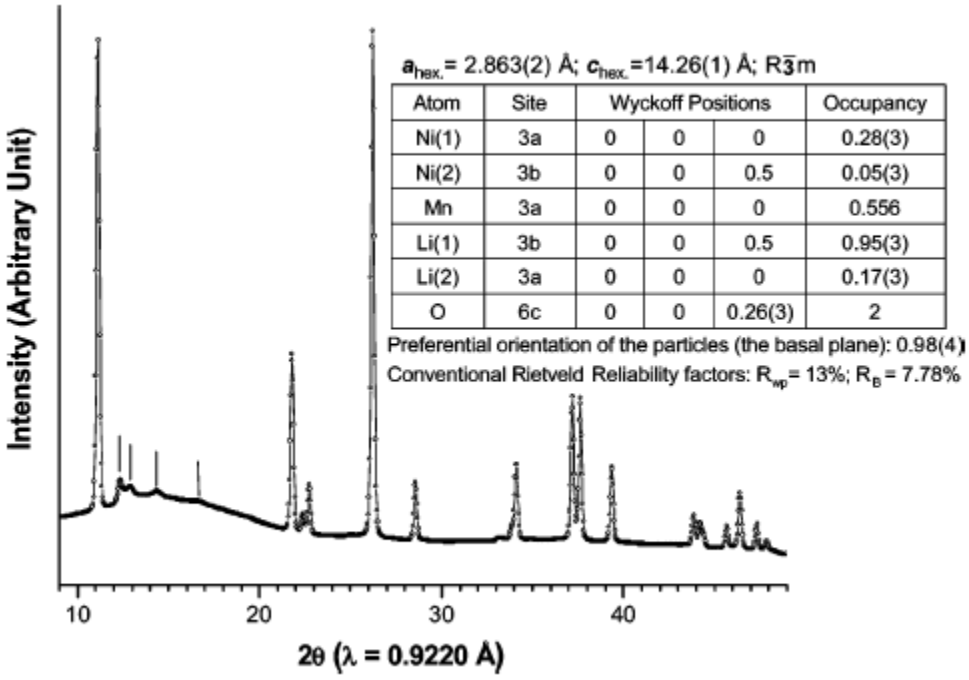

Figure 2.4: Synchrotron X-ray powder diffraction spectra of the $Li[Ni_{1/3}Li_{1/9}Mn_{5/9}]O_2$ sample and the Rietveld refinement results. Four strong superstructure peaks are marked by arrows.

2.3.2. Processing effect on the structure

2.3.2.1 X-ray diffraction

The XRD patterns of Li_2MnO_3 samples synthesized at 850°C are displayed in Figure 2.5. All the samples are found phase pure, and the XRD patterns can be indexed with *C/2m* space group. The broadening of the peaks in all the patterns is very similar, indicating that the crystallinity of these samples is not affected by heating time and cooling method at this temperature. Crystalline Li_2MnO_3 can be formed when it is heated at 850°C for 24 hours. Except the broadening of the peaks, the relative intensity of each peak, especially the superlattice peaks in the range of $6° \leq 2\theta \leq 11°$, remains the same in all the patterns, which indicates that the in plane ordering of the cations are very similar among these samples and not changed dramatically with these processing conditions. For the samples synthesized at 1000°C (Figure 2.6), the patterns can still be indexed with *C2/m* space group, indicating that the samples are phase pure and no impurities are introduced at high temperature. Compared to the samples heated at 850°C, the superstructure peaks are more pronounced in general. This suggests that the cations are well ordered in long range. For the sample Li_2MnO_3-1000°C-5days-sc, small difference is observed in the superstructure peaks region. The intensity of the peak (020) is slightly lower compared to that in other samples. The ratio of the peak intensity between (020) and (110) is close to 1:1. The relative intensity of these superstructure peaks is believed to be an attribute of the stacking faults of the layers. The detailed discussion will be addressed in chapter 3.

Figure 2.7 shows the XRD patterns of Ni1/3 samples synthesized at 900°C. All the patterns can be indexed with $R\bar{3}m$ space group and no additional peaks are observed, indicating all the samples are phase pure under these synthesis conditions. Again, no obvious broadening of the peaks is observed among samples. This suggests that heating time and cooling method do not affect the crystallinity at this synthesis temperature. The superstructure peaks are obvious in the Ni1/3-900°C-12hrs-q sample, but they are less pronounced in the other samples, indicating there may be less honey comb ordering in the transition metal layers in the long range. However, the superstructure peaks in the samples synthesized at 1000°C are more pronounced compared to 900°C syntheses (Figure 2.8). This suggests that the honey comb ordering is easier to form at higher temperature. All the patterns can still be indexed with $R\bar{3}m$ space group, and no additional peaks are observed. The samples remain the same structure after high temperature synthesis.

2.3.2.2 Solid state nuclear magnetic resonance

To probe the short range structure, solid state nuclear magnetic resonance was performed on the synthesized samples. The ^{6}Li NMR analysis of different Li_2MnO_3 samples is discussed in chapter 3. In this chapter, only the ^{6}Li NMR results of Ni1/3 samples will be described. Figure 2.9 shows the ^{6}Li NMR of Ni1/3 samples synthesized at 900°C heated for 12 hours and quenched by liquid nitrogen. Two groups of resonances are clearly observed in the spectrum, one at 737-587 ppm, and another at 1511-1341 ppm. Based on previous work[6, 7, 25, 26], these are assigned to the Li ions in lithium and in the

transition metal layers, respectively. The large width of the peaks at 737-587 ppm is due to the large variety of different local environments for Li ions in the Li layers, which result from the presence of varying numbers of Ni^{2+}, Mn^{4+}, and Li^{+} in the first and second cation coordination shells of Li. The broad peak at 737 ppm is a similar to that seen for the Li ions in the lithium layers of Li_2MnO_3[27], while the resonance at 1511 ppm is at the shift position for Li in the predominantly manganese layers of Li_2MnO_3, and is hence assigned to Li^{+} in the transition metal layers, surrounded by 6 Mn^{4+} ions ($Li(OMn)_6$). The resonance at 1341 ppm is assigned to Li^{+} surrounded by 5 Mn^{4+} and 1 Ni^{2+} ions.

Figure 2.10 shows the ^{6}Li NMR spectra of Ni1/3 samples synthesized at 900°C. No obvious difference is observed in all the spectra. Both the resonances for lithium in transition metal layers and lithium layers are present in all the samples, and the shape and the relative intensity of each peak remain the same, indicating the short-range ordering keeps the same and is not affected by the processing conditions at this temperature. As for the samples synthesized at 1000°C as shown in Figure 2.11, the samples heated for 72 hours show a little bit different features as compared to other spectra. The peak at around 1341 ppm, which corresponds to Li^{+} surrounded by 5 Mn^{4+} and 1 Ni^{2+} ions, is much weaker in both 72hrs-q and 72hrs-sc samples, compared to the samples heated for 12 hours. This suggests that more honey comb ordering is created in the transition metal layers after long period of heating at high temperature (1000°C), which is consistent with the XRD results where more pronounced superstructure peaks are observed in these samples heated at high temperature.

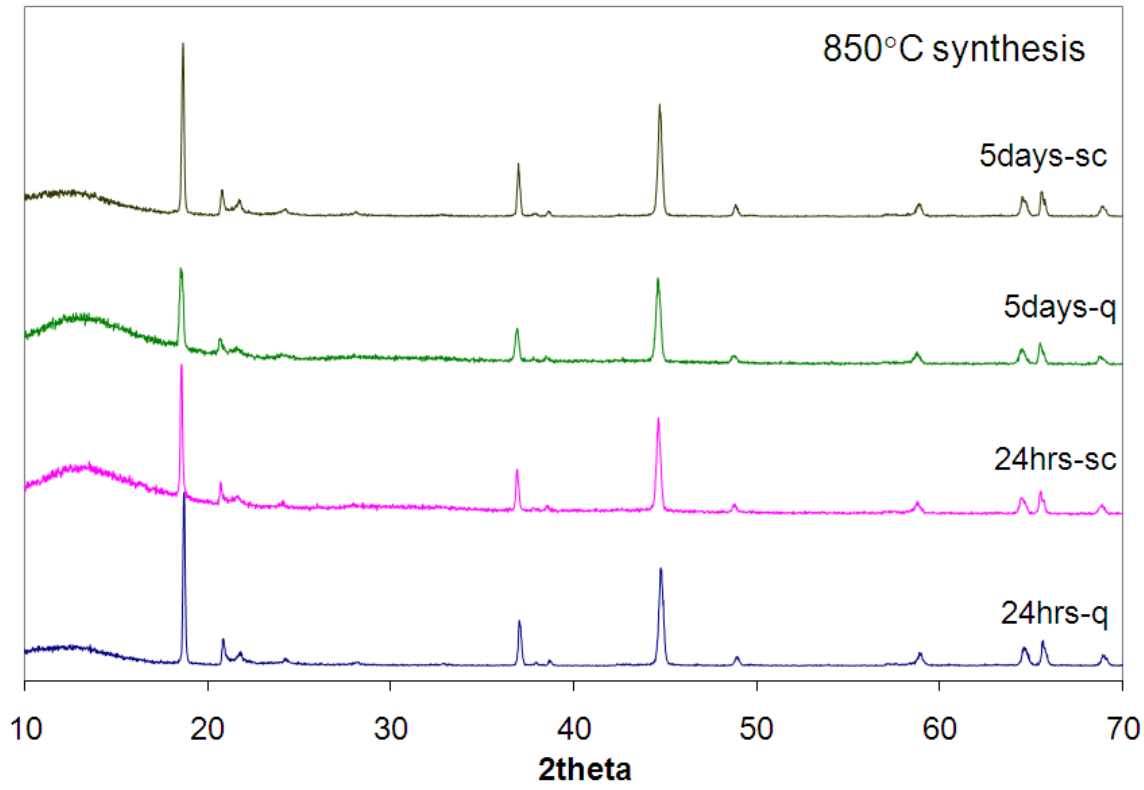

Figure 2.5: The XRD patterns of Li_2MnO_3 samples synthesized at 850°C. The data were collected on the Scintag diffractometer. The broad feature before 15° (2θ) is from the background of the sample holder. The synthesis conditions are labeled on the right of each pattern, in this and subsequent figures.

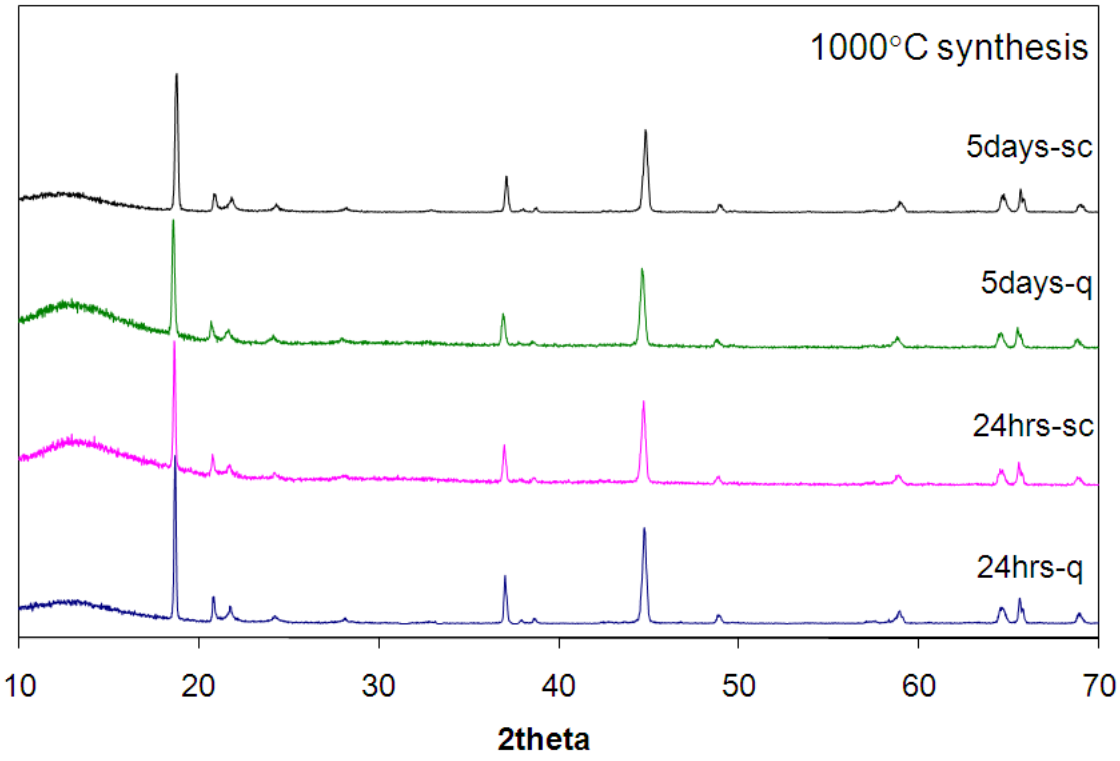

Figure 2.6: The XRD patterns of Li_2MnO_3 samples synthesized at 1000°C. The data were collected on the Scintag diffractometer. The broad feature before 15° (2θ) is from the background of the sample holder.

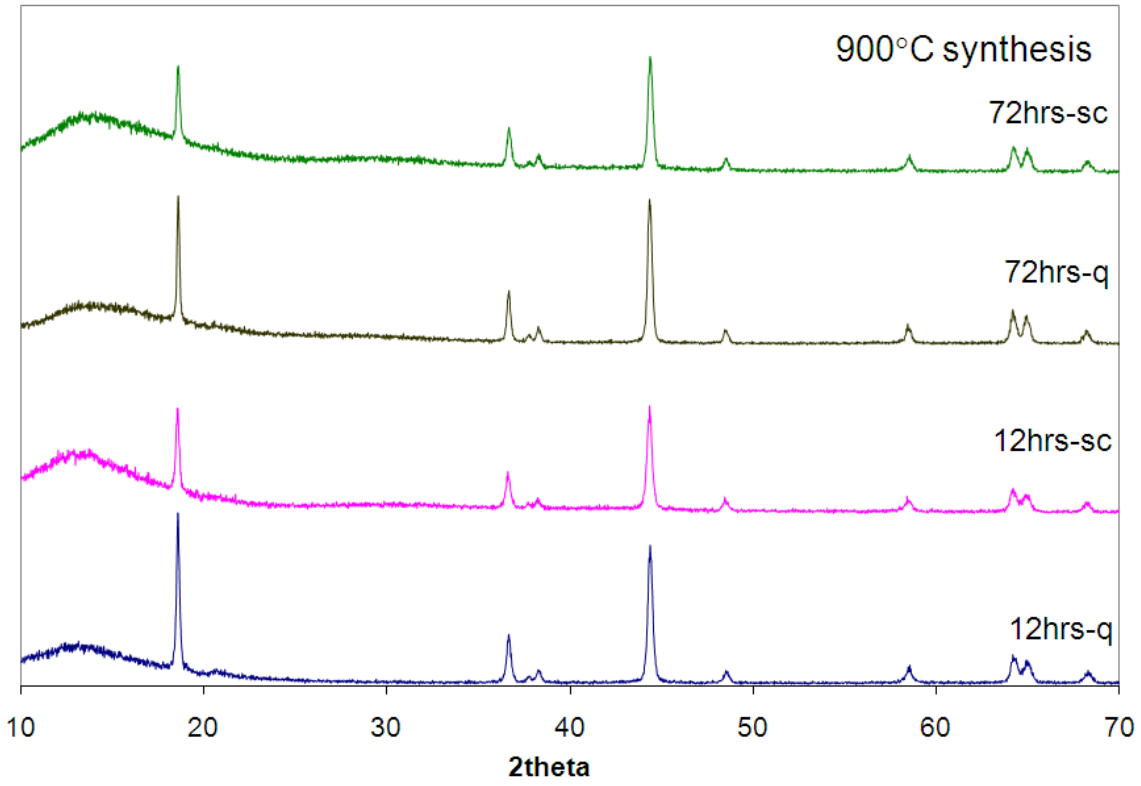

Figure 2.7: The XRD patterns of $Li[Li_{1/9}Ni_{1/3}Mn_{5/9}]O_2$ samples synthesized at 900°C. The data were collected on the Scintag diffractometer. The broad feature before 15° (2θ) is from the background of the sample holder.

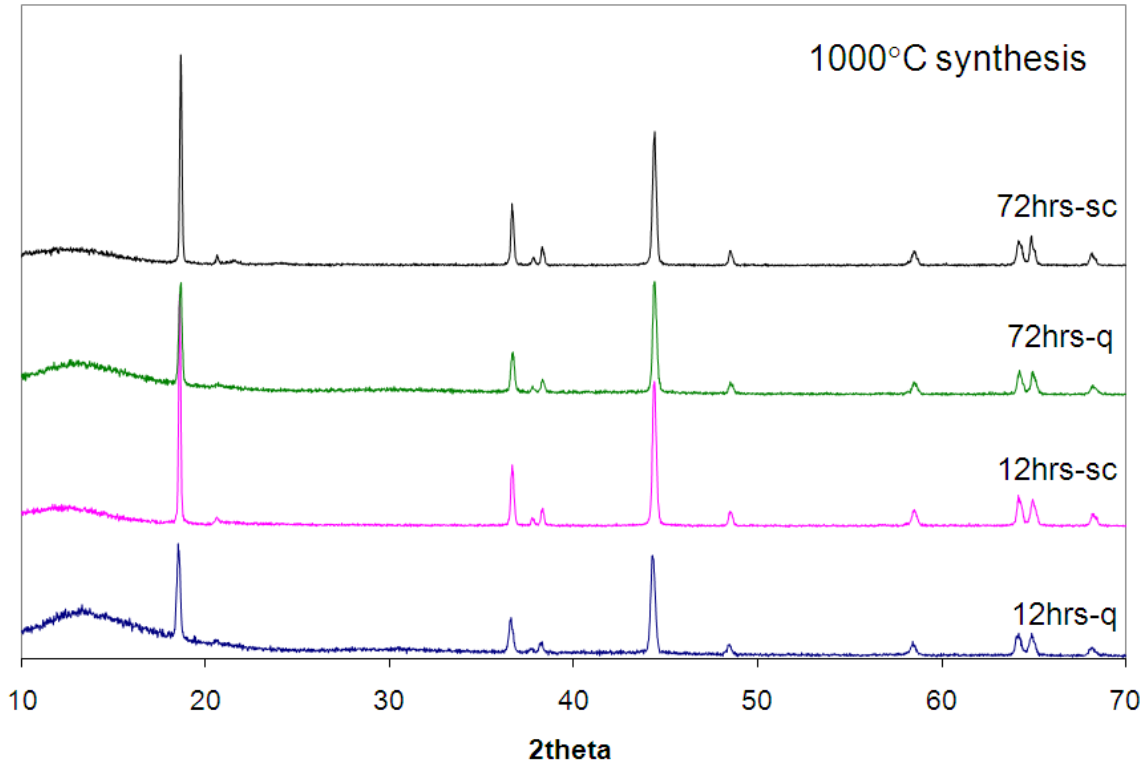

Figure 2.8: The XRD patterns of $Li[Li_{1/9}Ni_{1/3}Mn_{5/9}]O_2$ samples synthesized at 1000°C. The data were collected on the Scintag diffractometer. The broad feature before 15° (2θ) is from the background of the sample holder.

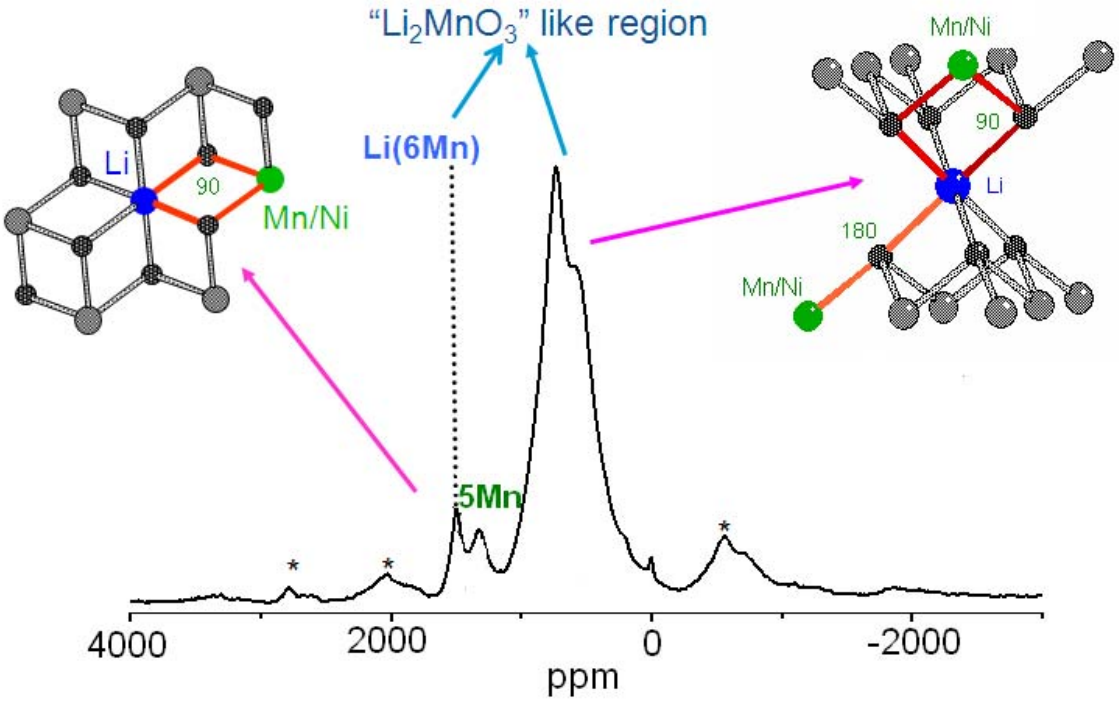

Figure 2.9: The ^{6}Li NMR spectrum of $Li[Li_{1/9}Ni_{1/3}Mn_{5/9}]O_2$ sample synthesized at 900°C for 12 hours and quenched by liquid nitrogen acquired at 38 kHz at room temperature. The spinning sidebands are labeled with asterisks. The sample used for this spectrum is ^{6}Li enriched. All samples are synthesized with regular Li(OH), unless specified.

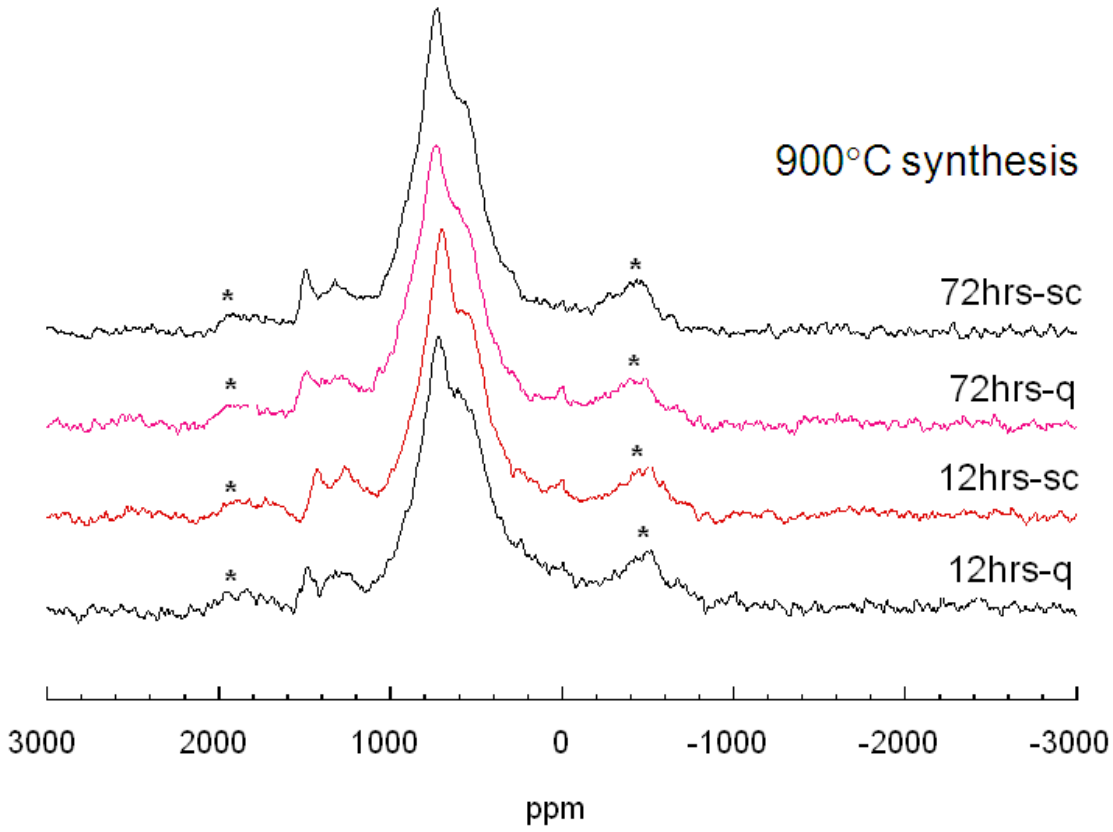

Figure 2.10: The ^{6}Li NMR spectra of $Li[Li_{1/9}Ni_{1/3}Mn_{5/9}]O_2$ samples synthesized at 900°C acquired at 38 kHz at room temperature. The spinning sidebands are labeled with asterisks.

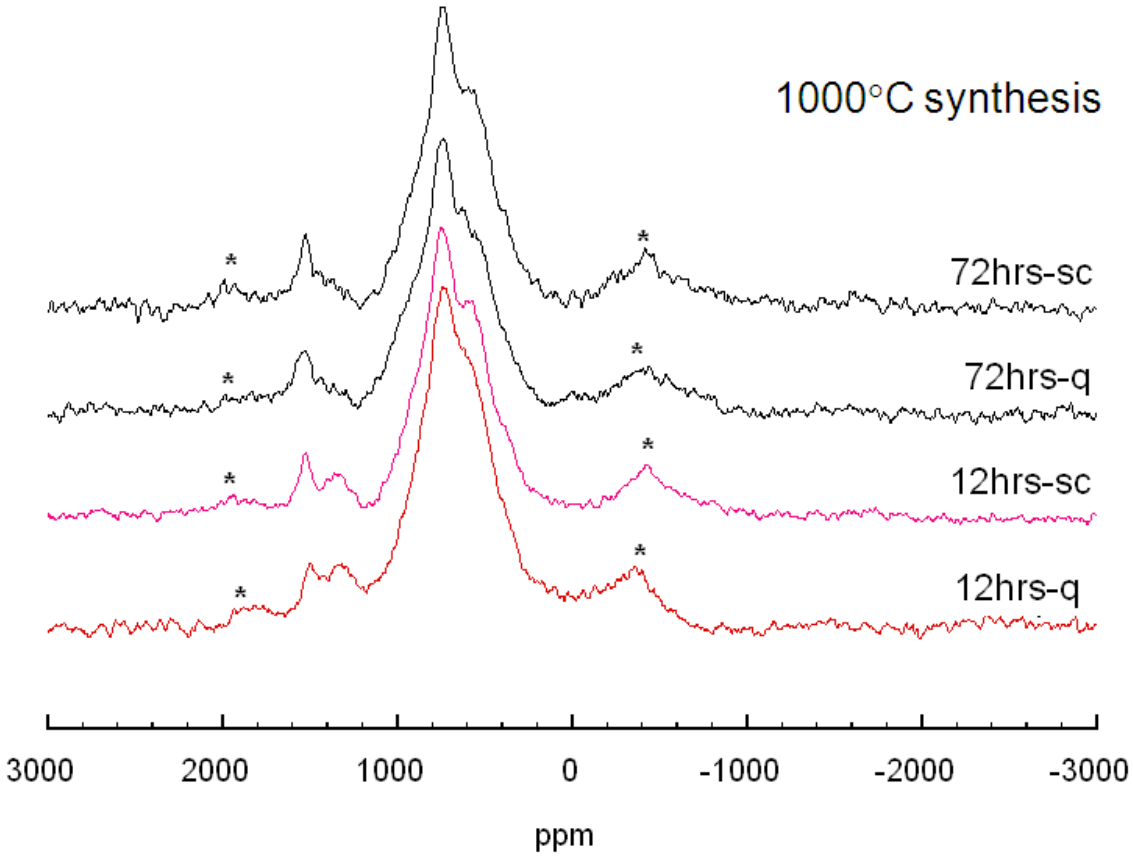

Figure 2.11: The ^{6}Li NMR spectra of $Li[Li_{1/9}Ni_{1/3}Mn_{5/9}]O_2$ samples synthesized at 1000°C acquired at 38 kHz at room temperature. The spinning sidebands are labeled with asterisks.

2.4 Conclusions

Two members of the layered compounds of the $Li[Ni_xLi_{1/3-2x/3}Mn_{2/3-x/3}]O_2$ ($0 < x < 1/2$) series, Li_2MnO_3 and $Li[Ni_{1/3}Li_{1/9}Mn_{5/9}]O_2$, are studied by XRD and solid state NMR. *C2/m* and $R\bar{3}m$ space group are used to index the XRD patterns of Li_2MnO_3 and $Li[Ni_{1/3}Li_{1/9}Mn_{5/9}]O_2$, respectively. The $\sqrt{3}\boldsymbol{a}_{hex} \times \sqrt{3}\boldsymbol{a}_{hex}$ (honey-comb) in-plane ordering in the transition metal layers is found in both samples. In the ^6Li NMR spectrum of $Li[Ni_xLi_{1/3-2x/3}Mn_{2/3-x/3}]O_2$, resonances belonging to both Li^+ in Li layers and transition metal years are observed separately. Especially for the Li^+ in transition metal layers, two peaks are present, which are assigned to the Li^+ surrounded by 6 Mn^{4+} and 5 Mn^{4+} and 1 Ni^{2+} ions.

The processing conditions were studied for both compounds. Only the Li_2MnO_3-1000°C-5days-sc sample show a slightly different XRD pattern than other samples, where the intensity ratio of the superstructure peaks I_{020}/I_{110} is lower than other samples, which indicates different stacking faults present in this sample. For $Li[Ni_{1/3}Li_{1/9}Mn_{5/9}]O_2$, the samples synthesized at 1000°C for 72 hours show more ordering in the transition metal layers compared to the samples heated for less time and lower temperature.

2.5 References

1. Lu, Z. H.; Dahn, J. R., *Journal of the Electrochemical Society* **2002,** 149, (7), A815-A822.

2. Lu, Z. H.; Beaulieu, L. Y.; Donaberger, R. A.; Thomas, C. L.; Dahn, J. R., *Journal of the Electrochemical Society* **2002,** 149, (6), A778-A791.

3. Lu, Z. H.; MacNeil, D. D.; Dahn, J. R., *Electrochemical and Solid State Letters* **2001,** 4, (12), A200-A203.

4. Meng, Y. S.; Ceder, G.; Grey, C. P.; Yoon, W. S.; Shao-Horn, Y., *Electrochemical and Solid State Letters* **2004,** 7, (6), A155-A158.

5. Yoon, W. S.; Iannopollo, S.; Grey, C. P.; Carlier, D.; Gorman, J.; Reed, J.; Ceder, G., *Electrochemical and Solid State Letters* **2004,** 7, (7), A167-A171.

6. Yoon, W. S.; Kim, N.; Yang, X. Q.; McBreen, J.; Grey, C. P., *Journal of Power Sources* **2003,** 119, 649-653.

7. Yoon, W. S.; Paik, Y.; Yang, X. Q.; Balasubramanian, M.; McBreen, J.; Grey, C. P., *Electrochemical and Solid State Letters* **2002,** 5, (11), A263-A266.

8. Yoon, W. S.; Grey, C. P.; Balasubramanian, M.; Yang, X. Q.; McBreen, J., *Chemistry of Materials* **2003,** 15, (16), 3161-3169.

9. Grey, C. P.; Yoon, W. S.; Reed, J.; Ceder, G., *Electrochemical and Solid State Letters* **2004,** 7, (9), A290-A293.

10. Yoon, W. S.; Grey, C. P.; Balasubramanian, M.; Yang, X. Q.; Fischer, D. A.; McBreen, J., *Electrochemical and Solid State Letters* **2004,** 7, (3), A53-A55.

11. Meng, Y. S.; Ceder, G.; Grey, C. P.; Yoon, W. S.; Jiang, M.; Breger, J.; Shao-Horn, Y., *Chemistry of Materials* **2005,** 17, (9), 2386-2394.

12. Lu, Z. H.; Chen, Z. H.; Dahn, J. R., *Chemistry of Materials* **2003,** 15, (16), 3214-3220.

13. Ohzuku, T.; Makimura, Y., *Chemistry Letters* **2001**, (8), 744-745.

14. Makimura, Y.; Ohzuku, T. 2003; 2003; pp 156-160.

15. Arachi, Y.; Kobayashi, H.; Emura, S.; Nakata, Y.; Tanaka, M.; Asai, T., *Chemistry Letters* **2003,** 32, (1), 60-61.

16. Vitins, G.; West, K., *Journal of the Electrochemical Society* **1997,** 144, (8), 2587-2592.

17. Shao-Horn, Y.; Hackney, S. A.; Armstrong, A. R.; Bruce, P. G.; Gitzendanner, R.; Johnson, C. S.; Thackeray, M. M., *Journal of the Electrochemical Society* **1999,** 146, (7), 2404-2412.

18. Reed, J.; Ceder, G.; Van der Ven, A., *Electrochemical and Solid State Letters* **2001,** 4, (6), A78-A81.

19. Kobayashi, H.; Sakaebe, H.; Kageyama, H.; Tatsumi, K.; Arachi, Y.; Kamiyama, T., *Journal of Materials Chemistry* **2003,** 13, (3), 590-595.

20. Strobel, P.; Lambertandron, B., *Journal of Solid State Chemistry* **1988,** 75, (1), 90-98.

21. Massarotti, V.; Bini, M.; Capsoni, D.; Altomare, A.; Moliterni, A. G. G., *Journal of Applied Crystallography* **1997,** 30, 123-127.

22. Van der Ven, A.; Aydinol, M. K.; Ceder, G.; Kresse, G.; Hafner, J., *Physical Review B* **1998,** 58, (6), 2975-2987.

23. Shao-Horn, Y.; Levasseur, S.; Weill, F.; Delmas, C., *Journal of the Electrochemical Society* **2003,** 150, (3), A366-A373.

24. Delmas, C.; Menetrier, M.; Croguennec, L.; Levasseur, S.; Peres, J. P.; Pouillerie, C.; Prado, G.; Fournes, L.; Weill, F., *International Journal of Inorganic Materials* **1999,** 1, (1), 11-19.

25. Pan, C. J.; Lee, Y. J.; Ammundsen, B.; Grey, C. P., *Chemistry of Materials* **2002,** 14, (5), 2289-2299.

26. Lee, Y. J.; Grey, C. P., *Journal of Physical Chemistry B* **2002,** 106, (14), 3576-3582.

27. Breger, J.; Jiang, M.; Dupre, N.; Meng, Y. S.; Shao-Horn, Y.; Ceder, G.; Grey, C. P., *Journal of Solid State Chemistry* **2005,** 178, (9), 2575-2585.

Chapter 3

High-resolution X-ray diffraction, DIFFaX, NMR and first principles study of disorder in the Li_2MnO_3–$Li[Ni_{1/2}Mn_{1/2}]O_2$ solid solution

Abstract

X-ray diffraction patterns of $Li[Li_{(1-2x)/3}Ni_xMn_{2/3-x/3}]O_2$ show reflections between 20° and 35°, 2θ (CuKa) due to Li_2MnO_3-like ordering of the transition metal (Ni, Mn and Li) layers. The ordering is rarely perfect, resulting in characteristic broadening and changes in the intensities of these reflections. ^{6}Li MAS NMR studies of Li_2MnO_3 show that the $[Li_{1/3}Mn_{2/3}]$ layers are well ordered, the disorder arising from the stacking of the layers in the c-direction. DIFFaX was used to model the Li_2MnO_3 XRD data and extract the stacking fault frequency. The results show that even well-ordered cation layers may show only weak or no superstructure reflections, if there is no or little ordering in the c-direction.

The chapter is formed on the basis of the paper: "High-resolution X-ray diffraction, DIFFaX, NMR and first principles study of disorder in the Li_2MnO_3–$Li[Ni_{1/2}Mn_{1/2}]O_2$ solid solution", Bréger, J.; Jiang, M; Dupré, N.; Meng, Y. S.; Shao-Horn, Y.; Ceder, G.; Grey,C. P. *J. Solid State Chem.* **2005**, *178*, 2575-2585. The DiFFaX simulations were performed by J. Bréger., and the calculations are the contributions from Y. S. Meng; and G. Ceder.

3.1 Introduction

The composition $Li[Li_{(1-2x)/3}Ni_xMn_{2/3-x/3}]O_2$ can be viewed as a solid solution between the two end members, Li_2MnO_3, and $Li[Ni_{1/2}Mn_{1/2}]O_2$. $Li[Ni_{1/2}Mn_{1/2}]O_2$ adopts an *R*3*m* space group and consists of "Li" layers containing approximately 90% Li^+ and 10% Ni^{2+} ions, and "transition metal" layers with Ni^{2+}, Mn^{4+} and some Li+ ions.[1, 2] Li_2MnO_3 may be rewritten as $Li[Li_{1/3}Mn_{2/3}]O_2$ in the notation used to describe many of these layered materials. The "transition metal" layer now comprises Li and Mn ions in an atomic ratio for Li:Mn of 1:2, rearranged to form a ''honey-comb'' ordering scheme (Fig. 3.1.a). This reduces the symmetry of Li_2MnO_3 and results in superstructure peaks between 20° and 35°, 2θ (Cu$K\alpha_1$) in the X-ray diffraction (XRD) pattern.[3, 4] XRD patterns of $Li[Li_{(1-2x)/3}Ni_xMn_{2/3-x/3}]O_2$ with intermediate values of x (e.g., x=1/9, 1/3, 1/6) also show superstructure reflections consistent with Li_2MnO_3-type ordering and electron diffraction patterns.[5, 6] of $Li[Ni_{1/2}Mn_{1/2}]O_2$ show superstructure peaks consistent with long-range ordering of the cations in the transition metal layers. In order to understand the ordering in the transition metal layers in the $Li[Li_{(1-2x)/3}Ni_xMn_{2/3-x/3}]O_2$ series, we have chosen, in the work presented in this paper, to investigate the ordering in the end member Li_2MnO_3 in some detail.

How the ordered transition metal layers are stacked in Li_2MnO_3 is still controversial. Different stacking configurations were previously proposed in literature, one resulting in the *C*2/*c* space group (Jansen, 1973; Riou, 1992) [7, 8] and another resulting in the *C*2/*m* space group (Strobel, 1988; Massarotti, 1997).[3, 4] Recent TEM studies by Meng et al.[5] showed that the stacking sequence that results in a $P3_112$ space group also needs to be considered for the other end member $Li[Ni_{0.5}Mn_{0.5}]O_2$. These stacking

schemes were proposed by Lang in as early as 1966.[9] Fig. 3.1. shows two different ways of stacking the honey-comb ordered ($Li_{1/3}Mn_{2/3}$) layers (containing Li atoms surrounded by 6 Mn atoms in the *ab* plane) along the *c*-axis, to generate *C*2/*m*- $A_1B_1C_1$ and $P3_112$-$A_1B_1C_2$ stacking. All structures derived from α-$NaFeO_2$ (i.e., O3 packing) contain ABCABC stacking of the $Li_{1/3}Mn_{2/3}$ layers (Fig. 3.1.) in the *c*-direction. Thus, each layer (or 2D net) is labeled A, B or C, denoting the position of the cations in the close packed layers. Honey-comb ordering results in an enlargement of the a-$NaFeO_2$ cell in the *a*–*b* plane to form a $3^{1/2}a \times 3^{1/2}a$ cell, where *a* is the cell parameter of the α-$NaFeO_2$ cell, and there are now three atoms per unit cell in the 2D net. This generates three possible 2D nets, A_1, A_2 or A_3, the subscript labeling the position of the Li ions in the unit cell (Fig. 3.1.a). Starting with the A_1 net, a second net may then be placed above this to generate the arrangement A_1B_1 (Fig. 3.1.b). The other possible arrangements, A_1B_2 and A_1B_3, are related to A_1B_1 by a 120° rotation and so are not unique. There are then two possibilities for the addition of a third net, generating either $A_1B_1C_1$ or $A_1B_1C_2$ stacking. $A_1B_1C_2A_1B_1C_2$ . . . stacking results in a 3-fold screw axis along the *c*-axis and the space group $P3_112$, while stacking involving the $A_1B_1C_1$ blocks results in the *C*2/*m* structure. Fig. 3.2. illustrates how the monoclinic *C*2/*m* unit cell[5] can be redrawn as a larger hexagonal unit cell, which is identical in size to that found for $P3_112$ stacking, allowing easy comparison between these two structures. More complicated stacking schemes are possible if the 3-layer blocks are combined with different ones. For example, the stacking block $A_1B_1C_2$ can be combined with an $A_2B_3C_1$ block, to form the six-layer repeat sequence $A_1B_1C_2A_2B_3C_1$. This stacking scheme results in the *C*2/*c* space group proposed

by some authors for Li_2MnO_3.[7, 8] These stacking schemes been found in other materials including Li_2SnO_3 and Li_2IrO_3.[7, 9, 10]

Clearly, many stacking schemes are possible for Li_2MnO_3 and related structures. The differences in energies between these schemes may not be large, since these layers are separated by three other (oxygen and lithium) layers, and intergrowths between these structures may be possible. The purpose of this paper is to explore the effect on the XRD patterns of these materials of stacking faults of these layers along the *c* axis, as a function of different heat treatments. DIFFaX[11] simulations are used to model these faults and ^{6}Li MAS NMR spectroscopy is used to investigate the local structure in these materials. In addition, first principles calculations are used to estimate the energy differences between different stacking sequences.

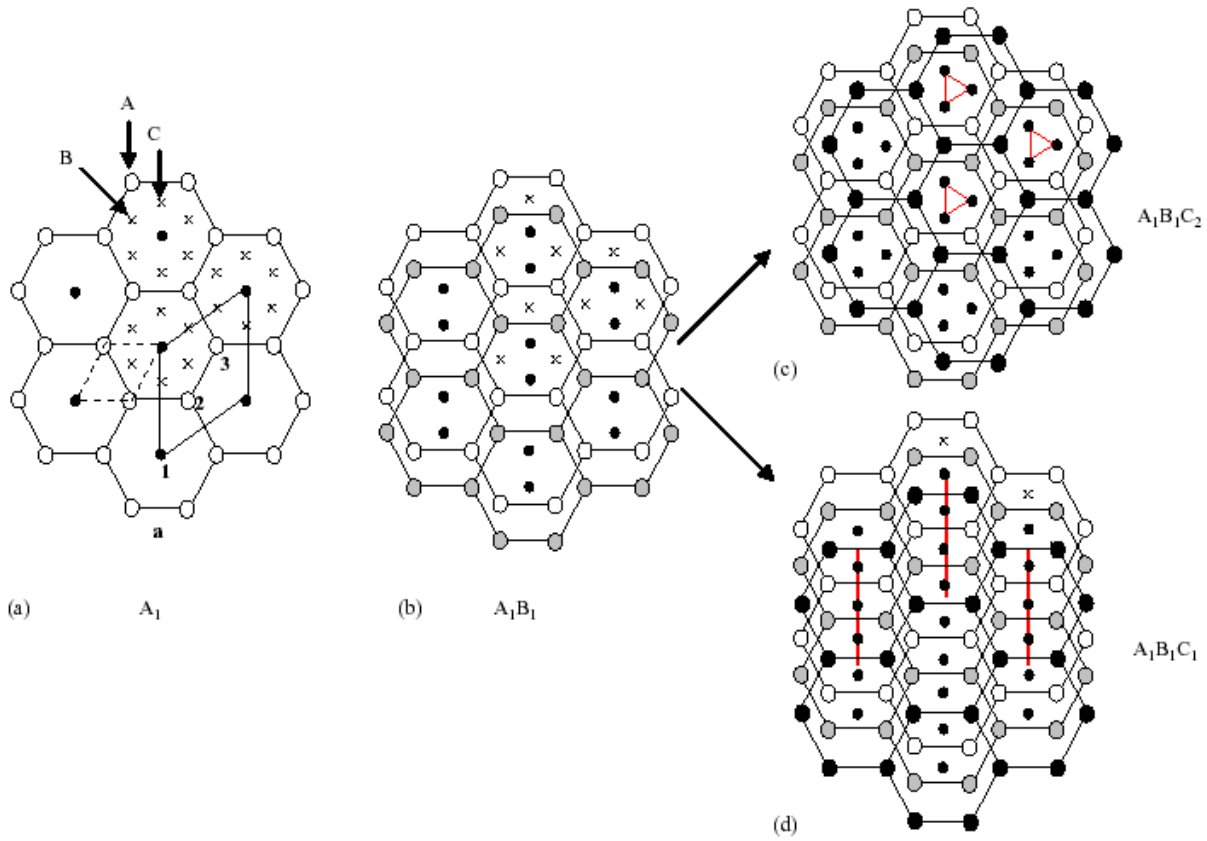

Figure 3.1: **.** Schemes generated by stacking "honey-comb" layers. (a) The first "honey-comb" $Li_{1/3}Mn_{2/3}$ layer, *A1*. The Mn and Li ions are denoted by white and black (smaller) circles, respectively. The crosses represent the locations in the *ab*-planes of the *B* and *C* holes in a close-packed array. The enlarged $3^{1/2}a \times 3^{1/2}a$ unit cell is shown along with the locations of three different atoms in this cell. The α-$NaFeO_2$ unit cell is also shown in dashed lines. (b) The addition of a second layer (gray and black circles), to generate A_1B_1 stacking. Two possibilities for the addition of the third layer (black circles) are possible, generating (c) a 3-fold screw axis (triangles), for $P3_112$ stacking ($A_1B_1C_2$) and (d) mirror planes (lines) for the $C2/m$ stacking ($A_1B_1C_1$).

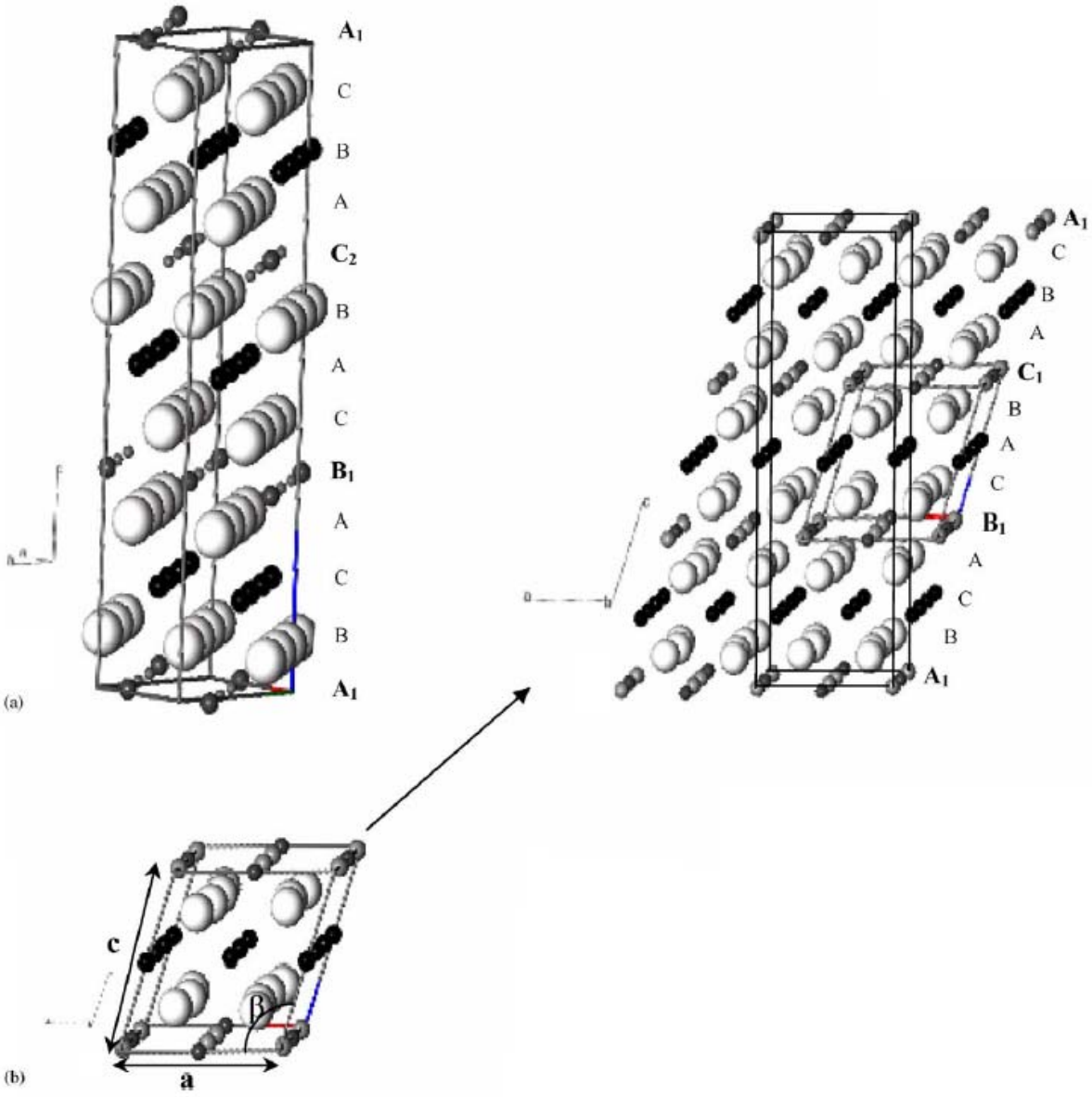

Figure 3.2: Two different unit cells generated by stacking honey-comb layers. (a) *$P3_112$* and (b) *C2/m* unit cells; (c) the *C2/m* unit cell may be redrawn as a larger, hexagonal cell, for a value of β for the monoclinic cell equal to π-$\cos^{-1}(a/3c)$. The O and Mn atoms are represented by white and light gray spheres, respectively. The Li in Li layers and transition metal layers are represented by black and dark gray spheres, respectively

3.2 Experimental

3.2.1 Synthesis

The Li_2MnO_3 samples were prepared in the same way as described in Chapter 2, and were slowly cooled to room temperature at a rate of 1 °C/min after heating. These samples are referred to as Li_2MnO_3-850-1d and Li_2MnO_3-1000-1m, respectively. $Li[Ni_{1/2}Mn_{1/2}]O_2$ and $Li[Li_{1/9}Ni_{1/3}Mn_{5/9}]O_2$ powders were prepared by the double-mixed hydroxide method.[12, 13] An aqueous solution of stoichiometric amounts of transition metal nitrates was prepared, which was slowly dripped (1–2 h) into 400mL of a stirred solution of LiOH using a burette, yielding a precipitate of $M(OH)_2$, where M=Mn and Ni, with a homogeneous cation distribution. The dried precipitate was mixed with $Li(OH)\bullet H_2O$ in stoichiometric proportions. The mixture was then heated in air at 480 1C for 12 h, and at 1000 °C for 3 days and slowly cooled at room temperature at a rate of 1 °C/min. These samples are referred to as $Ni_{1/2}$-1000-3d and $Ni_{1/3}$-1000-3d, for $Li[Ni_{1/2}Mn_{1/2}]O_2$ and $Li[Li_{1/9}Ni_{1/3}Mn_{5/9}]O_2$, respectively, according to their Ni content and heating procedures.

3.2.2 XRD

High-resolution synchrotron XRD of $Li[Ni_{1/2}Mn_{1/2}]O_2$, $Li[Li_{1/9}Ni_{1/3}Mn_{5/9}]O_2$ and Li_2MnO_3 were collected by Peter L. Lee at the 32-ID beamline at the Advanced Photon Source (APS), Argonne National Laboratories (λ=0.4958Å). XRD simulations were performed with the program DIFFaX (written by Newsam and Treacy[11]), in order to

model stacking faults along the *c*-axis. For clarity, the 2θ values in all the plots were converted so as to correspond to those seen for Cu$K\alpha_1$ wavelengths (λ=1.5406 Å).

3.2.3 MAS NMR Spectroscopy

To probe the local environment of Li atoms in Li_2MnO_3, ^6Li MAS NMR experiments were performed on the two Li_2MnO_3 samples at an operating frequency of 29.47 MHz and on a CMX-200 spectrometer. A 2 mm double resonance probe built by Samoson and coworkers was used to achieve 38 kHz spinning speed. All spectra were acquired with a rotor synchronized echo pulse sequence (90º-τ-180º-τ-acq), where $\tau = 1/\nu_r$. $\pi/2$ pulse width of 3.5 μs were used with pulse delays of 0.2 s. The spectra were acquired at "room temperature" (i.e. the spectra were acquired with no control of the temperature), which corresponds to a sample temperature of between 70-80 ºC.

3.2.4 Computations

First principles computations on the *C*2/*m*, *P*3$_1$12, and *C*2/*c* stackings were performed in the Generalized Gradient Approximation to Density Functional Theory as implemented in VASP. Ultrasoft GGA pseudo potentials were used, with Perdew-Wang exchange correlation functions (PW-GGA). As the energy differences between these structures are extremely small, dense k-point meshes were used for the Brillouin zone

integrations. These computations were performed by our collaborators in Prof. Ceder's group at the Massachusetts Institute of Technology (MIT).

3.3 Results

3.3.1 X-ray diffraction

Figure 3.3 shows the XRD patterns of Li_2MnO_3-850-1d, Li_2MnO_3-1000-1m, $Ni_{1/2}$-1000-3d and $Ni_{1/3}$-1000-3d. As shown in the enlargement in Figure 3.3.II, both Li_2MnO_3 samples exhibit very similar patterns, except for noticeable differences in the linewidths and intensities of the reflections in the 20-35°, 2θ region. The peak broadening decreases on longer heat treatment at the higher temperature, and the pattern is closer to that reported in the literature. Nonetheless, all the reflections can be indexed with the *C*2/*m* structure (as proposed by Strobel *et al.*[4]). All the peaks in the 20-35°, 2θ region are completely absent for the α-$NaFeO_2$ structure, with the $R\bar{3}m$ space group; these "superstructure" peaks result from the ordering of the Li/Mn ions in the *ab* planes. Similar XRD patterns are seen for $Li(NiMn)_{1/2}O_2$ and $Li(Li_{1/9}Ni_{1/3}Mn_{5/9})O_2$, samples, although the superstructure peaks in the 20-35°, 2θ region are weaker, especially for the x=0.5 sample. The presence of the superstructure peaks is consistent with the NMR spectra of these materials, where resonances due to Li surrounded by 5 or 6 Mn ions in the transition metal (Mn/Ni/Li) layer are seen.[14] Many of the reflections between 45 and 65°, 2θ show splittings in the pattern of the sample of Li_2MnO_3 annealed for a month. The same reflections are broadened in the patterns of Li_2MnO_3-850-1d and $Ni_{1/3}$-1000-3d, but individual reflections cannot be resolved. These reflections can only be indexed with a *C*2/*m* space group and not with the *P*3$_1$12 space group: The size of the splittings is related to the value of β in the monoclinic cell. For example, for a value of β equal to

($180°-\cos^{-1}(a/3c)$), where a and c are the cell parameters of the $C2/m$ monoclinic cell, no splitting is observed and the $C2/m$ cell may be redrawn as shown in Figure 3.2.b, as a hexagonal cell. In this case, it would be difficult to distinguish between the $C2/m$ and $P3_112$ cells, without further profile refinement. However, the observation of splitting provides clear evidence for a monoclinic distortion of the cell, and thus the $P3_112$ space group can be rejected for the ordered compound.

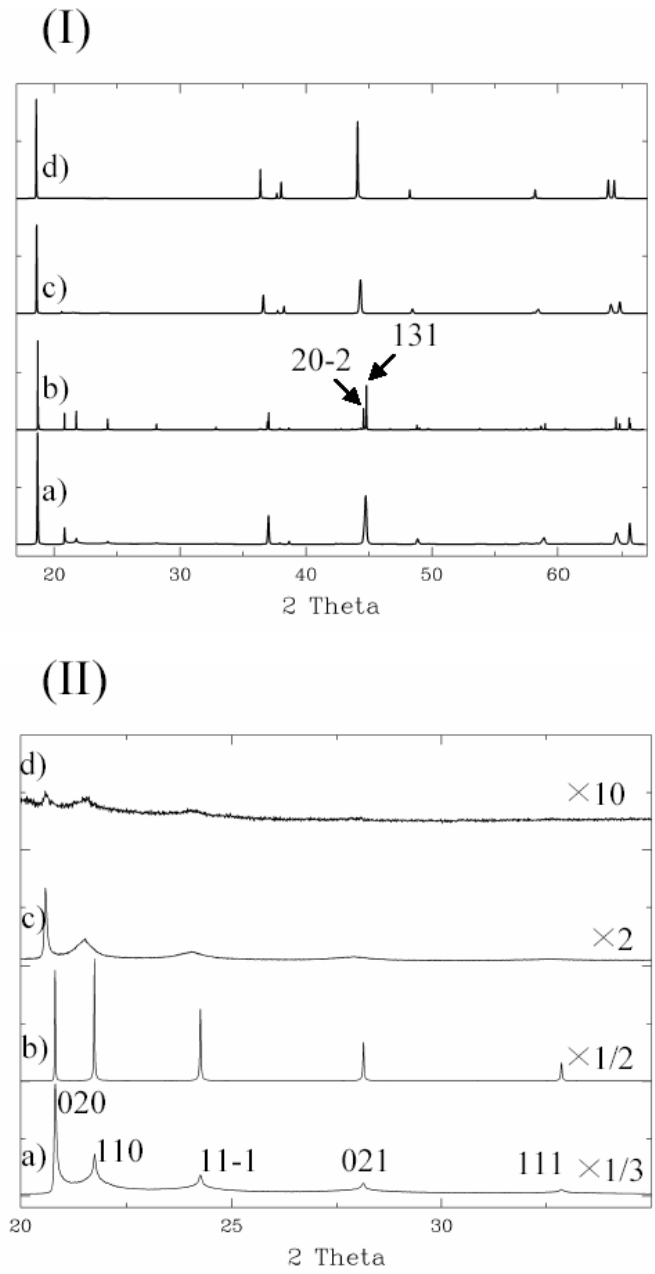

Figure 3.3: XRD patterns of (I): (a) Li_2MnO_3-850°C-1d, (b) Li_2MnO_3- 1000°C-1m, (c) $Li[Li_{1/9}Ni_{1/3}Mn_{5/9}]O_2$-1000 °C-3d, and (d) $Li[Ni_{1/2}Mn_{1/2}]O_2$-1000 °C-3d. These experimental patterns were collected at the APS (32-ID) with λ=0.4958Å. For clarity, the 2θ values were changed to correspond to those for Cu$K\alpha_1$ X-ray irradiation (λ=1.5406Å). (II): Enlargements of the XRD patterns of the four samples with the 2y range between 20° and 35°. The peaks were indexed with the *C2/m* space group.

3.3.2. NMR

Fig. 4 shows the ^{6}Li MAS NMR spectra of Li_2MnO_3-1000-1m and -850-1d. Two sets of isotropic resonances, at approx. 750 and 1510 ppm, are observed for both sets of materials, which can be assigned to Li ions in the Li layers and transition metal layers, respectively, based on the relative intensities of the resonances and their Fermi-contact shifts.[15-17] More careful examination of the spectra reveals that the peak at approx. 750 ppm in a spectrum of Li_2MnO_3-1000-1m is split into two resonances at 775 and 759 ppm with approximate intensities of 1:2, while a whole series of resonances are observed for the -850-1d, sample indicating that there are a wide range of different local environments for Li in the Li layers.

3.3.3. Calculations

The first principles results give very small energy differences between the *C*2/*m*, $P3_112$, and *C*2/*c* stackings, though *C*2/*m* consistently has the lowest energy for calculations with high k-point density. The *C*2/*c* structure is about 2MeV per formula unit higher in energy than the *C*2/*m* structure, while $P3_112$ is approximately 1MeV higher in energy than *C*2/*m*. While these numbers are small, we believe they are numerically significant.

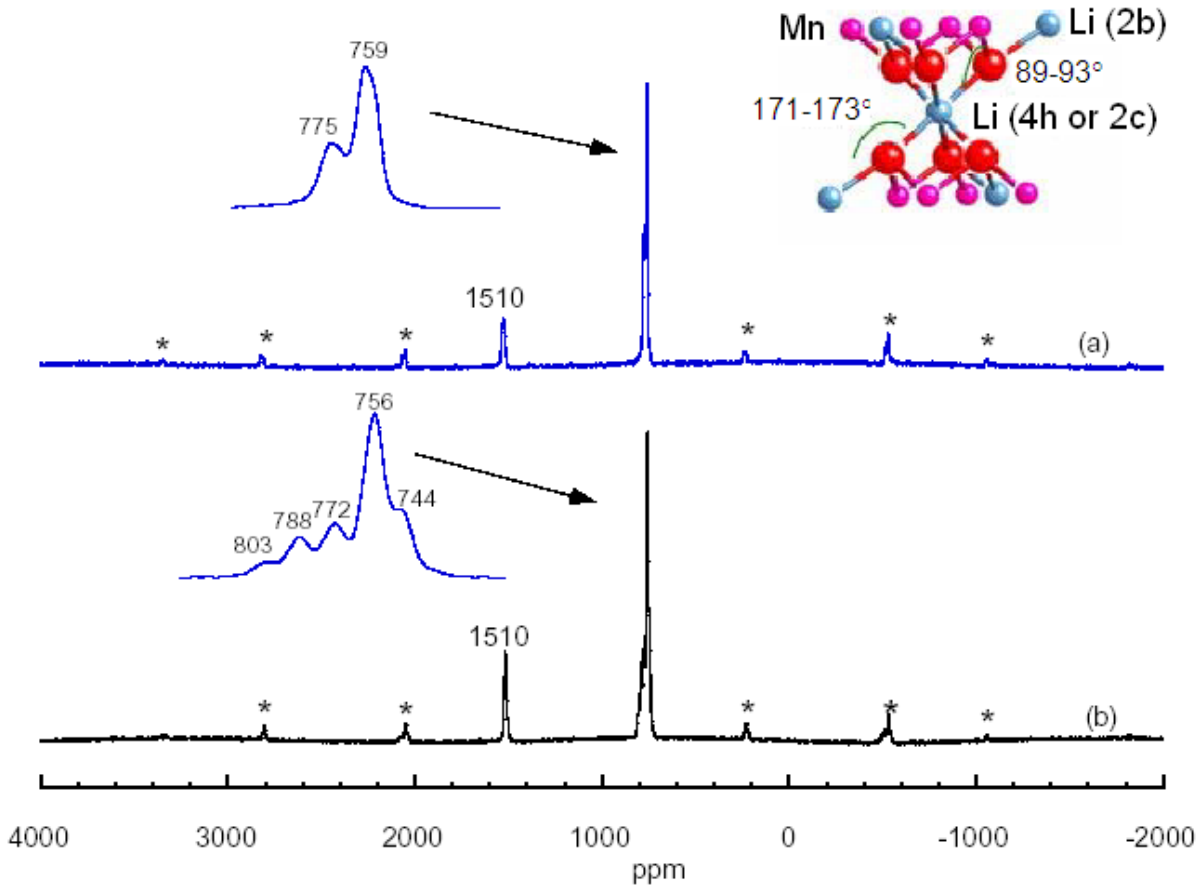

Figure 3.4: ^{6}Li MAS NMR spectra of (a) Li_2MnO_3-1000-1m and (b) Li_2MnO_3-850-1d. The isotropic resonances are labeled with their corresponding shifts; the remaining peaks are spinning sidebands, which are marked with *. The inserts on the left are enlargements of the peaks at approx. 750 ppm. The insert on the right shows the local environment for the Li ions in the Li layers.

3.4 Discussion

3.4.1 Implications from the probe of the short-range order, NMR

Each Li ion in the $Li_{1/3}Mn_{2/3}$ honey-comb layer is surrounded by six Mn ions in its first coordination shell; this corresponds to the *2b* crystallographic site in the *C*2/*m* structure. A Fermi contact (hyperfine) shift of 1500 ppm is predicted for this local environment, based on Li–O–Mn bond angles for this environment (close to 90°). No evidence for any disorder of the honey-comb layers is seen. Any Li–Mn site exchange will result in Li local environments containing fewer Mn^{4+} ions. For example, interchanging one set of Li and Mn ions in an adjacent Li–Mn pair will result in three new Li local environments, one nearby only four Mn and two nearby five Mn ions. These local environments will resonate at approx. 1250 and 1000 ppm, respectively. No resonances are seen in this shift range for both samples. Random occupancy of 1% of the Li ions on the Mn site, and 0.05% of the total Mn content on the Li sites, results in local environments $Li(Mn)_n$, n=6, 5, 4, 3 with concentrations of 92.3%, 5.6%, 0.3%, and 1.8%. (These local environments also contain six Li ions from the Li layers, but since only the Mn^{4+} ions give rise to large (hyperfine) shifts we shall ignore these ions in the subsequent discussion.) Our signal-to-noise (0.4%) is high enough to detect these resonances. Given the signal-to-noise value, we estimate that we should be able to detect levels as low as 0.2% for Li occupancy on the Mn site (where 1% of the Li in the $Li_{1/3}Mn_{2/3}$ layers will be present as $Li(Mn)_5Li$ environments). Thus our NMR results provide strong evidence for long-range ordering of Li and Mn in the honey-comb layers in both samples.

Stacking of two honey-comb layers generates two distinct local environments for the Li in the Li layers (the Li' ions) in between the two honey-comb layers, with a site multiplicity of 1:2. These differ in the arrangements of the Li and Mn in their first and second cation coordination shells. In the A_1B_1 stacking shown in Fig. 3.1.b, the Li' ions occupy the "*C*" positions in the A_1B_1 blocks, indicated by crosses in this figure. These sites correspond to the *2c* and *4h* sites in the *C*2/*m* structure. The *4h* and *2c* Li sites both contain four Mn ions in the first cation coordination shell, with on average eight Li–O–Mn bond angles of 93.1° and 92.5° and four more distant ions (in the second coordination shell) with on average four Li–O–Mn bond angles of 172.8° and 171.3°, respectively (Fig. 3.4).[3] (Again, we have ignored the six Li in the first coordination sphere from the Li layers. We have also used the structure of Massaroti *et al*.[3] to calculate the quoted bond angles; these angles do change significantly when using the values from our structural refinement presented below.) Since Li–O–Mn bond angles closest to 90° result in the largest positive shifts (approx. 250 ppm per Mn^{4+} ion, or 125 ppm per Li–O–Mn connectivity) and angles closest to 180° result in large negative shifts (approx. -70 ppm per Mn^{4+} ion or Li–O–Mn connectivity),[18] the shift for the *4 h* site is expected to be slightly smaller than that for the *2c* site, consistent with the observed shifts seen in Fig.3.4.(a) of the intense (759 ppm) and weaker (775 ppm) resonances.

The ^{6}Li MAS NMR spectrum (Fig. 3.4.(b) of Li_2MnO_3-850-1d contains a whole series of resonances at 750–800 ppm. This is not consistent with simple $A_1B_1C_1$ *(C*2/*m)* stacking where only two Li' sites are predicted. Similarly, $A_1B_1C_2$ *(P*$3_1$12*)* stacking of ideal layers, where the Li, Mn and O ions all occupy positions on a perfect α-$NaFeO_2$ lattice also generates only two Li sites (all the Li' layers are equivalent due to the 3_1 axis).

The additional resonances must arise from stacking faults or intergrowths of different structures. A Li ion in the A_1B_1 block contains Mn^{4+} ions in its first and second cation coordination shells in the A_1 and B_1 blocks. The closest Mn^{4+} ions in a C_1, C_2 *or* C_3 layer are more than 7Å away and are separated by six M–O bonds (M=Li, Mn). It is, therefore, unlikely that the Mn^{4+} ions in the C (C_1, C_2 *or* C_3) layers produce a significant contribution to the Fermi contact shift. Instead, the differences in shifts most likely arise from small changes in Li–O–Mn bond angles that arise from differences in the stacking. To illustrate this effect, we started with the Li_2MnO_3 *C*2/*m* structure and replaced half of the Mn ions by Li and all of the Li ions by Mn in one layer, to generate a fault in the sequence, which can be written as $A_1B_1C_1A_1B_2C_1A_1B_1C_1$ . . . In order to provide a rough estimate of the shift, we assumed that the M–O bond angles remain unchanged in a stacking fault. In this scenario, the Li' ions in A_1B_2 blocks will have slightly different Li–O–Mn bonds of 89.4° (×8) and 171.5° (×4) for the first environment and 89.4° (×8) and 172.5° (×4) for the second. Larger shifts than those seen for ordered *C*2/*m* environments are predicted for these local environments. Slightly different environments and new resonances are similarly generated for Li' ions in an A_1B_3 block. Thus, it is clear that even deviations from ideal stacking, caused by stacking faults of transition metal layers, will likely generate small local distortions, resulting in Li' resonances with slightly different shifts.

3.4.2. XRD refinements and simulations

Rietveld refinements were performed for the two Li_2MnO_3 samples and are presented here in order to illustrate some of the pitfalls and difficulties associated with the structural refinements of these heavily faulted materials. Fig. 3.5 shows the attempted Rietveld refinement with GSAS-EXPGUI[19] for the Li_2MnO_3-1000-1m sample. *C*2/*m* space group was used and cell parameters of a=4.9303(1)Å, b=8.5264(1)Å, c=5.0264(1) Å and β=109.43° were found. As discussed above, the $P3_112$ space group does not account for the splitting of some higher-order reflections. Unfortunately, the fit to the profile is poor due to both the differential line broadenings of the reflections, particularly in the 20–35° 2θ region, and the weaker intensities of these peaks in comparison to those predicted for the ideal Li_2MnO_3 structure. Previous workers (e.g., Massarroti *et al*.[3] for Li_2MnO_3 and Kobayashi *et al*.[10] for the *C*2/*c* structure of Li_2IrO_3) have attempted to improve the fit by introducing Li/Mn exchange between the sites in the honey-comb layers. Li/Mn exchange does indeed result in a slightly improved fit (R_{wp} from 30.6% to 29.7%, R_p from 24.5% to 23.5%). However, the obtained *R*-factors are still quite high and the profile fit is poor. Most importantly, the NMR spectra provide no evidence for this Li/Mn exchange and, hence, this approach does not appear justified. Attempts were also made to refine the structure of the Li_2MnO_3-850-1d sample, but the obtained Rietveld profile fit was even worse unless the 20–35°, 2θ (Cu$K\alpha_1$) region was excluded. Values of a=4.923(3)Å, b=8.516(4)Å, c=5.017(2)Å and β=109.25(3)° were found with the *C*2/*m* space group, along with *R*-factors of R_{wp}=8.9 and R_P=4.9% (for the profiles with the large excluded regions). Although no peak splitting was observed due to the monoclinic

distortion, the broadening of certain reflections (e.g., the $20\bar{2}$ and 131 *C*2/*m* reflections; 114 and $11\bar{4}$ in the ideal hexagonal $P3_112$ cell) could not be accounted for by using the $P3_112$ cell. The value of β is closer to the ideal value of β (109.11) than the value of β found for the Li_2MnO_3-1000-1m sample, indicating a smaller monoclinic distortion of the unit cell. Line broadening of the XRD peaks is most likely due to disorder in the stacking of transition metal layers. This hypothesis was tested by performing simulations of the XRD data with the DIFFaX program.[11] A wavelength of 1.5406Å and a pseudo-Voigt broadening profile function (u=0:1, v=-0.1, w=50 and σ=0.6) were used. For convenience, the hexagonal $P3_112$ cell was used in all the simulations. We chose cell parameters of a=4.92Å and c=14.217Å, which were obtained by indexing the Li_2MnO_3-1000-1m XRD pattern with the $P3_112$ cell. This cell will not account for the splittings of the higher-order reflections due to the monoclinic distortion.

The unit cell was divided into three layers (*A, B* and *C*), each layer consisting of an oxygen, a lithium (Li'), a second oxygen and a honey-comb layer composite block. There are then nine types of layers, (A_i, B_i and C_i, where i=1, 2 or 3), since there are three ways of arranging Li atoms in the honey-comb layers. This notation is identical to that introduced in Fig. 3.1 to describe the different stacking schemes. Structures are generated in DIFFaX by listing probabilities for a particular sequence of stacking vectors, each vector mapping one layer onto the next. For example, *C*2/*m* stacking is generated by setting probabilities *P* for the stacking vectors, $A_1 \rightarrow B_1$, $B_1 \rightarrow C_1$, and $C_1 \rightarrow A_1$ to one; the probabilities for all other vectors are set to zero. Similarly, $P3_112$ stacking involves setting probabilities of one for the following stacking vectors, $A_1 \rightarrow B_1$, $B_1 \rightarrow C_2$, $C_2 \rightarrow A_1$. A stacking fault is then introduced by setting P < 1 for some of the vectors. There are

a number of different ways of generating faults in the stacking of transition metal layers. The simple *C*2/*m* stacking fault …$A_1B_1C_1$—*f*—$A_2B_2C_2$ maintains the monoclinic distortion (Fig. 3.6(a)), while others involving a rotation of the stacking direction by 120° or 240° will result in loss of the monoclinic distortion (Fig. 6(b) and (c)). Even a simple *C*2/*m* "translational" stacking fault[20] (—f—) such as …$A_1B_1C_1$—*f*—$A_2B_2C_2$… requires that we define probabilities *P* for all the possible stacking vectors, as illustrated in the table provided in the Supplemental material. Figs. 3.7a and 3.8a display the XRD simulations for Li_2MnO_3 with varying degrees of stacking faults, and $P3_112$ and *C*2/*m* stacking schemes, respectively. Both space groups seem to model the differential broadening, when sufficient stacking faults are introduced.

A concentration of stacking faults of around 5% has to be introduced to model the XRD data if the $P3_112$ model is used, while a higher concentration of around 10% is required for the *C*2/*m* model for Li_2MnO_3-850-1d. (10% of stacking faults indicates that a fault occurs on average every 10 [$Li_{1/3}Mn_{2/3}$] layers). In contrast, only around 0.5% for the $P3_112$ model and 2% of faults for the *C*2/*m* model, are required to model the Li_2MnO_3-1000-1m data. This is illustrated in Figs. 3.7b and 3.8b, which show the 20–35°, 2θ region. Although the simulations model the experimental data well, the Li_2MnO_3-850-1d sample appears to be more heterogeneous than implied by our model, containing both more well-ordered and more disordered regions. The observation that a higher number of faults are required to model the experimental data, for models using *C*2/*m* vs. $P3_112$ stacking is ascribed to small differences in structure factors associated with the two stacking schemes. This is due to both the different packing arrangements of the two structures and the differences in symmetry. This is apparent from a simple visual

inspection of the two structures shown in Fig. 3.1b and c. For example, the $020_{C2/m}$ (i.e., *C*2/*m* indexing) reflections result from diffraction from the set of planes parallel to the mirror planes shown in (d). *C*2/*m* packing clearly results in a larger structure factor for this reflection (approximately a factor of two higher), since all the Li^+ ions are located on the planes. However, the $P3_112$ space group contains a 3-fold screw axis and thus, there are three equivalent (100) planes. This results in ratios of approx. 1:0.172 ($003:020_{C2/m}$) and 1:0.202 ($003:100_{P3112}$) for the intensities of the first two observed reflections for *C*2/*m* and $P3_112$ cells, respectively. Rietveld refinements of the structure and results from first principles calculations suggest that *C*2/*m* stacking is a more appropriate stacking scheme, at least for Li_2MnO_3, and thus the higher numbers of stacking faults obtained from the *C*2/*m* simulations should reflect the concentrations of faults present in these materials. Furthermore, the peak shapes of the $h\ 0\ l\ _{P3112}$ reflections obtained with the *C*2/*m* stacking are closer to the lineshapes seen experimentally for the Li_2MnO_3-1000-1m sample. As the disorder increases, it will eventually be impossible, and not even appropriate, to distinguish between $P3_112$ stacking and *C*2/*m* stacking with rotational stacking faults (Fig. 3.6(b) and (c)).

No large differences are seen for the 20–35°, 2θ regions between simulations made for the *C*2/*m* simple stacking faults shown in Fig. 3.6(a), vs. stacking faults that introduce 120° rotations in the stacking (Fig. 3.6(a–c)). However, we have not attempted to model these stacking faults for layers with non-ideal values of β. Stacking faults that introduce these rotations are expected to result in broadening of some of the reflections at higher values of 2θ, e.g., at 45°, as observed in the experimental data of the more disordered samples. These observations are consistent with XRD simulations performed

for the layered mineral Celadonite, where "rotational" vs. "translational" stacking faults could not be distinguished by XRD.[20] No *h k l* $_{P3112}$ reflections should be observed in the 20–35° region for random stacking of layers. In our simulations, a weak peak remains at the same 2θ value as the *h* 0 0 peak (0 2 0 $_{C2/m}$ indexing) remains. An enlargement of this region (insert in Fig. 3.7(a)) shows a reflection with a characteristic lineshape (a Warren peak[21]) from a 2D crystal, as observed, e.g., in samples of turbostatically disordered graphite[22, 23] or in $LiAl_2(OH)_7 \cdot 2H_2O$.[24]

This peak is tentatively ascribed to an *h k* reflection. Furthermore, this suggests that the experimentally observed broadening of the *h* 0 0 peaks in the Li_2MnO_3-850-1d and Ni^{2+}-containing materials is due to the finite sizes of the ordered domains in the *ab* planes. These results are consistent with the DFT calculations, where although the *C*2/*m* structure was found to be the ground state, only small differences in energy per formula unit between the stacking schemes were observed. These small energy differences indicate a small energy penalty associated with a shifting of the transition metal stacking. Since the experimentally determined concentration of stacking faults decreases on extended annealing, the faults seen in these materials are not ascribed to thermal stacking faults but rather to disorder arising from the slow kinetics associated with ordering both in the *a*–*b* plane and in the c-direction. The growth of long-range ordering in the *c*-direction is expected to be particularly slow, especially given the very small energy differences between the different stacking schemes. Whether such small energy differences will lead to thermal stacking faults depends on the coherence length of the Li–Mn ordering within the transition metal layer, as this determines the size of the domain over which the fault extends and hence its total energy. Only if this total energy

of the fault is of the order of the thermal energy can faults be stabilized by entropic effects. Hence, extremely high temperatures are likely required to increase the concentration of the thermal stacking faults in the more-well ordered materials.

Finally, the results here should be compared with our earlier single-crystal electron diffraction results.[5, 6] An apparent 3-fold axis along the *c*-direction was seen in all the zone axes that were investigated (e.g., the $[\bar{1}11]_{hex.}$and $[001]_{hex.}$ zones, where the cells are indexed based on the α-NaFeO2 cell (i.e., $[\bar{3}1\bar{6}]_{mon.}$ and $[103]_{mon.}$, respectively, using the *C*2/*m* indexing)).[8] The apparent 3- fold axis seen by electron diffraction is ascribed to the 120° rotational stacking faults, which may introduce apparent 3-fold rotation axes in single crystal diffraction patterns, for appropriate concentrations of stacking faults or configurations.[20] For sufficiently thick samples and high concentrations of defects, rotational stacking faults should result in three sets of reflections with equal intensity, due to the three different unit cells related by the 3-fold screw symmetry axis. For thinner samples, or for samples with very few faults, the reflections from the three different cells may have different intensities. Similar phenomena have been observed in other disordered layered materials. For example, in $LiAl_2(OH)_7{\bullet}2H_2O$, which contains ordered $[Li_{1/3}Al_{2/3}]$ layers, disorder in the stacking sequences leads to a hexagonal indexing of the diffraction pattern, although the structure is better described by the *C*2/*m* cell.[24] Simulations of the electron diffraction data of our systems are currently in progress to explore this in more detail.

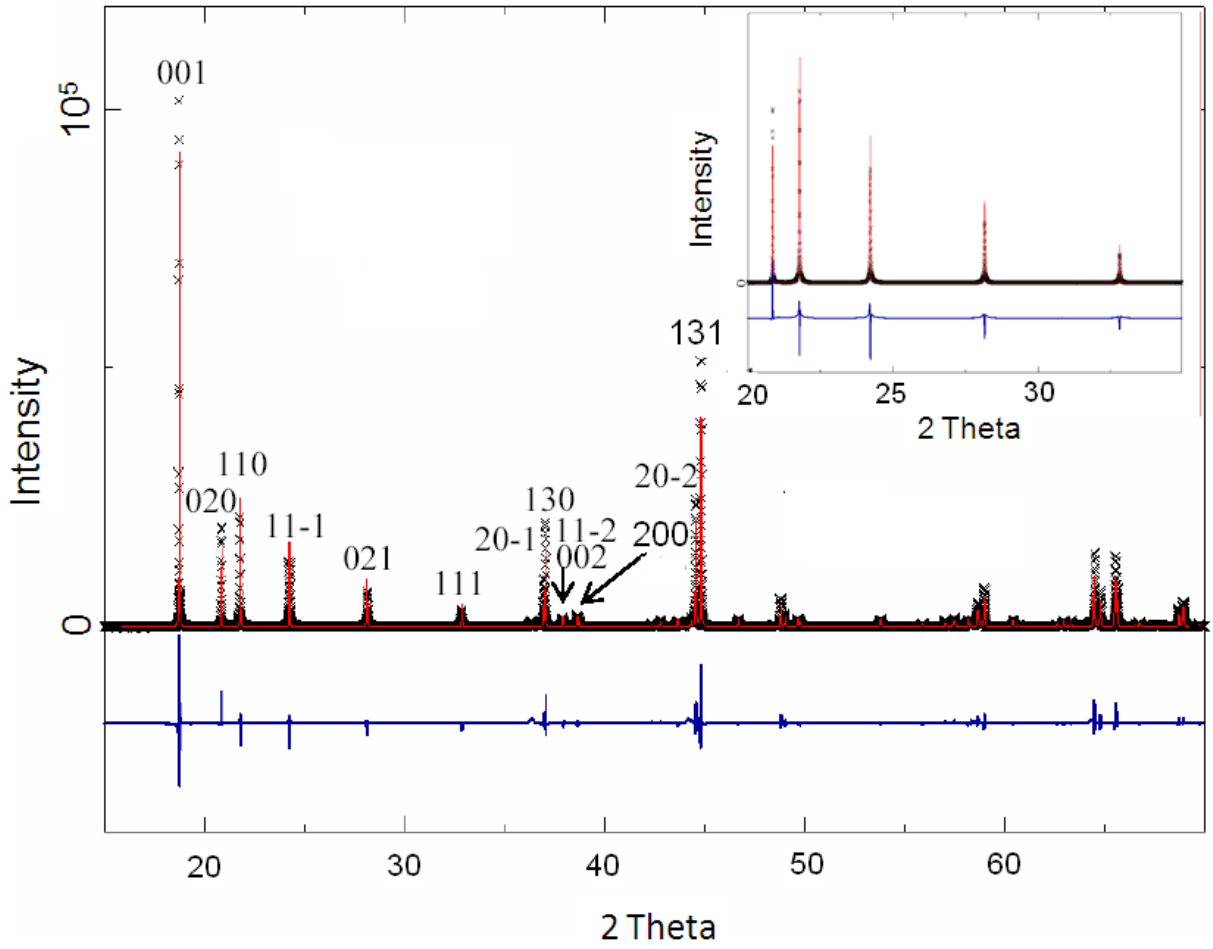

Figure 3.5: Rietveld refinement using the XRD pattern (λ=0.4958Å) of Li_2MnO_3-1000-1m. The crosses and the solid line represent the experimental data and the calculated pattern, respectively. The difference between the calculated and experimental patterns is shown below the data. For clarity, the 2θ values were changed to correspond to those for Cu$K\alpha_1$ X-ray irradiation (λ=1.5406 Å).

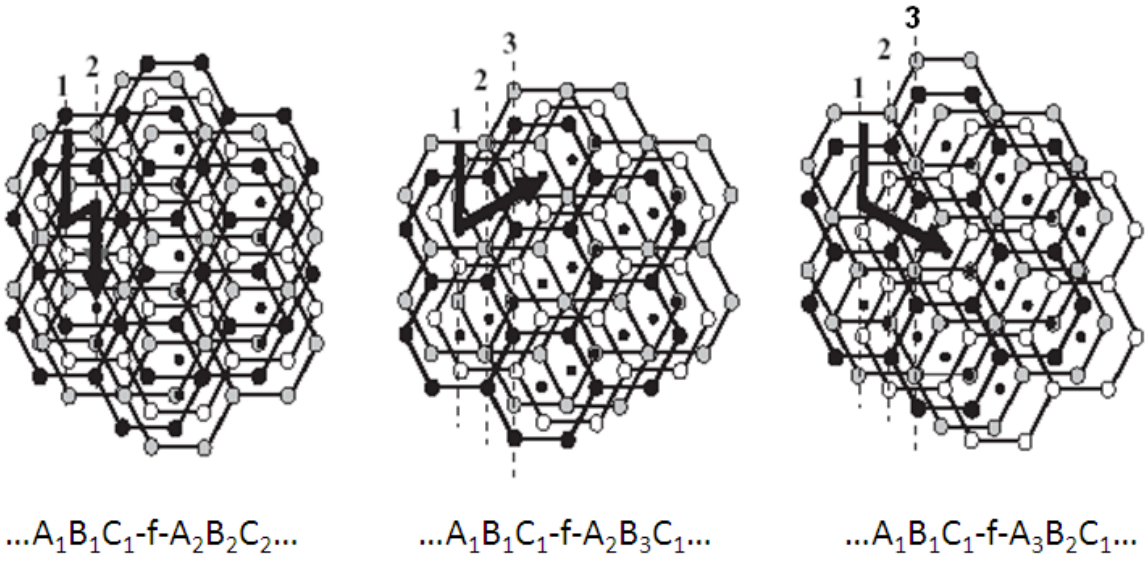

Figure 3.6: Examples of *C*2/*m*-type stacking faults. The arrows indicate the directions of the stacking faults.

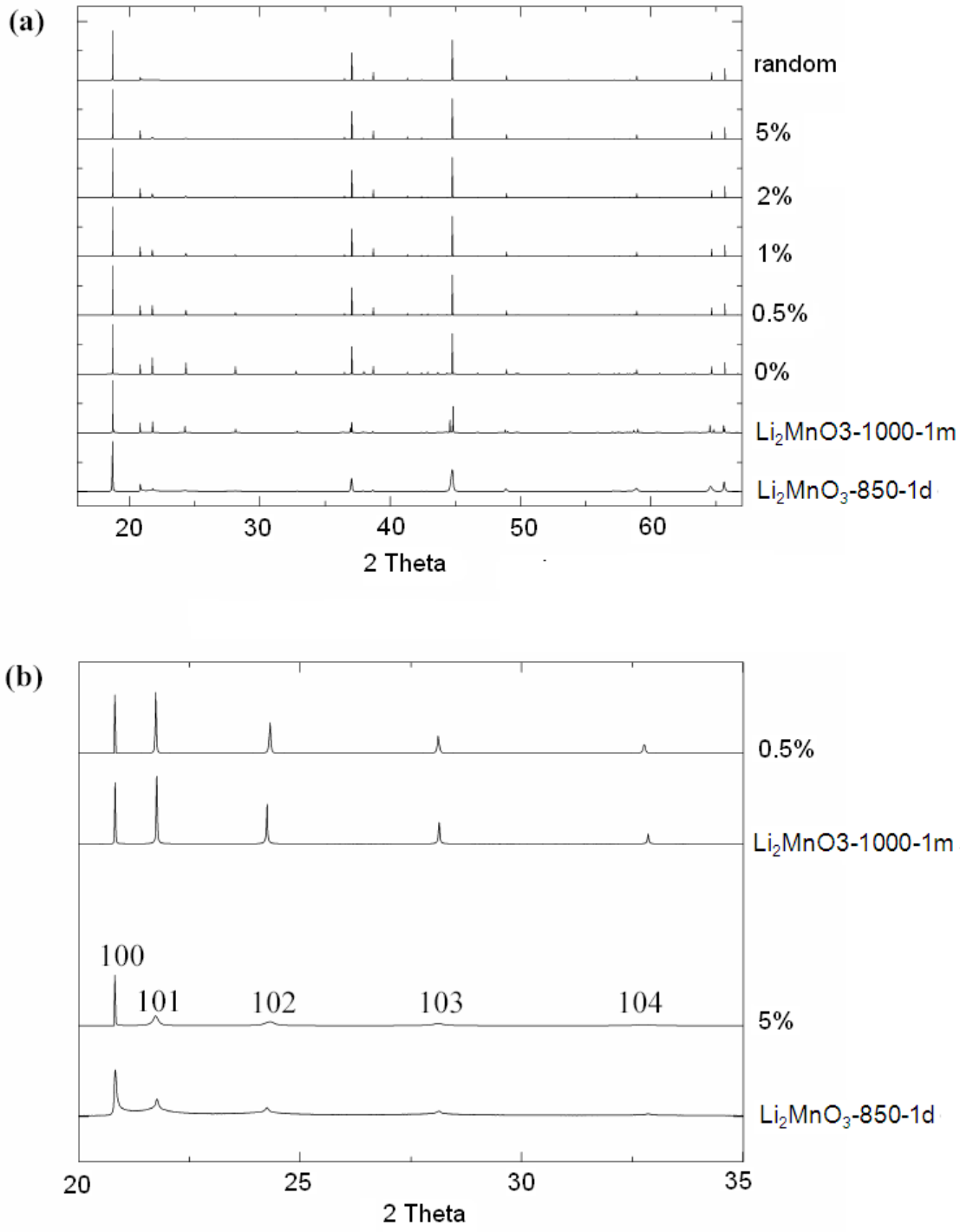

Figure 3.7: (a) Comparison between experimental and simulated XRD patterns between 20 and 35° (λ=1.5406 Å) of Li_2MnO_3 with $P3_112$ stacking with different percentages of stacking faults. The inset on top of the figure is a zoom of the 100 peak for the random case. (b) Enlargement between 20 and 35°, 2θ showing the best fit between experimental and simulated data. The Miller indexes for the $P3_112$ space group are shown.

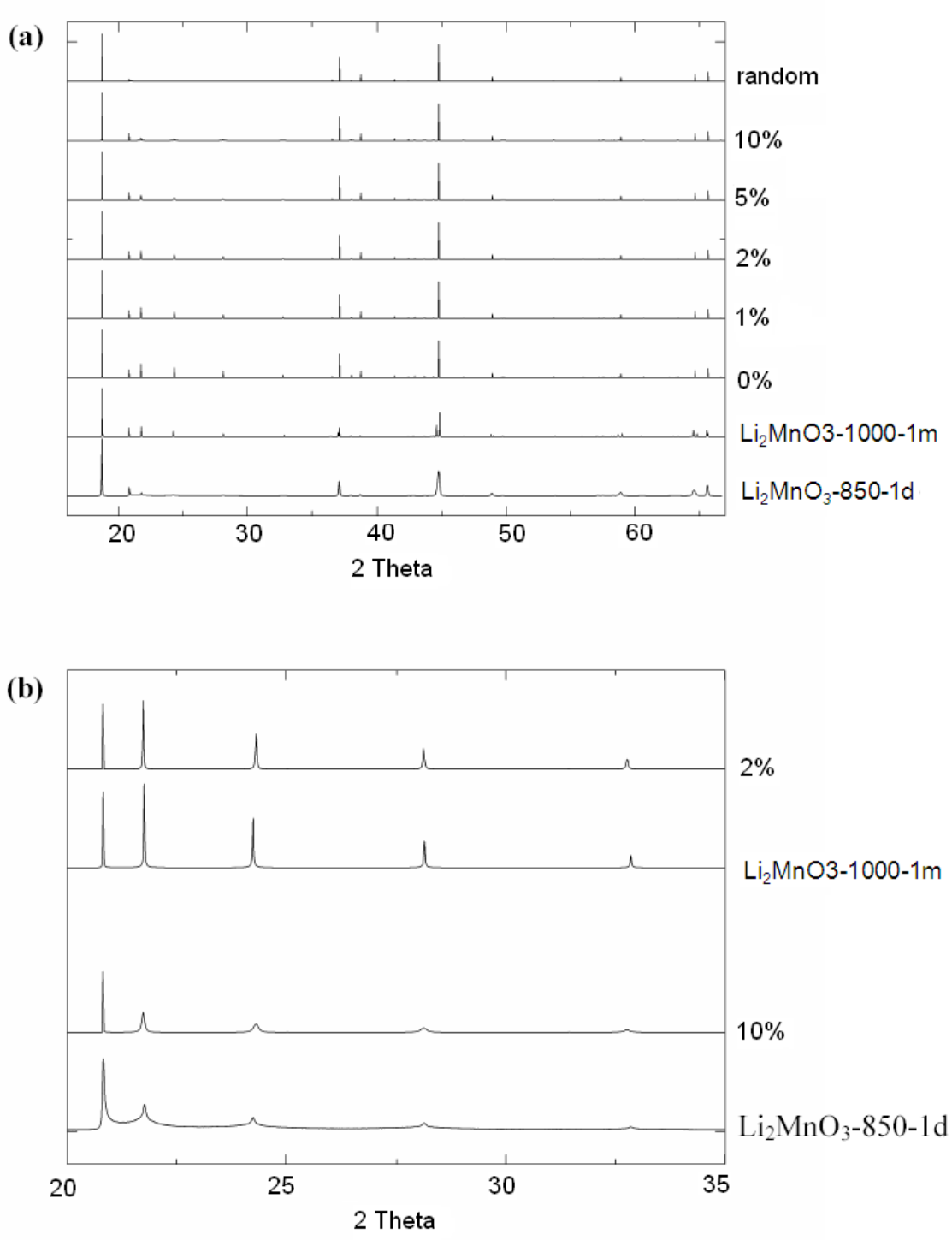

Figure 3.8: (a) Comparison between experimental and simulated XRD patterns (λ=1.5406 Å) of Li_2MnO_3 with *C2/m* stacking and different percentages of stacking faults. (b) Enlargement between 20 and 35° , 2θ showing the best fit between experimental and simulated data.

3.5. Conclusions

A combination of short- and long-range structural probes has been used to investigate ordering in the Li_2MnO_3–$Li[Ni_{0.5}Mn_{0.5}]O_2$ pseudo-binary. Li NMR experiments, which probe short-range order, show that the $[Li_{1/3}Mn_{2/3}]$ layers of Li_2MnO_3 are well ordered. Based on the signal-to-noise ratio of the experiments, an upper limit for Li/Mn disorder in these layers of 0.2% (Li occupancy on the Mn site) can be estimated. The NMR signals of Li ions in the Li layers, which separate the $[Li_{1/3}Mn_{2/3}]$ layers, suggest that the stacking of $[Li_{1/3}Mn_{2/3}]$ layers contains faults, particularly in the Li_2MnO_3 sample .red for a short period of time. These faults result in broadening of certain reflections (*h* 0 *l* reflections indexed using a hexagonal cell) resulting in poor profile fits to the experimental XRD data in Rietveld refinements of the structures of these materials. Slightly lower R-factors for the refinements were obtained by allowing Li/Mn exchange in the $[Li_{1/3}Mn_{2/3}]$ layers, an approach that has been used previously in the literature,[3] this changes the absolute and relative intensities of the reflections due to the Li/Mn ordering (e.g., the $020_{C2/m}$ and $111_{C2/m}$ reflections) improving the profile fit. However, the NMR results suggest that this approach is not necessarily justified.

DIFFaX simulations of the synchrotron XRD data were performed to model the effect of stacking faults on the XRD patterns. These simulations model the line broadenings and intensity changes of the superstructure peaks arising from ordering of the $[Li_{1/3}Mn_{2/3}]$ layers and allow the concentrations of stacking faults to be estimated. The XRD data are consistent with *C*2/*m* structure. The apparent 3-fold symmetry axis seen in the electron diffraction of these materials is ascribed to rotational stacking faults that

result in stacking in three different directions related by the 3-fold screw axis. Similar superstructure peaks are seen on Ni doping, the $[Li_{1/3}Mn_{2/3}]$-like ordering being better developed for lower Ni^{2+}-doping levels. Again, the XRD patterns are consistent with faults in the stacking of the layers. Even for $Li[Ni_{1/2}Mn_{1/2}]O_2$, weak superstructure peaks are seen. Our results suggest that care needs to be taken when interpreting XRD patterns of these classes of materials. Even when superstructure peaks are not observed, long-range order may still be present in the layers (i.e., in the *ab* plane); if there is no order, or only weak ordering of the stacking of the layers in the c direction, the superstructure peaks will either be absent or will be very weak.

3.6. References

1. Lu, Z. H.; Beaulieu, L. Y.; Donaberger, R. A.; Thomas, C. L.; Dahn, J. R., *Journal of the Electrochemical Society* 2002, 149, (6), A778-A791.

2. Breger, J.; Dupre, N.; Chupas, P. J.; Lee, P. L.; Proffen, T.; Parise, J. B.; Grey, C. P., *Journal of the American Chemical Society* 2005, 127, (20), 7529-7537.

3. Massarotti, V.; Bini, M.; Capsoni, D.; Altomare, A.; Moliterni, A. G. G., *Journal of Applied Crystallography* 1997, 30, 123-127.

4. Strobel, P.; Lambertandron, B., *Journal of Solid State Chemistry* 1988, 75, (1), 90-98.

5. Meng, Y. S.; Ceder, G.; Grey, C. P.; Yoon, W. S.; Shao-Horn, Y., *Electrochemical and Solid State Letters* 2004, 7, (6), A155-A158.

6. Meng, Y. S.; Ceder, G.; Grey, C. P.; Yoon, W. S.; Jiang, M.; Breger, J.; Shao-Horn, Y., *Chemistry of Materials* 2005, 17, (9), 2386-2394.

7. Jansen, M.; Hoppe, R., *Zeitschrift Fur Anorganische Und Allgemeine Chemie* 1973, 397, (3), 279-289.

8. Riou, A.; Lecerf, A.; Gerault, Y.; Cudennec, Y., *Materials Research Bulletin* 1992, 27, (3), 269-275.

9. Lang, G., *Zeitschrift Fur Anorganische Und Allgemeine Chemie* 1966, 348, (5-6), 246-&.

10. H. Kobayshi, M. T., M. Shikano, H. Kageyama, R. Kanno,J., *J. Mater. Chem* 2003, 13.

11. Treacy, M. M. J.; Newsam, J. M.; Deem, M. W., *Proceedings of the Royal Society of London Series a-Mathematical Physical and Engineering Sciences* 1991, 433, (1889), 499-520.

12. Ohzuku, T.; Makimura, Y., *Chemistry Letters* 2001, (8), 744-745.

13. Lu, Z. H.; MacNeil, D. D.; Dahn, J. R., *Electrochemical and Solid State Letters* 2001, 4, (12), A200-A203.

14. Yoon, W. S.; Kim, N.; Yang, X. Q.; McBreen, J.; Grey, C. P., *Journal of Power Sources* 2003, 119, 649-653.

15. Lee, Y. J.; Grey, C. P., *Journal of Physical Chemistry B* 2002, 106, (14), 3576-3582.

16. Morgan, K. R.; Collier, S.; Burns, G.; Ooi, K., *Journal of the Chemical Society-Chemical Communications* 1994, (14), 1719-1720.

17. Mustarelli, P.; Massarotti, V.; Bini, M.; Capsoni, D., *Physical Review B* 1997, 55, (18), 12018-12024.

18. Grey, C. P.; Lee, Y. J. 2003; 2003; pp 883-894.

19. Toby, B. H., *Journal of Applied Crystallography* 2001, 34, 210-213.

20. F. Muller, A. P.-o., G. Besson, V.A. Drits,, *Mater. Struct.* 1999, 6, 129.

21. Warren, B. E., *Physical Review* 1941, 59, (9), 693-698.

22. Yang, D.; Frindt, R. F., *Journal of Applied Physics* 1996, 79, (5), 2376-2385.

23. Shi, H.; Reimers, J. N.; Dahn, J. R., *Journal of Applied Crystallography* 1993, 26, 827-836.

24. Thiel, J. P.; Chiang, C. K.; Poeppelmeier, K. R., *Chemistry of Materials* 1993, 5, (3), 297-304.

Chapter 4

$LiNi_{0.5+\delta}Mn_{0.5-\delta}O_2$ – A high-rate, high-capacity cathode for lithium rechargeable batteries

Abstract

In single-cell tests, a $Li/LiNi_{0.5+\delta}Mn_{0.5-\delta}O_2$ (δ=0.04) battery is here shown to give a performance and cycle life comparable to that obtained with the $LiCoO_2$ cathode now used in cellular phones and lap-top computers. This was accomplished without the use of the expensive and toxic element cobalt and without compromising the volume energy density desired for hand-held devices. ^6Li Solid State NMR and Synchrotron XRD combined with Rietveld refinement reveal that the cation mixing in this compound is much less compared to $LiNi_{0.5}Mn_{0.5}O_2$.

This chapter is part of the paper: "$LiNi_{0.5+\delta}Mn_{0.5-\delta}O_2$ – A high-rate, high-capacity cathode for lithium rechargeable batteries", Schougaard, S. B.; Bréger, J.; Jiang, M.; Grey, C.P. and Goodenough, J. B.*; Advanced Materials,* **2006**, 18, 905-909. The sample synthesis and electrochemical characterization represent the contributions of S. B. Schougaard.

4.1 Introduction

Key to the electrochemical performance of $LiCoO_2$ is its layered α-$NaFeO_2$ structure shown in Fig. 4.1a. This $LiMO_2$ structure is known to support high Li^+-ion mobility when the Li^+ and M^{3+} ions are well ordered, as has been demonstrated with $Li_{1-x}CoO_2$.[1, 2] In a well ordered structure, the Li+-ions are free to move in the 2D space between strongly bonded MO_2 layers, a space that becomes larger on removal of Lithium.[3] This expansion is due to the electrostatic repulsion between close packed oxide-ion sheets, which readily overcomes any attractive van der Waals bonding between oxygen once the Li^+ ions are removed. Opening of the gap between MO_2 layers enlarges the bottlenecks between adjacent Li^+-ion sites, which lowers the motional enthalpy.

Unfortunately, materials with the α-$NaFeO_2$ structure commonly have a large degree of cation disorder. Introduction of M atoms into the Li^+-ion sites, as illustrated in Fig. 4.1b, not only disrupts the Li^+-ion pathways, it also holds the neighboring MO_2 sheets together, thus lowering the Li^+-ion mobility. To obtain a high discharge rate and a large electrode capacity, it is essential to minimize the entrance of the M atoms into the Li^+-ion sites not only in the initial synthesis, but also on removal of Lithium. Therefore, in addition to synthesis of a well-ordered $LiMO_2$ parent compound, it is also necessary to choose an M atom that gives a large voltage versus the Li+/Li anode and does not migrate to the Li sites on removal of Lithium. Migration from the MO_2 layer to the Li-ion sites is through a tetrahedral site, so M cations with large octahedral-site preference energy are required.

According to the theoretical calculation, $LiNiO_2$ should be well ordered. However, partial reduction of Ni^{3+} to Ni^{2+} during sintering combined with the volatility of Lithium, makes it difficult to synthesize $LiNiO_2$ without formation of $Li_{1-x}\ Ni_{1+x}O_2$.[4] The Ni^{2+} has nearly the same size as the Li^+-ion, so Ni^{2+} ions readily occupy the Li^+-ion sites. Therefore, a nominal $LiNiO_2$ cathode exhibits a large initial capacity (~150 mAh/g) only at low charge/discharge rates. Moreover, although the Ni^{4+}/Ni^{3+} couple gives a high voltage vs. Li^+/Li, nominal $LiNiO_2$ also exhibits a capacity fade that increases with each successive discharge/recharge cycle.[4-6] To overcome this problem, researchers have investigated substitution of numerous other first-row transition-metal ions for Ni in $LiNi_{1-x}M'_xO_2$ ($x<0.5$), M'= Ti, Mn, Fe, Co, Cu and combinations thereof.[5-10] In this context, the most interesting of these investigations was of $LiMn_{0.5}Ni_{0.5}O_2$ first reported almost simultaneously by Ohzuku et al.[8] and Lu et al,[11] and stable capacities of up to 200 mAh/g were reported. The Li^+/Ni^{2+} exchange is, however, significant for these materials with approximately 20% of the total Ni^{2+} content been found in the Li layers, 10%[12] of the total Li^+ ions residing in sites in the $Ni^{2+}Mn^{4+}$ in environments predominantly near the Mn^{4+}.[13] Less Li^+/Ni^{2+} exchange is seen for $LiMn_{1/3}Co_{1/3}Ni_{1/3}O_2$, but this compound contains Cobalt.[14] The Li^+/Ni^{2+} exchange is also reduced in $Li[Ni_xLi_{1/3-2x/3}Mn_{2/3-x/3}]O_2$ series, which may be viewed as a solid solution between $Li[Li_{1/3}Mn_{2/3}]O_2$ and $Li[Ni_{1/2}Mn_{1/2}]O_2$.[15]

In this work, we document the feasibility of producing a $LiNi_{0.5+\delta}Mn_{0.5-\delta}O_2$ ($\delta>0$) cathode material with high reversible capacity and rate capabilities without the use of cobalt by combining our understanding of the factors governing cation order with a simple synthetic technique that ensures good cation mixing. In this formulation, the

manganese is present as Mn^{4+}, which has a strong octahedral-site preference that prevents migration to the Li^{+}-ion sites. Similarly, the nickel is present as Ni^{2+}, Ni^{3+} and low-spin Ni^{4+}, all of which have a strong octahedral-site preference; thus, there is a lower probability that nickel or manganese passes through the tetrahedral into the octahedral site in the lithium layers once lithium has been partly removed. We chose $LiNi_{0.56}Mn_{0.44}O_2$ for two reasons (1) introduction of 0.04 Ni^{3+} per formula unit lowerst and (2) a nominal ratio Mn/Ni 0.44/0.56 rather than unity ensures that no Li_2MnO_3 is formed even in the decomposed precursor.

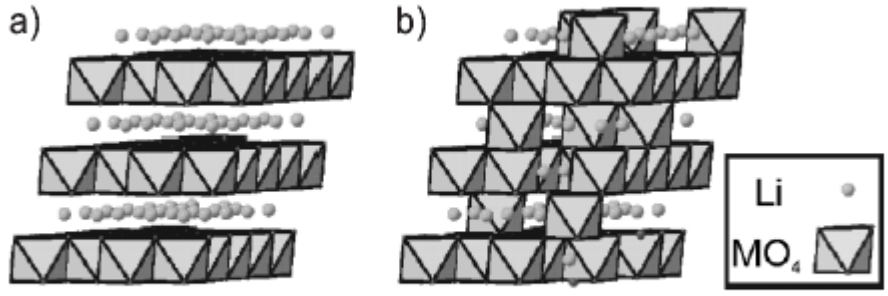

Figure 4.1: Schematic showing lithium diffusion obstructed when (a) the ordered α-$NaFeO_2$ structure (b) exhibits a high degree of mixing Li/M mixing, where M is a transition metal.

4.2. Experimental

4.2.1 Synthesis

$LiNi_{0.56}Mn_{0.44}O_2$ was prepared by co-precipitation method. Manganese(II) oxalate and nickel(II) oxalate, 0.44:0.56 molar ratio, was co-precipitated from an aqueous solution of nickel(II) acetate and mangenese(II) acetate in the presence of lithium acetate and excess acetic acid by addition of oxalic acid. A 15% excess of lithium was used to ensure a non-deficient final product. The precursor suspension was evaporated until dry on a hot plate with constant stirring before decomposition at 450 °C for 12–24 h in air. Synthesis was completed by sintering at 1000 °C for 10 h. The sample of $Li(Ni_{0.5}Mn_{0.5})O_2$ prepared for the ^6Li MAS-NMR experiment was prepared by a mixed hydroxide method[13, 15] which has been described in the previous chapter.

4.2.2 Sample Characterization:

Cation ratios were determined by ICPMS. The Mn/Ni ratio (0.44 ± 0.006:0.56 ± 0.001) was determined by a matrix-matched calibration-curve technique and confirmed by selective standard addition. The lithium/metal ratio (1.12 ± 0.12) was determined by standard addition in order to overcome matrix problems; this method inherently carries a greater standard deviation. Thus, an excess of lithium persisted in the final product. High-resolution synchrotron X-ray powder diffraction (XRD) data for $LiNi_{0.56}Mn_{0.44}O_2$ were collected at the X3B beam line at the National Synchrotron Light Source (NSLS),

Brookhaven National Laboratory (λ = 0.4958 Å). Attempted Rietveld refinement was performed with GSAS-EXPUGII. ^{6}Li MAS-NMR experiments were performed at an operating frequency of 29.47 MHz on a CMX-200 spectrometer with a double-resonance probe built by Samoson and co-workers. The sample was packed in a 2 mm rotor and a spinning frequency of 31 kHz (35 kHz for $Li(Ni_{0.5}Mn_{0.5})O_2$) was used. The spectrum was acquired with a rotor-synchronized echo-pulse sequence (90°–τ–180°– τ–acq), in which τ=1/ν_r. A π/2 pulse width of 3.5 μs was used with a pulse delay of 0.2 s.

4.2.3 Electrochemical Analysis

Charge and discharge profiles were collected by galvanostatically cycling between 2.75 and 4.3 V (Arbin BTS-2043). A 15 min rest period was employed between the charge and discharge steps. The electrochemical cells were button type (Cr2032, Hohsen Corp.), in which a circular lithium metal disk (Aldrich) 0.38 mm× 1.9 cm2 served as the anode and a 0.5 cm^2 circular disk made of thin sheets rolled from a mixture of the title material, acetylene black (Gunbai) and polytetrafluoroethylene (G-580, ICI), 70:25:5 (w/w/w), served as the cathode. The typical cathode mass, thickness, and densities were 5–9 mg, 0.03–0.08 mm, and 50–60 %, respectively. (see Supporting Information for the SEM images of the electrodes) The cells were flooded with 1M LiPF6 in a 1:1 ethylene carbonate/diethyl carbonate electrolyte (Ferro corp.); a thin sheet of microporous polyethylene (Celgard, K-849) insolated the positive electrode from the negative electrodes. Cell assembly was carried out in an argon-filled glove box.

4.3 Results and Discussion

The synthesis employed here ensures intimate mixing of Mn–Ni in the precursor at a molecular level.[16] This approach appears to be successful as the X-ray diffraction (XRD) pattern of the final product (Figure 4.2) can be assigned to the a-$NaFeO_2$ ($R\bar{3}m$) structure. Moreover, both the *c*/*a* ratio (4.97) determined from the unit-cell parameters (a = 2.87716(2) Å and c = 14.2716(1) Å) and the intensity ratio of the three peaks in the fingerprint region ($R_{(006+102)/101}$= 0.48) indicate a high degree of Li–M order in their respective layers.[9] This qualitative assignment is indeed confirmed quantitatively by the Li NMR spectrum displayed in Figure 4.3. Two classes of resonances are typically seen for $Li[Ni_xLi_{1/3-2x/3}Mn_{2/3-x/3}]O_2$ systems at approximately 700 and 1500 ppm, which can be assigned uniquely to Li^+ in the Li^+ layers and transition-metal layers, respectively, based on the relative intensities of the resonances and their Fermi-contact shifts.[17] These two sets of resonances are clearly seen for $LiMn_{0.5}Ni_{0.5}O_2$, a material with approximately 10% Li–Ni site exchange (based on the total lithium content, see Figure 4.3).

In comparison, the ^6Li magic-angle spinning NMR spectrum of the new material $LiNi_{0.56}Mn_{0.44}O_2$ contains only a very weak resonance at 1500 ppm, which can be assigned to Li^+ surrounded by six Mn^{4+} ions in transition metal layers. A weak resonance is also seen at approximately 1250 ppm (marked by an arrow), which is assigned to lithium surrounded by one Ni^{2+} and five Mn^{4+}. The NMR results show a much lower concentration of Li^+ in the transition-metal layers (ca. 5 %), compared to the $LiNi_{0.5}Mn_{0.5}O2$ reference sample; furthermore, the lithium local environments are also slightly different. A Rietveld refinement was performed on the structure of this material,

the fit is slightly improved when introducing a Li/Ni site exchange and the refined percentage of Li/Ni site exchange is 5.6(1) %. (Figure 4.2) The obtained R-factors are quite low (R_{wp} = 10.9 %, R_p = 8.4 %). It indicates that the nickel content in the lithium layer is noticeably lower than that seen for $LiMn_{0.5}Ni_{0.5}O_2$. Thus, it appears that a large fraction of the excess lithium detected by inductively coupled plasma mass spectrometry (ICP-MS) is not accommodated in the α-$NaFeO_2$ structure; it may however be present as a predominately amorphous surface layer of Li_2O, Li_2CO_3, or LiOH. Resonance arising from such a layer would give rise to long T_1 relaxation times and are suppressed in the spectrum of Figure 4.3. This surface layer would, owing to both the amorphous nature and the low scattering power of lithium and oxygen, be undetectable by XRD analysis. The surface layer would not hamper the electrochemistry as unperturbed surfaces are exposed during cathode fabrication.

Figure 4.4 shows the rate of discharge capability of the title compound. It is clear that even at rates approaching 5C, that is, 12 min discharge, capacities above 100 mAh/g are retained. The capacity loss due to increased rates is reversible; the capacity returned to its original value of 160 mAh/g at 0.1 $mAcm^{-2}$ after completion of the high-rates test. This observation and comparison with the results of Li(metal)/$LiCoO_2$ cells show that the cell potential and capacity at the highest rates are similar to those of $LiCoO_2$, and are not limited exclusively by the cathode material. A major limitation at high discharge rates is the ionic conductivity of the electrolyte- soaked separator membrane.

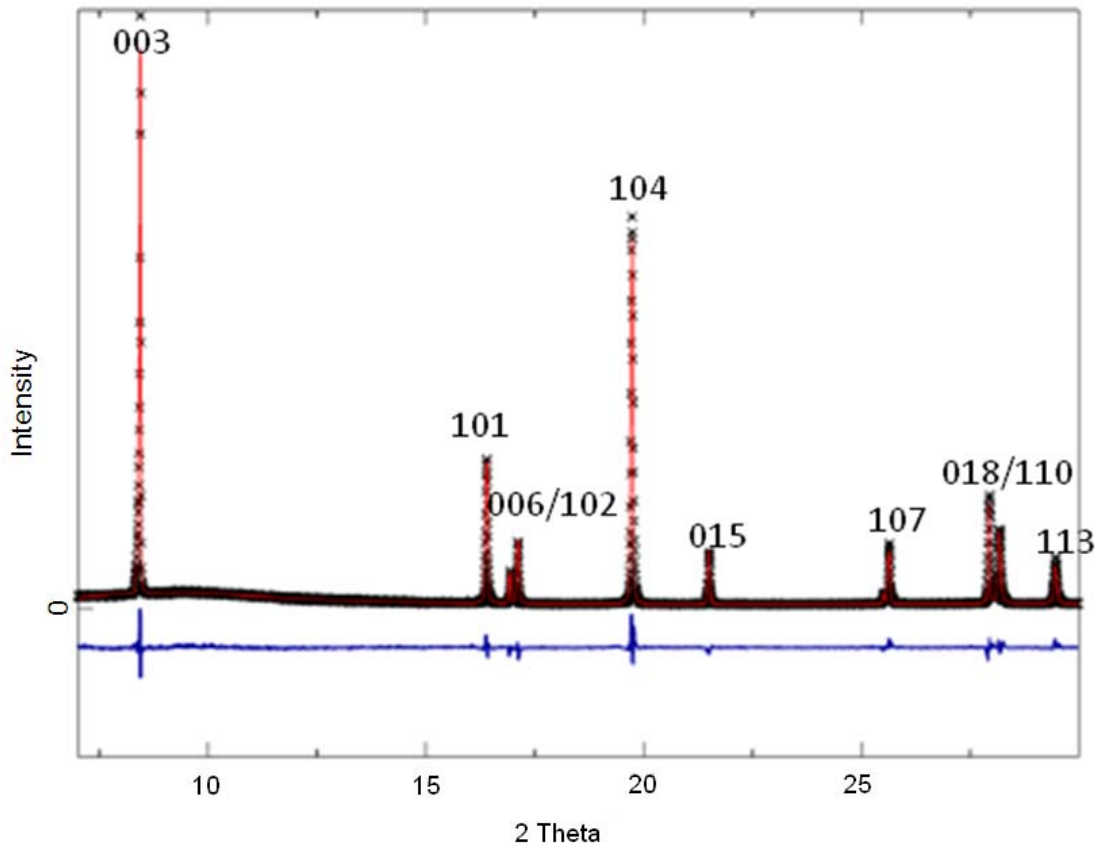

:

Figure 4.2: Rietveld refinement using the XRD pattern of $LiNi_{0.56}Mn_{0.44}O_2$ (λ = 0.4958 Å). The crosses and the solid red line represent the experimental and the calculated patterns, respectively. The difference between the calculated and experimental patterns is shown in blue below the data.

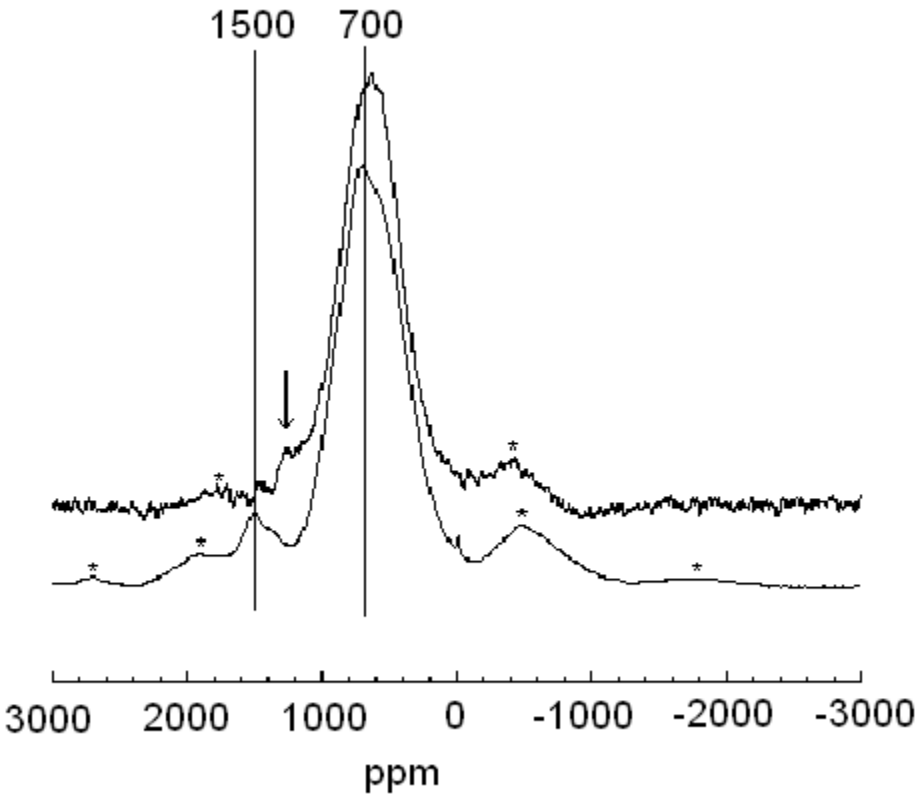

Figure 4.3: ^{6}Li MAS NMR of $LiNi_{0.56}Mn_{0.44}O_2$ (top, spinning frequency of 31 kHz) and $LiNi_{0.5}Mn_{0.4}O_2$ (bottom, spinning frequency of 35 kHz). The major isotropic resonances and spinning sidebands are marked with their shifts and asterisks, respectively.

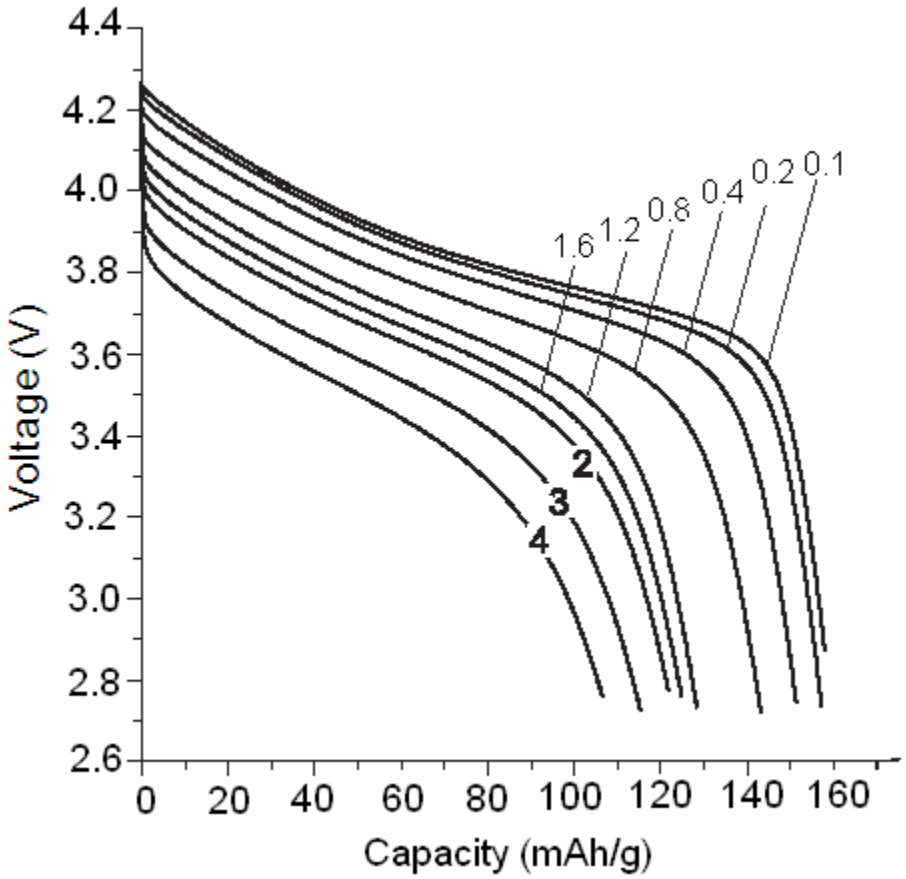

Figure 4.4: Discharge curves at different current densities indicated in $mAcm^{-2}$ on the graph (equivalent discharge times in hours: 11, 6, 3, 1, 0.7, 0.5, 0.4, 0.3, 0.2) from bottom to top.

4.4 Conclusions

In this work, we have fabricated a cathode material without the use of cobalt that exhibits a competitive discharge rate, weight, volume capacity, and cyclability comparable to $LiCoO_2$. The key factors contributing to this result are an understanding of the role of the relative ionic sizes to obtain a high degree of cation order, the relative positions of the redox energies relative to one another, and octahedral-site preference energies that inhibit migration of the transition-metal ions into the Li^+ sites upon removal of lithium. Synthesis of the ordered material that was employed does not depend critically on the lithium content of the starting constituents, provided that it is present in excess. Excess lithium is desirable because lithium is commonly volatilized during synthesis, making it difficult to control the lithium stoichiometry. Based on these findings, the $LiNi_{0.5+\delta}Mn_{0.5-\delta}O_2$ ($\delta > 0$) cathode material is an attractive candidate for replacing $LiCoO_2$, the cathode material now used in cellular telephones, laptop computers, camcorders, and other portable devices.

4.5 References

1. Abraham, K. M.; Pasquariello, D. M.; Willstaedt, E. M., *Journal of the Electrochemical Society* **1998,** 145, (2), 482-486.

2. Levi, M. D.; Salitra, G.; Markovsky, B.; Teller, H.; Aurbach, D.; Heider, U.; Heider, L., *Journal of the Electrochemical Society* **1999,** 146, (4), 1279-1289.

3. Levasseur, S.; Menetrier, M.; Suard, E.; Delmas, C., *Solid State Ionics* **2000,** 128, (1-4), 11-24.

4. Rougier, A.; Gravereau, P.; Delmas, C., *Journal of the Electrochemical Society* **1996,** 143, (4), 1168-1175.

5. Spahr, M. E.; Novak, P.; Schnyder, B.; Haas, O.; Nesper, R., *Journal of the Electrochemical Society* **1998,** 145, (4), 1113-1121.

6. Yoshio, M.; Todorov, Y.; Yamato, K.; Noguchi, H.; Itoh, J.; Masaki, O.; Mouri, T., *Journal of Power Sources* **1998,** 74, (1), 46-53.

7. Rossen, E.; Jones, C. D. W.; Dahn, J. R., *Solid State Ionics* **1992,** 57, (3-4), 311-318.

8. Ohzuku, T.; Makimura, Y., *Chemistry Letters* **2001**, (8), 744-745.

9. Joeng, J. W.; Kang, S. G., *Journal of Power Sources* **2003,** 123, (1), 75-78.

10. Kim, J.; Amine, K., *Journal of Power Sources* **2002,** 104, (1), 33-39.

11. Lu, Z. H.; MacNeil, D. D.; Dahn, J. R., *Electrochemical and Solid State Letters* **2001,** 4, (12), A200-A203.

12. Makimura, Y.; Ohzuku, T. 2003; 2003; pp 156-160.

13. Yoon, W. S.; Paik, Y.; Yang, X. Q.; Balasubramanian, M.; McBreen, J.; Grey, C. P., *Electrochemical and Solid State Letters* **2002,** 5, (11), A263-A266.

14. Ohzuku, T.; Makimura, Y., *Chemistry Letters* **2001**, (7), 642-643.

15. Lu, Z. H.; Dahn, J. R., *Journal of the Electrochemical Society* **2002,** 149, (7), A815-A822.

16. Mustarelli, P.; Massarotti, V.; Bini, M.; Capsoni, D., *Physical Review B* **1997,** 55, (18), 12018-12024.

17. Breger, J.; Dupre, N.; Chupas, P. J.; Lee, P. L.; Proffen, T.; Parise, J. B.; Grey, C. P., *Journal of the American Chemical Society* **2005,** 127, (20), 7529-7537.

Chapter 5

Electrochemical and Structural Study of Li-excess Material $Li[Li_{1/9}Ni_{1/3}Mn_{5/9}]O_2$

Abstract

The overcapacity mechanism and high voltage process of the Li-excess material $Li[Li_{1/9}Ni_{1/3}Mn_{5/9}]O_2$ are studied by solid state NMR, XRD, XAS and TEM. The cycling performance is improved dramatically when the material is cycled between 5.3-2.5V compared to 4.6-2.5V. A second phase is observed in the charged samples from high resolution XRD data, and the unit cell is expanded after the material is charged to 5.3V. The solid state NMR data of charged samples show that the high voltage process is associated with Li removal from the structure, but not only electrolyte decomposition. The NMR spectra of discharged samples indicate the cation rearrangement in the transition metal layers after high voltage process. XAS spectra suggest Ni^{2+} comes back and Mn^{4+} remains the same on discharge. However, the Ni edge shift to lower energy is observed from 4.6V to 5.3V on charge associated with the shape change of the spectra, indicating the local environment change. A mechanism of electrolyte oxidation by Ni^{4+} is proposed, which explains the overcapacity gained in the first charge, corresponding to further Li removal from the structure after the theoretical capacity based on Ni^{2+}/Ni^{4+} redox reaction.

5.1. Introduction

In the series of compounds $Li[Li_{1/3-2x/3}Ni_xMn_{2/3-x/3}]O_2$, when $x<1/2$, the total transition metal content in the sample is higher than the Li content, which is so-called Li-excess compounds. In these compounds, the amount of Li ions extracted, particularly in the 1st charge, is noticeably higher than the theoretical capacity calculated based on the Ni^{2+}/Ni^{4+} couple.[1-4] A flat, plateau-like region starting from 4.4V is always observed in the first charge, but this process is not reversible and is not seen in the first discharge and in subsequent cycles. Given the technological interest associated with these materials, much scientific effort has been devoted to determine where this overcapacity comes from. Lu *et al.* proposed an oxygen loss mechanism (removal of Li_2O) to balance the charge[2-4], which appears to be supported by Armstrong *et al.'s* observations of oxygen gas using *in situ* electrochemical mass spectroscopy measurements[5]. Unfortunately, the amount of oxygen gas produced was not quantified in these latter experiments, so it was not possible to determine whether the oxygen evolution accounts for all of the extra capacity. These authors also showed by using neutron and X-ray diffraction that the phase remained layered after the oxygen-loss process. However, significant questions remain: For example, how does migration of oxygen, nickel and manganese ions occur to form the new layered phase? If an ideal layered structure is formed, why does it only accommodate approx. 0.6 ~ 0.7 Li on deintercalation?

$Li[Li_{1/9}Ni_{1/3}Mn_{5/9}]O_2$ was chosen as a representative model compound in this work, in order to investigate the structural changes that occur during the first charge-discharge cycle in this series of compounds. ^{6}Li Magic Angle Spinning (MAS) Nuclear

Magnetic Resonance (NMR), high resolution X-ray Diffraction (XRD), X-ray absorption spectroscopy (XAS), and high resolution TEM experiments were all performed to study the short- and long-range structural and the accompanying morphology changes of the crystals during and after the high voltage process.

5.2. Experimental

5.2.1 Sample preparation

$Li[Ni_{1/3}Li_{1/9}Mn_{5/9}]O_2$ was prepared by double hydroxide method as described in Chapter 2. In this chapter, the sample was heated in air at 900ºC for 12hrs and quenched with liquid nitrogen. ^6Li enriched materials were prepared for the NMR experiments using ^6Li enriched $Li_2CO_3 \cdot H_2O$ as the starting material.

5.2.2 Electrochemistry

2032 type Lithium coin cells were used to study the electrochemical behavior of the compound and prepare cycled samples for solid state NMR, XRD, and TEM. $Li[Li_{1/9}Ni_{1/3}Mn_{5/9}]O_2$ was mixed with carbon (acetylene) black (10 wt %) and poly(vinylidenefluoride) binder (PVDF) (10 wt %). The mixture was then dispersed in acetone or NMP, dripped on a disk of aluminum foil of 9/16 inches diameter, and dried at 80ºC. The total electrode mixture on the aluminum disk is typically about 30mg. Lithium metal ribbon (Aldrich, 99,9%) and 1 M $LiPF_6$ in a 1:1 ethyl carbonate: dimethyl carbonate (EC: DMC) solution (Ferro) were used as anode material and electrolyte, respectively. Two pieces of Celgard separator (Celgard Inc. USA) were used as the separator. All the cell parts were assembled in an argon–filled glove box. The coin cells were cycled galvanostatically on an Arbin battery cycler (College Station, Texas) between 2.5 and 4.6V, or 2.5 and 5.3V at a C/50 rate, where C is the theoretical specific capacity of $Li[Ni_{1/3}Li_{1/9}Mn_{5/9}]O_2$ defined based on the Ni content. The samples for the

NMR, XRD and TEM studies were recovered from cycled batteries by disassembling them inside an argon-filled glove box, and scraping the powder mixture from the aluminum disks. In contrast, the electrode foils were kept intact and used directly for the XAS experiments after rinsing with DMC (dimethyl carbonate)[6]. In order to avoid contact with air, they were sealed between two layers of Kapton® tape.

The GITT experiment was performed between 5.3-2.5V by applying a current corresponding to a C/50 rate in intervals of 2 h, separated by a rest period of 5 h. The PITT experiment is a chronoamperometric method that is carried out by applying potential steps of 10 mV for 24 hours. The time periods were curtailed if the measured current falls below a threshold limit set at 0.1 μA, corresponding to a C/200 rate. The voltage window was set at 5.3-2.5V.

5.2.3 MAS NMR Spectroscopy

^{6}Li MAS NMR experiments were performed at an operating frequency of 29.47 MHz on a CMX-200 spectrometer (4.7 T). A 1.8 mm double resonance probe built by Samoson and coworkers (KBFI, Tallinn, Estonia) was used. All spectra were acquired at 38 kHz with a rotor synchronized echo pulse sequence (90º-τ-180º-τ-acq), where $\tau = 1/\nu_r$. A $\pi/2$ pulse width of 3.5 μs was used with pulse delays of 0.2 s. The spectra were acquired at "room temperature" (i.e., the spectra were acquired with no control of the temperature), which corresponds to a sample temperature of between 70-80 ºC.

5.2.4 TEM

Electron diffraction patterns and Transmission Electron Microscope (TEM) images were collected from both the as-prepared powders and the powders discharged to 2.5V after being charged to 5.3V. To minimize the exposure to air for the electrochemically charged/discharged samples, the samples were prepared in the Ar environment. The powders were suspended on a copper grid with lacey carbon under an accelerating voltage of 200kV on JEOL 2010F microscope with a field emission gun.

5.2.5 Synchrotron XRD

High-resolution synchrotron X-ray powder diffraction (XRD) were collected at 11-BM [7, 8] and 1-BM beamlines (λ= 0.619174 Å and λ=0.4017Å, respectively) at the Advanced Photon Source (APS), Argonne National Laboratory (ANL). For beamline 1-BM, the samples were packed in 1.0mm diameter glass capillaries. For 11-BM, 1.0 mm diameter Kapton® capillaries were used. Rietveld refinements were performed on the collected data with the EXPGUI-GSAS software.

5.3. Results

5.3.1 Electrochemistry

Figure 5.1 shows a comparison of the electrochemical curves resulting from applying different cut off voltages. Two types of theoretical capacities can be defined for this compound: One is based on the Ni content. Assuming that only these ions are electro-active, only 2/3 of Li ions should be removed from the structure on oxidizing x = 1/3 Ni^{2+} to Ni^{4+} (per formula unit $Li[Li_{1/9}Ni_{1/3}Mn_{5/9}]O_2$), yielding a capacity of 200mAh/g. The second definition is based on the total Li content in the material and assumes that all 10/9 Li^+ ions in $Li[Li_{1/9}Ni_{1/3}Mn_{5/9}]O_2$ can be removed, resulting in 331mAh/g. When the battery is cycled between 5.3-2.5V, 400mAh/g is obtained upon charge, and 200mAh/g upon discharge. However, when the battery is cycled between 4.6-2.5V, 230mAh/g is obtained upon charge, but only 160 mAh/g is recovered upon discharge, which corresponds to a 20% capacity loss. The voltage increases steadily from 3.8 to 4.4V, upon charge accounting for approx. 120mAh/g. This is followed by a *plateau*-like region between 4.4 and 4.6V. Given the voltage window of stability of the electrolyte used in these batteries, which has a maximum around 5.0V, it is likely that some of the capacity produced upon charge is due to its partial decomposition, accounting for the larger capacity obtained even over that assuming all the Li is removed. Nonetheless, the higher discharge capacity obtained with respect to a 4.6-2.5V cutoff voltage indicates that part of the extra capacity obtained after 4.6V is reversible. An additional process could be observed in the electrochemical curve, from 4.9 to 5.3V. Thus, there are at least three quite different processes during charge.

The cyclability of $Li[Li_{1/9}Ni_{1/3}Mn_{5/9}]O_2$ in different voltage windows is compared in Figure 5.4. A charge and discharge capacity around 130 mAh/g could be achieved at a C/20 rate after 10 cycles when the window is set at 4.6-2.5V. However, when the battery is cycled between 5.3-2.5V at the same current rate, both higher charge and discharge capacities, ca. 200 mAh/g, are obtained and a better capacity retention is found after 10 cycles. To avoid further decomposition of the electrolyte at very high voltages, another battery was charged to 5.3V only in the first cycle and then cycled between 4.8-2.5V in subsequent cycles. The electrochemical profiles of different cycles are shown as an inset in Figure 5.5. None of the two *plateau* were observed in the 2^{nd} and 5^{th} cycle, and the resulting profiles are very similar, indicating that the reactions that occur in the first cycle are different from those in later cycles. Additionally, the capacity obtained when cycling between 4.8-2.5V is very close to that obtained in the first cycle with a 5.3-2.5V voltage window. Thus, the reactions taking place at these high voltages can be viewed as an "activation" process that produces both an improvement in capacity and capacity retention. After the fifth cycle, the cycling rate was changed from C/50 to C/13. A decrease from 190 mAh/g at C/50 to 150 mAh/g at a C/13 rate was found.

Both galvanostatic intermittent titration[9] (GITT) and potentiostatic intermittent titration technique[10] (PITT) experiments were performed to study the reaction mechanisms associated with the two high voltage processes observed in the electrochemical curve. Almost no overpotential is observed until 4.4V in the GITT profile (Figure 5.2), the starting point of the first plateau. Above this value, an increasingly larger overpotential is found (for instance, it is about 50 mV at 4.6 V). After this point, the open circuit voltage stabilizes at about 4.5 V and the 4.6V, while the closed

circuit voltage curve traces the chronopotentiometric profile shown in Figure 5.1. This implies that the reactions that take place at these voltages are kinetically limited.

Figure 5.3a shows a zoom of the PITT profile between 3.6-4.0V. The current decay at each step shows a cottrellian ($1/t^{1/2}$) dependence, which indicates that this process is a solid solution insertion reaction.[11, 12] A similar behavior was also observed in Figure 5.3d, which shows the curve between 3.8-3.5V on discharge. These results are consistent with the gradual increase of voltage with capacity observed in the galvanostatic experiments. Figure 5.3b and 5.3c show the curves between 4.4-4.6V and 4.9-5.0V where the two *plateaus* appear in the galvanostatic profiles. Very different behavior is now observed. The current decreases rapidly to a very low value, and then reaches the limit value slowly. This behavior is usually observed in a two-phase reaction, confirming that the high voltage processes are indeed associated with plateau.

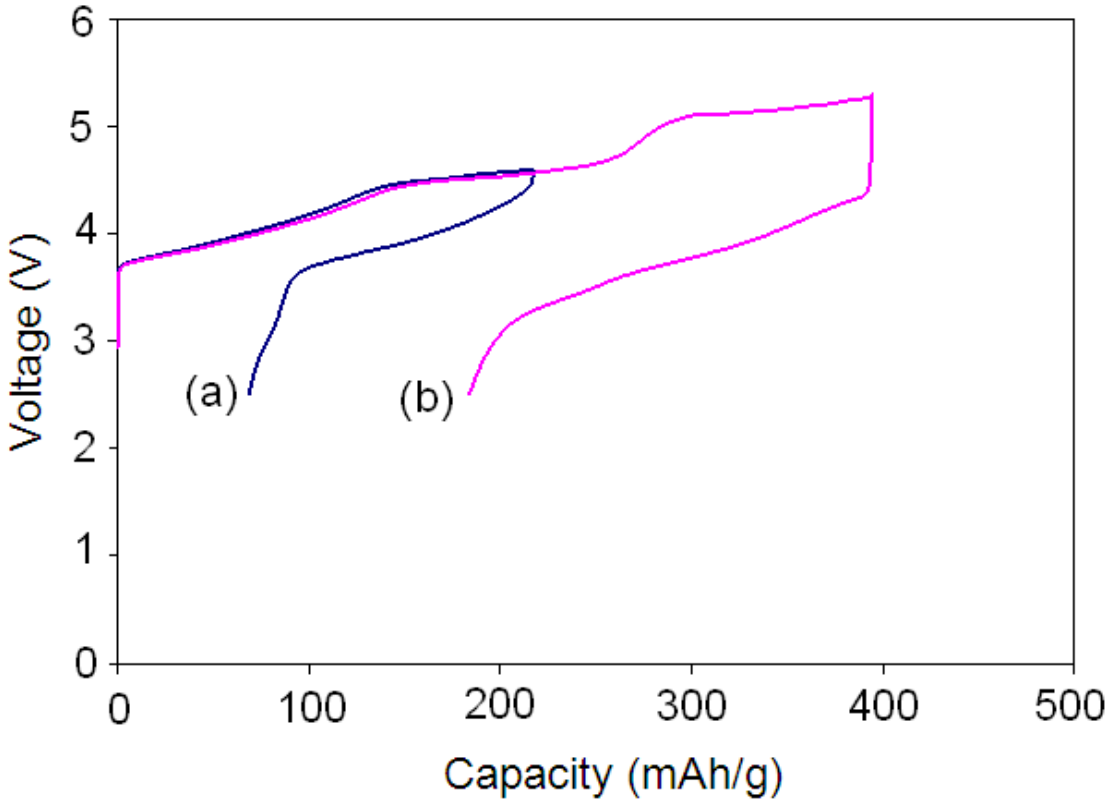

Figure 5.1: The electrochemical profile of $Li[Li_{1/9}Ni_{1/3}Mn_{5/9}]O_2$ with C/50 rate. The voltage window for curve (a) is 4.6-2.5V, and the voltage window for curve (b) is 5.3-2.5V.

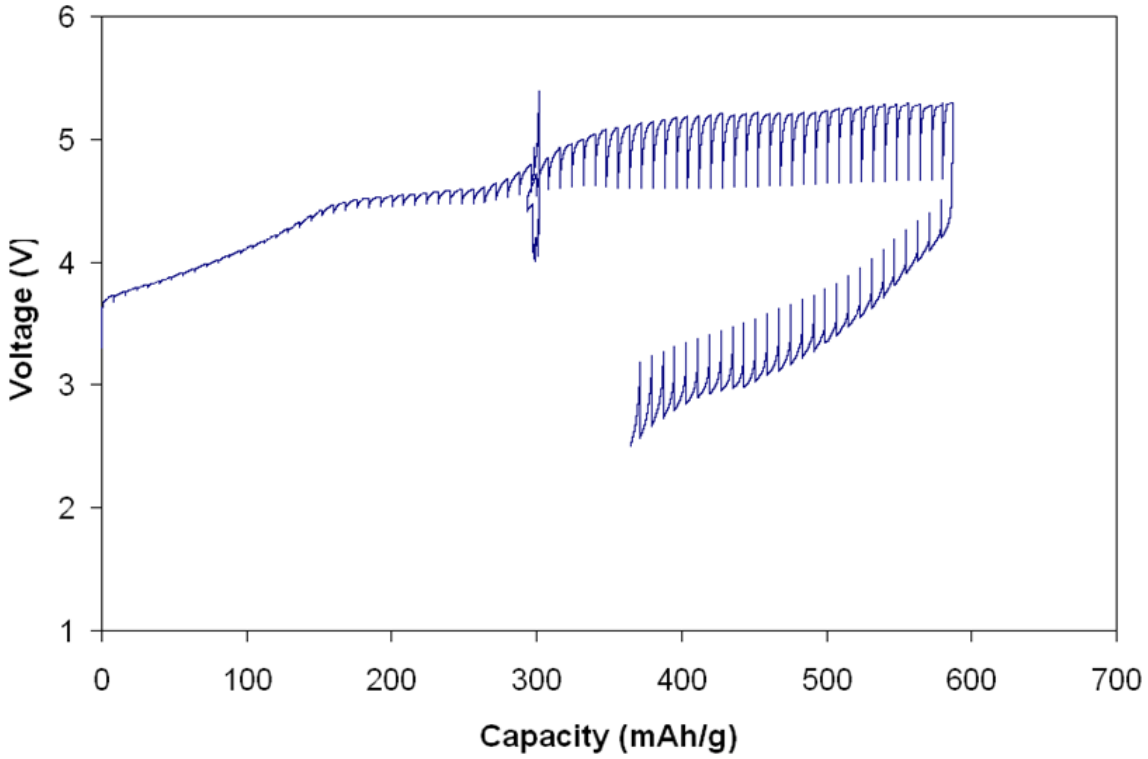

Figure 5.2: Galvanostatic intermittent titration (GITT) profile with C/50 between 5.3-2.5V. The charging time is two hours and followed by five hours of rest time. The spike at 300mAh/g is due to a spurious current glitch of the cycler.

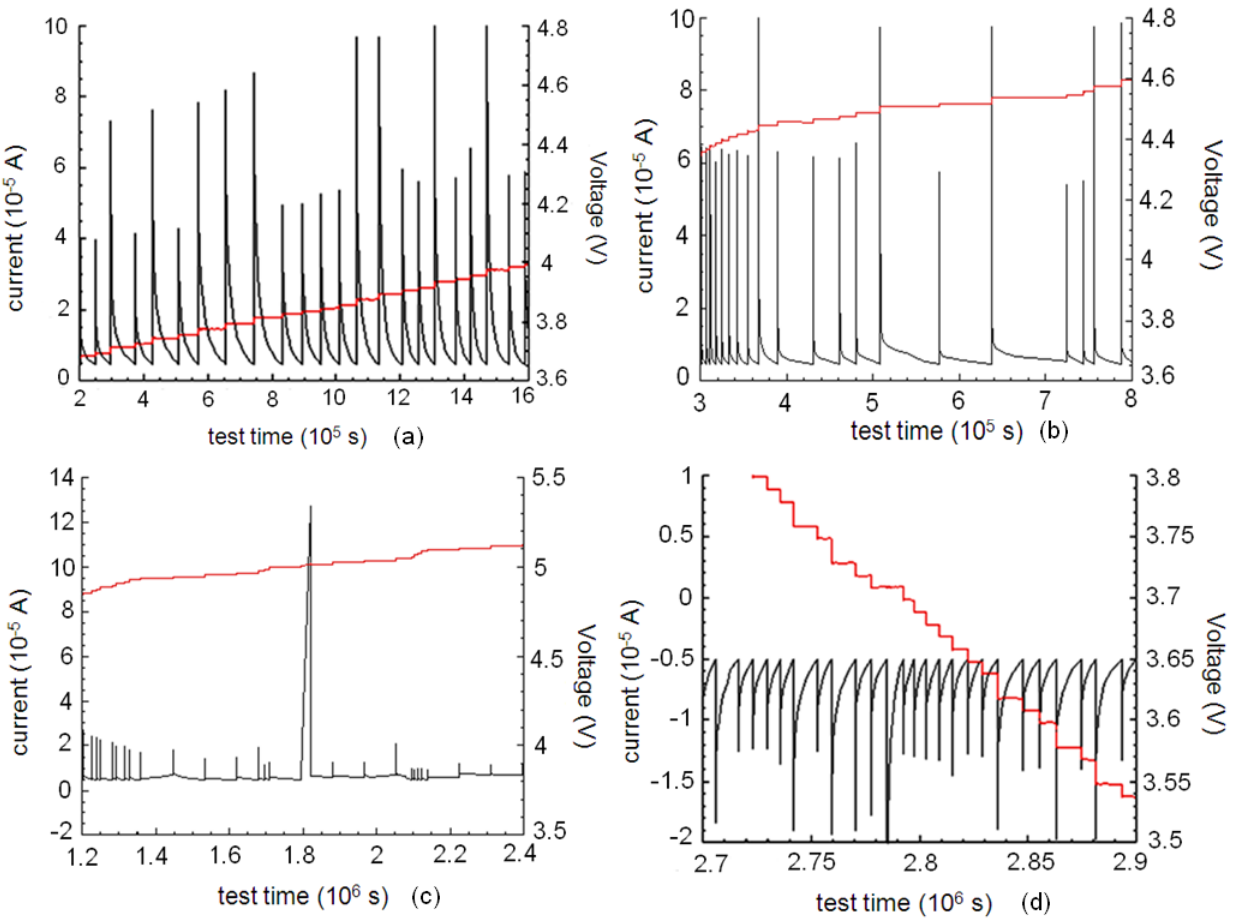

Figure 5.3: Potentiostatic intermittent titration technique (PITT) profiles acquired with a step size of 10 mA and current limit of 0.1μA which correspondes to C/200. The red curve shows the voltage vs. test time, and the black curve shows the current vs. test time. The four figures show different voltage windows: (a) 3.6-4.0, (b) 4.4-4.6, (c) 4.8-5.1, and (d) 3.8-3.55V. The first three figures are during the charge process, and the last figure is during discharge.

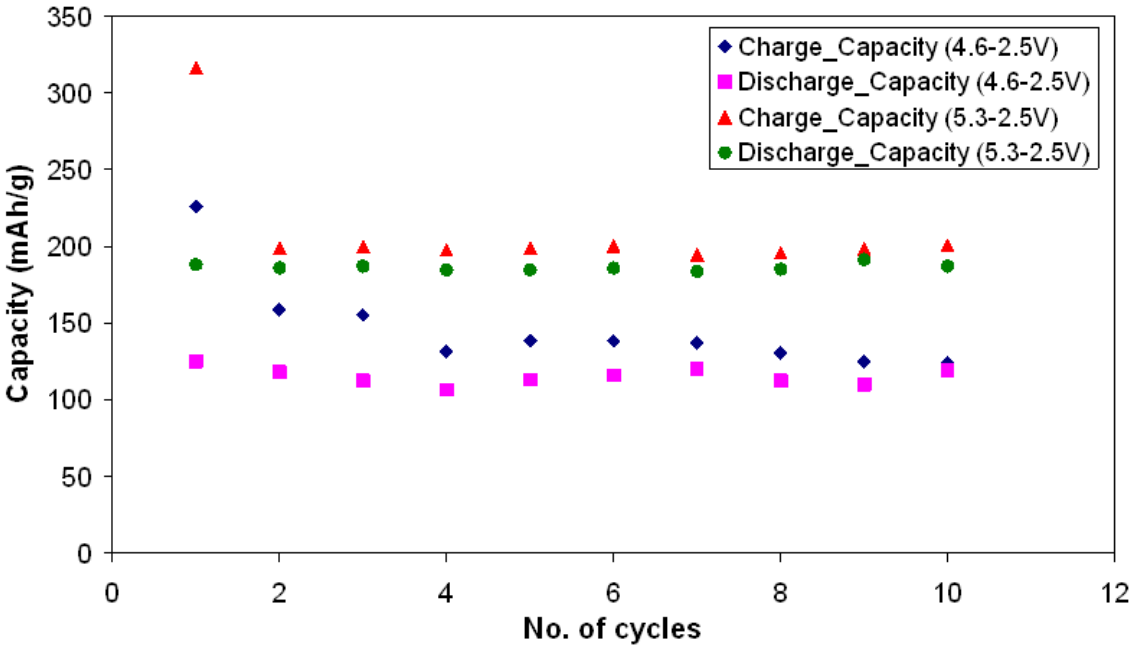

Figure 5.4: Comparison of the cyclability of $Li[Li_{1/9}Ni_{1/3}Mn_{5/9}]O_2$ with different voltage windows (4.6-2.5V and 5.3-2.5V). The cycling rate for both voltage windows is C/20.

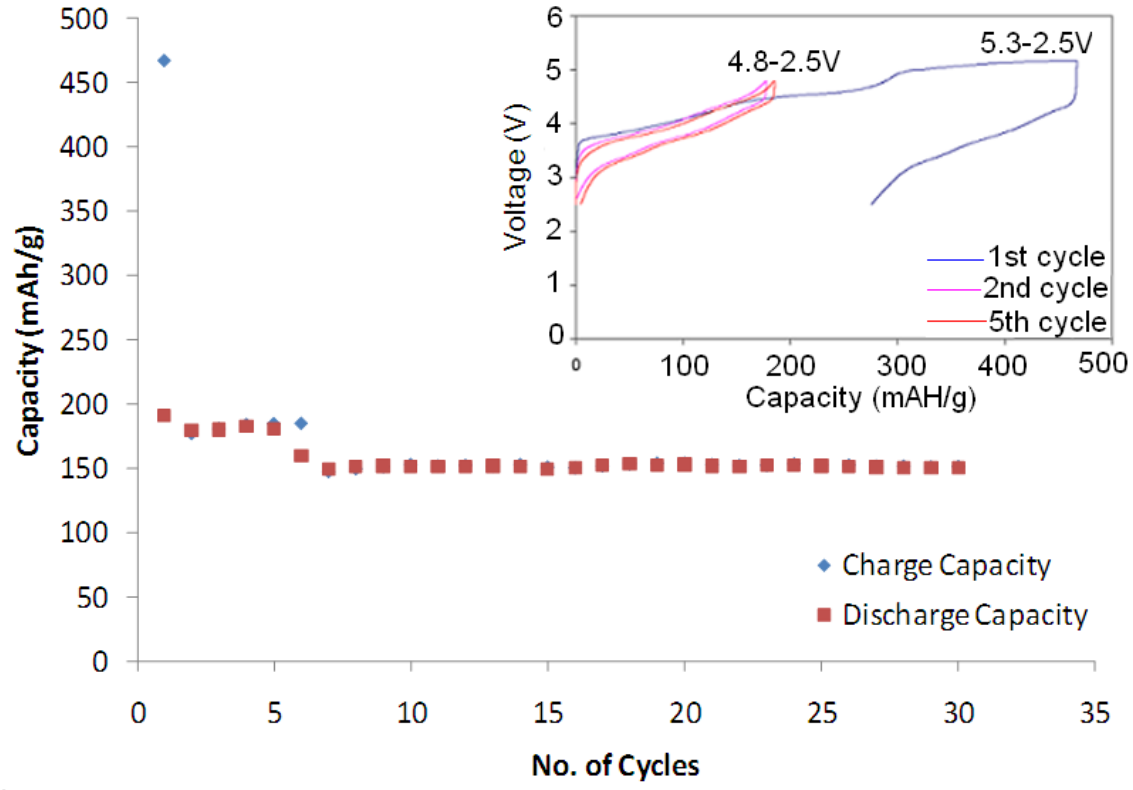

Figure 5.5: The cyclability of a battery charged to 5.3V for the first charge and cycled between 4.8-2.5V in the following cycles. The current rate for the first four cycles and the fifth charge process is C/50, and the subsequent rate is C/13. The inset is the electrochemical profile of the first, second and fifth cycles.

5.3.2 High resolution XRD

The high resolution XRD pattern of the pristine compound is displayed in Figure 5.6. All the reflections can be indexed with a hexagonal rhombohedral R$\bar{3}$m space group except for a series of additional superstructure peaks around 18 – 23º, 2θ, which are due to the honeycomb ordering of Li and Mn in the transition metal layers, as seen for Li_2MnO_3.[13] The ordering can be varied with slightly different heating time and quenching method during synthesis, which can result in the change in peak intensity. No obvious phase transitions are observed, and all the patterns can still be indexed with a layered structure, even when most of the Li ions are electrochemically removed. The superstructure peaks due to the honey comb ordering in the transition metal layers are present until 4.7V (see inset (a) in Figure 5.7), but they almost completely disappear at 5.3V, indicating that this ordering is lost at this voltage. A shoulder next to the 003 peak starts to appear at 4.4 V. This shoulder increases in intensity and shifts to lower angles from 4.4 to 5.3V, leading to a strong asymmetry of the 003 reflection, as seen in the inset (b) of Figure 5.7. These peaks can not be indexed with the same cell parameter when using R$\bar{3}$m space group, so they must come from a second phase. Since there is only one extra peak observed in the whole pattern, it is however very difficult to identify the second phase. It may adopt the same R$\bar{3}$m space group with slightly different cell parameters, or it may adopt a different space group which happens to have a strong reflection near 003 reflection of the R$\bar{3}$m, such as a spinel phase.

The XRD patterns of the discharged samples, following charging to different potentials, are compared in Figure 5.8. The layered-type unit cell with an R$\bar{3}$m space

group, as that in the pristine compound, could still be used to index the patterns, and only slightly different cell parameters were found. The superstructure peaks are still present in the 4.6-2.5V sample (inset (a)), but they are virtually absent in the 5.3-2.5V sample, indicating that the honeycomb ordering cannot be recovered on discharge. No shoulders are observed for the 003 peak in the discharged samples (inset (b)), which implies either the disappearance of the second phase after lithium is intercalated in the structure of this phase or that it has very similar c and a parameters.

The Rietveld refinement[14] results of the discharged samples are shown in Figure 5.9. Both *a* and *c* parameters increase as the sample is charged to higher voltages. The unit cell shows the largest expansion after the high voltage process, confirming the existence of a real structural change during the *plateau,* quite separate from any electrolyte decomposition that may be occurring. The content of transition metal ions in both the transition metal and the Li layers were also obtained from the refinement. Since the X-ray scattering lengths of Ni and Mn are very similar, the individual contents of Ni and Mn cannot, however be distinguished. Previous studies[15-17] have demonstrated the existence of crystallographic exchange only between Ni and Li, which leads to the presence of the Ni in the Li layers. Hence, only this exchange was assumed in our structural models. Given the small X-ray scattering length of Li, associated to its low electron density,[18] the refinements are not very sensitive to the Li content. As a consequence, the approximate Li contents used in this refinement were taken from the discharge capacity obtained in the corresponding batteries. The results of the refinements are plotted in Figure 5.9(c). The total transition metal content in the transition metal layers does not change with increase of the charging voltage remaining constant at

approximately 84-85%. In contrast, the Ni content in the Li layers increases from 5% to 9% on charging to 5.3 V.

The XRD patterns of the multiple cycled materials with a cut-off voltage window between 4.6-2.5V are compared in Figure 5.10. Both cycled samples were stopped at the fully discharged state. The layered structure with R$\bar{3}$m space group still remains after 10 cycles. However, the superstructure peaks representing honey comb ordering in the transition metal layers are much less pronounced in the sample stopped after 5 cycles, and have totally disappeared in the 10^{th} cycled sample. Clearly the loss of transition metal ordering can also happen after multiple cycles even when the material is cycled between the lower voltage window 4.6-2.5V. A shoulder next to 003 peak is observed in both the 5cycles sample and the 10cycles sample, which appears at the same position as that observed in the charged samples (Figure 5.7), indicating that the second phase is still present in the discharged sample after multiple cycles.

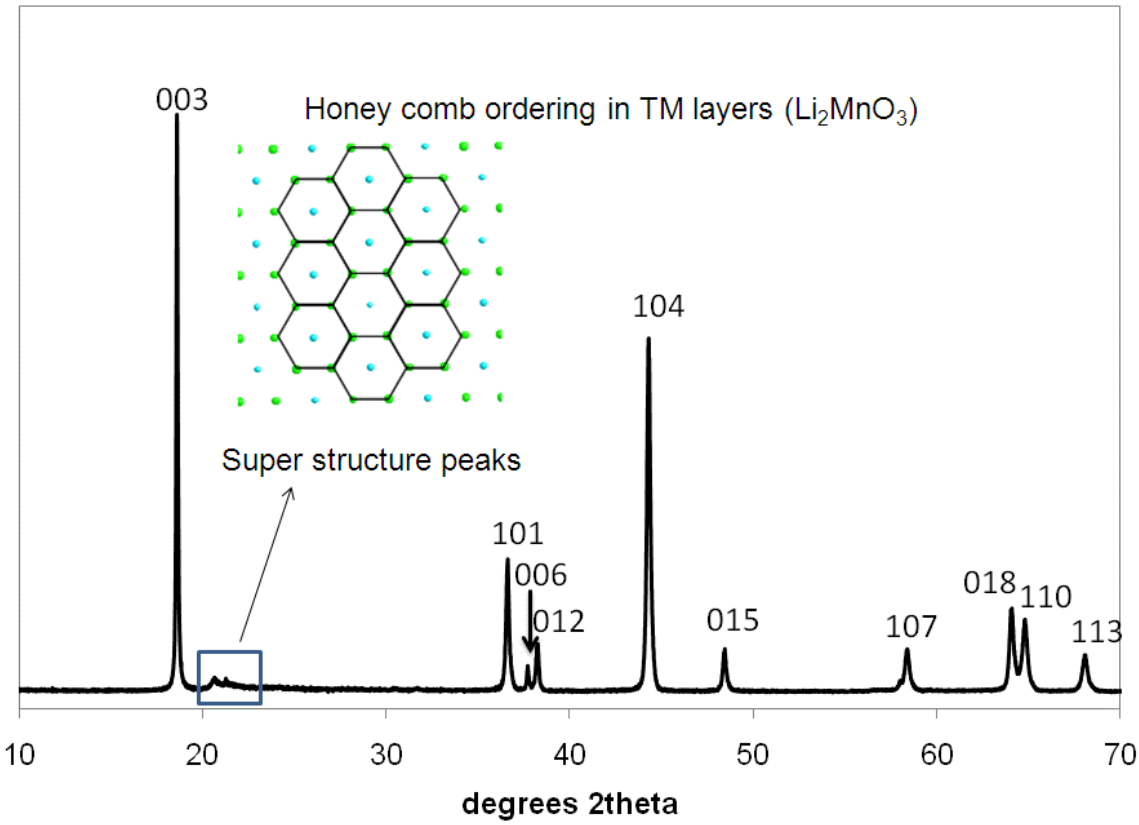

Figure 5.6: X-ray diffraction pattern of pristine $Li[Li_{1/9}Ni_{1/3}Mn_{5/9}]O_2$. All the peaks could be indexed with an $R\bar{3}m$ space group except the superstructure peaks introduced by the honey comb ordering of Mn in the transition metal layers. The green and blue balls represent Mn and Li atoms respectively in the representation of the $[Li_{1/3}Mn_{2/3}]$ layer of Li_2MnO_3, shown in the inset. In this and subsequent figures, the 2theta values are converted to Cu Kα wavelength (λ=1.54Å).

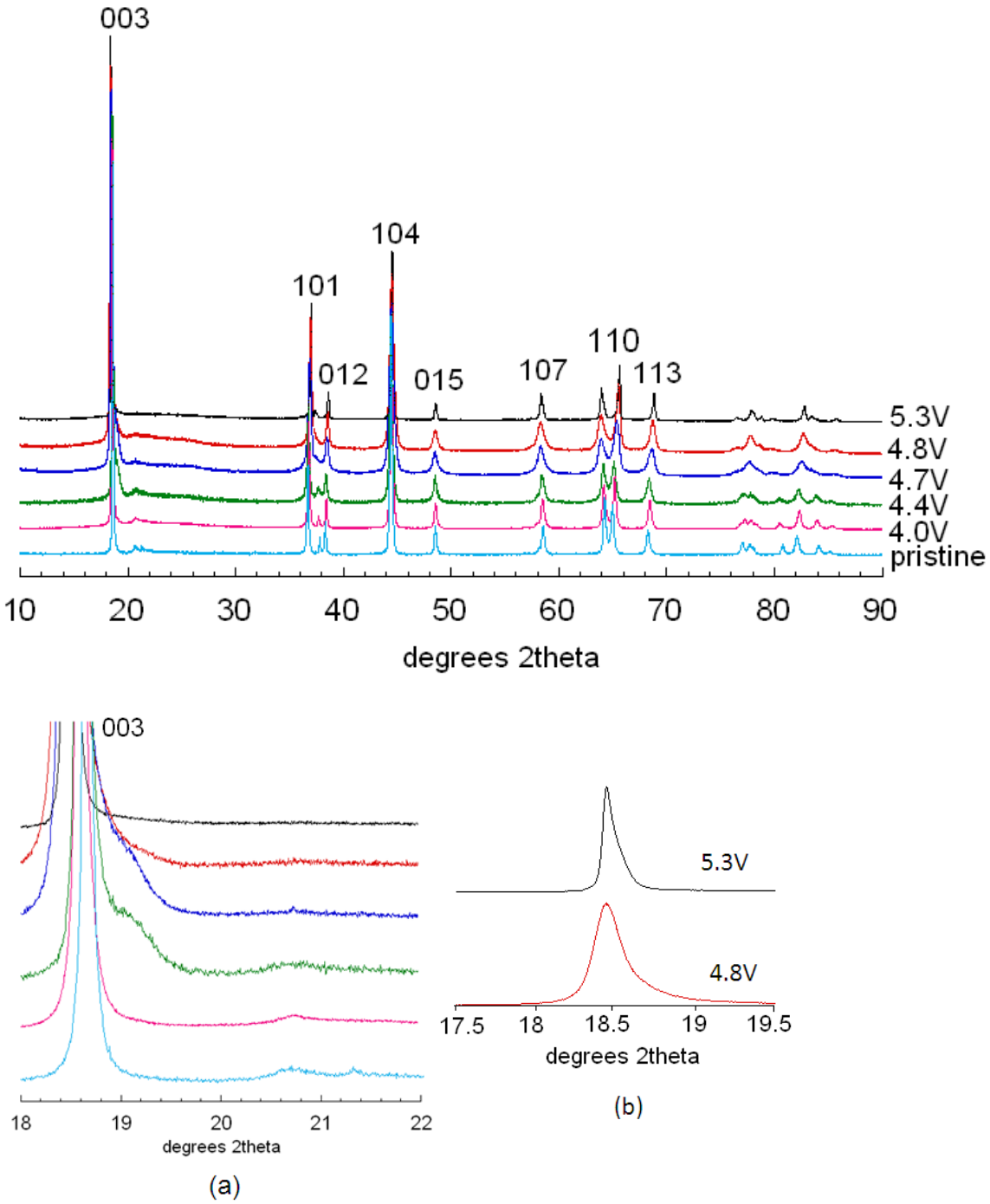

Figure 5.7: High resolution XRD of charged and pristine materials. The patterns are labeled with the voltage where the sample was stopped. The insets show the enlargement of different regions. The XRD patterns are labeled with the cutoff voltage of each sample.

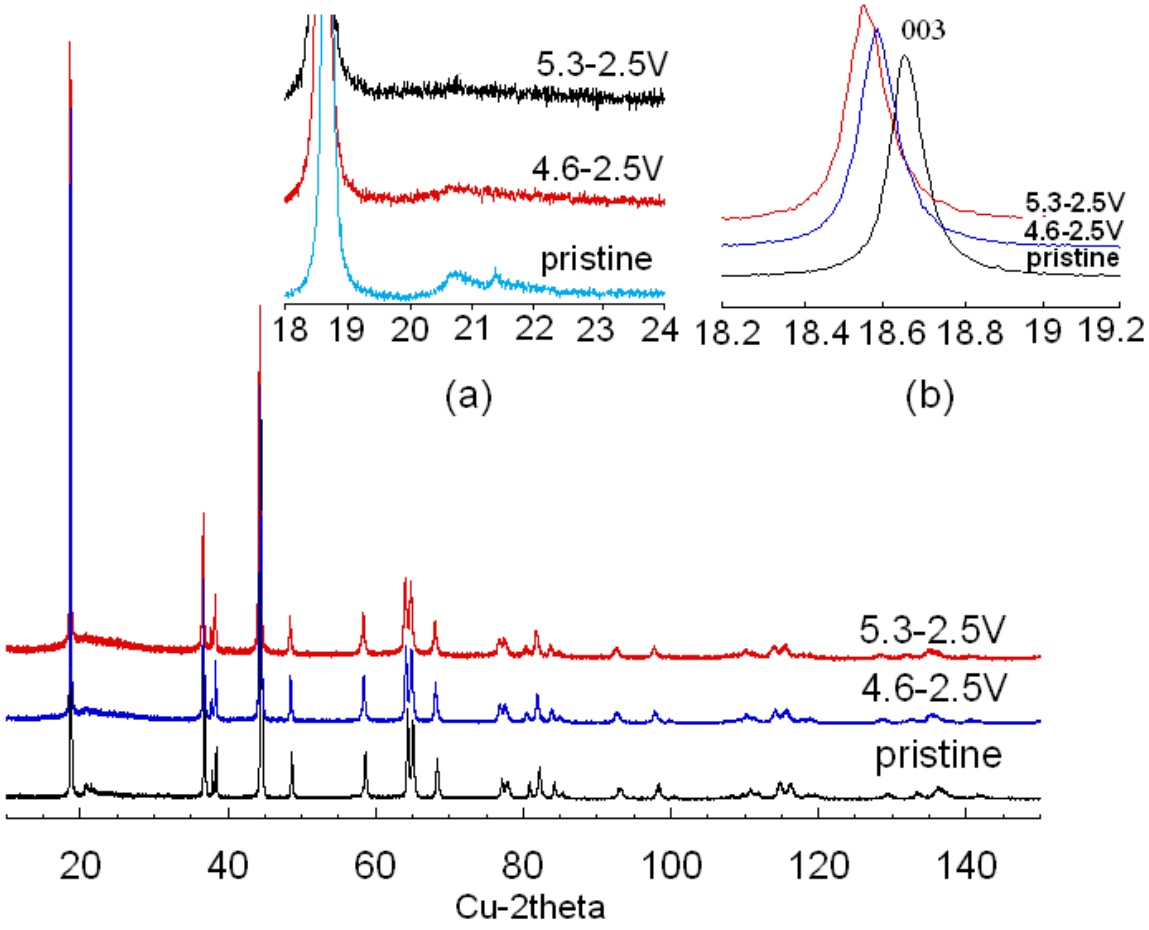

Figure 5.8: Comparison of high resolution XRD patterns of discharged samples and the pristine material. Both discharged samples were stopped at 2.5V, and the charge voltages are labeled on the patterns. The insets show enlargements regions containing the superstructure and 003 reflections.

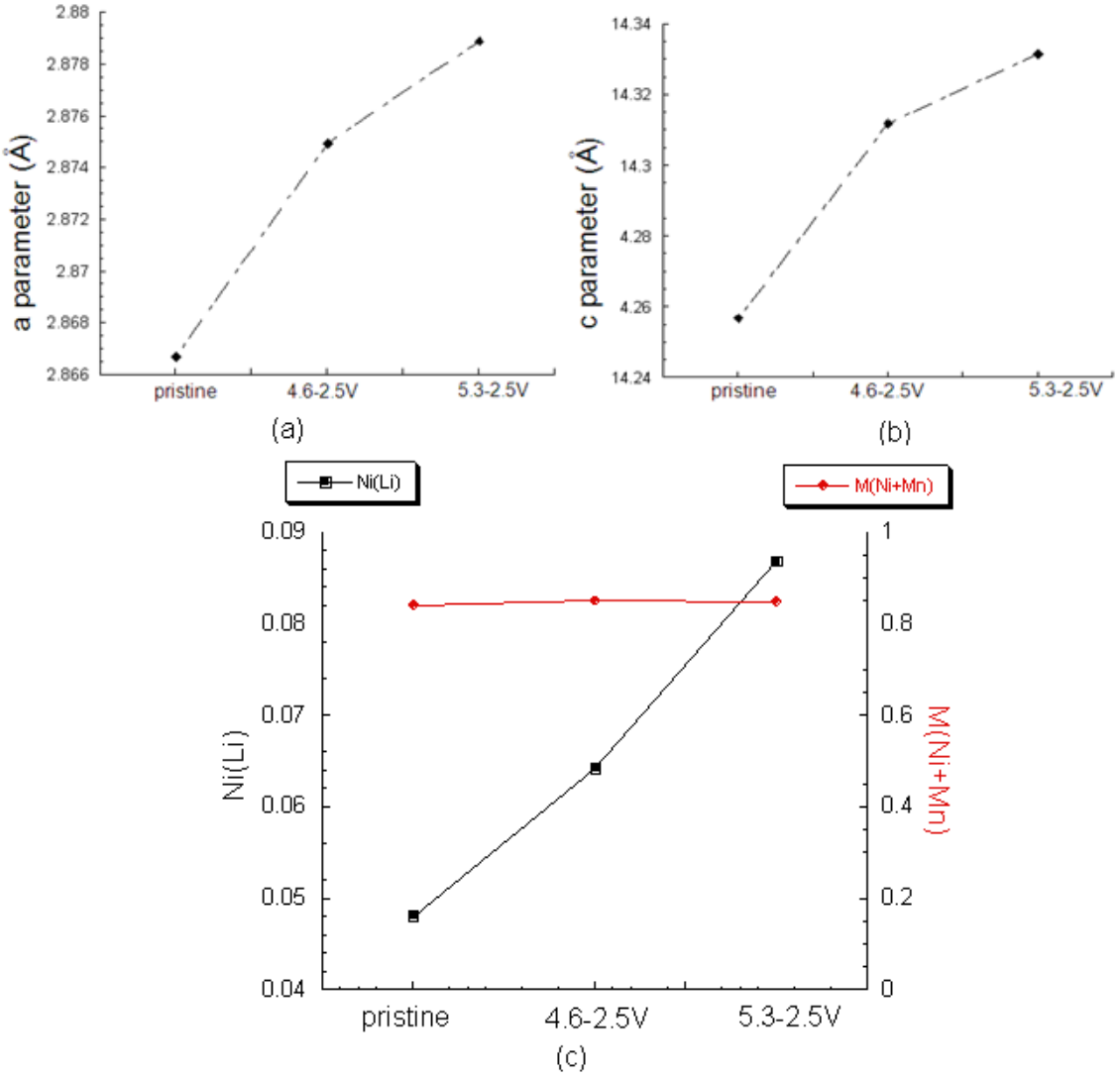

Figure 5.9: GSAS refinements results of the XRD patterns for discharged samples and pristine material. Figures (a) and (b) are the plots for cell parameters where the samples are labeled on the X axis. Figure (c) shows the plot of Ni content in the Li layers (black line) and total transition metal content in the transition metal layers (red line).

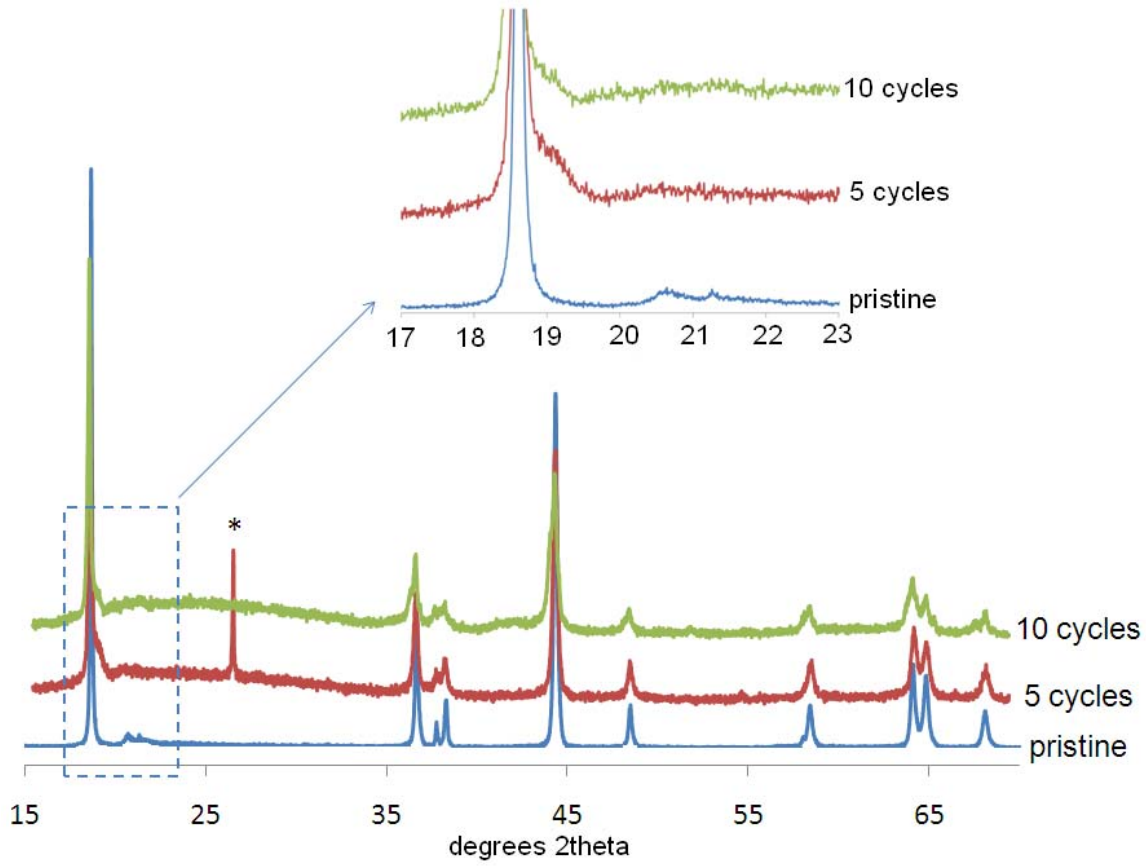

Figure 5.10: Comparison of the XRD pattern of the multiple cycled, fully discharged samples cycled with the cut-off voltage windows of 4.6-2.5V and the pristine material. The inset is the enlargement of the superstructure peaks region. The sharp peak marked with asterisk observed in the 5 cycles sample is from graphite.

5.3.3 ^{6}Li MAS NMR Spectroscopy

The ^{6}Li NMR spectrum of pristine of $Li[Li_{1/9}Ni_{1/3}Mn_{5/9}]O_2$ has been discussed in Chapter 2. (Figure 2.9) Figure 5.11 shows the ^{6}Li NMR spectra of $Li[Li_{1/9}Ni_{1/3}Mn_{5/9}]O_2$ as a function of the state of charge. The spectra have been normalized with the total number of scans and the weight of active material packed in the rotors, so that the intensity of each resonance can be directly related to the number of Li ions in each sample. When the compound is charged to 4.4V, the intensity of the peaks ascribed both to Li in the lithium layers and Li in the transition metal layers decrease, as previously observed[19], indicating that lithium is removed from both layers. At 4.6V, the 737 ppm peak, due to Li environments in the Li layers resembling those in Li_2MnO_3, has decreased noticeably in intensity and appears buried under a broader peak centered at 500-600 ppm. This latter peak likely contains Li environments in the Li layer where the Li is nearby Ni^{4+} (diamagnetic) ions and/or Li in the tetrahedral sites, adjacent to the Li vacancies in the transition metal layers. In contrast, the Li ions in the transition metal layers are still not completely removed at this voltage. From 4.6 to 5.3V, the intensity of the peaks around 600 ppm gradually decreases, consistent with the removal of lithium from the structure, and, thus, with the compound still being electrochemically active at these voltages. No peaks around 1500 ppm are observed at 5.3V, and only one broad symmetric peak remains at around 600 ppm, implying that all the Li ions have been removed from the transition metal layers, but also that there are still some Li ions left in the lithium layers. No extra peaks are observed in the charged materials except for one at 0 ppm, which arises from the Li ions in diamagnetic environments in the electrolyte salt ($LiPF_6$) or in the passivation layer on the surface of the electrode.[20] This peak gets

noticeably larger in the 5.3V sample, consistent with the electrolyte decomposition where a thicker passivation layer can be produced in this process.

A similar study was also performed on a series on samples prepared after one charge-discharge cycle, and the NMR spectra of discharged samples are displayed in Figure 5.12. The low natural abundance of ^{6}Li (7.43%) and the fact that the electrolyte and Li metal used in the batteries is not enriched imply that the ^{6}Li content in these samples can no longer be readily quantified. The two sets of resonances ascribed above to Li in the Li and the transition metal layers are still present in all the spectra. As before, the peaks at 0 ppm correspond to the presence of diamagnetic electrolyte/SEI environments. Two trends can be observed in the spectra as a function of maximum voltage on charge. First, the intensity of the peaks around 1500 ppm gradually decreases as the charge cutoff voltage is increased, and these peaks are almost absent in the 5.3-2.5V sample, indicating that only very few Li ions can be reintercalated into the transition metal layers on discharge after charging at high voltages. Second, the broad peak centered at 750 ppm becomes much more symmetric and featureless, in comparison to the same resonance in the pristine sample, for the sample cycled over a larger voltage window. This is evidence of cation rearrangement in the transition metal layers at high voltages. Taken together, this appears to suggest that either some of the vacancies left behind in the transition metal layers after the Li ions are removed from the transition metal layers are occupied by the other transition metal ions which can migrate from the adjacent sites or that significant rearrangement of Ni and Mn ions within the layers occurs. As a result, the honeycomb ordering is lost and the available sites for lithium re-insertion are either no longer present or not as energetically favorable, which is one

possible reason why no lithium goes back to the transition metal layers on reduction to 2 V. The ^{6}Li NMR results provide compelling evidence of a continued structural change of the material during the high voltage *plateau*.

The ^{6}Li NMR spectra of multiple cycled samples are compared in Figure 5.13. In the pristine compound, the peak at around 1340 ppm has lower intensity compared to the one shown in Figure 5.11 and 5.12, indicating more ordering is present in this sample which is due to slightly different synthesis conditions. All the cycled samples were charged to 4.6V and discharged to 2.5V. A similar trend is observed here as in Figure 5.12. The peaks at around 1500 ppm become less pronounced as a function of the number of cycles, and they totally disappear in the discharged sample after 11 cycles. This suggests that the lithium can not be intercalated back to the transition metal layers after multiple cycles. The peak corresponding to the Li in Li layers is much more symmetric compared to that in the pristine compound, indicating a cation rearrangement in the transition metal layers as discussed previously. The spectrum of the 11 cycles sample is actually very similar to the sample cycled between 5.3-2.5V. This is also consistent with the XRD data (Figure 5.10). The final structure of the multiple cycled sample with lower cycling voltage window (4.6-2.5V) becomes the same as the sample cycled between high voltage window (5.3-2.5V), Li largely being stored in the lithium layers, the honey comb ordering having disappeared in the transition metal layers.

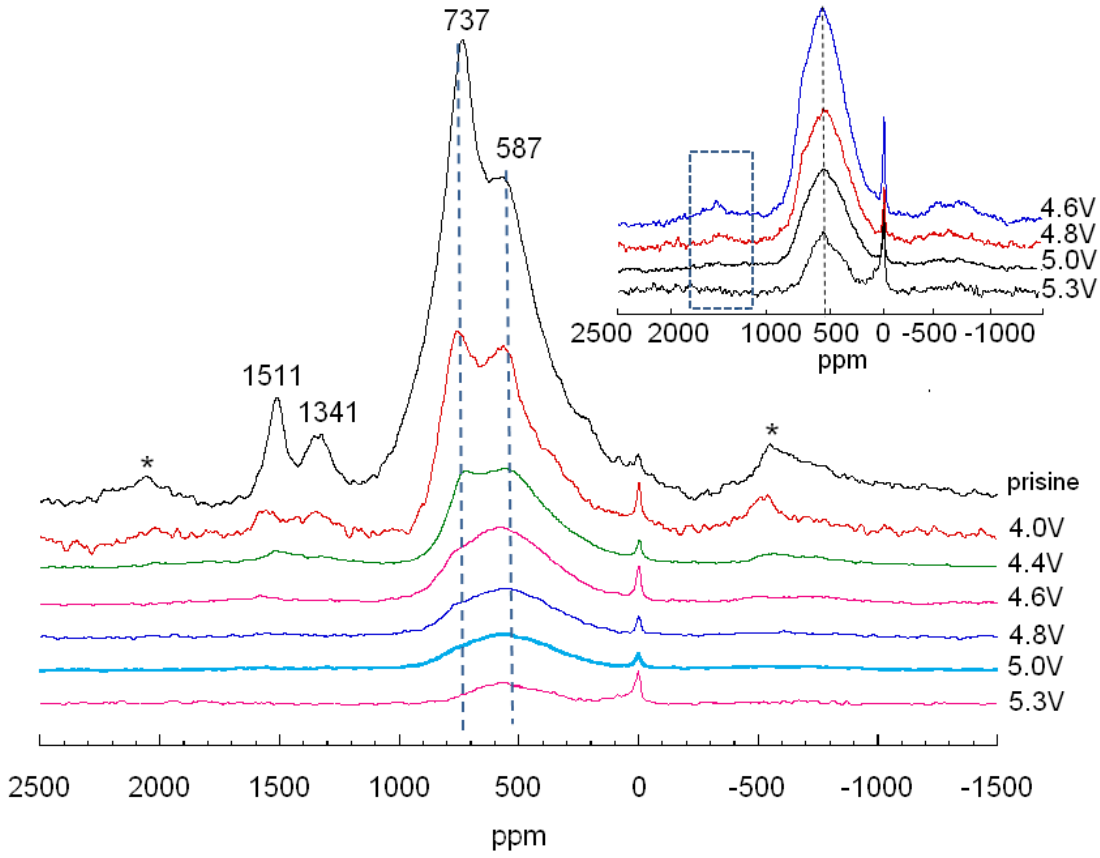

Figure 5.11: ^{6}Li MAS NMR spectra of the charged samples acquired at a 38 kHz spinning speed. The voltages where the samples were stopped are marked on the spectra. Sidebands are marked with asterisks. The inset shows an enlargement of the spectra of the high voltage samples.

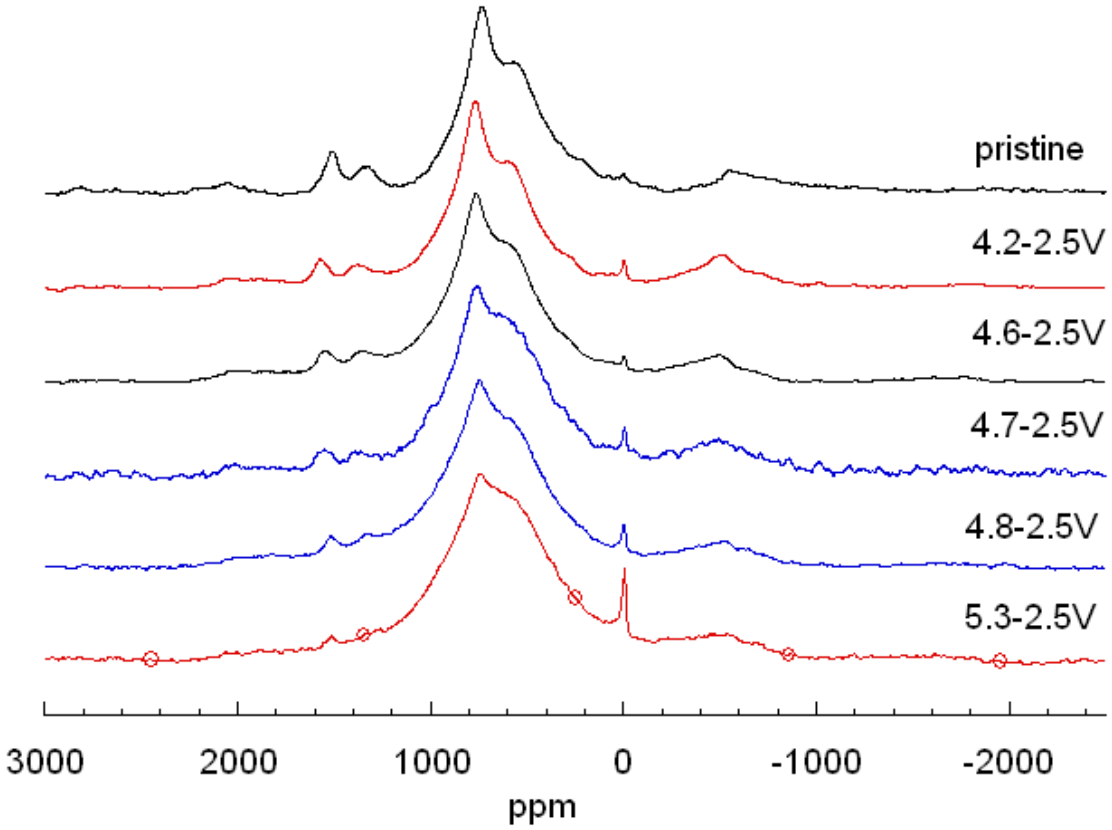

Figure 5.12: ^{6}Li MAS NMR spectra of discharged samples. The spectra are labeled by the voltage window used to charge and discharge the samples..

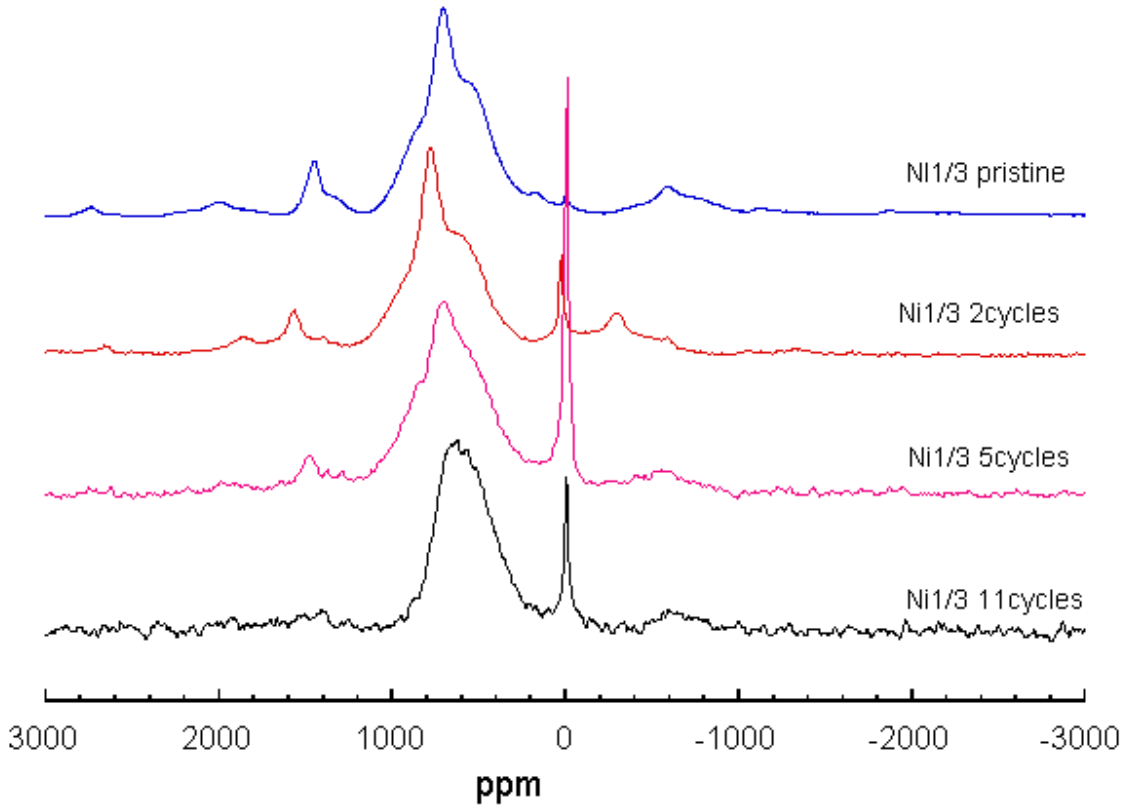

Figure 5.13: ^{6}Li MAS NMR spectra of the multiple cycled discharged samples with a cut-off voltage window of 4.6-2.5V.

5.3.4 X-ray absorption spectroscopy (XAS)

To study the change in the oxidation state of the transition metal ions during the electrochemical processes that take place in a battery, XAS experiments were performed on a series of cycled samples. Normalized Ni and Mn K-edge X-ray Absorption Near Edge Structure (XANES) spectra of cycled samples are displayed in Figure 5.14. Previous studies[19, 21, 22] have shown that Ni^{2+} and Mn^{4+} coexist in the $Li[Li_{1/9}Ni_{1/3}Mn_{5/9}]O_2$. At 4.6V, all the Ni^{2+} ions were found to be oxidized to Ni^{4+}, whereas the Mn^{4+} ions remain in the same oxidation state. However, the possible changes at higher voltages, such as 5.3 V, have not been evaluated before. Figure 5.14(a) shows the Ni K-edge spectra of the charged samples. The absorption edge gradually shifts to higher energy as the compound is charged to 4.4V, which is in agreement with the oxidation of Ni^{2+}. A smaller shift still takes place when the voltage is increased to 4.6V, but, contrary to what would be expected, when the voltage rises above 4.6V, the position of the main edge actually shifts back to lower energies, but the other part of the edge shifts in the opposite direction, and the whole shape of the spectra is different from that of the pristine compound, suggesting a significant local environment change of Ni ions at these voltages.

Figure 5.14(b) shows the Ni K-edge spectra of the three samples which were charged to different voltages, and discharged to 2.5 V, are compared with that of $Li[Li_{1/9}Ni_{1/3}Mn_{5/9}]O_2$. Both the shape and the edge position of these samples are very similar to that of the pristine compound, even for the sample which has been charged to 5.3V. Hence, all the Ni ions seem to be reduced to Ni^{2+} at the end of discharge. Figure

5.14(c) shows the Mn K-edge spectra of the same samples. The spectrum of the 4.6-2.5V sample is very similar to that of the starting phase. In contrast, the spectra of both 4.8-2.5V and 5.3-2.5V samples are different, which is an indication of a change in the Mn local environment as the compound is charged to high voltages since the shape of the Mn edge is very sensitive to the local geometry of the Mn atoms[21, 23]. The change of the local environment could be due to the rearrangement of the transition metal ions. Despite this shape changes, the spectra do not show a solid shift, which indicates that the Mn ions are in the same oxidation state as in $Li[Li_{1/9}Ni_{1/3}Mn_{5/9}]O_2$ and no reduction occurs upon the intercalation of Li.

5.3.5 TEM

High resolution TEM experiments were performed to study the morphology changes upon electrochemical cycling of $Li[Li_{1/9}Ni_{1/3}Mn_{5/9}]O_2$. Figure 5.15(a) shows the TEM pictures of a sample charged up to 5.3V. A thick passivation layer of about 10-20nm is observed on the surface of the electrode, which is ascribed to surface side reactions between the electrode and the electrolyte. In addition, obvious particle cracking was found in certain regions of some crystals (for instance, the expanded view of the region marked with an arrow in Figure 5.15(b)) of a sample charged to 5.3 and discharged to 2.5V. The similar phenomenon was also observed by Lei C.H *et al.*[24] in their HREM study, which was considered to be due to the oxygen losses. Other crystals from the same sample even show distinct diffraction domains, as revealed by the electron diffraction patterns of two different parts of the same particle in Figure 5.15(c). The

difference lies in their degree of crystallinity; while one of the domains is still crystalline (i.e., results in well resolved diffraction spots in the pattern), the diffraction pattern of the other is composed of less well defined spots that show considerable streaking. This broadening is most probably associated to a change in microstructure to produce nano-sized domains.

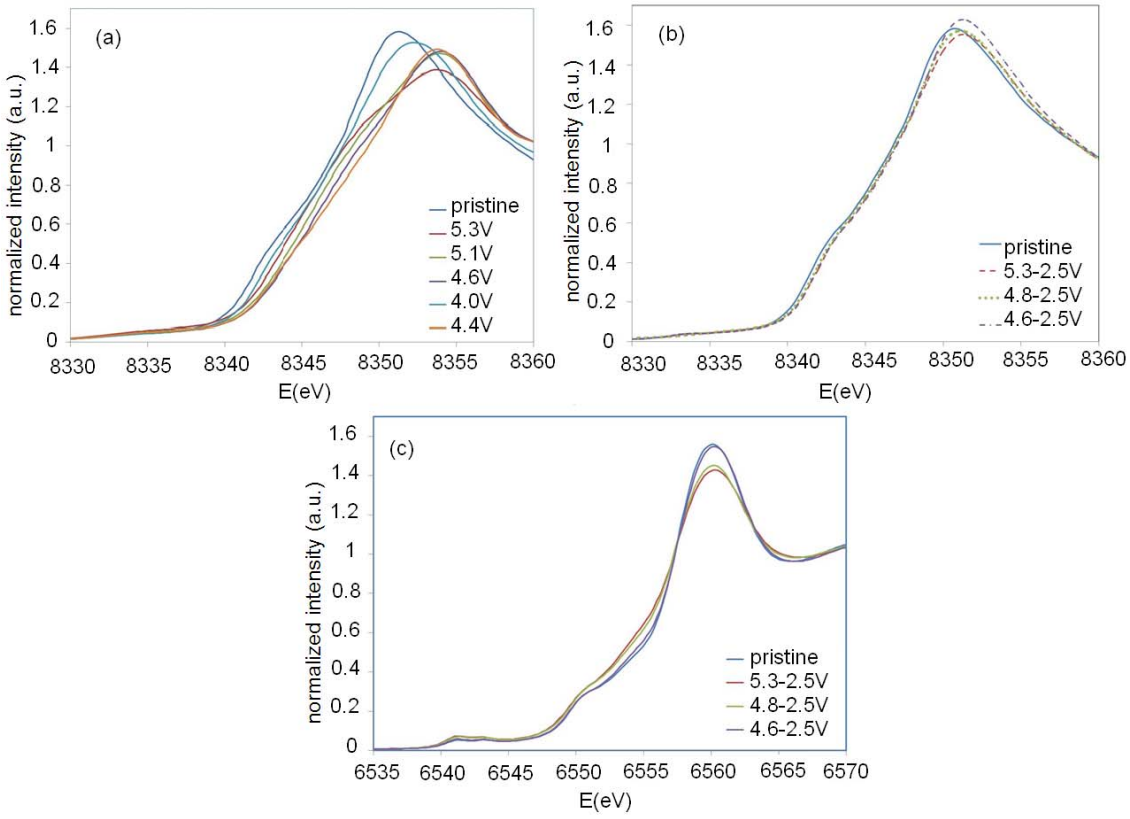

Figure 5.14: Normalized X-ray Absorption Near Edge Structure (XANES) spectra of Ni and Mn K-edge for pristine and cycled samples. (a) shows the Ni K-edge of pristine $Li[Li_{1/9}Ni_{1/3}Mn_{5/9}]O_2$ and charged samples, (b) shows the Ni K-edge of discharged samples, and (c) shows the Mn K-edge of the discharged samples.

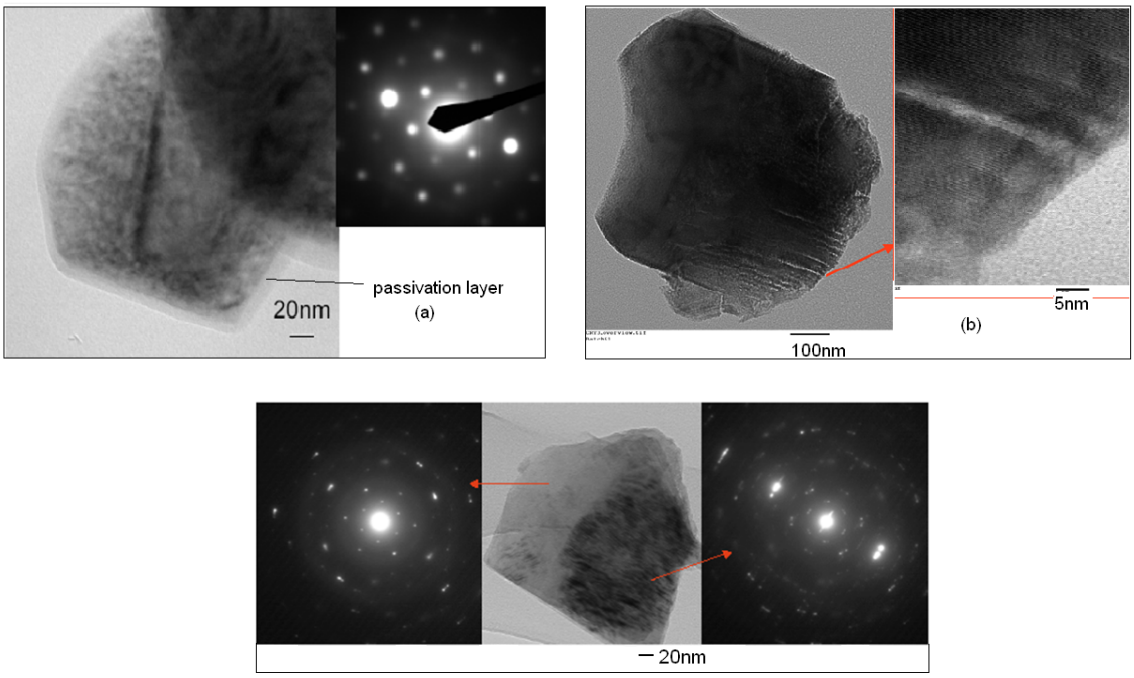

Figure 5.15: High resolution TEM pictures of cycled $Li[Li_{1/9}Ni_{1/3}Mn_{5/9}]O_2$: (a) the charged sample stopped at 5.3V, (b) the discharged samples which was charged to 5.3V then discharged back to 2.5V, and (c) another crystal from the same batch of sample as figure (b).

5.4. Discussions

The results of both the GITT and the PITT experiments confirm the existence of a *plateau* around 4.5V upon the first charge of a battery containing $Li[Li_{1/9}Ni_{1/3}Mn_{5/9}]O_2$ as a positive electrode, and this process is associated with the reaction involved more than one phase. Previous studies have proposed that the plateau at 4.5V is due to the oxygen loss mechanism,[5] that the removal of Li is accompanied by the loss of oxygen, resulting in an irreversible net loss of Li_2O from the structure. Mantia F. *et al*. have demonstrated direct evidence of oxygen evolution from the Li-excess material $Li_{1+x}(Ni_{1/3}Mn_{1/3}Co_{1/3})_{1-x}O_2$ at high potentials by in-situ Differential Electrochemical Mass Spectrometry (DEMS).[25] Oxygen gas was observed only in the Li-excess material during the first cycle, but not in the stoichiometric material and following cycles. CO_2 was also detected in both systems (Li-excess and stoichiometric) during the first cycle. However, it is absent in the Li-excess material in the second cycle, and is still observable in the stoichiometric sample. They believe the absence of CO_2 evolution in the Li-excess system in the second cycle is because a surface film composed of electrolyte oxidation products is formed during the first cycle. Our TEM study as shown in Figure 5.15(a) provides direct evidence of this passivation layer formation on the surface.

Based on these results, we propose a reaction mechanism that implies the reaction of DMC (Dimethyl Carbonate) and/or ethyl carbonate, one of the components in the electrolyte, with some oxide ions in the structure of the $Li[Li_{1/9}Ni_{1/3}Mn_{5/9}]O_2$ to induce a reduction of Ni^{4+} ions. More specifically, the EC or DMC is oxidized to an aldehyde (or ketone) as the Ni^{4+} ions are reduced to Ni^{3+}, with CO_2 and H_2O being generated as by-

products. The resulting aldehyde and more Ni^{4+} ions can further react with other O^{2-} ions to yield carboxylic acid and more Ni^{3+} ions. These Ni^{3+} ions would then become available to be simultaneously re-oxidized through the extraction of more Li ions from the structure. This results in the capacity being higher than the 200 mAh/g capacity expected solely from the oxidation of the initial Ni^{2+} ions. The whole proposed reaction mechanism can be summarized (for DMC) as follows:

$$CH_3\text{-}O\text{-}C(O)\text{-}O\text{-}CH_3 + 6Ni^{4+} + 3O^{2-} \rightarrow 2CH_2O + CO_2 + 2H_2O + 6Ni^{3+}$$
(in electrode)

$$2CH_2O + 2Ni^{4+} + O^{2-} \rightarrow HCO_2H + 2Ni^{3+}$$
(in electrode)

$$Ni^{3+} + Li^{+} \rightarrow Ni^{4+} + Li$$

O

ur ^6Li NMR results can now be used to evaluate which sites are vacated by the removal of Li^+ ions and the sequence of extraction during charge process (Figure 5.16). First, from OCV (3.5V) to 4.6V, the 2/3 Li^+ ions removed through charge compensation by the oxidation of Ni^{2+} to Ni^{4+} are extracted from both lithium layers and transition metal layers, and most of the lithium in transition metal layers are removed at this voltage, as seen in the ^6Li NMR spectra of the charged samples that the peak around 1500 ppm has almost disappeared in 4.6V sample. Then 2/9 Li ions drop into tetrahedral sites, and the residual Li ions still remain in the octahedral sites. Since the shifts of Li in tetrahedral sites and octahedral sites are very close in this system and the peak around 600 ppm is broad due to the complexity of Li environment, direct evidence can not be elucidated from NMR spectra. However, a similar mechanism has been proposed in $Li[Ni_{0.5}Mn_{0.5}]O_2$ system in the previous study, where a jump of the voltage at 4.8V was

observed as well.[15] The following process is the removal of the 1/9 Li corresponding to 63mAh/g capacity in octahedral sites, which is associated with the continuity of the first plateau at 4.6V. Then with the increase of the voltage, the Li ions in tetrahedral sites are removed which gives about 70mAh/g. The voltage increase in this process is due to the need of higher activation energy to extract Li from tetrahedral sites.

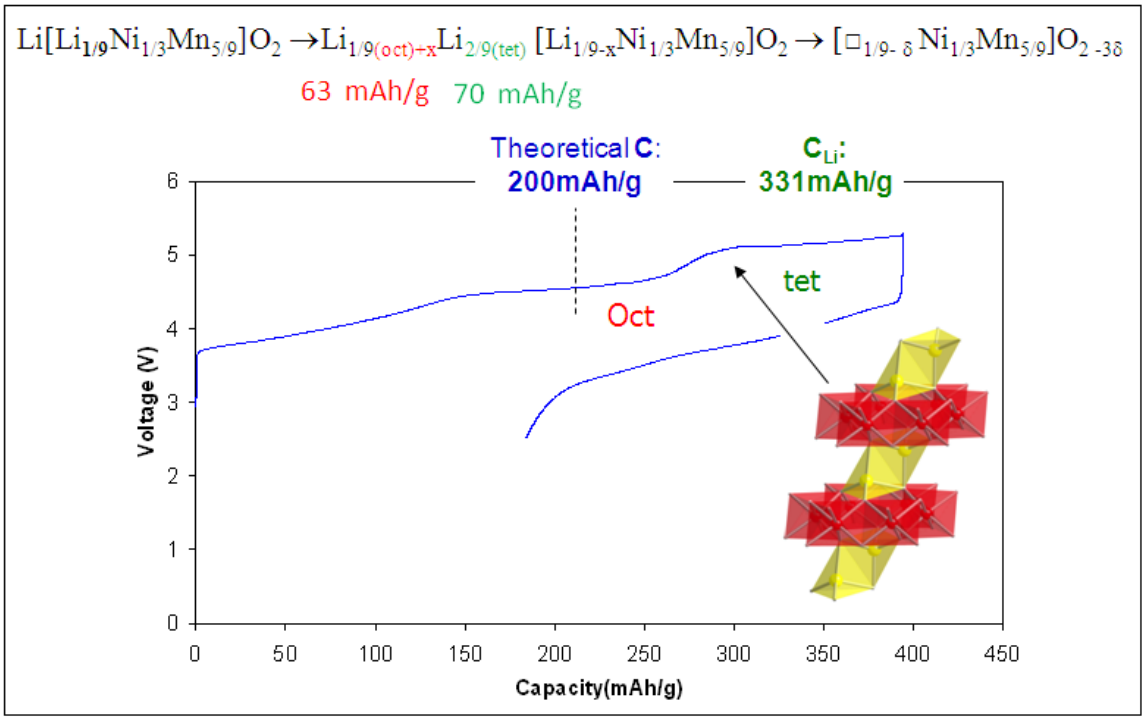

Figure 5.16: Demonstration of the Li removal process in the first charge process. Theoretical C is the capacity based on Ni content, and C_{Li} is the capacity based on Li content which could be removed from the structure.

5.5. Conclusions

The electrochemical behavior of layered $Li[Li_{1/9}Ni_{1/3}Mn_{5/9}]O_2$ as a positive electrode in lithium batteries has been investigated in this study. Two *plateau*-like regions are observed in the electrochemical profile when the battery is charged to 5.3V. GITT and PITT experiments have confirmed that the reaction(s) occurring at these voltages involve more than one phase. Both high capacity and better capacity retention are obtained after the material has been charged to high voltage.

Our ^{6}Li MAS NMR spectra show that the Li ions are removed from both the lithium and the transition metal layers upon charge, even at voltages above 4.6V, which is clear evidence that part of the capacity obtained at these high voltages can be ascribed to the phase and not only to electrolyte decomposition. High resolution XRD patterns show that the honeycomb ordering in the transition metal layers is lost when charging at 5.3V, which is likely to be associated to a migration of transition metal ions into the vacancies left by the extracted lithium ions, and the formation of a second phase above 4.4V. The honeycomb ordering cannot be recovered and the second phase is no longer present after Li ions are intercalated back into the structure. The Ni K-edge XANES spectra show evidence for Ni reduction above 4.6V, as proved by the edge shift to lower energies. High resolution TEM pictures show the formation of a passivation layer on the surface of the electrode particles. In addition, cracking and nano-size domains were observed in some crystals after charging to 5.3 V. These nano-sized domains may be associated with the improvement of the cycling electrochemical performance of the phase. In light of these results, a mechanism of reaction at high voltages with several steps is

proposed here. One implies the reaction between the electrode and the electrolyte. The Ni^{4+} ions are reduced to Ni^{3+} by Dimethyl Carbonate, one of the components in the electrolyte, then the reduced Ni^{3+} is oxidized to Ni^{4+} by removing Li ions from the structure. The second proposal is that the second *plateau* in the electrochemical profile is associated with the removal of tetrahedral Li ions. After most Li ions are removed from the structure, 2/9 Li ions drop to tetrahedral sites. Removal of this 2/9 Li ions gives about 70mAh/g capacity which is consistent with the real capacity gained on the high voltage *plateau*.

The Rietveld refinements of the samples after one charge-discharge cycle show an increase of the Ni content in Li layers which indicates Ni migration at high voltage. The ^{6}Li MAS NMR spectra of these samples also show that very few Li ions can be intercalated back into the transition metal layers after being charged at very high voltages, in agreement with the absence of. Honey comb type superstructure peaks in the XRD patterns. In addition, the change of the peak lineshape is indicative of the re-arrangement of transition metal ions in these layers. This re-intercalation of Li^{+} ions in the structure induces the reduction of nickel to Ni^{2+}, as proved by the XAS data. The Mn K-edge XANES spectra of the different cycled samples suggests a change in the local environment of the Mn^{4+} ions, but no obvious reduction is observed.

5.6 References

1. Lu, Z. H.; Beaulieu, L. Y.; Donaberger, R. A.; Thomas, C. L.; Dahn, J. R., *Journal of the Electrochemical Society* **2002,** 149, (6), A778-A791.

2. Lu, Z. H.; Dahn, J. R., *Journal of the Electrochemical Society* **2002,** 149, (7), A815-A822.

3. Lu, Z. H.; MacNeil, D. D.; Dahn, J. R., *Electrochemical and Solid State Letters* **2001,** 4, (12), A200-A203.

4. Robertson, A. D.; Bruce, P. G., *Electrochemical and Solid State Letters* **2004,** 7, (9), A294-A298.

5. Armstrong, A. R.; Holzapfel, M.; Novak, P.; Johnson, C. S.; Kang, S. H.; Thackeray, M. M.; Bruce, P. G., *Journal of the American Chemical Society* **2006,** 128, (26), 8694-8698.

6. Balasubramanian, M.; Sun, X.; Yang, X. Q.; McBreen, J., *Journal of Power Sources* **2001,** 92, (1-2), 1-8.

7. Lee, P. L.; Shu, D. M.; Ramanathan, M.; Preissner, C.; Wang, J.; Beno, M. A.; Von Dreele, R. B.; Ribaud, L.; Kurtz, C.; Antao, S. M.; Jiao, X.; Toby, B. H., *Journal of Synchrotron Radiation* **2008,** 15, 427-432.

8. Lee, Y. J.; Grey, C. P., *Journal of Physical Chemistry B* **2002,** 106, (14), 3576-3582.

9. Weppner, W.; Huggins, R. A., *Journal of the Electrochemical Society* **1977,** 124, (3), C135-C135.

10. Weppner, W.; Huggins, R. A., *Journal of the Electrochemical Society* **1979,** 126, (8), C305-C305.

11. Amarilla, J. M.; Tedjar, F.; Poinsignon, C., *Electrochimica Acta* **1994,** 39, (15), 2321-2331.

12. Chabre, Y.; Pannetier, J., *Progress in Solid State Chemistry* **1995,** 23, (1), 1-130.

13. Lu, Z. H.; Chen, Z. H.; Dahn, J. R., *Chemistry of Materials* **2003,** 15, (16), 3214-3220.

14. Rietveld, H. M., *Journal of Applied Crystallography* **1969,** 2, 65-&.

15. Breger, J.; Meng, Y. S.; Hinuma, Y.; Kumar, S.; Kang, K.; Shao-Horn, Y.; Ceder, G.; Grey, C. P., *Chemistry of Materials* **2006,** 18, (20), 4768-4781.

16. Breger, J.; Kang, K.; Cabana, J.; Ceder, G.; Grey, C. P., *Journal of Materials Chemistry* **2007,** 17, (30), 3167-3174.

17. Kang, K. S.; Meng, Y. S.; Breger, J.; Grey, C. P.; Ceder, G., *Science* **2006,** 311, (5763), 977-980.

18. Breger, J.; Dupre, N.; Chupas, P. J.; Lee, P. L.; Proffen, T.; Parise, J. B.; Grey, C. P., *Journal of the American Chemical Society* **2005,** 127, (20), 7529-7537.

19. Yoon, W. S.; Kim, N.; Yang, X. Q.; McBreen, J.; Grey, C. P., *Journal of Power Sources* **2003,** 119, 649-653.

20. Meyer, B. M.; Leifer, N.; Sakamoto, S.; Greenbaum, S. G.; Grey, C. P., *Electrochemical and Solid State Letters* **2005,** 8, (3), A145-A148.

21. Yoon, W. S.; Paik, Y.; Yang, X. Q.; Balasubramanian, M.; McBreen, J.; Grey, C. P., *Electrochemical and Solid State Letters* **2002,** 5, (11), A263-A266.

22. Yoon, W. S.; Grey, C. P.; Balasubramanian, M.; Yang, X. Q.; McBreen, J., *Chemistry of Materials* **2003,** 15, (16), 3161-3169.

23. Balasubramanian, M.; McBreen, J.; Davidson, I. J.; Whitfield, P. S.; Kargina, I., *Journal of the Electrochemical Society* **2002,** 149, (2), A176-A184.

24. Lei, C. H.; Bareno, J.; Wen, J. G.; Petrov, I.; Kang, S. H.; Abraham, D. P., *Journal of Power Sources* **2008,** 178, (1), 422-433.

25. La Mantia, F.; Rosciano, F.; Tran, N.; Novak, P. 2008; Springer: 2008; pp 893-896.

Chapter 6

A study of the lithium conversion mechanism of iron fluoride in a Li ion battery, by using solid state NMR, XRD and PDF analysis studies

Abstract

The structural transformations that occur when FeF_3 is cycled at room temperature in a Li cell, were investigated by using a combination study of X-ray diffraction (XRD), Pair distribution function (PDF) analysis, and solid state magic angle spinning nuclear magnetic resonance (MAS-NMR) spectroscopy. Two regions are seen on discharge, the 1st between Li=0 and 1.0 involving an insertion reaction. This reaction is comprised of two steps: first a two-phase reaction is seen between Li=0 and 0.5, the Li=0.5 phase giving rise to a ^{6,7}Li NMR resonance consistent with the presence of both Fe^{3+} and Fe^{2+} ions. The PDF data suggests that, locally, this phase is related to the rutile structure. Second, a single phase reaction between Li=0.5 and 1.0 occurs; this is accompanied by the shift of the Li NMR resonances to lower frequencies, indicating an increased concentration of Fe^{2+} ions. The 2nd region involves the conversion reaction. Superparamagnetic nano sized Fe metal (~3nm) is formed, as seen by XRD, along with some LiF and a third phase that is rich in lithium and fluorine. The charge process involves the formation of a series of intercalation phases with increasing Fe oxidation state. On the basis of the similarity between the Li resonances seen during the 1st step on

discharge, and those seen on charge, and the PDF data of a charged sample, the local structure in these intercalation phases appears to be structurally related to a disordered form of the trirutile structure. According to electrochemistry and Li NMR results, at the end of charge the average valence state of Fe is approximately $Fe^{2.5+}$. The reaction mechanism of FeF_3 is compared to that of FeF_2. The solid state NMR and XRD results for feF_2 indicate that insertion occurs, but this now involve first the extrusion of Fe and the insertion of Li into the structure. This is then accompanied by the formation of Fe nanoparticles and a disordered LiF phase.

6.1. Introduction

The cathode materials used in present commercial lithium ion batteries are layered compounds based on $LiCoO_2$ with a specific capacity of 120~150mAh/g. In these materials, lithium is stored in their framework structures and lithium deintercalation and intercalation reactions occur during the charge/discharge cycles without significant structural change.[2] This type of reaction gives excellent cycling performance, however it gives only a limited capacity because of the structure and corresponding restricted valence changes of the transition metals. Recently, 3d-transition metal binary compounds M_xX_y (M= Co, Fe, Ni, Cu etc.) (X=F, O, S, N etc.) have been extensively investigated as potential electrode materials for lithium ion batteries. Tarascon *et al*. demonstrated that they have specific capacities as high as 600～1000mAh/g along with excellent cycling reversibility.[3] Unlike the layered compounds, these materials react via a "conversion reaction" of the form:

$$M_xX_y + nyLi \rightarrow yLi_nX + xM \qquad (1)$$

In this reaction, the micron-sized M_xX_y (eg. M= Fe, Co, Ni, Cu etc. X=F, O, S, N etc.) decomposes to form a ~1-10nm metallic particle/Li_nX nano-composite in the first reduction reaction. This is followed by repetitive redox reactions in which the size of the particles remain unchanged. The electrochemically-driven nano-size confinement of the metal particles by the lithium salt Li_nX is believed to enhance their electrochemical activity, providing better reversibility to the Li_nX-M nanocomposite.

Of the M_xX_y materials, only the metal fluorides have sufficiently high operating voltage to be used as alternative cathodes for Li-ion batteries, because of their ionic

character.[4, 5] However, fluorides are usually insulators due to their large band gap, making it more difficult to develop these materials for Li-ion batteries. To overcome this difficulty, Badway *et al.* have proposed the use of carbon metal fluoride nanocomposites (CMFNCs).[6, 7] The drastic reduction of MF_y particle size and the highly conductive carbon matrix that connects each nano-grain, enhances the electrochemical activity dramatically in the first cycle and results in excellent reversibility in subsequent cycles due to the stability of surface coated by carbon materials.

Among all metal fluoride compounds, iron fluoride (FeF_3) has a theoretical capacity of approximately 200mAh/g in the 4.5-2.5V region and 400mAh/g in the 2.5-1.5V region during the conversion reaction. The electrochemical activity of FeF_3 was first reported by Arai *et al.,*[8] and subsequently Badway *et al.* and Li *et al.* have proposed reaction schemes for both regions as shown below. [5-7, 9]

$$FeF_3 + Li^+ \rightarrow LiFeFe_3 \quad (4.5\text{-}2.5V) \qquad (2)$$

$$LiFeF_3 + 2Li^+ \rightarrow Fe^0 + 3LiF \quad (2.5\text{-}1.5V) \qquad (3)$$

In the first region, [(2)], Li^+ is inserted into FeF_3 framework, first via a two-phase reaction to form $Li_{0.5}FeF_3$ and then via a single phase reaction to form $LiFeF_3$. This process appears to be fully reversible. FeF_3 adopts a rhombohedrally disordered version of ReO_3 structure (BX_3, space group R$\bar{3}$C) (Fig. 6.1). The structure is related to perovskite ABX_3 and comprises corner-sharing $FeF_{6/2}$ octahedra that are connected to form a 3D tunnel structure. The Fe^{3+} ions lie on the (102) planes, while the (024) planes contain the vacant A sites that are available for Li insertion. Li insertion, however, appears to result in a change in the structure of the Fe sublattice, since pronounced

changes in the XRD patterns are observed to occur on inserting 0.5 Li per FeF_3 unit.[6] One driving force for this structural rearrangement may come from the fact that the vacant A sites are actually too large for Li^+. In the subsequent step, [(3)], $LiFeF_3$ is reported to decompose to form LiF and Fe metal and this part of reaction also has been found to be reversible when using a carbon FeF_3 nanocomposite.

In the reconversion reaction, Badway *et al*. have proposed that the Fe metal and LiF react to form a "FeF_2 rutile-like" structure (Fig. 6.1), instead of the initial FeF_3 structure.[7] Consistent with this, the electrochemistry of FeF_2 is quite similar to that of FeF_3 after the first cycle. However, the observed capacity corresponding to the extraction of three Li can not be explained with this mechanism scheme. Recently, 1st principles calculations of Doe et al.,[10] suggested that a series of intermediate phases could be formed during the electrochemical process, the exact nature being controlled by the differences in the kinetics of the diffusion of the different ions or atoms in the system (F^-, Fe^{n+}, Li^+). Specifically, they proposed that the ReO_3 structure rearranges to form a series of stable phases derived from rutile on discharging; they also identify a new phase, the inverse spinel $Li_{3/2}Fe_{3/4}F_3$, which they suggest may be formed during the lower voltage process. Their calculations suggest that the defect tri-rutile structure, $Fe_{2/3}F_2$, (space group $P4_2/mnm$) is formed at the end of first charge, accounting for the capacity observed on the 1st charge, and in subsequent cycles. However, given the disorder and small particle sizes seen in this nanocomposite system, it is difficult to validate some of the hypotheses of this paper experimentally.

Nuclear Magnetic Resonance (NMR) is a powerful technique to probe short range ordering,[11] making it an ideal tool to understand the mechanism of reactions

involving nano-sized particles. The methodology is used in work presented in this paper to study the details of the conversion/reconversion reaction mechanisms for FeF_3. The results are combined with Pair Distribution Function (PDF) analysis of X-ray Diffraction (XRD) data, since this represents another powerful tool to probe short range ordering of disordered materials and nanoparticles.[12] To achieve the superior electrochemical performance of FeF_3, we prepared carbon-coated nano FeF_3 (CCN-FeF_3) and have investigated its structure on cycling by using NMR, obtaining additional supporting evidence from XRD and PDF analysis. The results are compared with the diffraction and NMR data following lithium insertion in FeF_2.

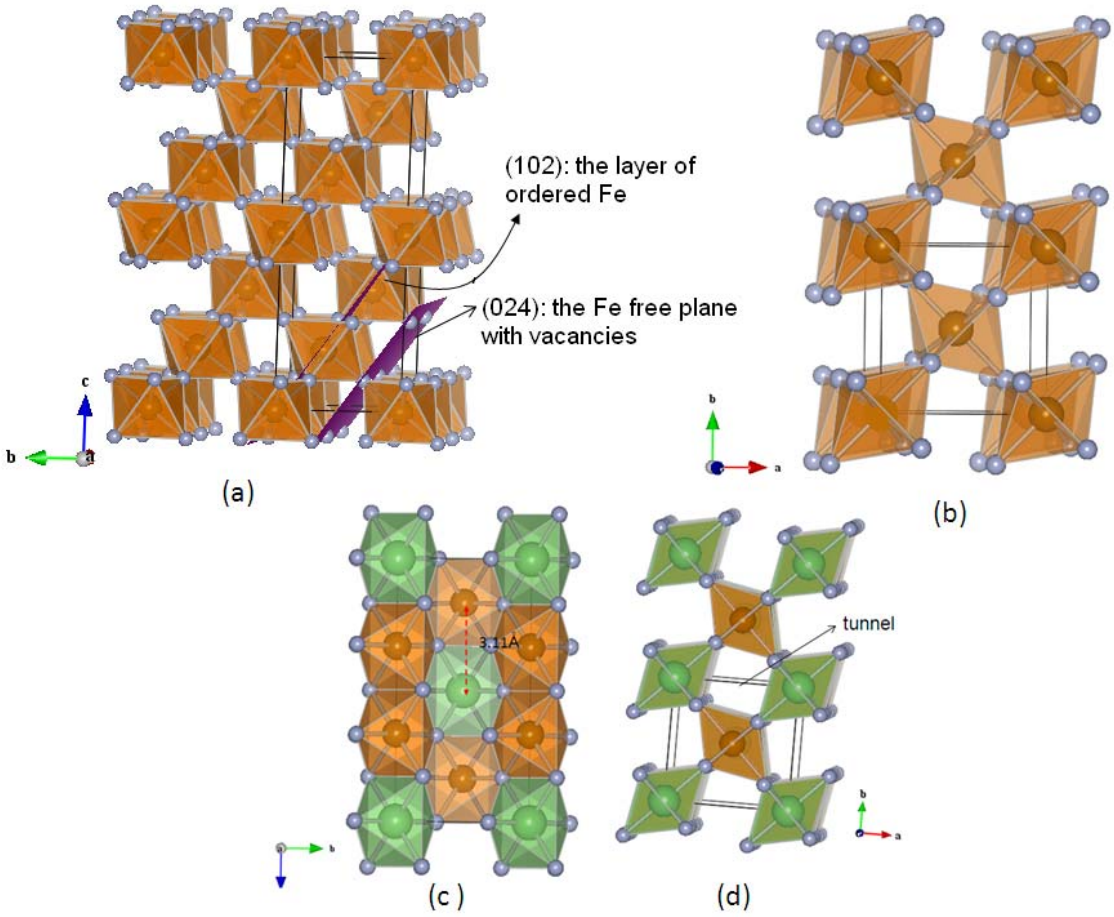

Figure 6.1: Structures of (a) FeF_3 unit cell showing the (024), the Fe free plane and (102), the layer of ordered Fe ($R\bar{3}C$ Perovskite type structure), (b) FeF_2 unit cell ($P4_2/mnm$ rutile structure, Tetragonal), (c) $Li_{1/2}FeF_2$ unit cell ($P4_2/mnm$ tri-rutile structure, Tetragonal) from a direction and (d) c direction. Blue, green and orange spheres correspond to F, Li and Fe, respectively.

6.2. Experimental

6.2.1. Materials preparation

CCN-FeF_3 was prepared by highly energy milling of R$\bar{3}$C FeF_3 (Kojundo) with Carbon Black (Ketjen Black International Company). Stoichiometric mixtures (FeF_3: Carbon Black = 80 wt%:20 wt%)[7] were placed inside a steel milling cell with Zirconium balls. Milling was performed for 3 hours in a high energy milling machine (Rotec) with 500rpm. Carbon coated nano-FeF_2 (CCN-FeF_2) was also prepared by using the same procedure as used for CCN-FeF_3.

6.2.2. Electrochemical characterization

Cathode electrodes were prepared by mixing 80 wt % of active material (CCN-FeF_3 or CCN-FeF_2), 15 wt % of Graphite as an electronic conductor, and 5 wt % of polyvinylidene fluoride (PVDF) as a binder in N-methylpyrrolidinone. The slurry was coated on aluminum foil and dried at 100 °C until the solvent had evaporated completely. Coin type (2032) cells were assembled in an argon-filled glove box with Li metal foil (^{6}Li metal for ^{6}Li NMR experiments) (Aldrich) as the anode, Polypropylene separators (Celgard) and a 1 M solution of $LiPF_6$ in EC (ethylene carbonate): DMC (dimethyl carbonate) = 1:1 as the electrolyte. No binder was used to prepare the samples for the synchrotron XRD. 85 wt% of active material (CCN-FeF_3 or CCN-FeF_2) and 15wt% of Carbon Black were used for the cathode mixture in Swagelok type cells with Whatman GF/D fiber as separators. Electrochemical experiments were carried out with a battery

cycler (Arbin Instruments, College Station, Texas) in galvanostatic mode at a C/100 rate of between 1.0 and 4.0 V.

6.2.3. X-ray Diffraction

For the characterization of the ball milled samples, bench type X-ray diffraction (XRD) was performed on a Rigaku powder X-ray diffractometer equipped with a Cr target X-ray tube (Cr $K\alpha_1$ λ= 2.2898 Å). A range of 2θ values from 20 to 120° with a scanning rate of 1° per minute and a step size of 0.02° was used. To analyze the structural change during cycling, high resolution (HR)-XRD was carried out on the cycled samples at beam line 11-BM at the Advanced Photon Source (APS) in Argonne National Laboratory (λ=0.4001 Å),[13, 14] and also at the X16C beam line at National Synchrotron Light Source (NSLS) at Brookhaven National Laboratory (λ=0.6881 Å). For convenience, the values shown in this paper were converted to those corresponding to Cu K_α (λ=1.5406Å).

6.2.4. Pair Distribution Function Analysis

To carry out the Pair Distribution Function (PDF) studies, X-ray synchrotron powder diffraction data of discharged CCN-FeF_3 were collected at the 11-ID-XOR beam line at the APS. The PDF data were acquired using a two-dimensional image-plate (IP) detector as previously described.[12] X-rays of 0.15359 Å wavelength were utilized in this experiment. A LaB_6 standard was employed to calibrate the sample-to-detector distance and the tilt of the IP to the beam path. Data were obtained from the powder sample in

transmission geometry. The IP data were integrated and converted to intensity readings versus 2θ with the Fit2D software. The PDF data were generated using PDFgetX. The measured intensity was corrected for the absorption of the glass capillary by background subtraction. Corrections for multiple scattering, X-ray polarization, sample absorption, Compton scattering, and Laue diffuse scattering were then applied, as described in Chupas *et al*. to obtain the structure function S(Q).[15] A detector efficiency correction was also included. Direct Fourier transform of the reduced structure function F(Q)=Q[S(Q) - 1] up to Q_{max} =23 $Å^{-1}$ gave G(r), the pair distribution function.

6.2.5. MAS NMR spectroscopy

^{7}Li and ^{6}Li MAS NMR spectroscopy were performed on discharged and charged CCN-FeF_3 samples with a 1.8 mm probe on a CMX-200 spectrometer using a magnetic field of 4.7 T. A spinning speed of 30 kHz and a rotor-synchronized spin-echo sequence (π/2–τ–π–τ–acq) were used to acquire the spectra. The ^{7}Li spectra were collected at an operating frequency of 77.10 MHz with π/2 pulses of 2.5 μs and a delay time of 1.0 s. The spectrum was referenced to 1 M ^{7}LiCl (in H_2O) at 0 ppm. ^{6}Li NMR spectra were collected at an operating frequency of 29.46 MHz with π/2 pulses of 3.5 μs and a delay time of 0.2 s. The spectrum was referenced to 1 M ^{6}LiCl (in H_2O) at 0 ppm. The spin-spin transverse-relaxation time T_2 was measured using an operating frequency of 77.10 MHz and the relevant experimental conditions described above by varying the value of τ in the spin-echo experiment.

^{19}F MAS NMR spectra were performed on cycled FeF_3 samples with a 3.2 mm probe on a CMX-360 spectrometer using a magnetic field of 8.46 T. The spectra were collected at an operating frequency of 338.73 MHz with spinning speed 20 kHz and a rotor synchronized spin-echo sequence. $\pi/2$ pulses of 5.75 and 3.5 μs (for different power level setting) were used, with a delay time of 1.0 s. The spectrum was referenced to monofluoro benzene (MFB) at -113.8 ppm.[16]

6.3. Results

6.3.1. Pristine CCN-FeF_3 characterization: Diffraction

XRD was used to confirm the structure of the FeF_3 ball milled with carbon black (CCN-FeF_3) and to check the purity of the sample (Fig. 6.2). The pattern of the ball-milled sample can be indexed with the same space group as the sample without milling, indicating that no significant structural changes and impurities are introduced in the milling process. However, a noticeable broadening of the Bragg peaks was observed. The crystallite size determined by the Scherrer formula[17] by using the (102) Bragg peak for CCN-FeF_3 was 8nm indicating that the particle size decreases considerably on ball-milling.

6.3.2. CCN-FeF_3: Electrochemical characterization

The electrochemical performance of CCN-FeF_3 was investigated in the voltage range between 4.0 and 1.0V (Li/Li^+) at room temperature at a C/100 rate (Fig.6.3). A short plateau at 3.3 V is 1^{st} observed, after which the voltage decreases gradually to approximately 2.5V, the capacity increasing steadily. A plateau-like region is then observed at 1.7V, the voltage dropping slowly after approximately 500 $mAhg^{-1}$ to 1.0 V. This behavior is similar to that found by Badway *et al*.,[6, 7] except that their operating voltage is slightly higher, presumably because of the higher operating temperature used in their study (70°C). The discharge reaction is divided into two parts as mentioned above. The first part between 3.5 and 1.7 V has been ascribed to an insertion reaction

involving Fe^{3+} to Fe^{2+} reduction (eqn. (1)), and the second part between 1.7 and 1.0V is due to a the conversion reaction region involving Fe^{2+} to Fe^{0} reduction (eqn. (2)).[7] Our specific capacities for these 2 regions are 233mAh/g and 500mAh/g respectively, which are very close to the theoretical capacities of 237mAh/g (Li=1.0) and 487mAh/g (Li=2.0). The slight overcapacity in the 2^{nd} region is ascribed to a contribution from Solid Electrolyte Interface (SEI) layer formation during discharge. On charge, no obvious plateau is observed and the voltage profile is very different from the discharge curve. A specific charge capacity of 606mAh/g was obtained and 127mAh/g (corresponding to 0.5 Li) was not recovered.

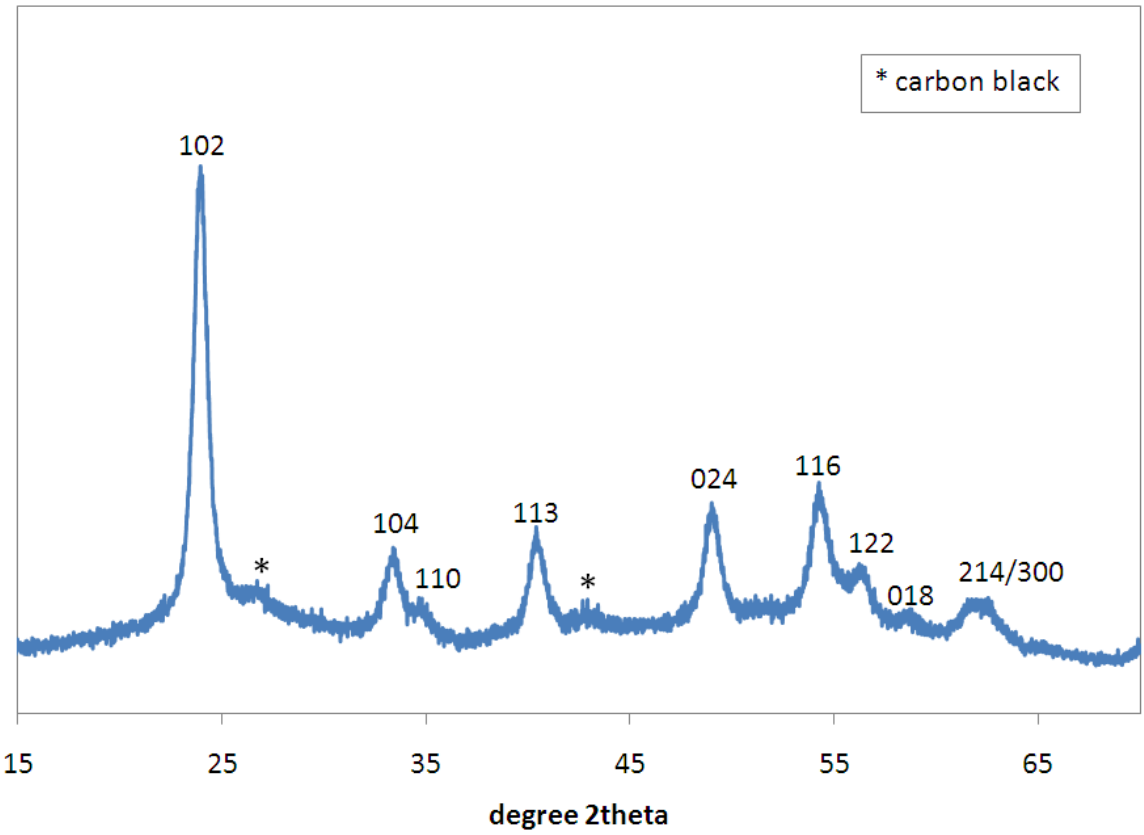

Figure 6.2: XRD pattern of CCN-FeF_3 prepared by high energy ball milling. The peaks are indexed with an R$\bar{3}$C space group.

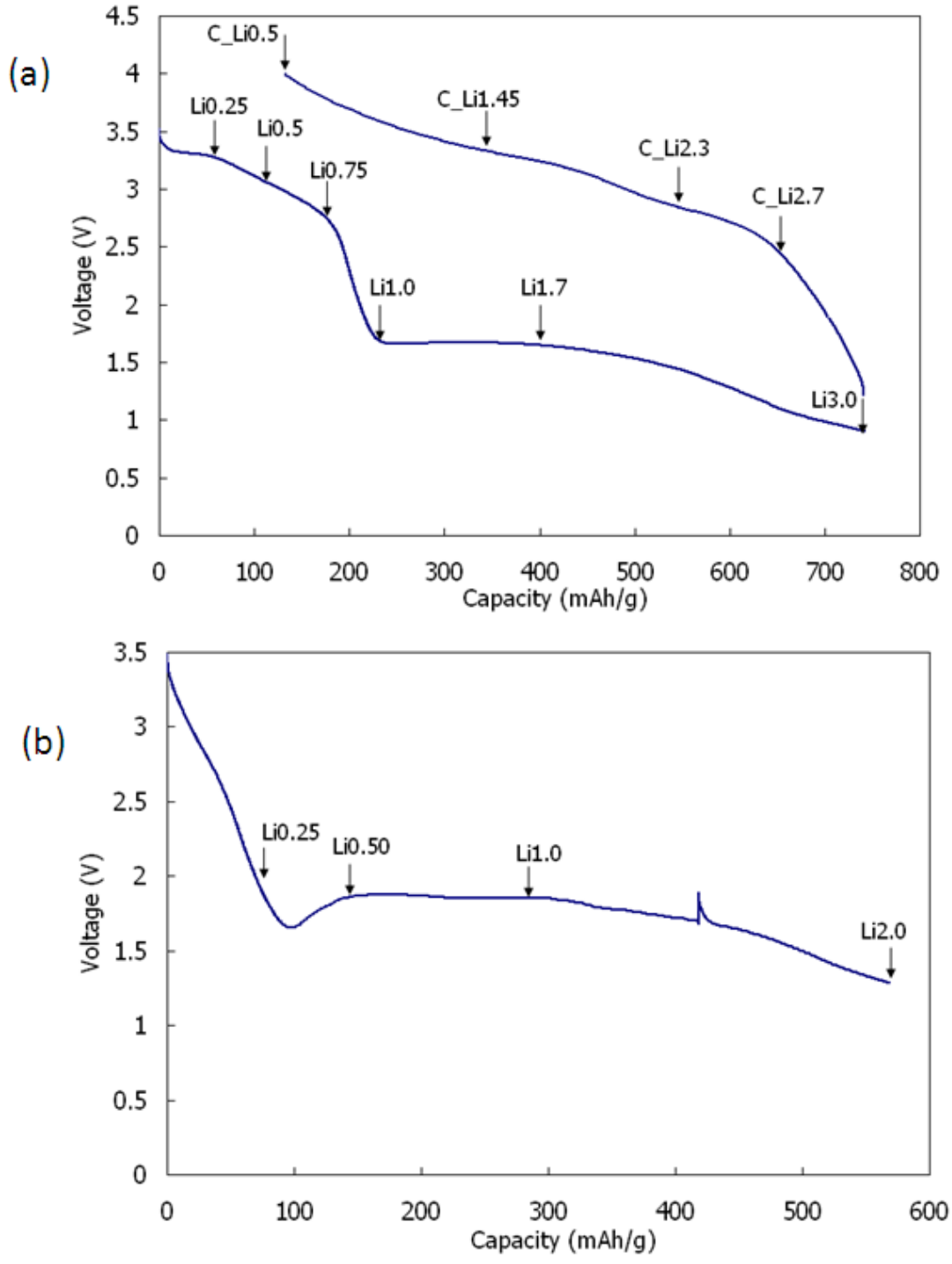

Figure 6.3: The Electrochemical curve of (a) CCN-FeF_3 and (b) CCN-FeF_2 cycled at room temperature at C/100.

6.3.3. High resolution-XRD

6.3.3.1. Discharged CCN-FeF_3

Fig.6.4 shows the XRD patterns of discharged CCN-FeF_3 samples between Li=0.25 and 3.0. The peak positions of the reflections of Li0.25 sample are very similar to those of the pristine CCN-FeF_3 sample except that the intensity of the reflections assigned to the FeF_3 phase decrease slightly in intensity. A series of sharp peaks below 24°, 2θ are observed, which appear to be due to the decomposition of the sample, even though it was sealed in a glass capillary for the XRD measurement. The same measurement was repeated for a different sample with the identical Li content, but now the sample was sealed in a kapton capillary. Again a new series of additional reflections with 2θ values of less than 24°, are seen. However, all of the other major reflections remained in the same position, suggesting that the reflections at lower angles are due to side-reactions and decomposition of the sample after it is removed from the battery and are not inherent to the original electrochemical reaction. This Li content sample appears to be noticeably more reactive than any other composition. A noticeable change is observed in the XRD pattern of Li=0.5 sample. The most intense peak at 24°, 2θ in the CCN-FeF_3 phase is no longer visible, and two reflections at 40° and 53°, (which are in the same position as the (113) and (116) peaks of the CCN-FeF_3 phase) grow in intensity. Two new broad reflections at 35° and 63° appear, which suggests that a new phase is present. The disappearance of the reflections due to the CCN-FeF_3 phase and appearance of a new phase at Li=0.5, (Li_xFeF_3) is consistent with the plateau-like region at 3.3V observed in the electrochemical profile, which also suggests that a 2-phase reaction

occurs. The reflections observed in the Li=0.5 sample remain until Li=1.0, and peak positions shift gradually to lower 2θ values. This is consistent with the presence of a solid solution reaction in this range, the cell-parameters of the new phase increasing on Li insertion, as expected as more Fe^{3+} is reduced to Fe^{2+}. In previous work, the new Li_xFeF_3 phase was assumed to be related to the original FeF_3 phase largely due to the presence of reflections at close to 40° and 63°, 2θ in both phases.[7] Based on this study, it appears that the positions of the two sets of reflections are coincidentally similar, but this may indicate that some structural motifs are common to both phases. We have not been able to index the pattern on the new phase satisfactorily, largely due to the considerable breadth of the reflections.

After Li=1.0, a gradual decrease in intensity of the reflections from the new Li_xFeF_3 phase is observed. However, very weak peaks at 37.5°, 39.5° and 51°, 2θ appear to remain from this insertion phase, indicating that there is still a small amount of this phase left at the end of discharge. The reflections from LiF and α-Fe start to appear in the XRD patterns, and those from Fe grow steadily with Li content below Li1.7. The size of the Fe particles, determined from the Scherrer formula by using the (102) Bragg peak in sample Li3.0, is only ~3-4nm. Surprisingly, sharp LiF reflections are seen for Li = 1.7 and 2.5, while the reflections are much broader for Li = 3.0, and much less distinct, suggesting that if LiF is present in this phase, it is associated with very small particle sizes or considerable disorder. There are also some very weak reflections from LiF at Li = 0.75 and 1.0. In addition to the LiF, Fe metal and the Li_xFeF_3 phase, several broad peaks are also observed, the strongest reflections being seen at 21 and 31°, 2θ, which appear to be from a new phase, most likely containing Fe^{2+} (in addition to Li^+ and F^-).

This suggests the process at lower voltages is much more complicated than suggested by equation (2).

6.3.3.2 Charged CCN-FeF_3:

The XRD patterns observed on charging are displayed in Fig. 6.5. The reflections from the Fe metal become weaker with increased state of charge, which suggests that the conversion reaction is reversible. Weak LiF reflections are still seen in the C_Li0.5 sample. The reflections at approximately 21° and 31°, 2θ stay in the same position in all the charged samples, but decrease gradually in intensity, and disappear at the end of charge. Another set of weaker peaks including those at 37.5°, 39.5° and 51°, 2θ which were ascribed to the Li_xFeF_3 phase, as discussed above, are visible until the end of charge, although significant shifts are observed for these reflections from the fully discharged sample to the C_Li0.5 sample, making any further analysis extremely difficult. All the reflections for the charged samples are generally broad and weak, and no highly crystalline phases are observed in all the samples, which suggests that the reaction in charge process is associated with nano-sized particles, at least for reactions performed at room temperature.

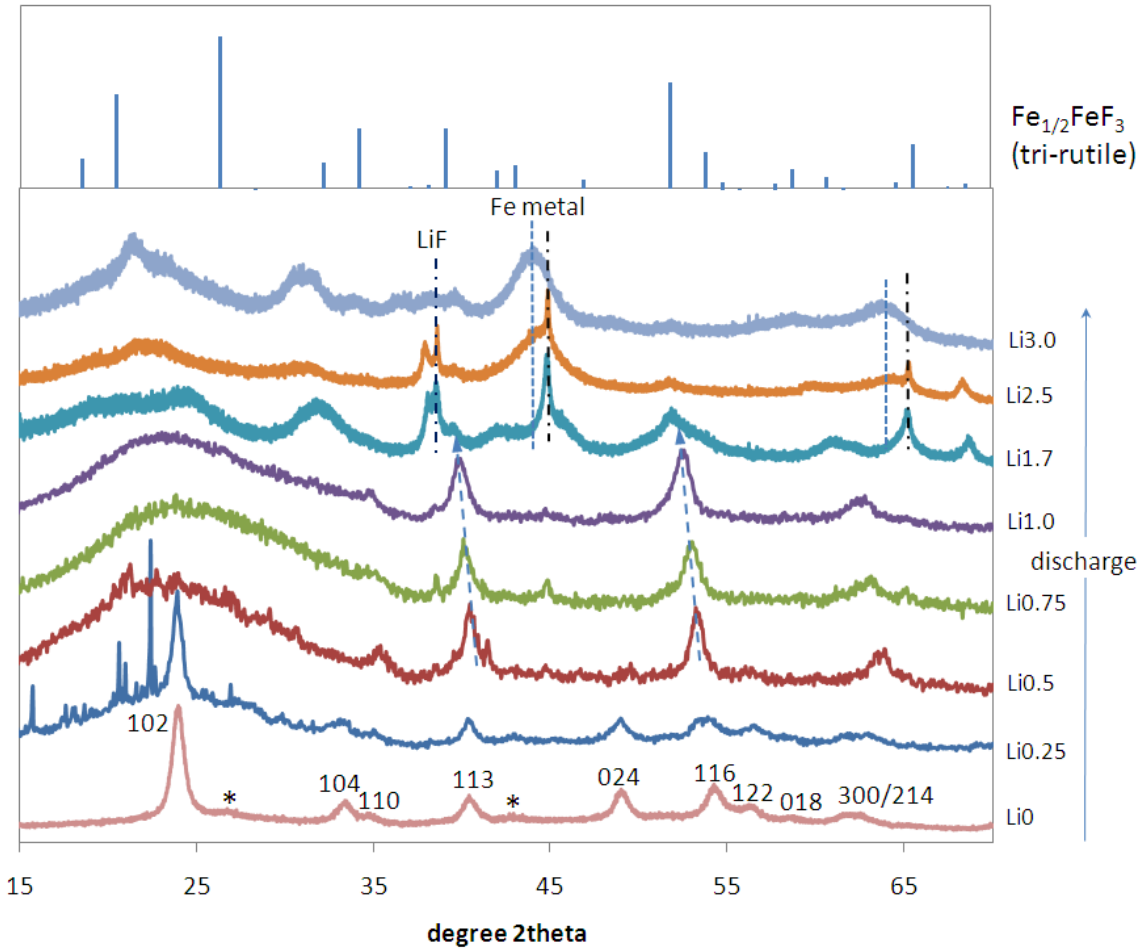

Figure 6.4: The XRD pattern of discharged FeF_3 samples. In this and subsequent figures the Li content in each sample is calculated from the cycle capacity and shown on the right hand side. The reflection peaks from LiF, Fe metal and carbon are marked with black dashed lines, blue dashed lines and asterisks respectively. The samples Li0.25, Li0.5, Li0.75, and Li1.0 were measured at X16C beam line in NSLS, and all the other samples were measured at 11-BM beam line in APS.

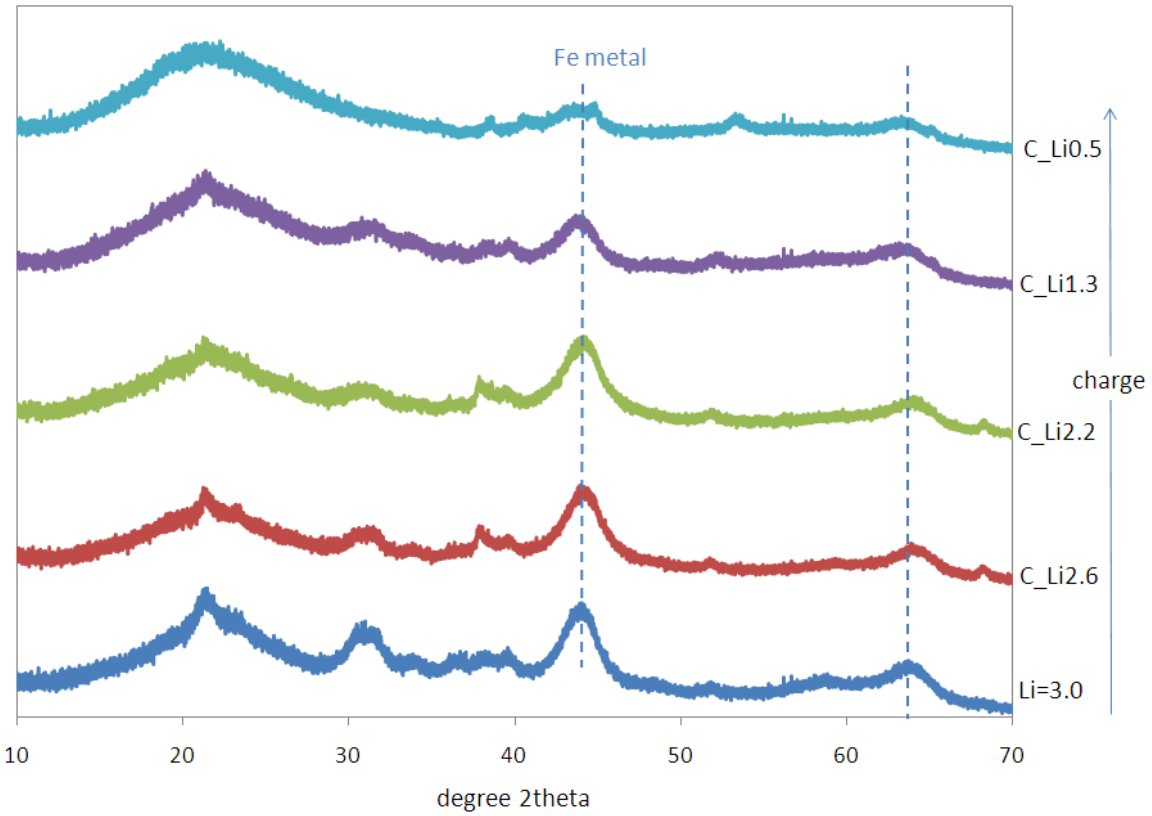

Figure 6.5: The XRD pattern of the charged FeF_3 samples. The "C" in labels means the samples were stopped on charged. The peaks from Fe metal are labeled with blue dashed lines. All the data in this figure were collected at 11-BM beam line in APS.

6.3.4. ^{6,7}Li-MAS-NMR Spectroscopy

6.3.4.1. Discharged CCN-FeF_3

Two major resonances are observed in the ^{7}Li MAS-NMR spectra of discharged CCN-FeF_3 samples between Li=0.25 and 1.0 (Fig. 6.6), one around 0 ppm and the other between 104 and 172 ppm. The small shift of the resonance at 0 ppm indicates that it is due to diamagnetic materials, such as Li_2O, LiF *etc,* present in the SEI layer, or from salts in the electrolyte. The increase of this resonance is due to SEI layer formation during the discharge process, and possibly the formation of some LiF. Based on our previous work, the large shift seen for the second resonance, is ascribed to the transferred hyperfine (Fermi contact) interaction between the lithium nuclear spins and the unpaired electrons located on the transition metal ions, which occurs via Li-O-$Fe^{2+/3+}$ bonds.[11] This observation of the shifted resonance provides clear evidence that lithium is inserted into an iron fluoride structure, and that the lithium is in close proximity to the Fe ions (Fe^{2+} and Fe^{3+}). The broadening of the resonance is ascribed to the presence of a range of Li local environments and the short spin-lattice (T_1) and spin-spin (T_2) relaxation time of the ^{7}Li nuclei. Based on our earlier studies of a series of $LiFeO_2$ polymorphs, whose ^{6}Li spectra contained resonances at frequencies of between 280 – 520 ppm,[18, 19] we ascribe the smaller shift of 172 ppm to the presence of both Fe^{2+} and Fe^{3+} ions in the local coordination environment of Li, Fe^{2+} ions resulting in smaller hyperfine shifts than Fe^{3+} ions, due to the smaller number of unpaired electrons and the decreased covalence of the Fe-O bonds. The peak position remains constant at 172 ppm, for both the Li=0.25 and Li=0.5 samples, its intensity gradually increasing with Li content. This indicates that the

Fe ions in the 1st Li cation coordination shell in both samples have the same average oxidation state. This is consistent with the two-phase region proposed based on the electrochemical results, involving a "Li free" phase CCN-FeF_3, and second Li_yFeF_3 (y≈0.5) phase. A gradual shift to low frequency of the 172 ppm resonance is observed from Li = 0.5 to 0.75. This is consistent with a solid solution reaction, Li inserting into the $Li_{0.5}FeF_3$ structure with the concomitant reduction of Fe^{3+} to Fe^{2+}. However, the intensity of the ^{7}Li resonance does not increase with further Li insertion, but instead broadens noticeably and almost disappears into the baseline in the spectrum for the Li=1.0 sample. The broadening is in part ascribed to the short spin–spin transverse-relaxation time, T_2, of this sample, which appears to be related to the presence of high-spin Fe^{2+} ions. T_2 values were measured for the samples and gave 238 μs for the 172 ppm resonance in the Li0.5 sample and 172 μs for the peak at 104 ppm in the Li1.0 sample. These short T_2s result in significant loss of signal intensity, particularly for the Li1.0 sample, in the spin-echo experiment used to acquired the spectra (where 2τ = 67 μs, resulting in approximately 30% loss of signal).

^{6}Li NMR was performed on the same discharged Li = 0.5 to 1.0 samples, to ensure that all the lithium signals are observed. ^{6}Li (I =1) has smaller quadrupolar and gyromagnetic moments compared to ^{7}Li, which generally results in higher resolution spectra for paramagnetic materials, with fewer spinning sidebands, making their interpretation easier[11]. The ^{6}Li spectra (Fig. 6.7) are consistent with the ^{7}Li NMR results: two resonances are observed in the spectra, one at 0 ppm and the other one between 104 and 172 ppm. The spectrum of the Li = 1.0 sample clearly confirms the presence of the

104 ppm resonance, also confirming that no significant shift in this resonance is seen between Li 0.75 and 1.0.

The ^{7}Li NMR spectra of discharged CCN-FeF_3 samples in the second region between Li=1.0 and Li=3.0 (Fig. 6.8a) are noticeably different than those in the 1st region. Only the resonance at 0 ppm is now clearly observed, along with sidebands that now spread over more than 5000 ppm. The width of the sideband envelope and broadening of the individual peaks within the sideband manifold both increases significantly at deeper discharge, consistent with the formation of iron nanoparticles. In general, the ferromagnetic properties of iron should cause significant problems for the NMR experiment, especially while spinning the sample and tuning the NMR probe. However, no problems were encountered during the NMR experiment and spectra were obtained with the same experimental conditions as used for the other lower lithium content samples. This is indicates that the iron metal is not ferromagnetic, but instead that superparamagnetic particles are formed. This is in agreement with the diffraction data, which suggested that the Fe particle size was ~3-4 nm, particle sizes of 6.6 nm and below exhibiting superparamagnetic properties.[20] The large sideband manifolds are ascribed to the dipolar interactions between the Li ions in the diamagnetic phases and the local fields caused by the superparamagnetic particles in the static field inside the NMR magnet.

The ^{6}Li NMR spectra of the same samples (Fig 6.8b) similarly contain broad sideband envelopes, but these are smaller than those seen in the ^{7}Li NMR spectra, due to the smaller gyromagnetic ratio, γ, of ^{6}Li (and thus smaller Fe-Li dipolar couplings). A resonance at 86 ppm can now be clearly observed in Li=1.7 sample. This resonance is assigned to a lithium environment in an insertion phase, with a higher Fe^{2+}/Fe^{3+} ratio.

The intensity of this resonance is much weaker than the intensity of the 104 ppm resonance in the ^{6}Li spectrum of the Li=1.0 sample, presumably due to the onset of the conversion reaction.

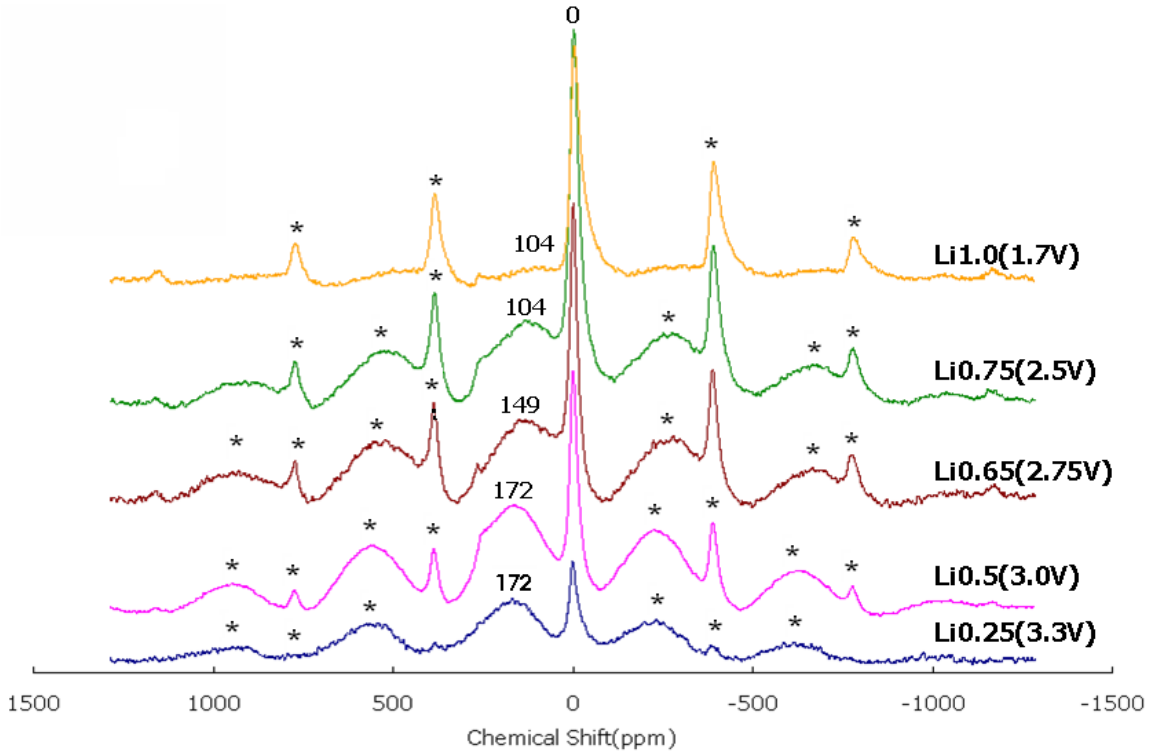

Figure 6.6: ^{7}Li MAS NMR spectra of discharged CCN-FeF_3 samples between Li=0.25 and Li=1.0. The numbers in parentheses show the cut off voltages. The isotropic resonances and spinning sidebands are marked with their shifts and asterisks respectively in this and subsequent figures. A very weak resonance is seen at 256 ppm, which is observed in a variety of different samples. Although the shift is identified to that of metallic Li, it may also arise from Li in carbon.

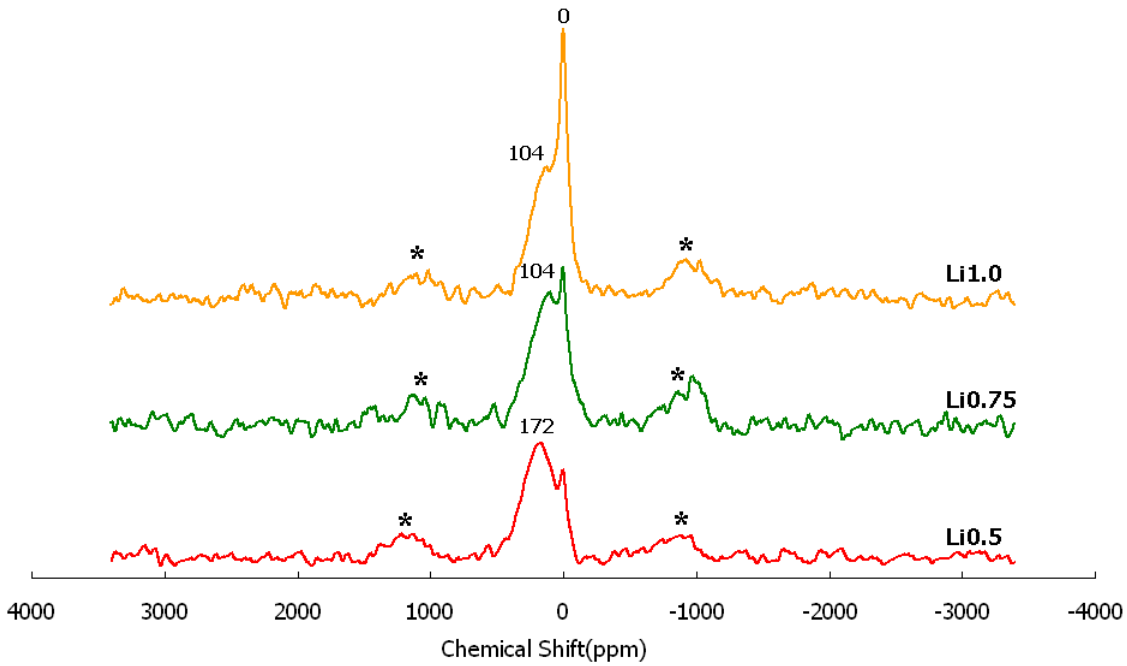

Figure 6.7: ^{6}Li MAS NMR spectra of discharged CCN-FeF_3 between Li=0.5 and Li=1.0.

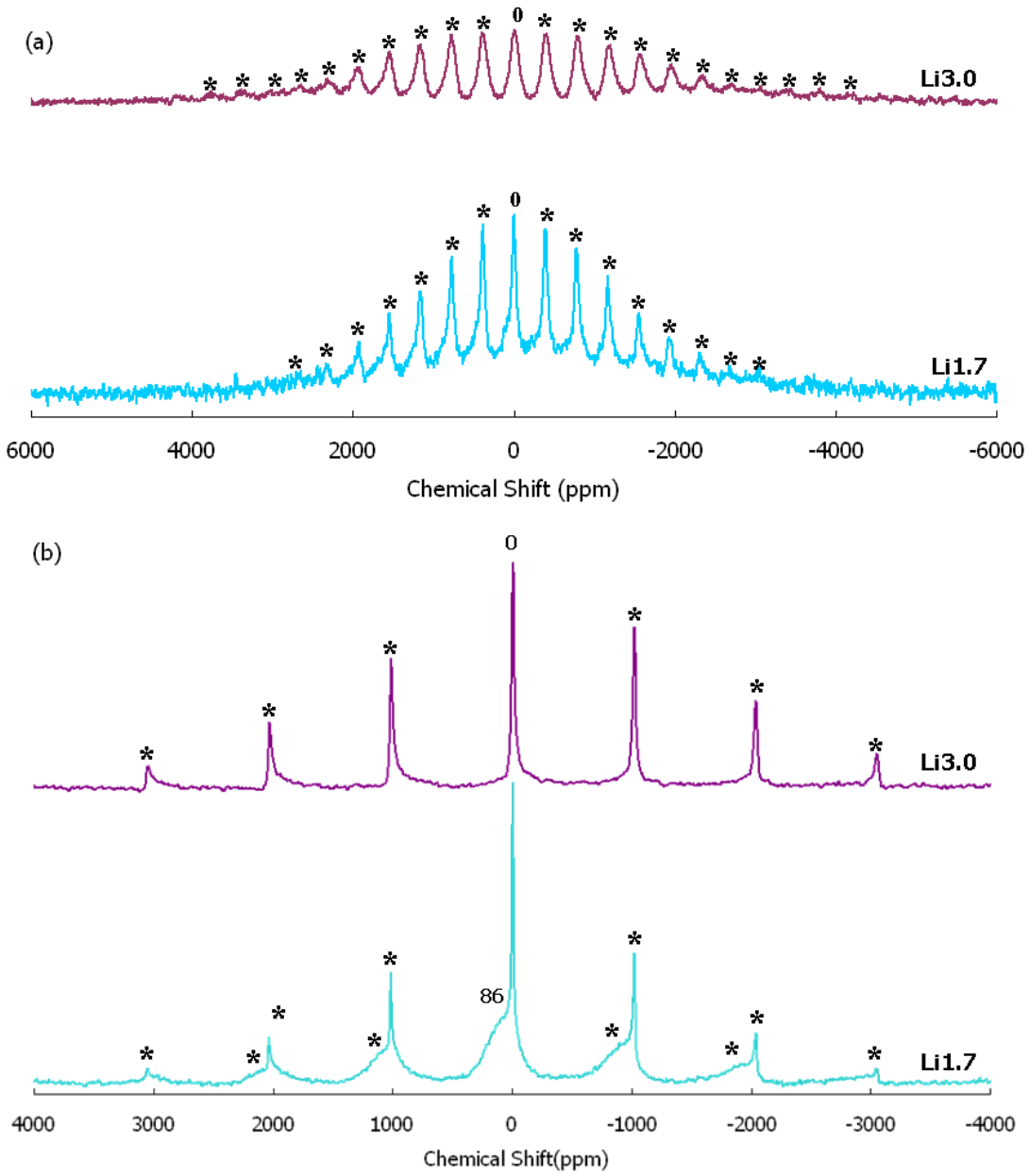

Figure 6.8: The (a) ^{7}Li and (b) ^{6}Li NMR spectra of discharged CCN-FeF_3 with Li=1.7 and Li=3.0.

6.3.4.2. Charged CCN-FeF_3

The ^{6}Li NMR spectra of the charged CCN-FeF_3 samples between Li=0.5 and Li=3.0 (Fig.6.9) are similar to those seen on discharge and consist of two sets of isotropic resonances, one at 0 ppm and the other one between 119 and 168 ppm. The width of the spinning sideband manifolds of the 0 ppm resonance, along with an increase in the intensity of the resonance between 80 and 168 ppm, and gradual shift in frequency are observed from sample C_Li2.0 to C_Li0.5. The former indicates that the concentration of superparamagnetic iron nanoparticles decreases on charging. The presence of the shifted resonances at very similar hyperfine shift positions to those seen on discharge suggests that the same lithium insertion environments return almost immediately on charge. The shift of the resonance seen in the C_Li0.5 spectrum (168 ppm) is similar to that seen for the Li0.5 sample obtained on discharge (172 ppm). This suggests that Fe^{2+} and Fe^{3+} co-exist at the end of charge and that the iron valence state is close to $Fe^{2.5+}$.

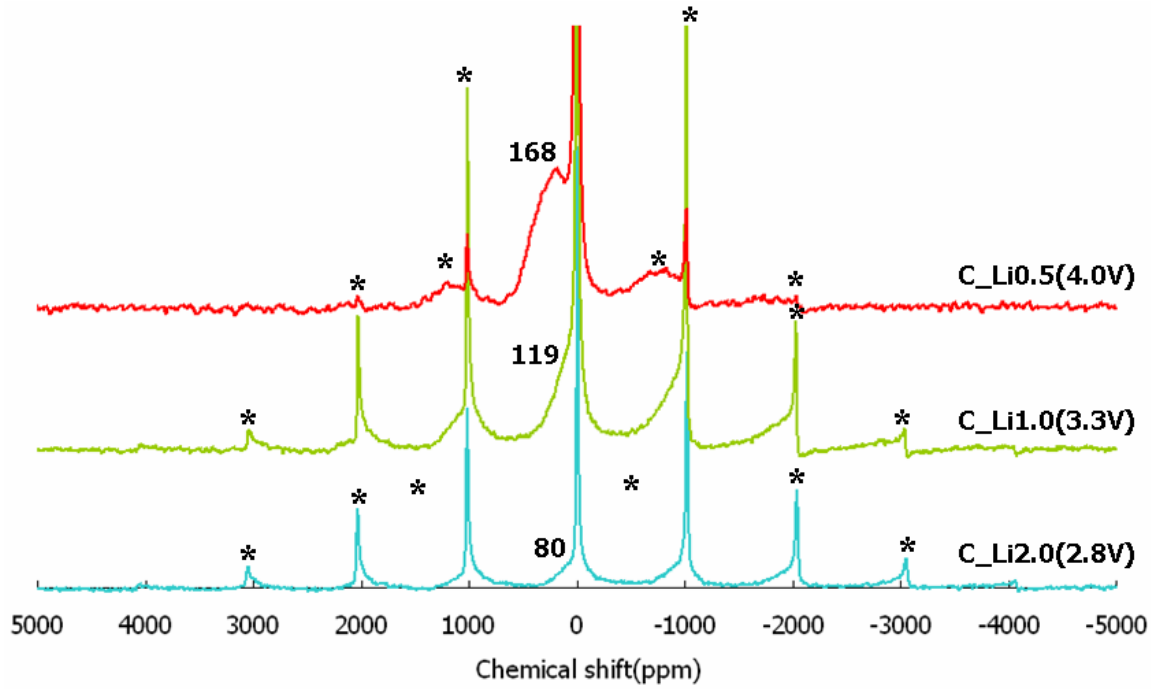

Figure 6.9: ^{6}Li MAS NMR spectra of charged CCN-FeF_3 between Li=0.5 and Li=2.0

6.3.5. ^{19}F-MAS-NMR

Since the ^{6,7}Li signal of LiF overlaps with the signal from the diamagnetic components from electrolyte and SEI layers, ^{19}F (I = ½, 100% natural abundance) NMR spectroscopy was performed on both the discharged and charged CCN-FeF_3 samples. Fig.6.10a shows the ^{19}F NMR spectra of the discharged CCN-FeF_3 samples in the first region between Li=0.5 and Li=1.0. The ^{19}F NMR signal in FeF_3 is not readily observed because F is directly bound to the Fe^{3+} paramagnetic ions. A broad component centered around -100 ppm is observed, which is due to the fluorine background in the probe. Other than this signal, no more isotropic resonances are observed until Li=0.75, where a peak at -85ppm is seen in Li1.0 sample. The assignment of this peak will be discussed later. No resonance due to LiF (which resonates at -200 ppm[21]) is observed in these spectra, indicating that this species is not formed in significant concentrations, consistent with the ex situ XRD results shown in Fig.6.4.

The ^{19}F NMR spectra of discharged CCN-FeF_3 samples after Li=1.0 and charged CCN-FeF_3 sample Li0.5 are displayed in Fig.6.10b. In the spectrum of the discharged sample Li1.7, significant peak broadening is seen similar to that seen in the ^{6,7}Li NMR spectra. Again only one resonance at -85 ppm is clearly resolved. The peak broadening is consistent with the formation of superparamagnetic iron nanoparticles. The effect of the Fe particles on the ^{19}F NMR spectrum is more severe than on the ^{6,7}Li spectra, due to ^{19}F's higher γ and the higher magnetic field used to acquire the spectra. The peak at -85 ppm is ascribed to fluorine in the SEI layer. $LiP_xO_yF_z$ compounds are represent one component of the SEI layer when EC/DMC/$LiPF_6$ is used as electrolyte.[22] It represents a

hydrolysis product of PF_6^- due to water present in the system. It may also be formed as a result of the decomposition of the electrolyte, which generates protons. After Li=1.7, the spectra are so broad, and the interactions with the Fe nanoparticles becomes extremely severe. Spectra were acquired at different spinning speeds to confirm that nothing is hidden under the spinning sideband seen in Fig. 6.11 (b) at -200 ppm, but these experiments did not reveal any evidence for LiF, although this should be observed in this voltage range. This indicates that either LiF is not present, or, if it is present, it is either so intimately surrounded by Fe nanoparticles, that the interactions with these particles are so large, that they wash out the LiF signal, or it is heavily doped with Fe^{2+}. The observation of an SEI signal, but not a LiF signal, in the Li1.7 sample, where the latter environment is seen by XRD, suggests that the SEI forms around the whole $LiF/Fe/Li_xFeF_3$ nanocomposite rather than on the Fe nanoparticles. The return of the -85 ppm resonance in the spectrum of the charged CCN-FeF_3 sample C_Li0.5, confirms that the SEI layer does not disappear in the Li = 3.0 sample, but rather must be washed out by the dipolar interactions with the Fe nanoparticles.

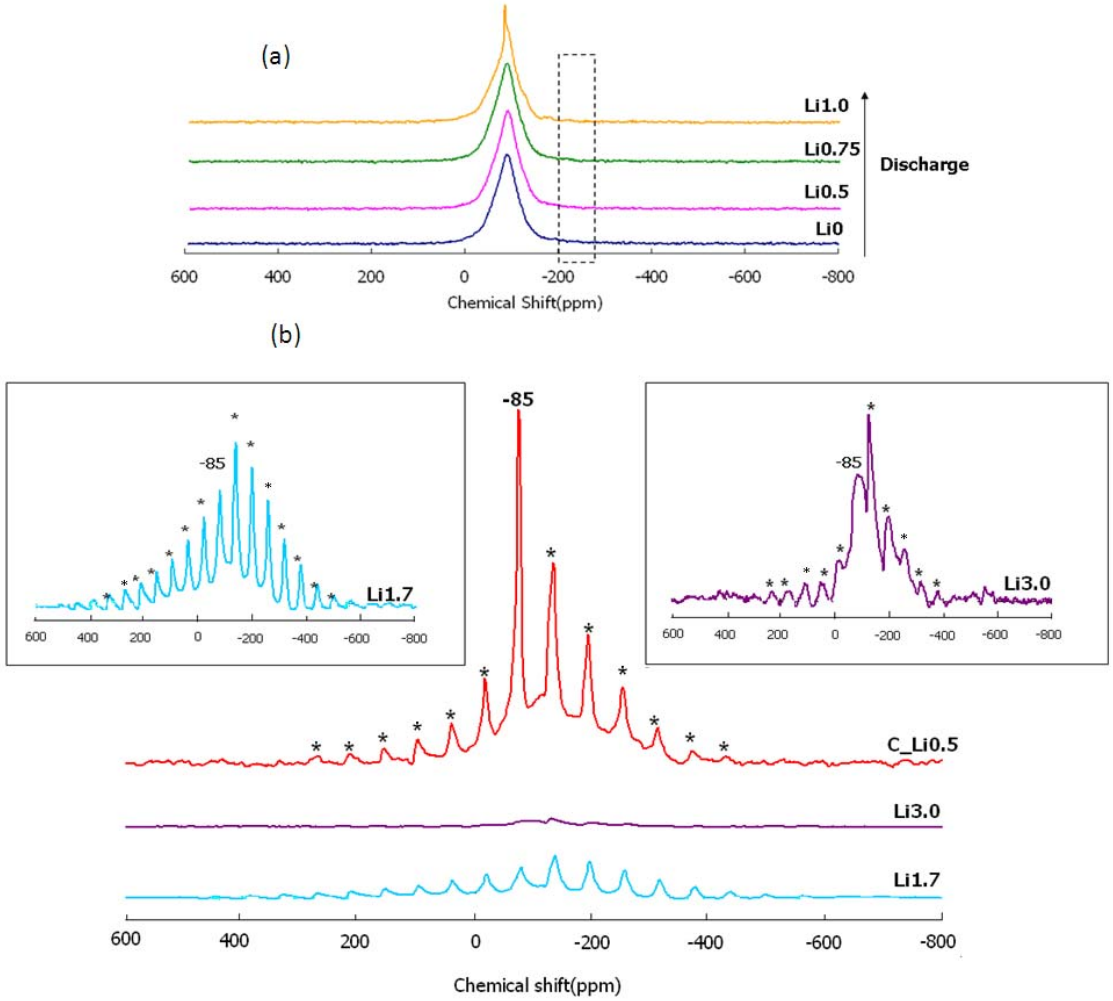

Figure 6.10: ^{19}F MAS NMR spectra of discharged CCN-FeF_3 between Li=0 and Li=1.0 (a) and Li=1.7, Li=3.0 and charged CCN-FeF_3 with Li=0.5(b). The insets are the enlargements of the spectra of CCN-FeF_3 with Li=1.7 and 3.0 between -600 to 800 ppm. The dashed rectangle indicates the expected chemical shift range of LiF.

6.3.6. Pair Distribution Function (PDF) Analysis of the Conversion Reaction

The PDF analysis of the XRD data of the cycled CCN-FeF_3 samples is shown in Fig.6.11. The pattern of Li=0.25 sample is similar to the simulated pattern of FeF_3. However, the peak around 5.2 Å, due to F-F and Fe-Fe correlations along the [001] direction of the FeF_3 cell is not obvious in this sample. This is tentatively ascribed to the disappearance of the FeF_3 phase and overlap of this peak with peaks from a new phase. Small damping factors were used in the simulations of the crystalline phases, and the much more rapid decay in intensity seen in all the experimental patterns is due to the much poorer crystallinity and smaller particle sizes of these materials. The patterns are very similar from Li = 0.5 to 1.0, but noticeably different from that of the Li0.25 sample, consistent with the XRD results. The peak positions move higher value in this range, as the structure expands and Fe^{3+} is reduced to Fe^{2+}. Interestingly, the pattern of Li=0.5 is very close to the simulated tri-rutile structure $Li_{1/2}FeF_3$[23] suggested by Doe *et al.*. A characteristic peak is observed at 3.11 Å which corresponds to the short Fe-Fe (or Li-Fe) distances of the edge-sharing FeF_6 (or LiF_6 – FeF_6) octahedra that are present along the c-direction of the rutile (or tri-rutile) structure (as marked in Fig.6.1c). A broader peak is seen at approx. 4.8 Å, which corresponds to the cell dimension in the [100] direction of the rutile structure. The change in the 1st correlation (the Fe-F distance) is consistent with the reduction of Fe^{3+} to Fe^{2+}. The results provide compelling evidence that the rutile structure is present in this range, but more detailed analysis of this data (via for example Reverse Monte Carlo simulations[12, 24]), is required to determine the extent of Li-Fe ordering present in this structure.

Two new peaks are observed in the Li 2.5 sample at 2.45 Å and 2.89 Å which correspond to the Fe-Fe distances in α-Fe. This provides more evidence that a conversion reaction takes place after Li=1.0. The two correlations become more obvious in the pattern Li=3.0 sample, as expected. The almost complete loss of the peak at 3.8 Å in this sample, which is assigned to the Fe-Fe distances in rutile or ReO_3 derived structures indicates that these phases have almost completely reacted. However, the pattern of the charged sample C_Li1.3 is very close to that of the discharged Li2.5 sample, providing strong evidence that the local structures of the two phases are very similar, and thus both likely related to rutile.

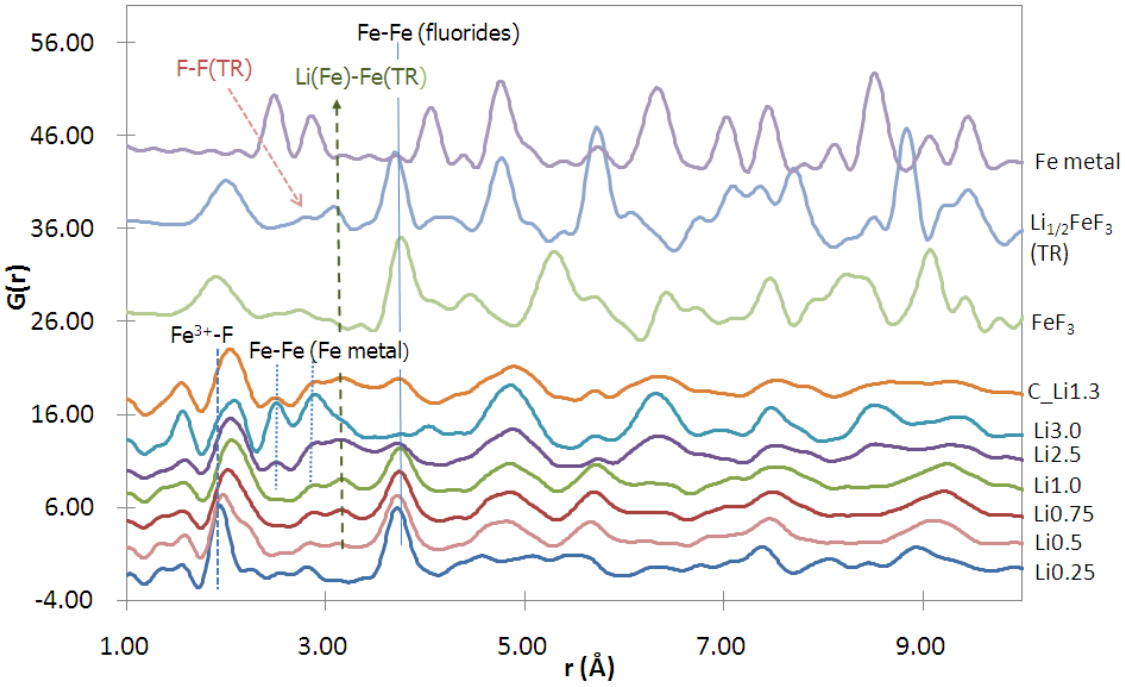

Figure 6.11: The PDF pattern of a series of cycled CCN-FeF_3 samples. The patterns for FeF_3, $Li_{1/2}FeF_3$ and Fe metal are simulated pattern with known crystal structure. The corresponding distance of each peak is labeled near the lines with possible phase in parentheses.

6.3.7. Study of the model compound FeF_2

In order to help determine the role of the rutile structure in the FeF_3 conversion reactions, discharged CCN-FeF_2 was investigated by ^{6}Li and ^{19}F NMR and XRD. Three isotropic resonances are observed in the ^{6}Li spectra of the discharged CCN-FeF_2 samples Li0.25 and Li0.5 (Fig.6.12) at 0, 87 and 172 ppm, although given the resolution and signal-to-noise of these spectra, it is difficult to be sure that the latter two peaks really correspond to distinct resonances. The peak at 0 ppm is ascribed to LiF and the SEI layer as described previously in this paper. The shifts at 87 and 172 ppm provide clear evidence for the interaction between lithium spins and unpaired electrons of iron ions, indicating that the lithium ions insert into an iron fluoride lattice. The concentration of these environments decreases from Li0.25 to Li0.5, presumably as more Fe metal is formed. Significantly, the shifts of these resonances are similar to those of the discharged CCN-FeF_3 samples Li0.5 and Li1.0, as shown in this figure for comparison.

Two isotropic resonances are observed in the ^{19}F NMR spectra of the discharged CCN-FeF_2 samples (Fig.6.13). The peak at -75 ppm is assigned to $LiPF_6$ from electrolyte,[21] and the peak at -85 ppm is from the SEI layer, as discussed previously. The peak at -200 ppm is a spinning sideband, but not from LiF. This was confirmed by acquiring a spectrum with a different spinning speed. However, sharp reflections from LiF are seen in the XRD pattern for Li=0.25 sample as shown in Fig.6.14; as before we ascribe this to either Fe^{2+} doping in LiF, strong interactions between the LiF and the Fe nanoparticles, and/or the relatively low concentration of this environment, relative to the large ^{19}F background of the probe (N.b. reflections from α-Fe are not very obvious for

this sample, most likely due to the small particle sizes and their low concentrations). This indicates that the conversion reaction happens during the early stages of discharge for CCN-FeF_2, but that the mechanism also involves the creation of a lithiated iron fluoride. The reflections from FeF_2 decrease steadily on lithiation, shifting slightly to lower angle between Li1.0 and Li0.25. Unlike the FeF_3 series, no extra peaks are observed in all the discharged samples except for the ones from LiF and Fe, indicating that the insertion phase adopts the same space group as that of pristine CCN-FeF_2. As was found in the FeF_3 case, a sharper LiF reflection is 1st observed and then this broadens noticeably on deeper discharge.

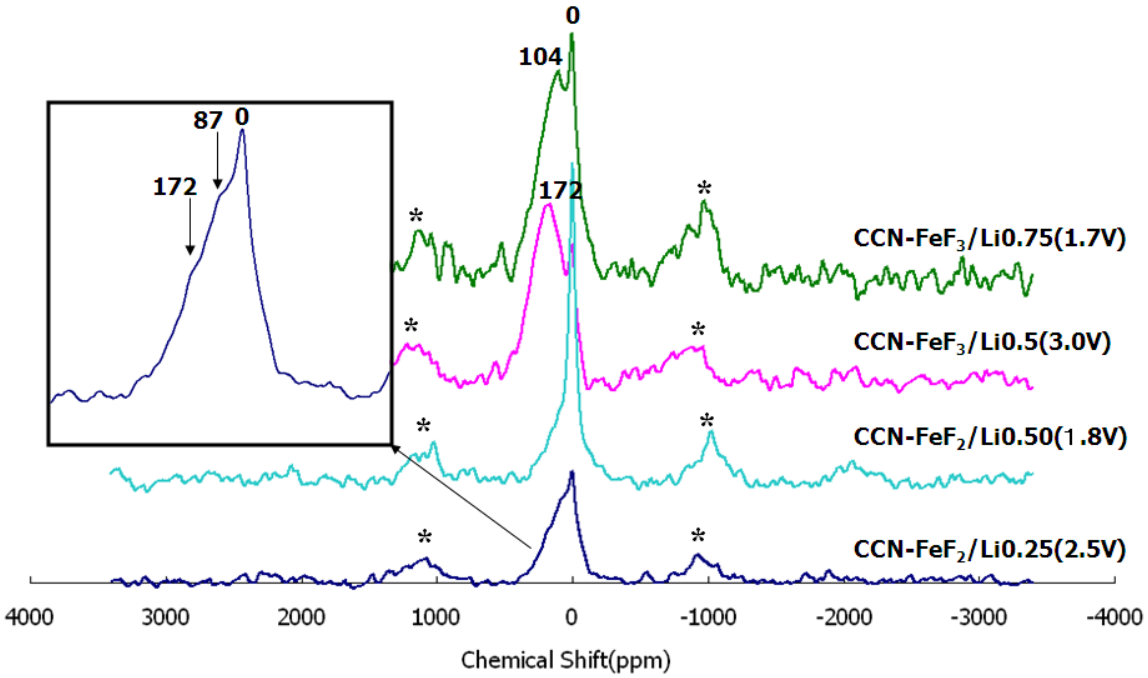

Figure 6.12: ^{6}Li MAS NMR spectra of the discharged CCN-FeF_2 with Li=0.25 and 0.5 compared with the discharged CCN-FeF_3 with Li=0.5 and 0.75. The inset is the enlargement of the spectrum for CCN-FeF_2 with Li=0.25 between -500 to 500ppm.

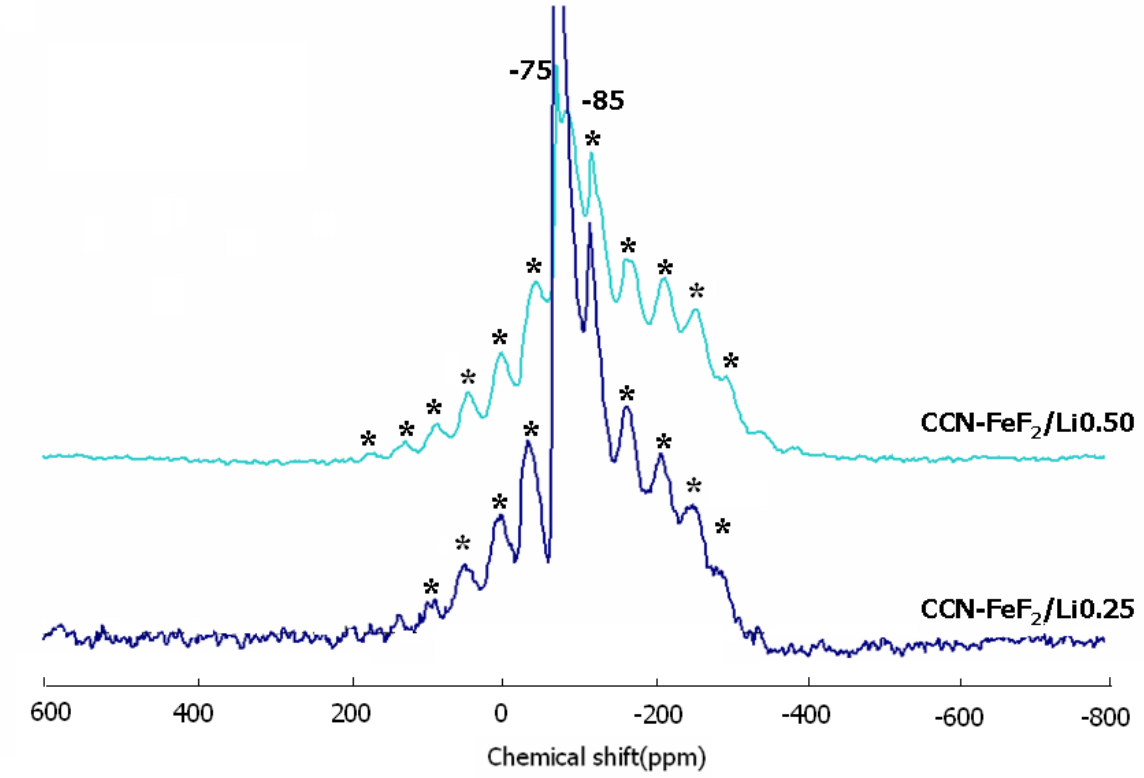

Figure 6.13: ^{19}F NMR of the discharged CCN-FeF_2 with Li=0.25 and Li=0.5.

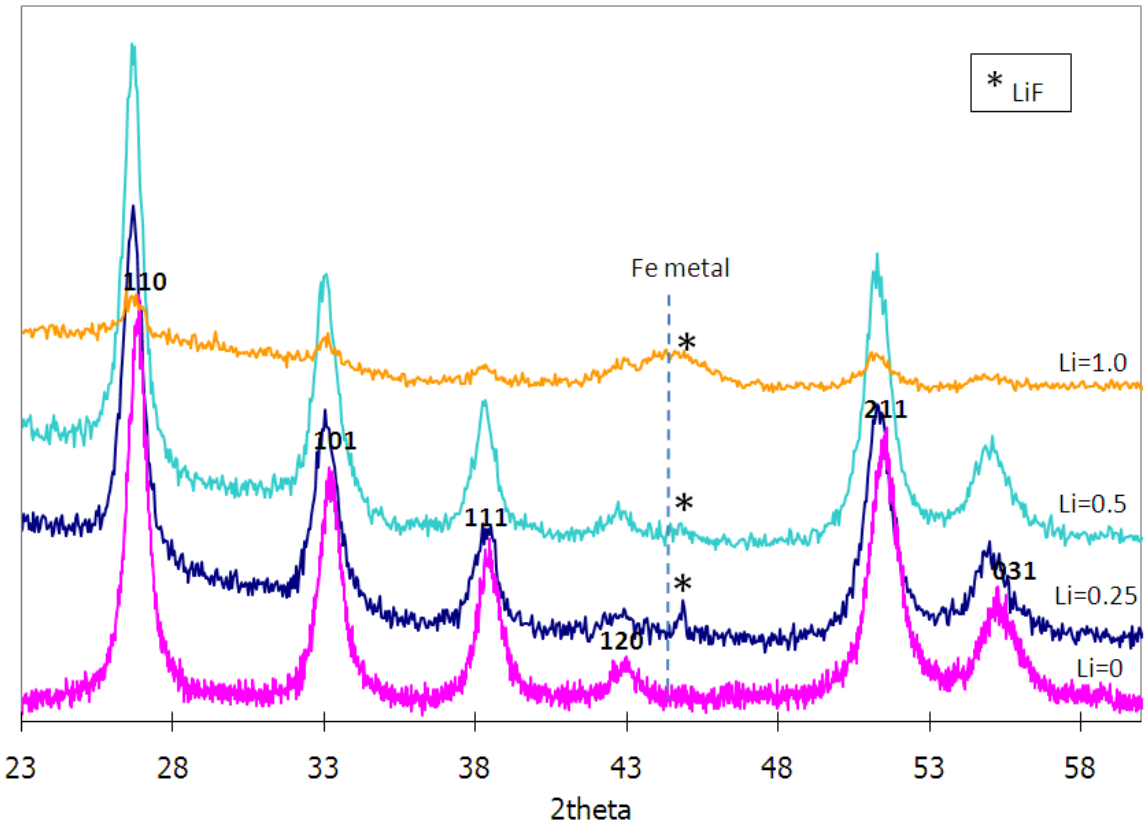

Figure 6.14: The ex-situ XRD patterns of the discharged CCN-FeF_2 between Li=0 and Li=1.0. The Li content is labeled with numbers. The pristine CCN-FeF_2 is indexed with *$P4_2/mnm$* space group. The reflection peaks from LiF are labeled with asterisks, and the blue dashed line indicates the position of the Fe metal reflections.

6.4. Discussion

6.4.1. The discharge reaction mechanism

The first region (Li = 0 to approx. 1.0) of the discharge mechanism of FeF_3 occurs 1st via first-order process (a two-phase region), as indicated by the observation of a ^{6,7}Li resonance at 172 ppm, whose frequency remains constant from Li > 0 to 0.5, and a phase transition from the ReO_3-structure to a new phase, Li_yFeF_3, ($y \approx 0.5$) as observed by XRD. From Li=0.5 to 1.0, the Li resonance shifts gradually to lower frequency, and the reflections of the new phase shift to lower 2θ values, indicating that a solid solution reaction is taking place in this regime involving reduction of Fe^{3+}. This mechanism is in qualitative agreement with the electrochemical results, where a plateau like region exists at 3.3V (to approx. Li0.25), the voltage dropping steadily thereafter to Li0.75. The experimentally observed decrease in voltage between Li0.25 and Li0.5 suggests that there is a competition between the conversion of FeF_3 to the new $Li_{0.5}FeF_3$ phase and the insertion (or reaction) of further Li into (with) the already formed, new phase during this region, since the latter process may be more kinetically favorable, for the experiments performed galvanostatically. Since the XRD and NMR experiments are performed on samples that have been allowed to rest before opening the battery, these experiments probe samples that are closer to thermodynamic equilibrium (or at least a thermodynamic local minimum). N.b., the GITT experiments of Badway *et al*. demonstrated that this plateau region extends to approx. Li =0.4.[7] The PDF patterns of the new Li_xFeF_3 phase indicate that M-M correlations due to edge sharing FeF_6, octahedra, which are characteristic to the rutile structure, are present for Li 0.5 – 1.0, strongly suggesting that

this new phase is derived from a rutile, and not from a ReO_3 structure. The similarity of the NMR in this regime, and that of the discharged FeF_2 sample is in agreement with this. We should stress, however, that we have not surveyed all possible $LiFe_xF_y$ phases, nor have we attempted, in this current study, to quantify the numbers of Fe-Fe short contacts and the extent of any Li/Fe ordering (expected for a trirutile structure).

Doe *et al*. have suggested that $Li_{1/4}FeF_3$ and $Li_{1/2}FeF_3$ (with average Fe oxidation states of 2.75 and 2.5, respectively) exist as stable phases on reduction of FeF_3.[25] These phases are derived from the rutile structure (see Fig. 6.1 for the trirutile $Li_{1/2}FeF_3$), by ordering Li and Fe on the metal site. Our NMR does not provide any clear evidence for $Li_{1/4}FeF_3$ but do suggest that a phase with a composition close to $Li_{1/2}FeF_3$ does exist. The crystallinity of the XRD data is to poor to determine whether any Li/Fe ordering occurs in this phase. Doe *et al*. then suggest that further lithiation can occur, particularly in the nanocomposites to form phases $Li_{1/2-x}Fe_{1+x}F_3$ (for example, $Li_{1/4}Fe_{5/4}F_3$; Fe oxidation state = 2.2). These structures are derived from the trirutile, the Fe replacing Li in the metal sites of the structure, eventually forming FeF_2. This can occur via the following reaction:

$$Li_{1/2}FeF_3 + 3x/(2+2x)Li \rightarrow (1/1+x)Li_{1/2-x}Fe_{1+x}F_3 + (3x/1+x)\ LiF\ (x \leq 0.5) \quad (4)$$

So-called 1x1 tunnels are observed along the c-direction of the rutile and triretile structure (Fig 6.1c and d), and a second mechanism, by analogy with rutile, TiO_2, and nano-particles of β-MnO_2, which have both been shown to accommodate Li, by intercalation in their 1x1 tunnels, is also possible:

$$Li_{1/2}FeF_3 + x\ Li \rightarrow Li_x[Li_{1/2}Fe]F_3 \qquad (x \leq 0.5) \qquad (5)$$

The distance between Fe-Fe tri-rutile structure (4.75Å) is even larger than the Ti-Ti distance (4.59 Å) of rutile, suggesting it is feasible. Neither mechanism involves the precipitation of Fe, consistent with the voltage profile until Li0.75. Distinct from the 2nd mechanism, the 1st involves the diffusion of Fe ions into the material and the formation of LiF. Some LiF is observed by XRD, suggesting that the 1st mechanism may be occurring; however, the LiF concentration is not large as it is not clearly seen by ^{19}F in this range. It is also possible that (5) occurs during the electrochemical reaction because it may be kinetically favored, but that the lithiated phase can then react while the battery relaxes to precipitate out LiF and form the products given by equation (4). The electrochemical profiles suggest that different mechanisms are in operation (or dominate) between Li0.5 and 0.75 and between Li0.75 and 1.0. The NMR resonances shift in the 1st range but remain constant in the later range. This together with the noticeable drop in potential may indicate that some Fe^0 is already starting to form after Li0.75.

Reflections from LiF and Fe are observed, along with a number of unindexed peaks, in the second region (i.e., between Li=1.0 and 3.0). The $^{6,7}Li$ and ^{19}F NMR signals broaden noticeably, also indicating the formation of superparamagnetic particles of α-Fe. The resonance due to the insertion phase shifts between Li = 1.0 and 1.7, decreasing in intensity, and then has essentially disappeared at Li = 3.0, indicating that the Li_xFeF_3 phase decomposes during this range. However, the shift of the Li resonance suggests that this decomposition process involves intermediate phase(s), with a lower Fe oxidation state (presumably close to 2+). Furthermore, this confirms that even at Li1.0, the average Fe oxidation state of the Li_xFeF_3 intercalation phase must still above 2+, consistent with the suggestion that Fe^0 formation occurs from Li > 0.75.

The presence of sharp LiF reflections in the Li1.7 sample which have disappeared for Li3.0, and the lack of significant reflections due to α-Fe are quite striking. We suggest that these LiF reflections may arise from LiF formed during a conversion reaction of the form given in equation (4), while the decomposition of the $Li_{1/2-x}Fe_{1+x}F_3$ phase results in much smaller (and/or disordered) LiF (and α-Fe) particles, so that only broad XRD reflections are observed for these phases. The PDF data suggests that the rutile phase is still present in this range, while other broad reflections are also observed, indicating that other unidentified lithium iron fluoride phase may be present in this range, including Fe^{2+} doped LiF derived phases, or possibly the inverse spinel phase $Li_{3/2}Fe_{3/4}F_3$ proposed by Doe *et al*..[10]

6.4.2. Charge reaction mechanism

During the CCN-FeF_3 charge process, the steady decrease of the reflections due to α-Fe indicates that a reconversion reaction is taking place. The particle sizes of the reconverted products must be small, because the reflections due to the reconverted phases are extremely broad, preventing identification of the products. However, a series of weak reflections are observed in the fully charged sample (C_Li0.5) at a similar position to those of the discharged sample Li0.5 (Fig.6.15). The observation of ^{6}Li resonances in the charged samples shifting from 80 ppm for Li = 2.0 to around 168 ppm at Li = 0.5 indicate that the conversion products contain Li. The similar shift of the fully charged sample, and the Li0.5 sample formed on discharge, indicate that the Li environments and Fe oxidation states are similar. This suggests that the rutile structure is again reformed on

charging, consistent with the PDF pattern of this material. On charge, only 2.5 lithium can be extracted from the material, and the observation of the Li signal suggests that the reconversion reaction is not totally reversible. The charge process can be described as follows:

$$Fe + 3LiF \rightarrow (1/1+x)\ Li_{1/2-x}Fe_{1+x}F_3 + 3x/(1+x)\ LiF \qquad (6)$$

6.4.3 Comparison with FeF_2

The Li NMR clearly shows that FeF_2 system conversion involves Li insertion. This cannot occur via a simple insertion of Li into the 1x1 tunnels of the structure since Fe^{2+} reduction to Fe^{1+} is not likely. Thus the reaction must formally involve some Fe^{2+} disproportionation to Fe^0 and Fe^{3+}, and then reduction of the Fe^{3+} along with Li insertion. Based on the ^{6}Li NMR data of CCN-FeF_3, the peaks at 172 and 87 ppm in the ^{6}Li-NMR spectra of CCN-FeF_2 correspond to Li nearby Fe with an average oxidation state of approximately 2.5+ and 2+. Disproportionation will result in the extrusion of Fe out of the FeF_2 structure. Thus, this mechanism is not a strict insertion reaction, and the discharge mechanism for FeF_2 at the early stages (until Li=0.5) can be written as formally as follows:

$$FeF_2 + Li \rightarrow 2/3\ FeF_3 + 1/3\ Fe \qquad (7)$$

$$2/3\ FeF_3 + 1/3\ Li \rightarrow 2/3\ Li_{1/2}FeF_3 \qquad (8)$$

involving a combination of an insertion reaction and conversion reaction. This reaction will compete with the simple conversion reaction:

$$FeF_2 + Li \rightarrow LiF + Fe \qquad (9)$$

At the beginning of discharge, the disproportionation/insertion reaction competes with the simple conversion reaction, and on the basis of the intensity of the Li resonance at around 172 ppm in the Li=0.25 sample, occurs in preference to the conversion reaction. As the discharge process proceeds, more and more FeF_2 is involved in the direct conversion reaction, and the insertion phase decomposes to form LiF and Fe, resulting in a decrease in intensity of the 172 ppm peak in the Li=0.5 sample.

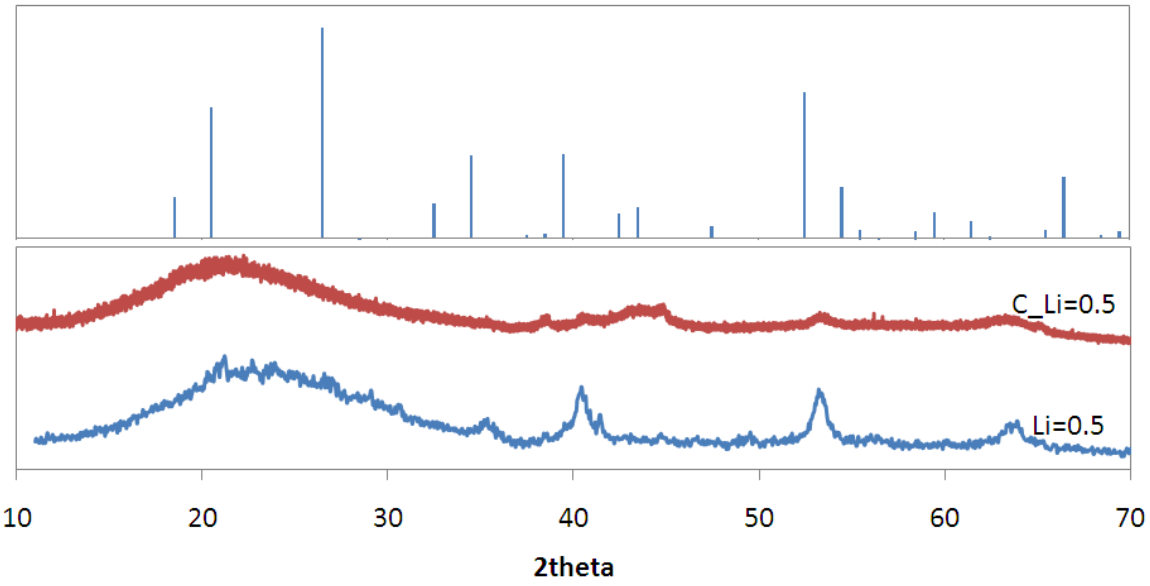

Figure 6.15: The comparison of XRD patterns between discharged CCN-FeF_3 with Li=0.5, a charged sample with Li=0.5 and the simulated tri-rutile pattern suggested by Doe *et al*. Space group P 4_2/mnm was used for the simulation with cell parameters a=4.756 and c=9.339 Å.

6.4.4. Proposed phase transition

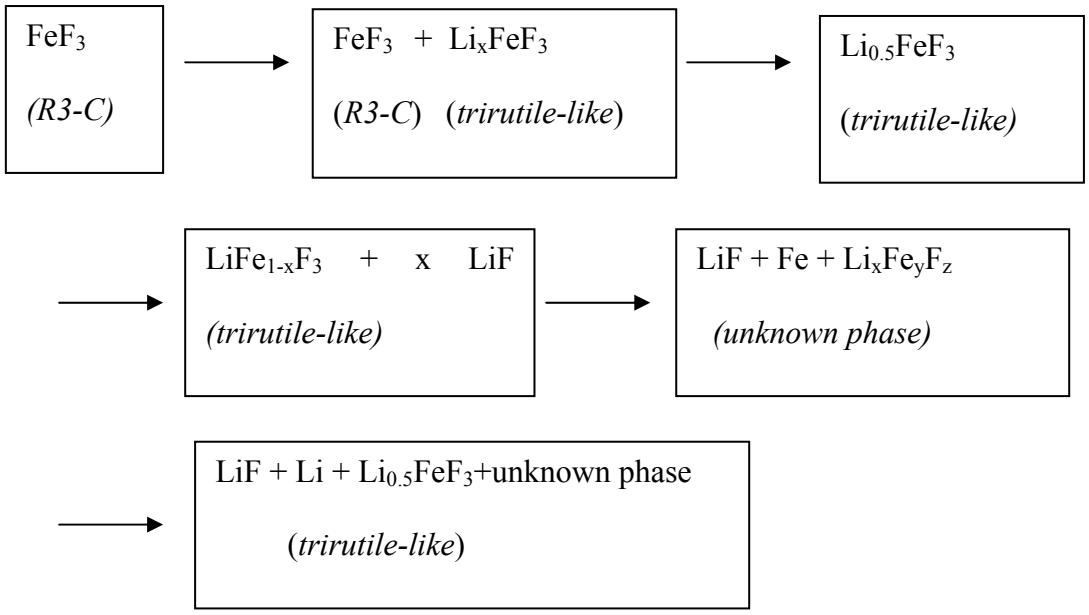

6.5. Conclusions

The reaction mechanisms of CCN-FeF_3 during both charge and discharge have been investigated by using a combination solid state NMR, XRD and PDF. In particular, NMR and PDF studies are sensitive to local structural changes that occur in these poorly crystalline materials. The results provide compelling evidence for the structural transformation of the FeF_3 phase from a ReO_3 to a lithiated rutile structure, with a Fe oxidation state of close to 2.5 and a composition close to $LiFe_2F_3$ on the 1st discharge, as suggested by Doe et al..[25] This material can accommodate more lithium by reducing the Fe to 2.0+ and extruding LiF from the matrix. Some intercalation of Li into the tunnels of the rutile phase is also possible. The lithiated phase then decomposes to form nanoparticles of LiF and α-Fe, along with other, as yet unidentified lithium iron fluoride phases. Both the NMR and PDF data show that the reconversion reaction occurs via the reformation of a lithiated rutile phase, the lithium incorporation and iron oxidation state increasing with state of charge. The final material, at least in our room temperature studies has a composition close to $Li_{0.5}FeF_3$ consistent with the capacity estimated from the electrochemical curve. The results were compared with those for the rutile FeF_2, which was also lithiated on reduction; the mechanism by which this occurs is similar to one mechanism for the reduction of $LiFe_2F_3$; reaction of FeF_2 with Li resulting in disproportionation to form 2 $Fe_{1-x}F_2$ (or $Fe_{3/2-x}F_3$) + xFe. The $Fe_{1-x}F_2$ can then react with Li to form $Li_xFe_{1-x}F_2$.

Although transition metal compounds are one of the promising next generation electrode materials with much higher capacity compared to many current materials, the

work highlights the complexity of this system, which involves the formation of nano-sized particles, and the formation of a series of intermediate phases. To achieve the good performance from these materials and control the reaction, further fundamental studies are required to understand more clearly the processes with these different phases react so as to optimize the reversibility and rate performance of this system.

6.6 References

1. Tarascon, J. M.; Armand, M., *Nature* **2001,** 414, (6861), 359-367.

2. Mizushima, K.; Jones, P. C.; Wiseman, P. J.; Goodenough, J. B., *Materials Research Bulletin* **1980,** 15, (6), 783-789.

3. Poizot, P.; Laruelle, S.; Grugeon, S.; Dupont, L.; Tarascon, J. M., *Nature* **2000,** 407, (6803), 496-499.

4. Li, H.; Richter, G.; Maier, J., *Advanced Materials* **2003,** 15, (9), 736-739.

5. Li, H.; Balaya, P.; Maier, J., *Journal of the Electrochemical Society* **2004,** 151, (11), A1878-A1885.

6. Badway, F.; Cosandey, F.; Pereira, N.; Amatucci, G. G., *Journal of the Electrochemical Society* **2003,** 150, (10), A1318-A1327.

7. Badway, F.; Pereira, N.; Cosandey, F.; Amatucci, G. G., *Journal of the Electrochemical Society* **2003,** 150, (9), A1209-A1218.

8. H. Arai, S. O., Y. Sakurai, J. Yamaki, *Journal of Power Sources* **1997,** 68.

9. Cosandey, F.; Al-Sharab, J. F.; Badway, F.; Amatucci, G. G.; Stadelmann, P., *Microscopy and Microanalysis* **2007,** 13, (2), 87-95.

10. Roert E. Doe, K. A. P., Y. Shirley Meng, Gerbrand Ceder, *in preparation* **2008**.

11. Grey, C. P.; Dupre, N., *Chemical Reviews* **2004,** 104, (10), 4493-4512.

12. Breger, J.; Dupre, N.; Chupas, P. J.; Lee, P. L.; Proffen, T.; Parise, J. B.; Grey, C. P., *Journal of the American Chemical Society* **2005,** 127, (20), 7529-7537.

13. Lee, P. L.; Shu, D. M.; Ramanathan, M.; Preissner, C.; Wang, J.; Beno, M. A.; Von Dreele, R. B.; Ribaud, L.; Kurtz, C.; Antao, S. M.; Jiao, X.; Toby, B. H., *Journal of Synchrotron Radiation* **2008,** 15, 427-432.

14. Lee, Y. J.; Grey, C. P., *Journal of Physical Chemistry B* **2002,** 106, (14), 3576-3582.

15. Chupas, P. J.; Qiu, X. Y.; Hanson, J. C.; Lee, P. L.; Grey, C. P.; Billinge, S. J. L., *Journal of Applied Crystallography* **2003,** 36, 1342-1347.

16. Hinedi, Z. R.; Chang, A. C.; Borchardt, D. B., *Water Research* **1997,** 31, (4), 877-883.

17. West, A. R., *Solid State Chemistry and it's Application*. John Wiley & Son: New York: 1992.

18. Kim, J.; Nielsen, U. G.; Grey, C. P., *Journal of the American Chemical Society* **2008,** 130, (4), 1285-1295.

19. Nielsen, U. G.; Paik, Y.; Julmis, K.; Schoonen, M. A. A.; Reeder, R. J.; Grey, C. P., *Journal of Physical Chemistry B* **2005,** 109, (39), 18310-18315.

20. Liao, P.; MacDonald, B. L.; Dunlap, R. A.; Dahn, J. R., *Chemistry of Materials* **2008,** 20, (2), 454-461.

21. Meyer, B. M.; Leifer, N.; Sakamoto, S.; Greenbaum, S. G.; Grey, C. P., *Electrochemical and Solid State Letters* **2005,** 8, (3), A145-A148.

22. Plakhotnyk, A. V.; Ernst, L.; Schmutzler, R., *Journal of Fluorine Chemistry* **2005,** 126, (1), 27-31.

23. Shachar, G.; Shaked, H.; Makovsky, J., *Physical Review B* **1972,** 6, (5), 1968-&.

24. Breger, J.; Kang, K.; Cabana, J.; Ceder, G.; Grey, C. P., *Journal of Materials Chemistry* **2007,** 17, (30), 3167-3174.

25. Roert E. Doe, K. A. P., Y. Shirley Meng, Gerbrand Ceder, *in preparation* **2008**.

Chapter 7

An Investigation of the Conversion Reaction Mechanisms for Cu compounds by Using Solid State NMR Spectroscopy

Abstract

The conversion reaction mechanisms of CuS, CuF_2 and CuO during electrochemical process are studied by solid state ^{63}Cu, ^{19}F, ^{7}Li Nuclear Magnetic Resonance (NMR) and X-ray Diffraction (XRD). For CuS, a two-step reaction is observed, which is associated with an insertion reaction and followed by a conversion reaction. The evidence for an insertion phase is found from both the NMR spectra and XRD patterns. A direct conversion reaction is found for CuF_2. From the ^{7}Li NMR results, an insertion phase is observed in a discharged CuO sample. An insertion mechanism is also confirmed for CuO at the beginning of discharge. The correlation between the cycliablity, crystal size and interaction between Cu metal and Li compounds produced in the conversion reaction is discussed. Our Rotational-Echo Adiabatic-Passage DOuble-Resonance (REAPDOR) results show the interaction between Cu metal and Li compounds is in the order of CuS > CuO > CuF_2, which happens to be the same order of the cycliability of these three compounds.

7.1 Introduction

Graphite and carbonaceous materials represent commercial anode materials with a specific capacity of ~372 mAh/g[1, 2]. These materials operate by reversible intercalation of Li between the carbon layers. A significant advance in the field came with the discovery of materials that operate in a conversion mechanism, which was firstly demonstrated by Y. Idota *et al*. in 1997 where a tin-based amorphous oxide was used as the anode material in a Li ion battery. The reaction mechanism relies on the formation of metal particle surrounded by oxide.[3-5].

3d-transition metal compounds M_xX_y (M= Co, Fe, Ni, Cu etc.) (X=F, O, S, N etc.) have now been investigated for their potential application in lithium batteries because of their high capacities. Since the various compounds have different voltage windows, they can have potential applications as both cathodes and anodes. The work presented in this chapter uses solid state Magic Angle Spinning (MAS) Nuclear Magnetic Resonance (NMR) to study the conversion/reconversion reaction mechanisms, with supporting evidence from high resolution X-ray Diffraction (XRD). In this study, the Cu compounds CuF_2, CuS and CuO are chosen as model compounds, since their magnetic properties make them more amenable to NMR studies than many other transition metals: transition metal particles are generated in the conversion reaction, and unlike other metals such as cobalt, iron and nickel, copper metal is not ferromagnetic.

Of the copper compounds, CuF_2 is a very attractive cathode material because it has a high theoretical potential of 3.55 V based on thermodynamic calculations[6, 7] and a specific capacity of 528 mAh/g. However, no one has yet demonstrated the full

utilization of this compound at an appropriate voltage in part due to the hydrated impurities often found together with this phase and problems due to Cu dissolution. In addition, like all the other fluorides, CuF_2 is an insulator. To overcome the last problem, Badway *et al*. have proposed the use of mixed conductive matrix (MCM) and demonstrated a full utilization of this material by using carbon and/or a conducting oxides such as MoO_3 etc..[8]. The drastic reduction of particle size shorten the tunneling lengths for electrons, and increase the interface for the interaction with Li. The highly conductive materials connected each nano-grain, which enhanced the electrochemical activities dramatically.

CuS is a also promising cathode material for use in a low voltage battery system, due to its high specific capacity of 561 mAh/g and good electronic conductivity of 10^{-3} Scm^{-1}[9-11]. There are two plateau in the CuS discharge profile, one at 2.05V and the other one at 1.68V. The following reactions have been proposed by Chung *et al*. [12]:

$$CuS + xLi^+ + xe^- \rightarrow Li_xCuS \text{ (First plateau)} \quad (1)$$

$$1.96Li_xCuS + (2\text{-}1.96x)\ Li^+ + (2\text{-}1.96x)\ e^- \rightarrow Li_2S + Cu_{1.96}S \quad (2)$$

$$Cu_{1.96}S + 2Li^+ + 2e^- \rightarrow Li_2S + 1.96\ Cu \text{ (Second plateau)} \quad (3)$$

The first plateau comprises an insertion reaction, the product of the insertion reaction Li_xCuS then reacting with more Li to generate $Cu_{1.96}S$ and Li_2S during this process. Subsequently, on the second plateau, $Cu_{1.96}S$ is converted to Li_2S and copper metal. However, Tarascon *et al* reported different mechanism in 2006. [13]. They proposed that Cu_2S forms as an intermediate phase which then transforms into Cu and Li_2S, as described as follows:

$$CuS + e^- + Li^+ \rightarrow \tfrac{1}{2}\ Cu_2S + \tfrac{1}{2}\ Li_2S \quad (4)$$

$$\tfrac{1}{2}\,Cu_2S + e^- + Li^+ \rightarrow \tfrac{1}{2}\,Li_2S + Cu \qquad (5)$$

The final material CuO has a specific capacity of 674 mAh/g and several discharge reaction mechanisms have been also proposed by X-ray analysis for this material.[14-17].

In this paper, these three Cu compounds with three different anions (F^-, S^{2-} and O^{2-}) are chosen as model compounds. The redox reaction mechanisms are investigated for the three Cu compounds by solid state NMR and X-ray Diffraction (XRD), and their electrochemical performance and reaction mechanism are discussed and compared.

7.2. Experimental

7.2.1 Materials preparation

Commercial CuS (Kojundo) and CuO (Kanto) were used in this study without further treatment. For CuF_2, carbon coated nano-CuF_2 (CCN-CuF_2) was prepared by high energy ball milling of CuF_2 (Kojundo) with carbon black (Ketjen Black International Company). Stoichiometric mixtures (CuF_2: Carbon Black = 80 wt% : 20 wt%) were placed inside a steel milling cell (Rotec) with zirconium balls. The milling was performed for 3h with 500rpm.

7.2.2 Electrochemical characterization

The cathodes were prepared by mixing 80 wt % of CuS, CuO or CCN-CuF_2, 15 wt % of graphite as an electronic conductor, and 5 wt % of polyvinylidene fluoride (PVDF) as a binder in N-methylpyrrolidinone. The slurry was coated on aluminum foil and dried at 100 °C until the solvent had evaporated completely. Coin type (2032) cells were assembled in an argon-filled glove box with Li metal foil (Aldrich) as the anode, polypropylene separators (Celgard) and 1 M solution of $LiPF_6$ in EC (ethylene carbonate) : DMC (dimethyl carbonate) =1:1 as the electrolyte. Swagelok type cells were also assembled with a mixture of 85 wt% of CuS, CuO or CCN-CuF_2 and 15wt% of carbon black as the cathode and Whatman GF/D fiber as separator. The other components are the same as used in the coin cells. Electrochemical experiments were carried out on a battery cycler (Arbin Instruments, College Station, Texas) in galvanostatic mode at a

C/35 rate, between 1.0 and 3.0V. The Li content in each cycled sample is calculated from the capacity, assuming 100% columbic efficiency.

7.2.3 X-ray Diffraction

X-ray diffraction (XRD) was used to confirm the structure of the CCN-CuF_2 and study the phase transition that occurs during electrochemistry process. Laboratory XRD was performed on a Rigaku powder X-ray diffractometer equipped with a Cr target X-ray tube (Cr Kα_1:λ=2.2898 Å). A range of 2θ values from 20 to 120°, with a scanning rate of 1° per minute and a step size of 0.02° 2θ were used. High resolution (HR)-XRD was carried out at the 11-BM beam line at the Advanced Photon Source (APS) in Argonne National Laboratory (λ=0.4001 Å)[18, 19], and at the X16C beam line at National Synchrotron Light Source (NSLS) in Brookhaven National Laboratory (λ=0.6881Å). Ex situ XRD was accomplished by disassembling the Swagelok type cells in an argon-filled glove box after batteries had been cycled to the desired voltages. If it is not specified, the XRD data shown in this paper were collected at 11-BM beam line at the APS.

7.2.4 MAS NMR spectroscopy

^{7}Li MAS NMR spectroscopy was performed on cycled CuS, CuO and CCN-CuF_2 samples with a 1.8 mm probe on a CMX-200 spectrometer using a magnetic field of 4.7 T. A spinning frequency of 38 kHz and a rotor-synchronized spin-echo sequence (90–τ–180–τ–acq) were used to acquire the spectra. The spectrum was collected at an operating frequency of 77.10 MHz. π/2 pulses of 2.5 μs were used, with a delay time of 1.0 s. The

spectrum was referenced to 1 M ^{7}LiCl (in H_2O) at 0 ppm. For better resolution, ^{7}Li NMR spectra of cycled CuS samples were also acquired on a Varian InfinityPlus-360 spectrometer equipped with a 4 mm HXY probe with a pulse width 3.25 μs and pulse delay 10 s at a 10kHz spinning speed. The same chemical shift reference as above was used.

^{19}F MAS NMR spectroscopy was performed on discharged CCN-CuF_2 samples with a 3.2 mm probe on a CMX-360 spectrometer using a magnetic field of 8.46 T. The spectrum was collected at an operating frequency of 338.73 MHz. A spinning speed of 20 kHz and a rotor-synchronized spin-echo sequence (90–τ–180–τ–acq) were used to acquire the spectra. A π/2 pulse of 5.75 μs was used, with a delay time of 1.0 s. The spectrum was referenced to fluorobenzene (MFB) at -113.8 ppm.[20].

^{63}Cu MAS NMR spectroscopy was performed with a 4mm HXY probe on a Varian InfinityPlus-360 spectrometer using a magnetic field of 8.46T and on a Chemagnetics200 spectrometer using a magnetic field of 4.7 T. The spectrum was collected at an operating frequency of 95.53 MHz at 8.46 T and 53.07 MHz at 4.7 T. A spinning speed of 10 kHz and a rotor-synchronized spin-echo sequence (π/2–τ– π–τ–acq) were used to acquire the spectra. π/2 pulses of 5.0 μs in 8.46T and 3.25 μs in 4.7T were used, with a delay time of 1.0 s. The static ^{63}Cu NMR spectrum were performed on a static probe with silver coil on a Chemagnetics200 spectrometer. A one pulse sequence with a π/2 of 2.0 μs was used with a delay time of 1.0 s. The spectra were referenced to solid CuCl at -319 ppm.[21].

The REAPDOR experiment was performed on a Varian InfinityPlus-360 spectrometer in a magnetic field of 8.46T at an operating at the frequency of 138.78 MHz for Li and 95.53 MHz for Cu. Li was used as the observe nucleus.[22]

7.3. Results

7.3.1 Pristine CCN-CuF_2 characterization

To examine the effect of ball-milling, X-ray diffraction was performed on the CCN-CuF_2 sample (Fig. 7.1). After the milling treatment, significant broadening of the Bragg peaks was observed. The crystalline size, as determined by the Scherrer formula[23] by using the (011) Bragg peak for CCN-CuF_2, was ~16 nm. No extra peaks are observed, indicating no impurities are introduced during milling and that the structure remains unchanged.

7.3.2 Electrochemical characterization

The electrochemical performances of CCN-CuF_2, CuS and CuO were investigated in a voltage window between 3.0 and 1.0V (Li/Li^+) at room temperature at a C/35 rate (Fig.7.2 (a)-(c)). The discharge profile of CCN-CuF_2 shows a plateau at 3.0V until Li=1.0 and then the voltage drops slowly reaching approximately 1.0V at Li=2.1. A specific capacity of 566mAh/g is achieved on discharge, which is slightly above the theoretical capacity of 528mAh/g. This is due to the SEI formation and electrolyte decomposition at low voltage and the onset of the reaction with carbon. Unfortunately, negligible capacity is observed on charge.

The discharge profile of CuS shows two plateaus, one at 2.05V and the other one at 1.68V, although a closer examination of the 1st "plateau" suggests that the behavior may be more complex. The capacity from the first and the second plateau (including the

voltage drop at the end) are 240mAh/g and 231mAh/g, which correspond to Li0.85 and Li0.82, respectively. A total capacity of 471mAh/g (Li1.7) was obtained during discharge which is 85% of the theoretical capacity of 561 mAh/g. On charge, the curve shows quite different features from those seen on discharge. The charge capacity is 377 mAh/g, which corresponds to 79% of the discharge capacity and 100 mAh/g (Li0.35) is not recovered.

In CuO system, the voltage decrease gradually until Li=0.3 and then a plateau is seen at 1.35V. The specific capacity is 600mAh/g for discharge, which is 90% of the theoretical capacity (674mAh/g). However, only 1/3 of this capacity (200mAh/g) was obtained on charge.

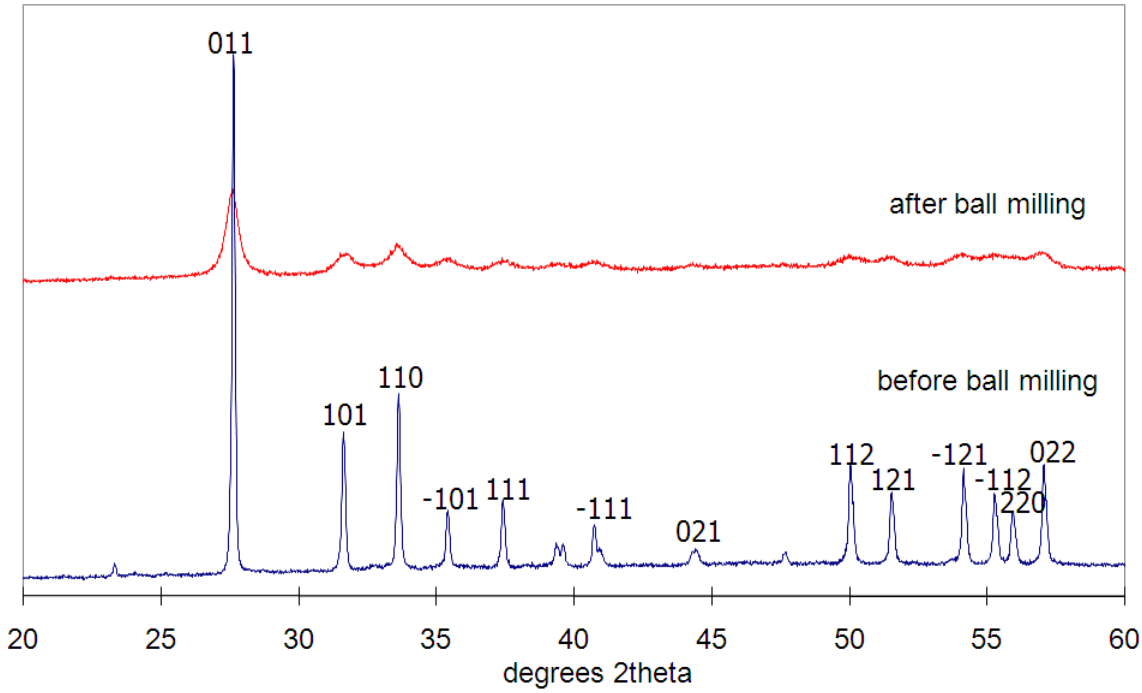

Figure 7.1: XRD pattern of CCN-CuF_2 prepared by high energy ball milling. The peaks are indexed with a P21/c space group.

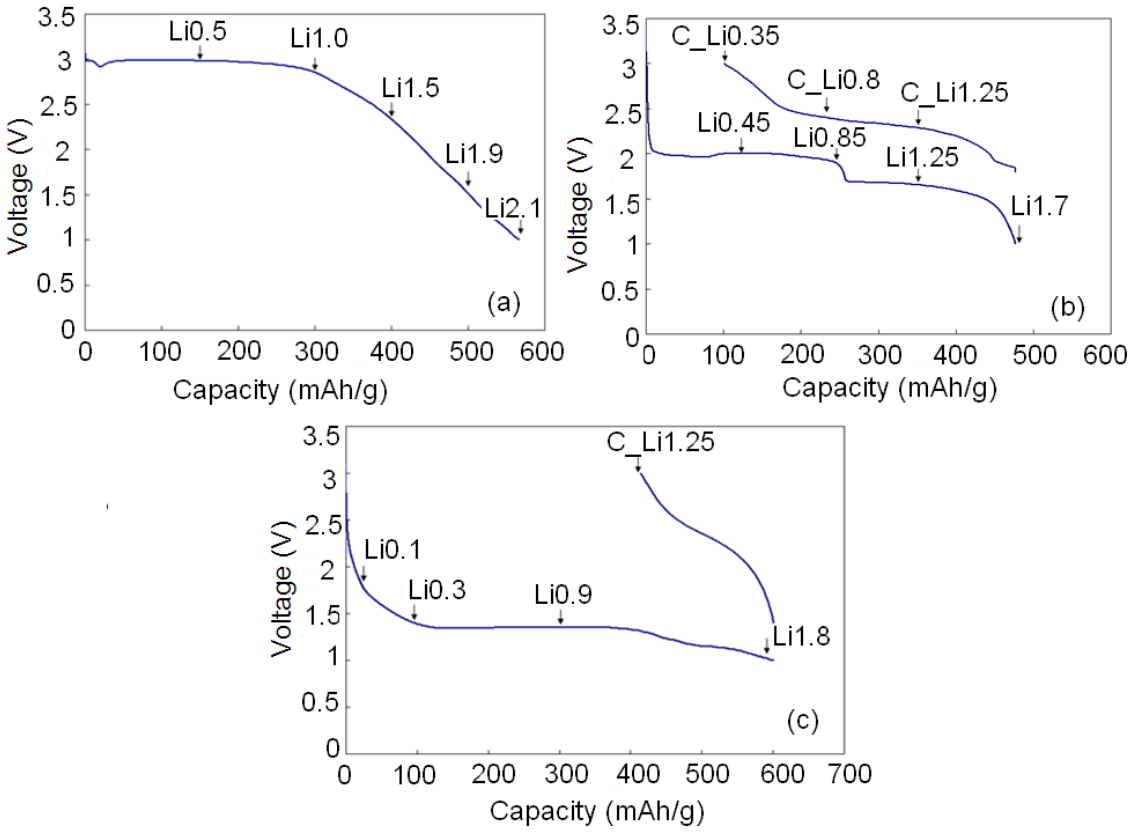

Figure 7.2: The Electrochemical curve of CCN-CuF_2 (a), CuS (b), CuO (c) cycled at room temperature at C/35. The different samples prepared as part of this study are indicated with arrows.

7.3.3 Investigation of discharge and charge reaction process

7.3.3.1 High resolution XRD

In order to investigate the phase transitions that accompany to electrochemical process, high resolution X-ray diffraction was performed on a series of cycled materials. The XRD patterns of the discharged CuF_2 samples are displayed in Fig 3. In the sample of Li0.5, the main peaks from CuF_2 are still present, but now reflections from Cu metal are also clearly observed. Peaks from LiF are not clearly visible, which may be due to small particle sizes and low concentration. In the Li1.5 sample, the reflections from Cu metal and LiF start to become more pronounced. At this point, very little CuF_2 appears to be present in the sample; the loss of CuF_2 reflections may also arise from a reduction in CuF_2 particle size during discharge which can broaden the peaks beyond detection. The three peaks marked with asterisks are from Cu_2O which is likely due to the contamination of the sample when it was kept in the kapton capillary for the XRD measurement. At the end of discharge, only the reflections from Cu metal and LiF can be observed.

Fig.7.4 shows the XRD patterns of the CuS samples as a function of state of discharge. The pattern of the pristine CuS compound (Li0) shows that it is phase pure, and all the reflections can be assigned to a $P\,6_3\,/mmc$ space group. From Li0.25 to Li0.85, i.e. during the first "plateau" on the electrochemical curve, all the XRD patterns of these samples are quantitatively similar to that of the pristine compound, and only a few changes are observed. As shown in Fig. 7.5a, the CuS (002) peak at 10.7°, 2θ stays at the same position in all the samples from Li0 to Li0.85, but it broadens noticeably on lithiation, its intensity getting smaller with higher Li content and becoming totally

invisible for the Li0.85 sample, indicating that the ratio of CuS phase in these samples decreases on discharge. The noticeable peak broadening in these discharged samples indicate particle crushing during this process. An additional peak near 46.3°, which is not observed in the pristine compound, starts to appear in the Li0.45 sample, and gets more intense and more well resolved from the (107) peak in the Li0.85 sample. Fig.7.5b clearly shows that the peaks stay at the same position in all the discharged samples, but they are shifted noticeably in comparison to the pristine CuS. Including the new peak at 46.3°, all the shifted peaks are also believed to belong to the new phase, which has lots of similarity in structure with CuS phase. This indicates that the insertion reaction on the first plateau is not only a simple single phase reaction as proposed previously, but it includes the formation of a new phase. No reflections from Cu metal and Li_2S are observed until Li=0.85.

The sample Li1.25 is in the middle of the second plateau, and its XRD pattern shows a mixture of several different phases. Reflection from Cu metal and Li_2S are clearly observed. The peaks at 30° and 47° 2θ are reflections from the Li0.85 phase. At the end of the discharge Li1.7, the XRD pattern is very complicated. In addition to the peaks from Cu metal and Li_2S, a series of reflection peaks from $Cu_{1.96}S$ are also observed.

Fig.7.6 shows the XRD patterns of the charged CuS samples. Once Li is extracted from the Li1.7 sample (fully discharged state), the XRD patterns show quite different features. The reflections from Cu and Li_2S are not obvious in the pattern of C_Li1.25 and all the other reflections are at similar positions to those seen in the other two charged samples C_Li0.8 and C_Li0.35 except the peaks at around 32° 2θ which seem to correspond to the reflections from the $Cu_{1.96}S$ phase that remain in the C_Li1.25 sample.

Interestingly, the pattern is closer to the discharged sample Li0.85 than that of the pristine CuS (sample Li0), although most of the peaks in this pattern can also be observed in the pristine CuS sample. From sample Li1.7 to C_Li0.45, all the peaks are gradually shifted in the same direction to lower angle. This behavior is usually associated with solid solution reaction.

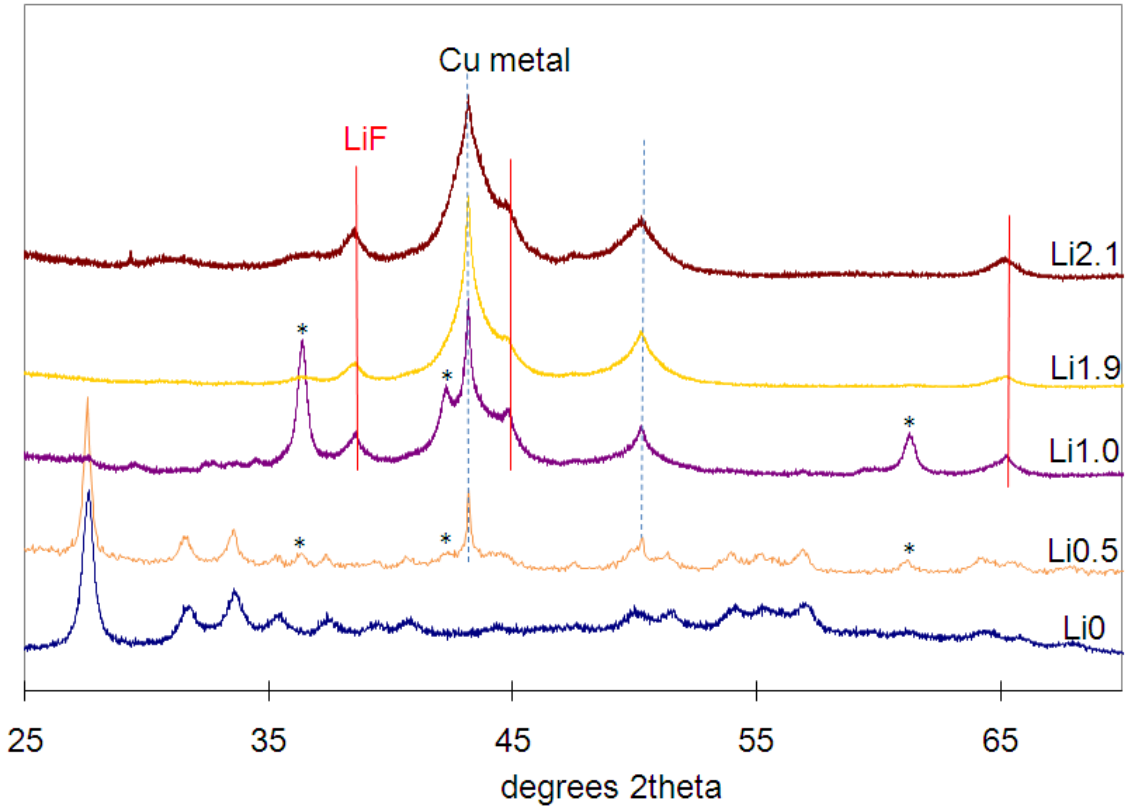

Figure 7.3: The XRD pattern of discharged CCN_CuF_2 samples. The Li content (Lix) in each sample is calculated from the discharge capacity in this and subsequent figures. The reflections from LiF and Cu metal are marked with dashed lines and solid lines, respectively. The peaks marked with asterisks are from Cu_2O.

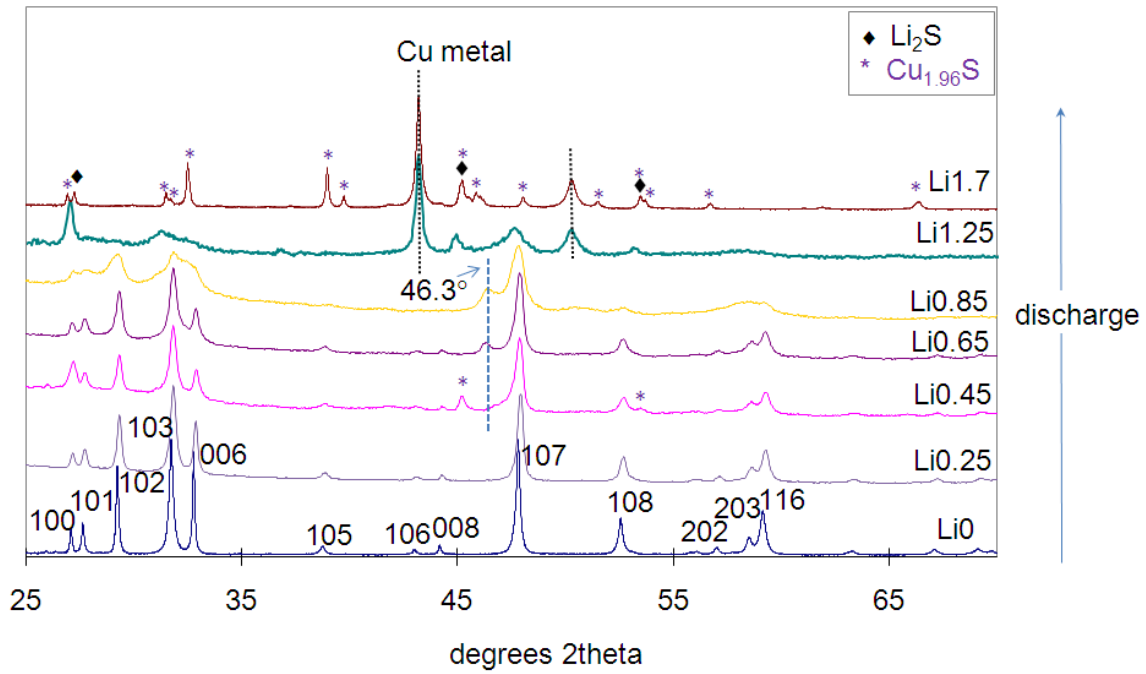

Figure 7.4: The XRD pattern of the discharged CuS samples. The peaks from Cu metal are labeled with dashed lines, and Li_2S and $Cu_{1.96}S$ is labeled with ♦ and *, respectively. The sample Li1.25 was measured at X16C at the NSLS, and all the other samples were measured at 11-BM beamline at the APS.

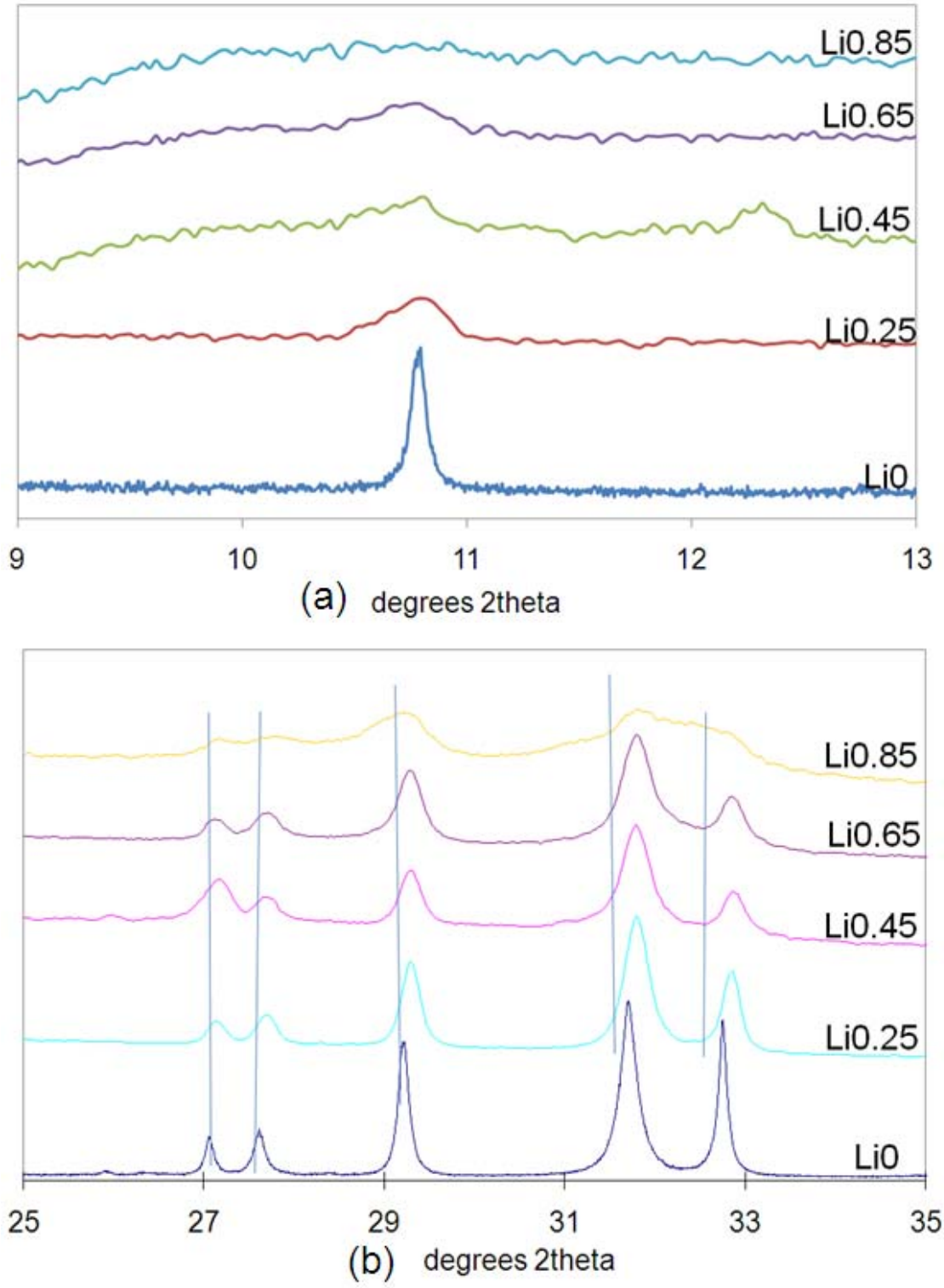

Figure 7.5: An enlargement of the XRD patterns for discharged CuS for Li=0 to 0.85 (on the first plateau) between 9 and 13°, 2θ (a) and between 25 and 35° (b).

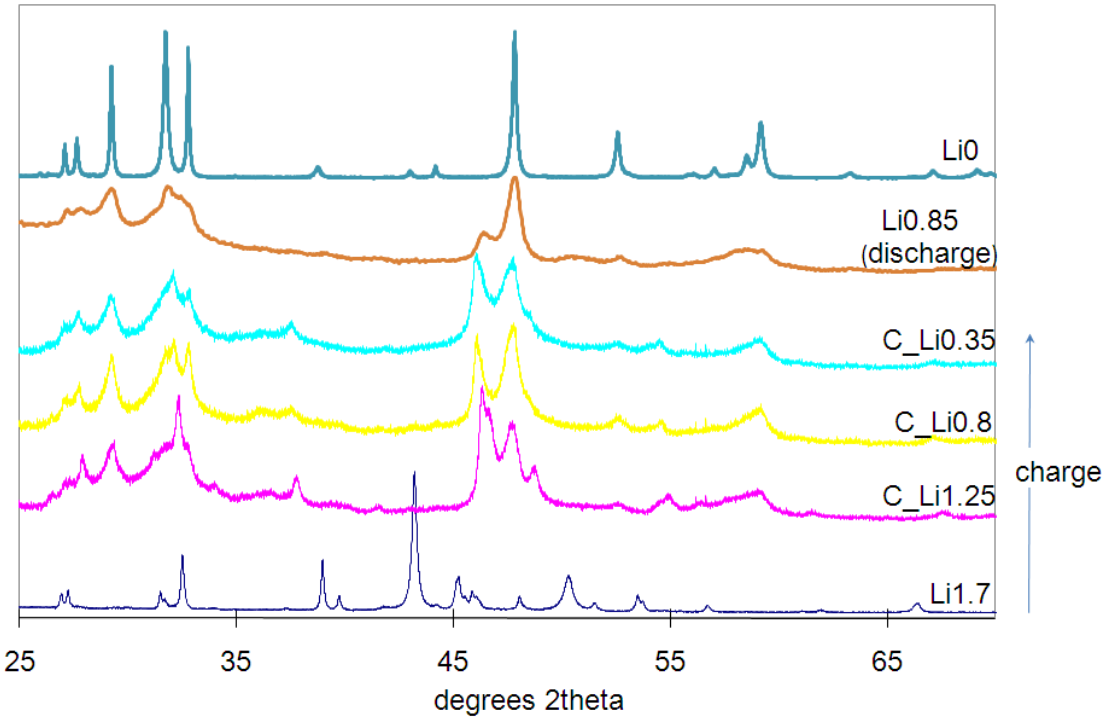

Figure 7.6: The XRD pattern of charged CuS samples. The "C" in the labels means the samples were extracted during the charge. The patterns are compared with pristine CuS compound and the discharged sample with 0.85 Li.

7.3.3.2 MAS-NMR

7.3.3.2.1 CCN-CuF_2

In order to study the local structural changes that occur during the discharge process, a series of discharged CCN-CuF_2 samples, stopped at different voltages, were investigated by ^{7}Li, ^{19}F and ^{63}Cu NMR. Fig. 7.7 shows the ^{7}Li NMR spectra of discharged CCN-CuF_2 samples between Li=0.5 and Li=2.1. In the spectra, one isotropic resonance is observed at -3.0 ppm whose peak intensity increases gradually with state of discharge. This small chemical shift is a signature of diamagnetic material (ex. Li_2O, LiF etc.), and in this case, the increase of the peak at -3.0 ppm can be assigned to the formation of LiF and salts in the SEI layer.

^{19}F NMR was performed in order to distinguish between LiF and fluorinated components in the SEI layer. The spectra of the discharged CCN-CuF_2 samples are shown in Fig.7.8. Since Cu^{2+} is paramagnetic and F is directly bound to Cu, the ^{19}F signal in pristine CCN-CuF_2 can not be observed. In the spectra of pristine CCN-CuF_2 (Li0), an isotropic resonance at -90 ppm is observed, which is due to the fluorine background in the probe. In the sample Li0.5, except the peak around -90 ppm, two more isotropic resonances at around -205 and -85 ppm appear, which are assigned to LiF and SEI component (eg. $LiP_xO_yF_z$)[24], respectively. The intensity of these two peaks increases with state of discharge. This indicates that LiF is formed at the beginning of discharge, although the reflections of LiF in the XRD pattern of sample Li0.5 are not obvious (Fig. 7.3). In the spectra of the sample Li2.1, the peak at -85ppm is much more pronounced than that in the sample Li1.0, which suggests that the SEI formation is significant at the

end of discharge. The signals from PVDF (-90 ppm) and $LiPF_6$ (-70 ppm) overlap with the background signal.

To study the local environment of Cu and formation of Cu metal during electrochemical process, ^{63}Cu- NMR was performed on the discharged CCN_CuF_2 samples. The ^{63}Cu and ^{65}Cu isotopes both have spin I = 3/2 with natural abundances of 69.09 % and 30.91 % respectively and have large quadrupole moments. Although the gyromagnetic ratio (γ-value) for ^{63}Cu is 0.934 of the value for ^{65}Cu, this gain in sensitivity is not sufficient to compensate for lower natural abundance of ^{65}Cu. The quadrupole moment eQ of ^{63}Cu is 1.07 times greater than that for ^{65}Cu. Then quadrupole broadening of ^{63}Cu spectrum is just marginally larger than that of ^{65}Cu. Thus ^{63}Cu tends to be a preferred nucleus for most NMR studies.

Fig. 7.9 shows ^{63}Cu NMR spectra of the sample Li1.0, Li2.1 and an empty rotor. Only one isotropic resonance is observed at 2000 ppm in all of the spectra over a wide range of chemical shifts, and no obvious intensity increase of the this peak is observed. This signal corresponds to the Cu r.f. coil in the probe. However, according to the XRD data, the peaks from Cu metal start to be present even in the early discharged samples. The NMR signal loss of Cu metal generated during discharge could be due to the small particle size of Cu, the large electric field gradient present in these nano particles, and this large quadrupolar interaction presumably broadening the signal beyond detection. In contrast, the Cu metal with large particle size has face centered cubic structure where no quadrupolar coupling is present in this highly symmetric structure, and thus the signal of Cu coil is easily observed. Static ^{63}Cu NMR was also performed to confirm the formation of Cu metal as shown in Figure 7.10. Since the r.f. coil used in this probe is silver, signals

from the background is subtle. The spectra shown in this figure are subtraction results from the background. A very weak peak is observed at 1979 ppm in the spectrum of the fully discharged CCN-CuF_2. Comparing with CuS, the Cu metal signal in this compound is small. The signal loss is due to the same reason as described above.

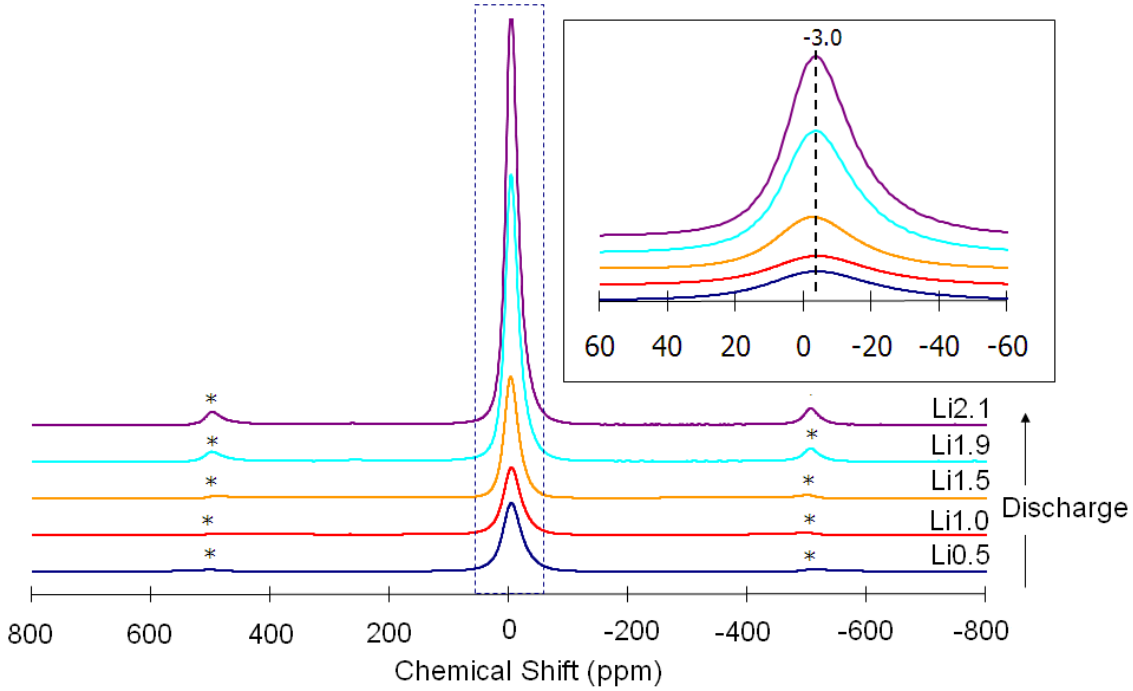

Figure 7.7: ^{7}Li MAS NMR spectra of discharged CCN-CuF_2 between Li=0.5 and 2.1. The isotropic resonances and spinning sidebands are marked with their shifts and asterisks, respectively in this and subsequent NMR spectra. The inset is the enlargement of the isotropic resonance.

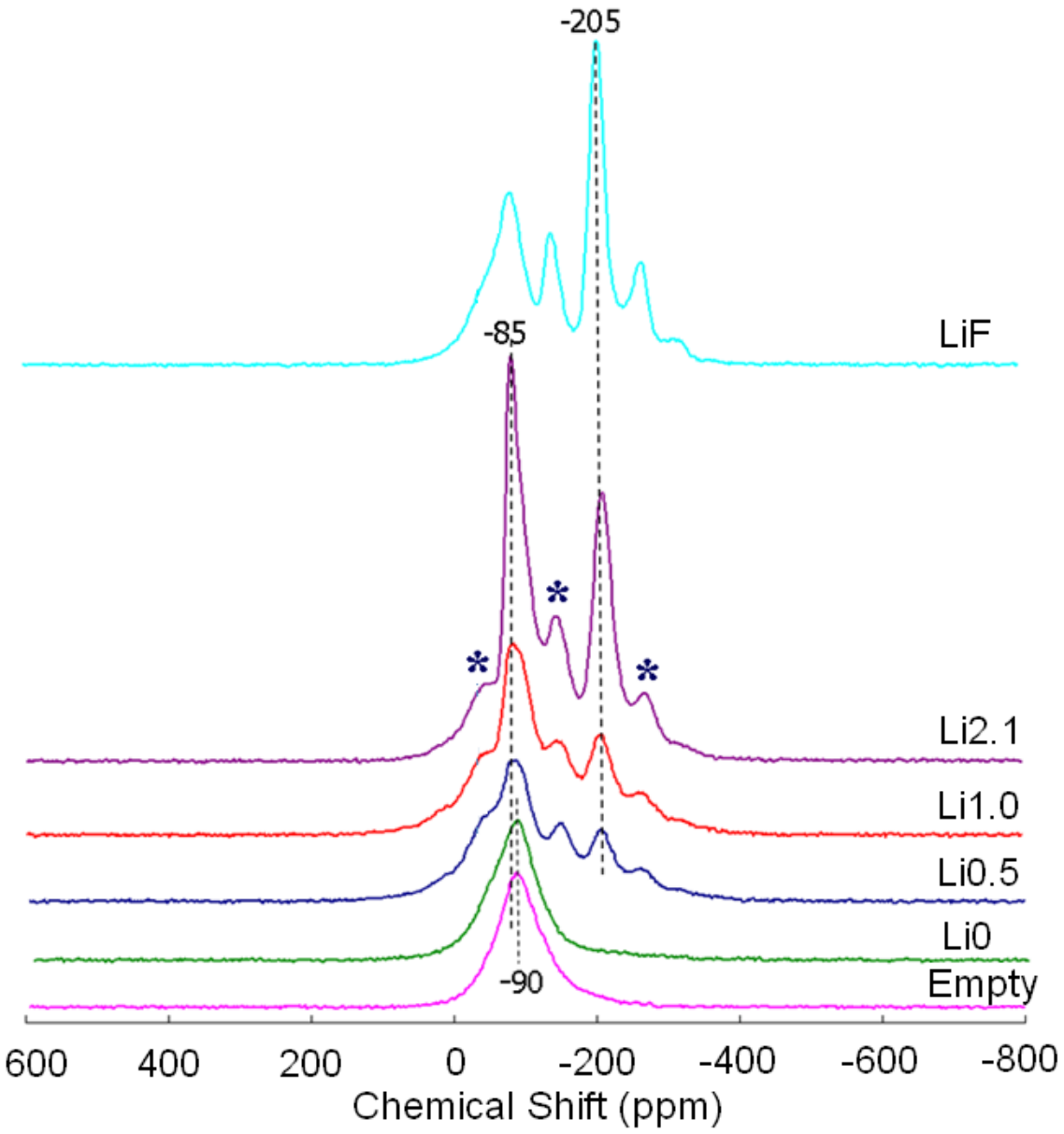

Figure 7.8: ^{19}F MAS NMR spectra of discharged CCN-CuF_2 between Li=0.5 and Li=2.1. For comparison, the spectra of an empty rotor (Background) and LiF are shown in the same figure.

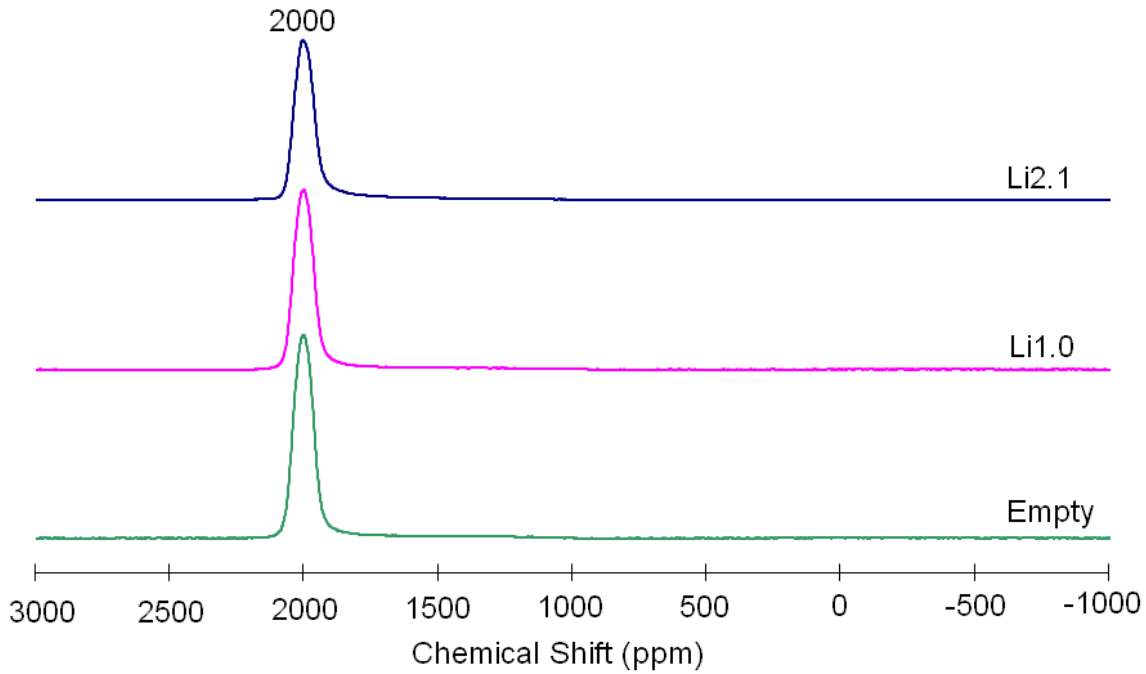

Figure 7.9: ^{63}Cu MAS NMR spectra of discharged CCN-CuF_2 with Li=1.0 and Li=2.1. For comparison, the spectrum of an empty rotor (background) is shown in the same figure.

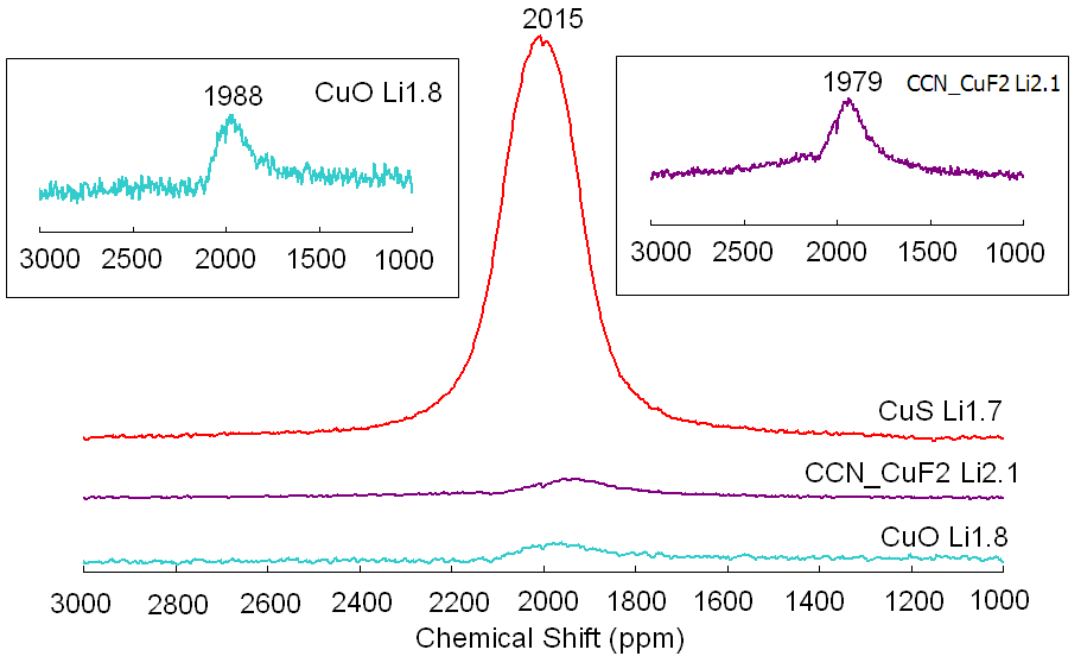

Figure 7.10: Static ^{63}Cu MAS NMR spectrum of fully discharged CuS, CuF_2 and CuO with Li=1.8. The enlargements are the spectra of the fully discharged CuF_2 and CuO.

7.3.3.2.2 CuS

Fig.7.11 shows the ^{7}Li NMR spectra of the discharged and charged CuS samples. In these spectra, an isotropic resonance is observed at around -1 ppm. This peak shifts to higher frequency and the intensity increases gradually as discharge proceeds. By contrast, the peak shifts to lower frequency and the intensity decreases gradually as charge proceeds. Interestingly, the peak shape shows an asymmetric future and it looks it comprises more than one peak until Li=0.85 which is the end of the first plateau on the discharge curve. To resolve the different peaks, ^{7}Li NMR was carried out using a higher magnetic field of 8.46 T (Fig. 7.12). In the spectrum of the Li0.4 sample, two resonances are observed in the diamagnetic resonance region: one at -1 ppm, and the other one at -10 ppm. The peak at -1 ppm is assigned to SEI layer and electrolyte salt, and it can also be from LiCuS phase as proposed previously.[12] The peak at -10 ppm is assigned to an insertion phase Li_xCuS where paramagnetic Cu^{2+} ion is present in this compound, which can cause larger shift of Li. In the spectra of the sample Li0.85, the peak at -10 ppm is less obvious, and the peak from Li_2S at 2 ppm starts to appear. With more Li ions in inserted into the material, this peak is more and more pronounced, which is consistent with Li_2S formation during this process. During charge process, from the sample Li1.7 to C_Li0.45, the intensity of the Li_2S peak is decreases gradually, and only the peak from SEI is observed at the end of charge. Since there were problems with the spectrometer during data acquisition, a direct comparison of the peak intensity between samples could not be performed in this case. To illustrate the formation of Li_2S during discharge, the peak intensity ratio of Li_2S to that of SEI layer is plotted in Fig.7.13 for each sample. The ratio increases with the state of discharge, and decreased with the state of charge. This

suggests that the formation of Li_2S starts on the second plateau region (1.68V) after Li=0.8, and Li_2S phase is reconverted on charge. The amount of SEI layer was assumed to be constant in this study. Even if it grows with the function of discharge, the conclusion of formation of Li_2S is not affected.

Fig.7.14 shows ^{63}Cu NMR spectrum of pristine CuS and two resonances are observed at 2000 ppm and 680 ppm. The peak at 2000 ppm corresponds to Cu metal from the coil as mentioned above, while the peak at 680 ppm must correspond to CuS itself. In order to confirm this assignment a series of discharged CuS samples were examined as shown in Fig.7.15. The intensity of this peak in pristine CuS sample, Li0, is the highest, and it decreases with more Li content in the sample. The peak is totally invisible in the discharged sample Li0.85 as well as in the charged C_Li0.5 sample. As suggested previously,[25] the CuS has a valence configuration of (Cu^{2+} $S_2^{2-}$$Cu_2^{2+}$ S^{2-}). Since Cu^{2+} (d^9) is paramagnetic, the shift of the Cu^{2+} ion will be extremely large and can not be observed in the frequency range of the experimental set up. Thus, the 680 ppm peak is ascribed to the Cu^+ ions in this material. However, if the peak at 680 ppm is only from Cu^+, an increase of the peak intensity should be expected on discharge since Cu^{2+} will be reduced to Cu^+ during discharge. This peak is not due to Cu_2S, which has the configuration of ($Cu_2^{2+}S^{2-}$), since no resonance is observed in the region between -3000 and 7000 ppm. With these evidences, the peak at 680 ppm is assigned to the configuration of (Cu_2^{2+} S_2^{2-}).

Fig.7.16 (a) shows the spectra of the discharged CuS samples in the 2000 ppm region. Only the peak from Cu coil is observed in the samples from Li0.45 to Li0.85. However, in the spectra of the samples Li1.25 and Li1.7, which are on the second plateau

in the discharge profile, an extra resonance at 2015 ppm is observed, which is well resolved from the peak of the Cu coil. Spinning side bands from this resonance are observed as well (Fig. 7.16(d)), which explains that this signal arises from a material in the NMR rotor. The peak intensity in Li1.7 is higher than that in Li1.25, so this peak is assigned to the Cu metal formed during the discharge. This suggests that the conversion reaction takes place mostly after Li=1.0 and results in the formation of Cu metal. The ^{63}Cu NMR spectra of the charged samples are shown in Fig. 7.16 (b). The Cu metal peak decreases in intensity dramatically in the samples C_Li1.25 and C_Li0.80 compared to the signal of the fully discharged sample Li1.7, and it disappears completely in the sample C_Li0.45. At the end of charge, no Cu metal remains in the sample. It should be noted that the Cu metal peak in the spectrum of the fully discharged sample Li1.7 (Fig 16 (c)) acquired in the high magnetic field 8.45T is much more intense compared to the spectrum acquired in the magnetic field 4.75T shown in Fig.7.16 (a). And also the signal from Cu coil in this spectrum is reduced noticeably. This is due to the different tuning of the probe when Cu metal is present in the sample. The static ^{63}Cu NMR spectrum of the fully discharged sample confirms the formation of Cu metal at the end of discharge as well (Fig. 7.10).

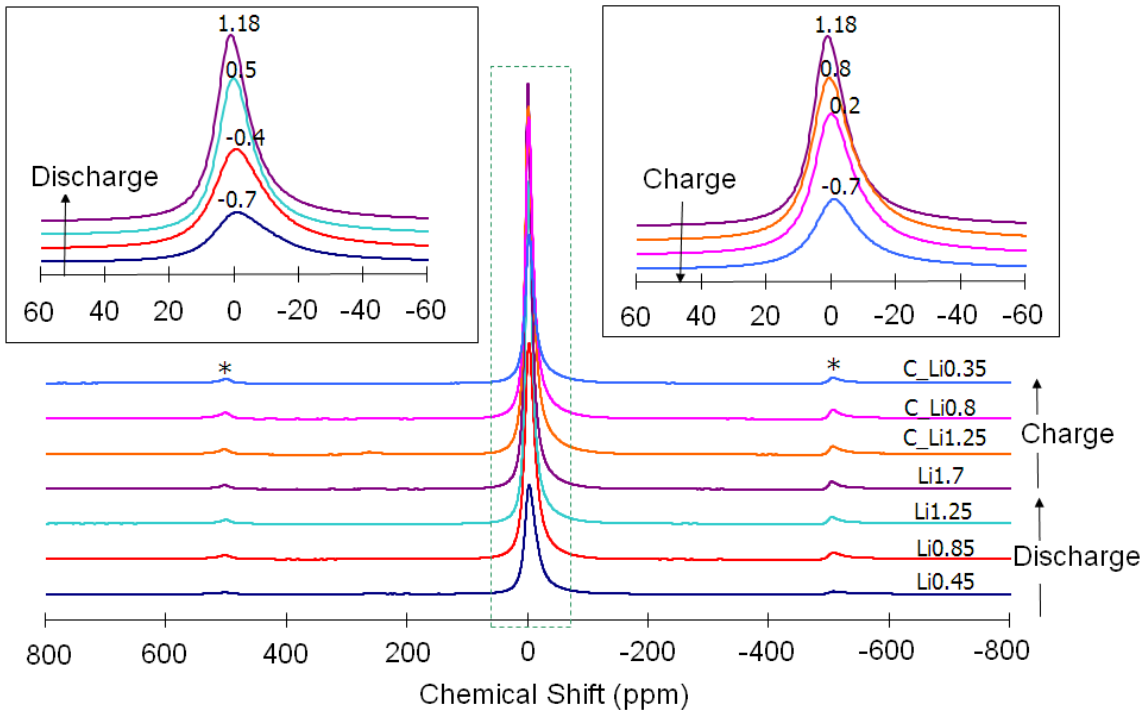

Figure 7.11: ^{7}Li MAS NMR spectra of discharged CuS between Li=0.5 and Li=2.1 and charged CuS between Li=1.7 and Li=0.35. The inset is the enlargement of the spectra between -50 and 50 ppm.

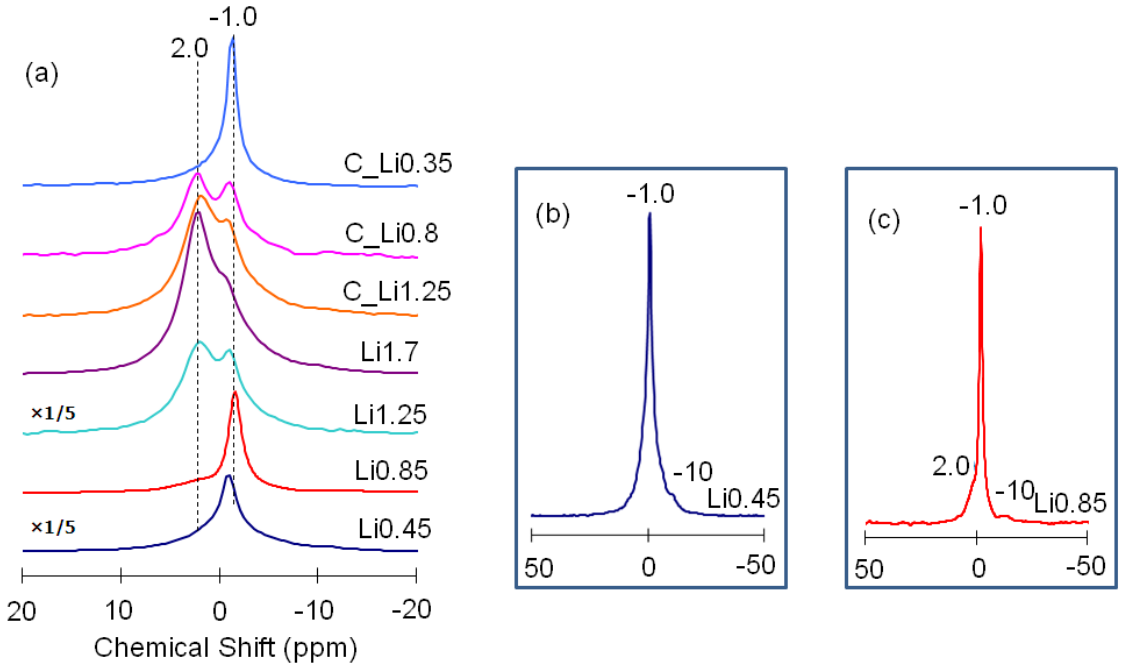

Figure 7.12: ^{7}Li MAS NMR spectra of discharged CuS between Li=0.5 and Li=1.7 and charged CuS between Li=1.7 and 0.35 acquired in the field of 8.46 T. (b) and (c) show the spectra of the discharged CuS with Li=0.45 and 0.85 samples over a large shift range.

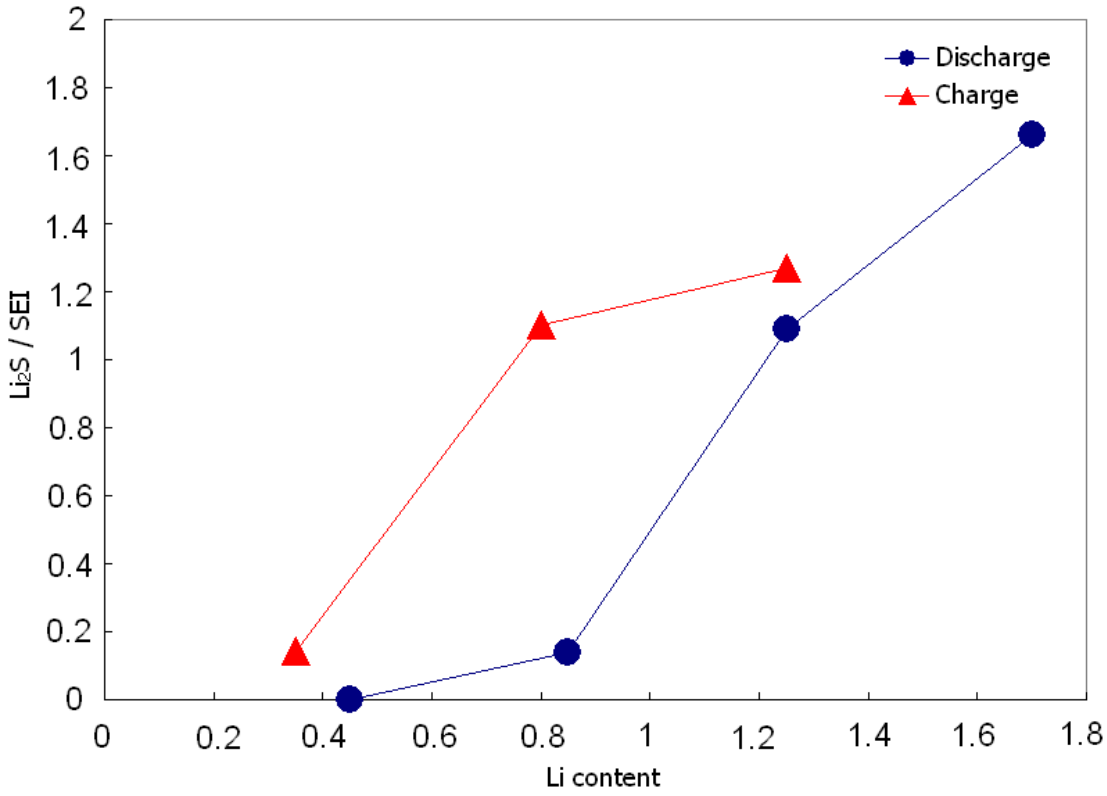

Figure 7.13: Li_2S / SEI ratio plotted as the function of Li content for discharge and charge of CuS.

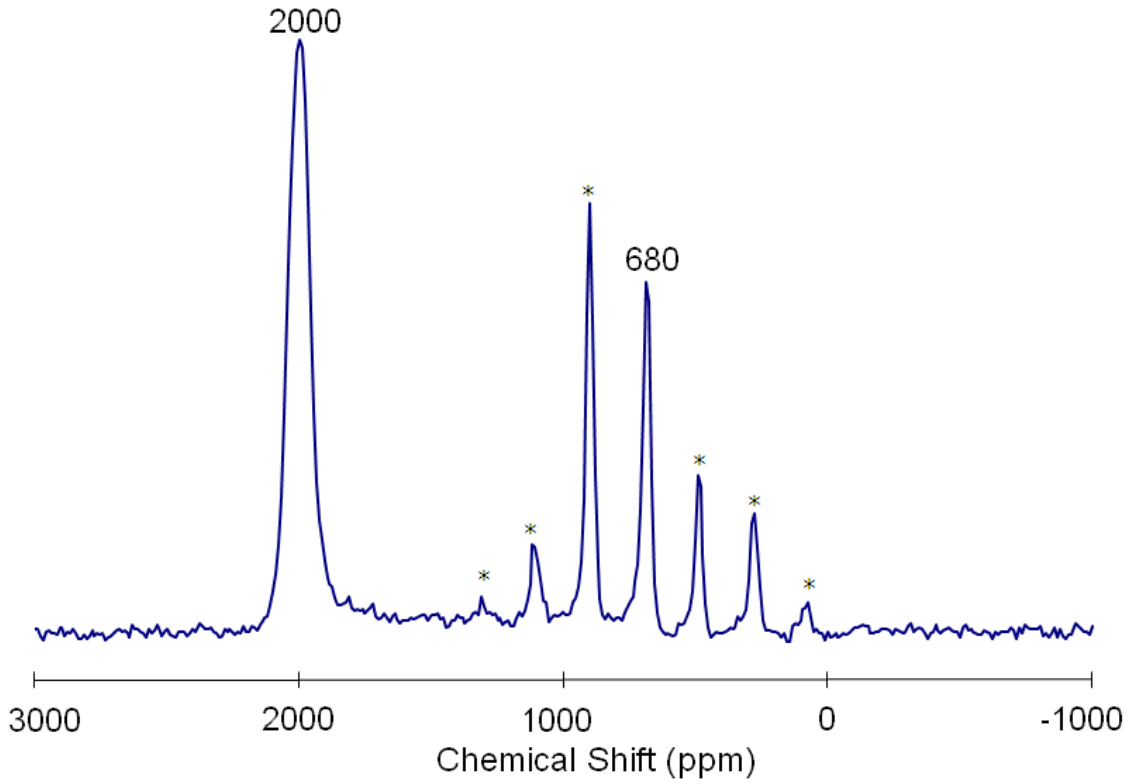

Figure 7.14: ^{63}Cu MAS NMR spectra of pristine CuS acquired in the magnetic field of 4.7T.

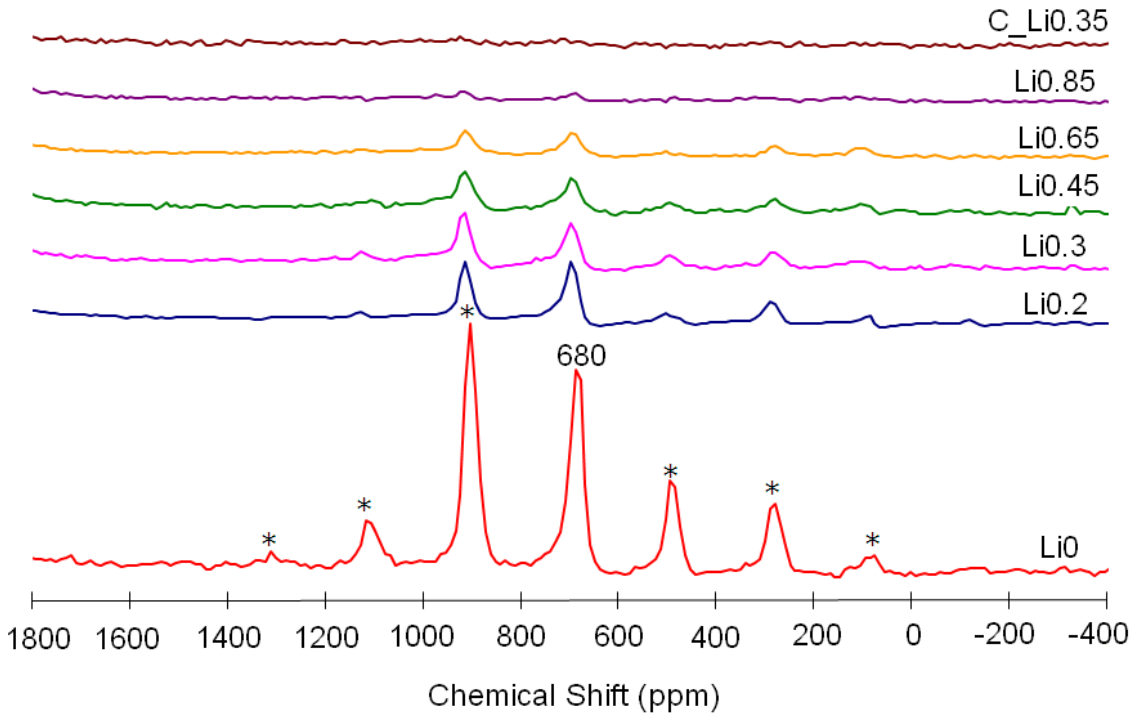

Figure 7.15: ^{63}Cu MAS NMR spectra of discharged CuS between Li=0 and Li=0.85 and charged CuS with Li=0.35 in the region between -400 and 1800 ppm.

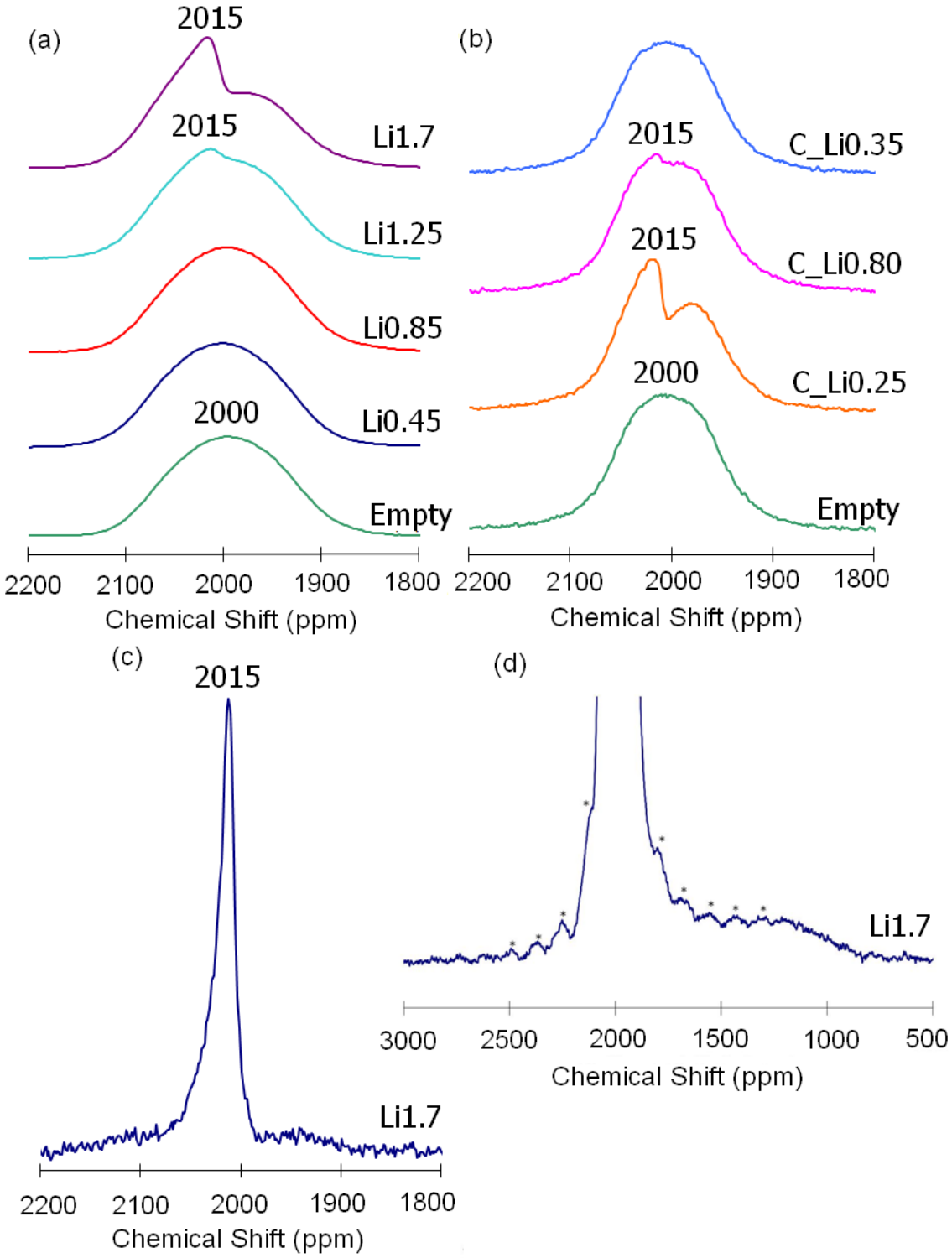

Figure 7.16: ^{63}Cu MAS NMR spectra of (a) discharged and CuS between Li=0.45 and Li=1.7 acquired in 4.7T, (b) charged CuS between Li=0.35 and Li=1.7 ppm acquired in 8.46T, (c) fully discharged sample Li1.7 acquired in 8.46T, and (d) the fully discharged sample Li1.7 acquired in 4.7T showing the spinning side bands of the peak at 2015 ppm.

7.3.3.2.3 CuO

Fig.7.17 shows the ^{7}Li NMR spectra of the discharged CuO samples. In the spectrum of sample Li0.1, an isotropic resonance is observed around -3.6 ppm. This peak is shifted to higher frequency and the intensity increases gradually as discharge proceeds, corresponding to the formation of SEI layer and Li_2O whose resonance is 2.8 ppm. The peak position is not at exactly the same position as Li_2O at the end of the charge, and it may be due to the overlapping with signals from SEI layer. In addition, the peak shape in the samples Li0.1 and Li0.3 is asymmetric, which suggests more than one peak contribute to this shift. Since the typical shift of SEI layer is around -1.0 ppm, the peak at -3.6 ppm should have a large contribution from a more negative shift. This indicates that an insertion phase like Li_xCuO is formed during discharge. Actually, Novak *et al*[19] suggested the electrochemical insertion of the lithium into CuO structure according to the following reaction:

$$CuO + xLi \rightarrow Li_xCuO \ (0 < x < 1) \qquad (6)$$

Fig.7.18 shows ^{63}Cu NMR spectra of the discharged CuO sample Li1.8 (at the end of discharge) and the empty rotor. Only one isotropic resonance corresponding to Cu coil is observed, and the intensity is not increased in the discharged sample compared to the empty rotor. The signal loss of Cu metal should be from the same reason as CuF_2 that small particle size is formed during discharge. A very week peak at 1988 ppm is also observed in the static ^{63}Cu NMR spectrum of the fully discharged sample (Fig. 7.10).

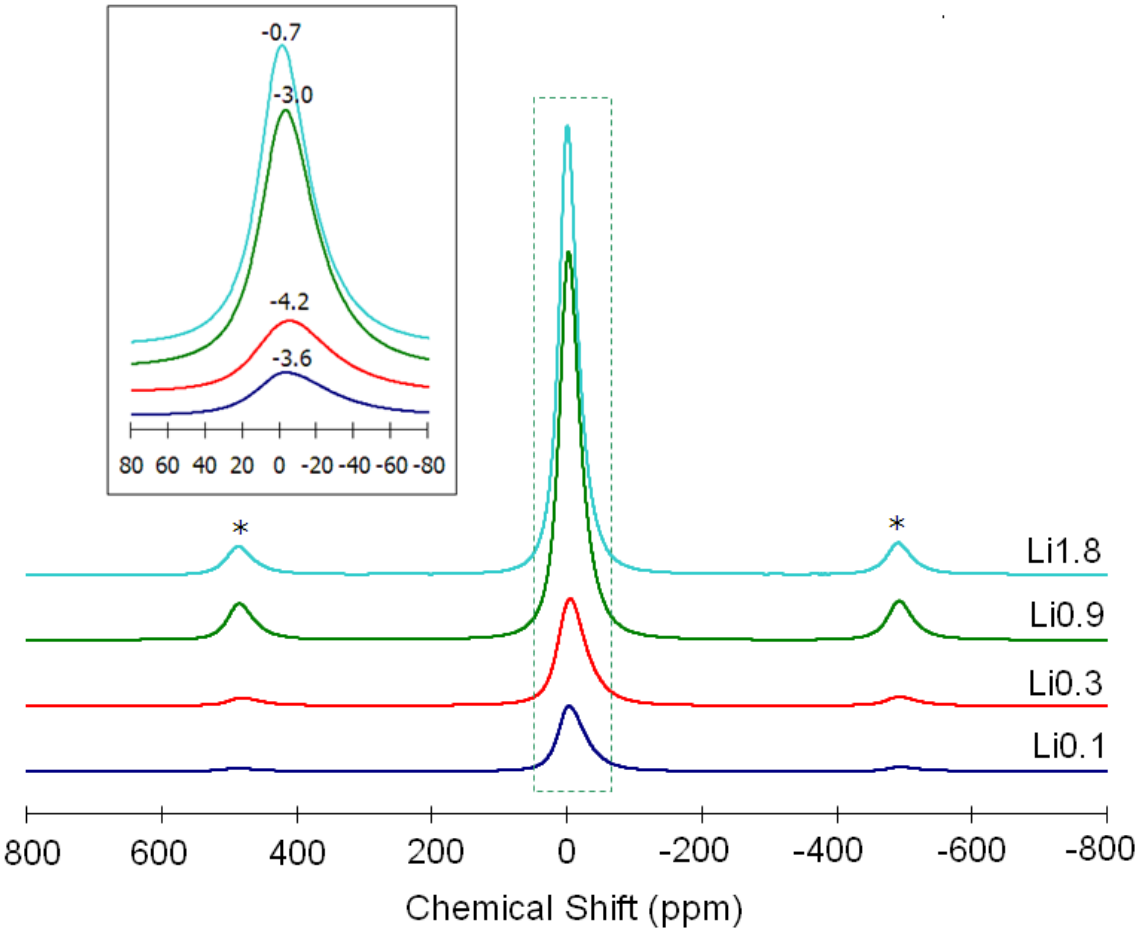

Figure 7.17: ^{7}Li MAS NMR spectra of discharged CuO between Li=0.1 and Li=1.8. The inset shows the isotropic resonances.

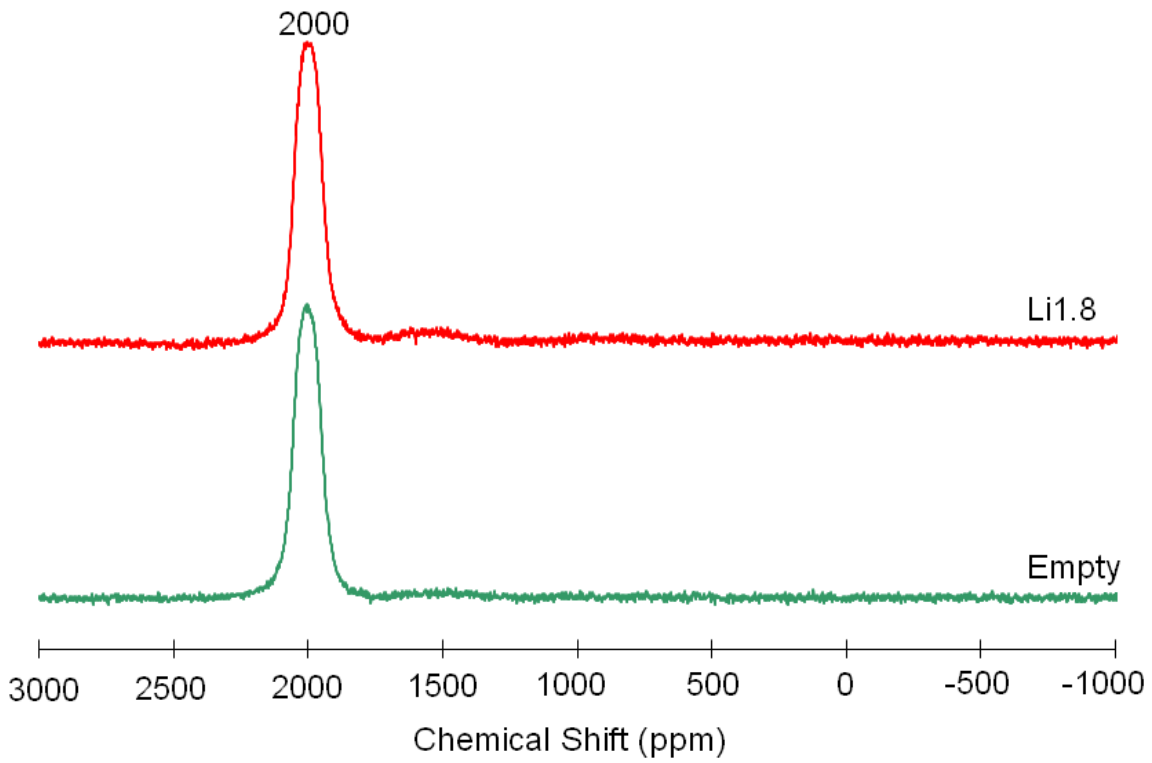

Figure 7.18: ^{63}Cu MAS NMR spectrum of discharged CuO with Li=1.8. For the comparison the spectrum of empty rotor (background) is shown in the same figure.

7.3.3.2.5 ^{63}Cu{^{7}Li}REAPDOR

Rotational-Echo Adiabatic-Passage DOuble-Resonance NMR (REAPDOR) is developed by Gullion et al [22, 26]to recover the weak dipolar interactions between spin 1/2 and quadrupolar nuclei. This experiment is a combination of the TRAnsfer-of-Populations DOuble-Resonance (TRAPDOR) NMR and the Rotational-Echo DOuble-Resonance (REDOR) NMR, which gets rid of the difficulties in both experiments and can provide the information about weak dipolar coupling of quadrupolar nuclei.

A train of π pulse is applied to the ^{7}Li nucleus during the dipolar evolution period of N_{Li} rotor cycles, and short radio frequency "adiabatic-passage pulse" of length τ is applied to quadrupolar nuclei ^{63}Cu in the middle of the dipolar evolution period. The REAPOR is composed of two experiments with different pulse sequences, one is "control experiment" and the other one is "double resonance experiment". In control experiment, the adiabatic-passage pulse is not omitted and the average dipolar evolution period are opposite in sign, and the dipolar interaction is refocused, which produces the full signal. In double resonance experiment, the adiabatic-passage pulse is applied and the populations of ^{63}Cu spins are interchanged, which has an effect on the dipolar dephasing of ^{7}Li spins. The transverse magnetization is no longer fully refocused resulting in a reduction of the signal. Through the $\Delta S_{ctrl\text{-}dr}$ value calculated by subtracting the reduced signal from full signal, the information of the magnitude of dipolar coupling can be obtained, that is to say, interaction between ^{7}Li and ^{63}Cu nuclei.

To study the interaction between the copper metal and the lithium compounds generated in the discharge process, REAPDOR experiment was curried out on the fully

discharged samples of all the model compounds. For comparison, the discharged CuS sample Li1.0 which should have the insertion structure (Li_xCuS) was also measured. Fig. 7.19(a)-(d) shows the dependence of $\Delta S_{ctrl\text{-}dr} / S_{ctrl}$ on N_{Li} rotor cycles and the spectra acquired with 16 rotor periods for each samples. This dependence is plotted for each resonance observed in CuF_2 (-1 ppm: LiF/SEI), CuS (2 ppm: Li_2S; -1 ppm: SEI; -10 ppm: LiCuS), and CuO (2.8 ppm: Li_2O; -1 ppm : SEI).

In CuS Li1.0, the signal loss ($\Delta S_{ctrl\text{-}dr} / S_{ctrl}$) of the peak at -10 ppm is observed at 2 rotor periods and it reaches 35% at 16 rotor periods. This is ascribed to the interaction between copper and lithium since they are in the same structure. As for CuF_2 Li2.0, $\Delta S_{ctrl\text{-}dr} / S_{ctrl}$ value is almost 0 even following 16 rotor periods and no REAPDOR effect is observed. On the other hand, in the figure of CuS Li2.0, $\Delta S_{ctrl\text{-}dr} / S_{ctrl}$ value gradually increases from 2 rotor periods to 16 periods, and 30% of REAPDOR effect is observed in 16 rotor periods for both peaks from Li_2S and SEI. As for CuO, although it is difficult to estimate the REAPDOR effect on the peak from Li_2O at more rotor periods because it is not obvious due to short T_2 delay time, REAPDOR effect of the sample CuO Li2.0 is much smaller than that of the sample CuS Li2.0 and only 18% of REAPDOR effect is seen in 16 rotor periods. To summarize the results above, the magnitude of the REAPDOR effect is CuS>CuO>CuF_2. Interestingly, their electrochemical performances from the aspect of reversibility (Charge capacity / Discharge capacity) in the first cycle also have the same sequence: (CuS: 79% > CuO: 30% > CuF_2: 0%). The degree of interaction between copper metal and lithium compounds in fully discharged state might affect their reversibility.

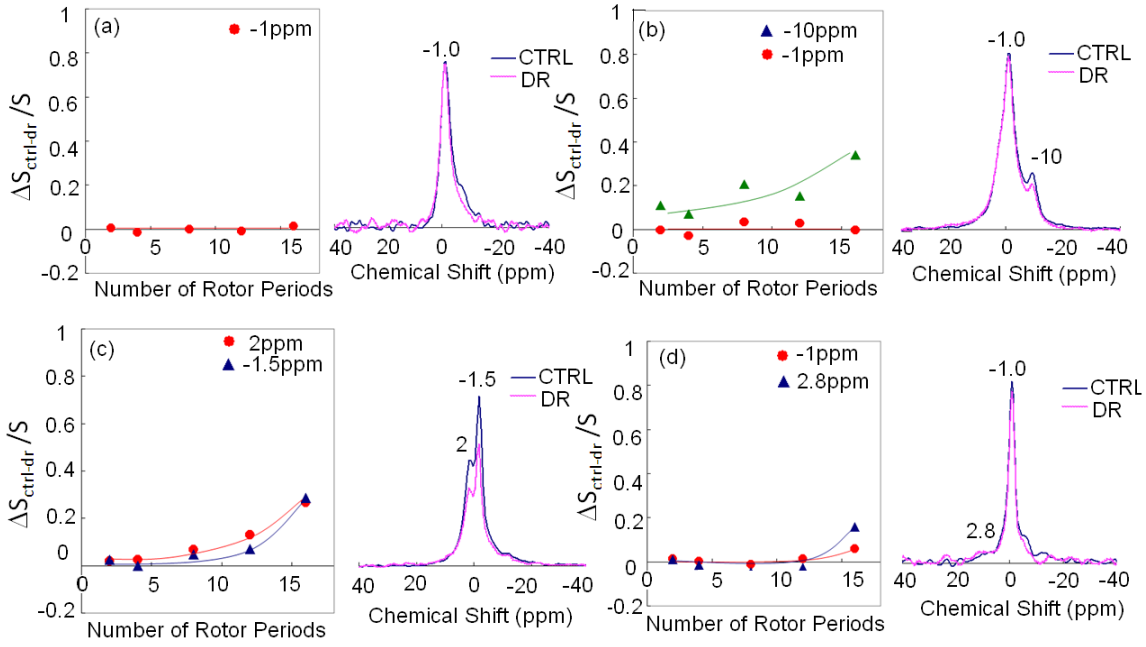

Figure 7.19: The dependence of the measured ratio $\Delta S_{ctrl-dr}$ / S on the number of rotor period for each sample, CCN_CuF_2 with Li=2.0 (a), CuS with Li=1.0 (b), CuS with Li=2.0 (c) and CuO with Li=2.0 (d). The ^{7}Li NMR spectra of control experiment (CTRL) and double resonance experiment (DR) are also shown for each sample.

7.4. Discussion

7.4.1 Discharge reaction mechanism in CuF_2 system

The discharge reaction of CuF_2 is relatively straightforward. Cu is formed right from the beginning of discharge as seen by XRD. Although the reflections from LiF are not very pronounced at the early stage of discharge, which may be due to its small particle size, the ^{19}F NMR signal of LiF can be clearly observed in the discharged Li0.5 sample. Other than the isotropic resonance at -3 ppm which is assigned to LiF and Li Salts in the SEI layer, no more peaks are observed in the ^{7}Li NMR spectra. In addition, the reduction from Cu^{2+} to Cu^{+} is also unlikely in this compound, since higher operation voltage will be expected.[8] Based on this data, a simple conversion reaction taking place from the beginning of discharge until the end can be concluded, and the reaction mechanism of CuF_2 can be written as follows:

$$CuF_2 + 2Li^+ + 2e^- \rightarrow Cu + 2LiF \quad (7)$$

The discharge curve can be divided into two regions: a "plateau-like" region from Li0 to Li1.0 which is associate the conversion reaction described in eqn. (7), and a sloppy region from Li1.0 to Li2.1. As shown in the XRD patterns (Fig. 7.3), the reflections from Cu metal in the samples Li0.5 is sharp, and they start to broaden in the sample Li1.0. In the fully discharged sample Li2.1, the reflections of Cu metal seem to be the combination of a sharp component and a broad component. This indicates that the crystal size of Cu metal is big at the early stage of discharge, and then a part of them starts to crush to smaller particles, which results in the voltage drop after Li1.0.

7.4.2 Discharge and charge reaction mechanism in CuS system

The discharge process of CuS can be divided into two steps according to the electrochemical profile. From Li0 to Li0.85, which is the range of the first plateau, no evidence of Cu metal and Li_2S formation is observed either from the ^{63}Cu and ^{7}Li NMR and XRD patterns. However, a two phase behavior is present in the XRD pattern, where the peak from CuS phase at 10.7° (2θ) disappears and a peak from a new phase at 46.3° (2θ) appears during the discharge process. In addition, a resonance at -10 ppm is observed in the ^{7}Li NMR which was assigned to an intercalation phase Li_xCuS. To conclude, the first process of the discharge is an intercalation reaction with a formation of the new phase Li_xCuS, which is associated with the first plateau on the electrochemical profile. This process can be described as follows:

$$Li + CuS \rightarrow Li_xCuS\ (0 \leq x \leq 1) \qquad (8)$$

This mechanism is consistent with the J. S. Chung *et al*'s results,[12] but it is different from J. M. Tarascon *et al's* theory,[13] which involves the formation of Cu_2S and Li_2S in the first step. However, no ^{7}Li resonance from Li_2S is observed in the spectra before Li1.25, which gives a strong supporting evidence to disapprove their mechanism. In addition, more supporting structural information is given here by NMR and XRD. Especially from Cu NMR, a detailed reduction procedure can be clarified. As discussed in NMR results, the peak at 680 ppm in Cu NMR spectra is assigned to the configuration (Cu_2^{2+} S_2^{2-}). Since a gradual intensity decrease of this peak with the discharge process as shown in Fig. 7.14, which is associated a two-phase reaction, the reductions from S_2^{2-} to S^{2-} and from Cu^{2+} to Cu^{+} are simultaneous, otherwise a peak intensity increase at the beginning of

discharge would be expected if Cu^{2+} is reduced to Cu^{+} first. Then the whole reduction procedure can be described as such: $(Cu^{2+}Cu^{+}Cu^{+}\ S_2^{2-}S^{2-}) \rightarrow (Cu^{+}Cu^{+}\ Cu^{+}S^{2-}S^{2-}S^{2-})$.

The second process is associated with a conversion reaction since Cu metal and Li_2S are observed from NMR and XRD. In the XRD pattern of fully discharged sample Li2.0, in addition to the reflections from Cu and Li_2S, a series of peaks from $Cu_{1.96}S$ are also observed. The appearance of $Cu_{1.96}S$ is ascribed to the disproportionation product of the Li_xCuS phase. This is different than that suggested in J. S. Chung *et al.*'s[14] paper that the formation of $Cu_{1.96}S$ is an electrochemical process. The reflections from $Cu_{1.96}S$ are not always observed in all the discharged samples and there is no systematic trend of the appearance/disappearance of this phase. Since a capacity of only 477mAh/g corresponds to a 1.7 Li discharge capacity, suggests not all the LiCuS being converted to Cu metal and Li_2S, and part of this phase is involved in the disproportionation reaction. Then the second process can be described as follows:

$$LiCuS + 0.7\ Li^{+} + e^{-} \rightarrow 0.7Li_2S + 0.7Cu + 0.3LiCuS \qquad (9)$$

At the same time, the disproportionation reaction can occur:

$$0.3LiCuS \rightarrow 0.15\ Cu_{1.96}S + 0.06Cu + 0.15Li_2S \qquad (10)$$

During charge, the conversion reaction is reversed. Both the XRD and Cu NMR results show the disappearance of Li_2S and Cu metal. In the charged sample C_Li1.25, the peaks from Cu can barely be observed. However, the Cu metal signal in the NMR spectrum is still present in this sample, even though it is much smaller compared to the fully discharged sample. This indicates that there is still some Cu metal left in this sample, but the sample amount is so small that it can barely be detected by XRD. The XRD patterns are quite similar for all the charged samples, which are close to the intercalation

phase. It seems that the charge process follows the same track as the intercalation reaction, that a "Li_xCuS" like phase forms during charge. The reaction of charge can be written as follows:

$$0.85Li_2S + 0.76\ Cu + 0.15Cu_{1.96}S \rightarrow Li_xCuS \rightarrow Li_{0.35}CuS + 1.35Li \quad (11)$$

The Li content is calculated based on the charge capacity obtained in the electrochemistry.

7.4.3 Difference of electrochemistry between CuS and CuF_2

The crystal size of the Cu metal formed at the end of discharge can be derived from XRD patterns. Comparing the XRD pattern of fully discharged samples of CuS and CuF_2, the crystal size of Cu is very different between these two samples. The Cu metal formed in CuS system is very crystalline, and the crystal size calculated by Scherrer formula is 37.5 nm. The Cu metal size formed in CuF_2 is about 9 nm, which is much smaller than that formed in CuS system. Generally, one believes that the small particle size of the transition metals formed in the conversion reaction would help the electrochemical activity. However, the electrochemical study shows that the reversibility of CuS is much better than that of CuF_2. About 75% of theoretical capacity was obtained on charge for CuS, but CuF_2 can hardly be charged. It seems like the particle size of Cu metal is not the only reason which affects the electrochemical activity.

The REAPDOR results give another explanation of the electrochemical reversibility. The REAPDOR effect is associated with the distance between the two observed nuclei. The closer the two nuclei, the bigger the REPDOR effect is. When two nuclei are close, more interaction between these two nuclei will be expected. The nuclei observed in REAPDOR experiments in this study are Cu and Li, so the distance between

Cu metal and Li compounds can be investigated. As shown in the REAPDOR results, the effect of CuS, CuF_2 and CuO is CuS>CuO>CuF_2, so the distance between the Cu metal and Li compounds is in the same order. Then the interaction between Cu metal and Li_2S is expected to be the biggest among these three compounds. It could be the part of the reason that the electrochemical reversibility of these compounds is different.

7.5 Conclusions

Different reaction mechanisms of CuS, CuF_2 and CuO during electrochemical process are discussed in this paper. For CuS, the direct evidence of an insertion phase from both NMR and XRD results are demonstrated for the first time, which supports the insertion reaction mechanism for the first process of the electrochemistry. The second plateau is associated with a conversion reaction of the insertion phase Li_xCuS since Cu metal and Li_2S start to be observed only after the first plateau. Then a two-step reaction mechanism is confirmed for CuS, which is consistent with the results J. S. Chung *et al*. proposed previously. However, we have different opinions of formation of $Cu_{1.96}S$ is given in our study. The direct conversion reaction mechanism is found for CuF_2 with the observance of Cu metal and LiF at the beginning of discharge. For CuO, an evidence of the intercalation phase is found by ^{7}Li NMR, which gives a side proof of the intercalation reaction at the beginning of discharge. The crystal size of Cu metal formed in CuS is much bigger than that in CuF_2 as studied in XRD pattern. However, the interaction between Cu metal particles and Li compounds in CuS is also stronger than that in CuF_2. Then the electrochemical reversibility of these copper compounds is not only related to particle size of the products formed in the conversion reaction, but also the interaction between the particles plays an important role in the electrochemical reaction.

7.6 References

1. Dahn, J. R.; Zheng, T.; Liu, Y. H.; Xue, J. S., *Science* **1995,** 270, (5236), 590-593.

2. Megahed, S.; Scrosati, B., *Journal of Power Sources* **1994,** 51, (1-2), 79-104.

3. Courtney, I. A.; Dahn, J. R., *Journal of the Electrochemical Society* **1997,** 144, (9), 2943-2948.

4. Courtney, I. A.; Dahn, J. R., *Journal of the Electrochemical Society* **1997,** 144, (6), 2045-2052.

5. Idota, Y.; Kubota, T.; Matsufuji, A.; Maekawa, Y.; Miyasaka, T., *Science* **1997,** 276, (5317), 1395-1397.

6. Li, H.; Balaya, P.; Maier, J., *Journal of the Electrochemical Society* **2004,** 151, (11), A1878-A1885.

7. Li, H.; Richter, G.; Maier, J., *Advanced Materials* **2003,** 15, (9), 736-739.

8. Badway, F.; Mansour, A. N.; Pereira, N.; Al-Sharab, J. F.; Cosandey, F.; Plitz, I.; Amatucci, G. G., *Chemistry of Materials* **2007,** 19, (17), 4129-4141.

9. Gabano, J. P.; Gerbier, G.; Jammet, J.; Dechenau.V, *Journal of the Electrochemical Society* **1972,** 119, (4), 459-&.

10. Okamoto, K.; Kawai, S., *Japanese Journal of Applied Physics* **1973,** 12, (8), 1130-1138.

11. Etienne, A., *Journal of the Electrochemical Society* **1970,** 117, (7), 870-&.

12. Chung, J. S.; Sohn, H. J., *Journal of Power Sources* **2002,** 108, (1-2), 226-231.

13. Debart, A.; Dupont, L.; Patrice, R.; Tarascon, J. M., *Solid State Sciences* **2006,** 8, (6), 640-651.

14. Grugeon, S.; Laruelle, S.; Herrera-Urbina, R.; Dupont, L.; Poizot, P.; Tarascon, J. M., *Journal of the Electrochemical Society* **2001,** 148, (4), A285-A292.

15. Ikeda, H.; Narukawa, S., *Journal of Power Sources* **1983,** 9, (3-4), 329-334.

16. Matsuda, Y.; Teraji, K.; Takasu, Y., *Denki Kagaku* **1976,** 44, (5), 363-364.

17. Novak, P., *Electrochimica Acta* **1985,** 30, (12), 1687-1692.

18. Lee, P. L.; Shu, D. M.; Ramanathan, M.; Preissner, C.; Wang, J.; Beno, M. A.; Von Dreele, R. B.; Ribaud, L.; Kurtz, C.; Antao, S. M.; Jiao, X.; Toby, B. H., *Journal of Synchrotron Radiation* **2008,** 15, 427-432.

19. Lee, Y. J.; Grey, C. P., *Journal of Physical Chemistry B* **2002,** 106, (14), 3576-3582.

20. Hinedi, Z. R.; Chang, A. C.; Borchardt, D. B., *Water Research* **1997,** 31, (4), 877-883.

21. Liu, H. M.; Sullivan, R. M.; Hanson, J. C.; Grey, C. P.; Martin, J. D., *Journal of the American Chemical Society* **2001,** 123, (31), 7564-7573.

22. Gullion, T., *Chemical Physics Letters* **1995,** 246, (3), 325-330.

23. West, A. R., *Solid State Chemistry and it's Application*. John Wiley & Son: New York: 1992.

24. Plakhotnyk, A. V.; Ernst, L.; Schmutzler, R., *Journal of Fluorine Chemistry* **2005,** 126, (1), 27-31.

25. Pattrick, R. A. D.; Mosselmans, J. F. W.; Charnock, J. M.; England, K. E. R.; Helz, G. R.; Garner, C. D.; Vaughan, D. J., *Geochimica Et Cosmochimica Acta* **1997,** 61, (10), 2023-2036.

26. Ba, Y.; Kao, H. M.; Grey, G. P.; Chopin, L.; Gullion, T., *Journal of Magnetic Resonance* **1998,** 133, (1), 104-114.

Chapter 8

Conclusion

Two types of electrode materials for Li ion batteries, intercalation compounds and conversion compounds, are studied in this dissertation by electrochemistry, X-ray diffraction, solid state nuclear magnetic resonance and X-ray absorption spectroscopy. For the intercalation compounds, two members of the series of layered compounds $Li[Ni_xLi_{1/3-2x/3}Mn_{2/3-x/3}]O_2$, Li_2MnO_3 and $Li[Li_{1/9}Ni_{1/3}Mn_{5/9}]O_2$, so-called Li-excess materials, were investigated for their demonstrated higher capacity as positive electrode materials in lithium ion batteries. Experiments have been performed to understand the effect of synthesis conditions on the structure of these two compounds. XRD, NMR and Diffax simulation were combined to study the different stacking faults of the layers and cation ordering in the transition metal layers. Various techniques were used to understand the overcapacity mechanism and the structural changes of $Li[Li_{1/9}Ni_{1/3}Mn_{5/9}]O_2$ during electrochemical process. A combination study of XRD and NMR yields the information about both short and long range ordering. Superstructure peak loss and the disappearance of Li resonances in transition metal layers both indicate that the cation rearrangements in the transition metal layers takes place in the samples which have been charged to high voltage (5.3V). TEM pictures gave information about the morphology of the particles, and the oxidation state change of the transition metal ions was observed in XAS spectra.

A mechanism describing the reaction between the electrolyte and the electrode material is proposed to explain the overcapacity mechanism in this Li-excess material.

Solid state NMR was used to probe the local atomic and electronic structure of nano-sized particles formed in the conversion reaction systems, with supporting information from XRD. Two series of conversion compounds were investigated to understand the reaction mechanisms involved in the electrochemical process. In the FeF_3 system, the discharge process was divided into two parts, the insertion reaction, and the conversion reaction. Several intermediate phases are formed in this process. The comparison study of FeF_2 shows that the oxidation state of Fe in the charged Li_xFeF_3 sample is about 2.5, and the Li_xFeF_3 insertion phase remains at the end of charge.

Different reaction mechanisms were observed in the Cu compounds. A two-step reaction is observed in the discharge process of CuS and CuO compounds, where an insertion reaction takes place first then followed by a conversion reaction. For CuF_2, a direct conversion reaction happens at the beginning of discharge. The electrochemical reversibility of the Cu compounds seems to correlate with the interaction between the copper metal particles and lithium compounds formed at the end of conversion reaction.

Finally, a , combination study of different techniques including solid state NMR, XRD and XAS allowed us to probe both short and long range structure of these electrode materials to understand the reaction mechanism within each system, and to give some fundamental information about how to gain further improvements in their electrochemical performance.

References

Chapter 1

1. Armstrong, A. R.; Robertson, A. D.; Gitzendanner, R.; Bruce, P. G. 1999; Academic Press Inc: 1999; pp 549-556.

2. Tarascon, J. M.; Armand, M., *Nature* **2001,** 414, (6861), 359-367.

3. Bruce, P. G., *Chemical Communications* **1997**, (19), 1817-1824.

4. Megahed, S.; Scrosati, B., *Journal of Power Sources* **1994,** 51, (1-2), 79-104.

5. Markovsky, B.; Talyossef, Y.; Salitra, G.; Aurbach, D.; Kim, H. J.; Choi, S., *Electrochemistry Communications* **2004,** 6, (8), 821-826.

6. Ein-Eli, Y.; Howard, W. F.; Lu, S. H.; Mukerjee, S.; McBreen, J.; Vaughey, J. T.; Thackeray, M. M., *Journal of the Electrochemical Society* **1998,** 145, (4), 1238-1244.

7. Ohzuku, T.; Takeda, S.; Iwanaga, M. 1999; 1999; pp 90-94.

8. Kawai, H.; Nagata, M.; Kageyama, H.; Tukamoto, H.; West, A. R., *Electrochimica Acta* **1999,** 45, (1-2), 315-327.

9. Dahn, J. R.; Zheng, T.; Liu, Y. H.; Xue, J. S., *Science* **1995,** 270, (5236), 590-593.

10. Poizot, P.; Laruelle, S.; Grugeon, S.; Dupont, L.; Tarascon, J. M., *Nature* **2000,** 407, (6803), 496-499.

11. Armand, M.; Tarascon, J. M., *Nature* **2008,** 451, (7179), 652-657.

12. Lu, Z. H.; MacNeil, D. D.; Dahn, J. R., *Electrochemical and Solid State Letters* **2001,** 4, (12), A200-A203.

13. Ohzuku, T.; Makimura, Y., *Chemistry Letters* **2001**, (8), 744-745.

14. Makimura, Y.; Ohzuku, T. 2003; 2003; pp 156-160.

15. Lu, Z. H.; Dahn, J. R., *Journal of the Electrochemical Society* **2002,** 149, (7), A815-A822.

16. Lu, Z. H.; Beaulieu, L. Y.; Donaberger, R. A.; Thomas, C. L.; Dahn, J. R., *Journal of the Electrochemical Society* **2002,** 149, (6), A778-A791.

17. Johnson, C. S.; Kim, J. S.; Kropf, A. J.; Kahaian, A. J.; Vaughey, J. T.; Fransson, L. M. L.; Edstrom, K.; Thackeray, M. M., *Chemistry of Materials* **2003,** 15, (12), 2313-2322.

18. Yoon, W. S.; Paik, Y.; Yang, X. Q.; Balasubramanian, M.; McBreen, J.; Grey, C. P., *Electrochemical and Solid State Letters* **2002,** 5, (11), A263-A266.

19. Yoon, W. S.; Grey, C. P.; Balasubramanian, M.; Yang, X. Q.; McBreen, J., *Chemistry of Materials* **2003,** 15, (16), 3161-3169.

20. Grey, C. P.; Yoon, W. S.; Reed, J.; Ceder, G., *Electrochemical and Solid State Letters* **2004,** 7, (9), A290-A293.

21. Meng, Y. S.; Ceder, G.; Grey, C. P.; Yoon, W. S.; Shao-Horn, Y., *Electrochemical and Solid State Letters* **2004,** 7, (6), A155-A158.

22. Meng, Y. S.; Ceder, G.; Grey, C. P.; Yoon, W. S.; Jiang, M.; Breger, J.; Shao-Horn, Y., *Chemistry of Materials* **2005,** 17, (9), 2386-2394.

23. Kim, J. S.; Johnson, C. S.; Vaughey, J. T.; Thackeray, M. M.; Hackney, S. A., *Chemistry of Materials* **2004,** 16, (10), 1996-2006.

24. Johnson, C. S.; Kim, J. S.; Lefief, C.; Li, N.; Vaughey, J. T.; Thackeray, M. M., *Electrochemistry Communications* **2004,** 6, (10), 1085-1091.

25. Reed, J.; Ceder, G., *Electrochemical and Solid State Letters* **2002,** 5, (7), A145-A148.

26. Yoon, W. S.; Kim, N.; Yang, X. Q.; McBreen, J.; Grey, C. P., *Journal of Power Sources* **2003,** 119, 649-653.

27. Armstrong, A. R.; Holzapfel, M.; Novak, P.; Johnson, C. S.; Kang, S. H.; Thackeray, M. M.; Bruce, P. G., *Journal of the American Chemical Society* **2006,** 128, (26), 8694-8698.

28. Robertson, A. D.; Bruce, P. G., *Electrochemical and Solid State Letters* **2004,** 7, (9), A294-A298.

29. Robertson, A. D.; Bruce, P. G., *Chemical Communications* **2002**, (23), 2790-2791.

30. Robertson, A. D.; Bruce, P. G., *Chemistry of Materials* **2003,** 15, (10), 1984-1992.

31. Thackeray, M. M.; David, W. I. F.; Goodenough, J. B., *Materials Research Bulletin* **1982,** 17, (6), 785-793.

32. H. Arai, S. O., Y. Sakurai, J. Yamaki, *Journal of Power Sources* **1997,** 68.

33. Badway, F.; Pereira, N.; Cosandey, F.; Amatucci, G. G., *Journal of the Electrochemical Society* **2003,** 150, (9), A1209-A1218.

34. Badway, F.; Cosandey, F.; Pereira, N.; Amatucci, G. G., *Journal of the Electrochemical Society* **2003,** 150, (10), A1318-A1327.

35. Bervas, M.; Badway, F.; Klein, L. C.; Amatucci, G. G., *Electrochemical and Solid State Letters* **2005,** 8, (4), A179-A183.

36. Badway, F.; Mansour, A. N.; Pereira, N.; Al-Sharab, J. F.; Cosandey, F.; Plitz, I.; Amatucci, G. G., *Chemistry of Materials* **2007,** 19, (17), 4129-4141.

37. Plitz, I.; Badway, F.; Al-Sharab, J.; DuPasquier, A.; Cosandey, F.; Amatucci, G. G., *Journal of the Electrochemical Society* **2005,** 152, (2), A307-A315.

38. Roert E. Doe, K. A. P., Y. Shirley Meng, Gerbrand Ceder, *in preparation* **2008**.

39. Pan, C. J.; Lee, Y. J.; Ammundsen, B.; Grey, C. P., *Chemistry of Materials* **2002,** 14, (5), 2289-2299.

40. Lee, Y. J.; Grey, C. P., *Chemistry of Materials* **2000,** 12, (12), 3871-3878.

41. Lee, Y. J.; Grey, C. P., *Journal of the Electrochemical Society* **2002,** 149, (2), A103-A114.

42. Lee, Y. J.; Wang, F.; Grey, C. P., *Journal of the American Chemical Society* **1998,** 120, (48), 12601-12613.

43. Lee, Y. J.; Wang, F.; Mukerjee, S.; McBreen, J.; Grey, C. P., *Journal of the Electrochemical Society* **2000,** 147, (3), 803-812.

44. Lee, Y. J.; Grey, C. P., *Journal of Physical Chemistry B* **2002,** 106, (14), 3576-3582.

45. Lee, Y. J.; Park, S. H.; Eng, C.; Parise, J. B.; Grey, C. P., *Chemistry of Materials* **2002,** 14, (1), 194-205.

46. Andrew, E. R.; Bradbury, A.; Eades, R. G., *Nature* **1958,** 182, (4650), 1659-1659.

47. Grey, C. P.; Dupre, N., *Chemical Reviews* **2004,** 104, (10), 4493-4512.

48. Drago, R. S.; Zink, J. I.; Richman, R. M.; Perry, W. D., *Journal of Chemical Education* **1974,** 51, (6), 371-376.

49. Drago, R. S.; Zink, J. I.; Richman, R. M.; Perry, W. D., *Journal of Chemical Education* **1974,** 51, (7), 464-467.

50. Kittel, C., *Introduction to Solid State Physics*. John Wiley & Sons: New York, 1986.

51. Fermi, E. Z. Z., *Phys.* **1930,** 60, 320.

52. Jesson, J. P., *NMR of Paramagnetic molecules: Principles and Applications* Academic Press: New York, 1973.

53. McConnell, H. M.; Berger, S. B., *Journal of Chemical Physics* **1957,** 27, (1), 230-234.

54. McConnell, H. M.; Robertson, R. E., *Journal of Chemical Physics* **1958,** 29, (6), 1361-1365.

55. Nayeem, A.; Yesinowski, J. P., *Journal of Chemical Physics* **1988,** 89, (8), 4600-4608.

56. Mehring, M., *Principle of High Resolution NMR in Solids*. Springer-Verlag: New York, 1983.

57. Haeberlen, U., *High-Resolution NMR in Solids*. Springer-Verlag: New York, 1983.

58. Bertini, I. L., C.; Parigi, G., *Solution NMR of Paramagnetic Molecules*. Elsevier: Amsterdam, 2001.

59. Kurland, R. M., B.R., *J. Mag. Reson.* **1970,** 2, 286.

60. Rietveld, H. M., *Journal of Applied Crystallography* **1969,** 2, 65-&.

61. Young, R. A., *The Rietveld Method*. Oxford Univeristy Press: 1993.

62. Young, R. A.; Wiles, D. B., *Journal of Applied Crystallography* **1982,** 15, (AUG), 430-438.

63. Caglioti, G.; Paoletti, A.; Ricci, F. P., *Nuclear Instruments & Methods* **1958,** 3, (4), 223-228.

64. Thompson, P.; Cox, D. E.; Hastings, J. B., *Journal of Applied Crystallography* **1987,** 20, 79-83.

65. Howard, C. J., *Journal of Applied Crystallography* **1982,** 15, (DEC), 615-620.

66. Stephens, P. W., *Journal of Applied Crystallography* **1999,** 32, 281-289.

67. McCusker, L. B.; Von Dreele, R. B.; Cox, D. E.; Louer, D.; Scardi, P., *Journal of Applied Crystallography* **1999,** 32, 36-50.

68. West, A. R., *Solid State Chemistry and it's Application*. John Wiley & Son: New York: 1992.

69. W., J. R., *The optical properties of the diffraction of x-rays*. Ox Bow press: Woodbridge, 1962.

70. J., B., *Neutron and synchrotron radiation for condensed matter studies* Springer Verlag: Berlin, 1993.

71. E., K. E., *Handbook on Synchrotron Radiation*. Northolland Publishing Company: Amsterdam, 1983.

72. J., S., *NEXAFS Sepctroscopy* Springer Verlag: Berlin, 1992.

73. Konningsberger, R., *X-ray absorption, principles, applications, techniques of EXAFS SEXAFS and XANES*. John-Wiley & Sons: New York, 1988.

74. Bianconi, A., *Applied Surface Science* **1980,** 6, (3-4), 392-418.

75. Williams, A. R.; Lang, N. D., *Physical Review Letters* **1978,** 40, (14), 954-957.

76. B., R. B., *Z. Phys.* **1929,** 55, 119.

77. A., K. B. L. G., *Phys. Rev.* **1930,** 36, 648.

Chapter 2

1. Lu, Z. H.; Dahn, J. R., *Journal of the Electrochemical Society* **2002,** 149, (7), A815-A822.

2. Lu, Z. H.; Beaulieu, L. Y.; Donaberger, R. A.; Thomas, C. L.; Dahn, J. R., *Journal of the Electrochemical Society* **2002,** 149, (6), A778-A791.

3. Lu, Z. H.; MacNeil, D. D.; Dahn, J. R., *Electrochemical and Solid State Letters* **2001,** 4, (12), A200-A203.

4. Meng, Y. S.; Ceder, G.; Grey, C. P.; Yoon, W. S.; Shao-Horn, Y., *Electrochemical and Solid State Letters* **2004,** 7, (6), A155-A158.

5. Yoon, W. S.; Iannopollo, S.; Grey, C. P.; Carlier, D.; Gorman, J.; Reed, J.; Ceder, G., *Electrochemical and Solid State Letters* **2004,** 7, (7), A167-A171.

6. Yoon, W. S.; Kim, N.; Yang, X. Q.; McBreen, J.; Grey, C. P., *Journal of Power Sources* **2003,** 119, 649-653.

7. Yoon, W. S.; Paik, Y.; Yang, X. Q.; Balasubramanian, M.; McBreen, J.; Grey, C. P., *Electrochemical and Solid State Letters* **2002,** 5, (11), A263-A266.

8. Yoon, W. S.; Grey, C. P.; Balasubramanian, M.; Yang, X. Q.; McBreen, J., *Chemistry of Materials* **2003,** 15, (16), 3161-3169.

9. Grey, C. P.; Yoon, W. S.; Reed, J.; Ceder, G., *Electrochemical and Solid State Letters* **2004,** 7, (9), A290-A293.

10. Yoon, W. S.; Grey, C. P.; Balasubramanian, M.; Yang, X. Q.; Fischer, D. A.; McBreen, J., *Electrochemical and Solid State Letters* **2004,** 7, (3), A53-A55.

11. Meng, Y. S.; Ceder, G.; Grey, C. P.; Yoon, W. S.; Jiang, M.; Breger, J.; Shao-Horn, Y., *Chemistry of Materials* **2005,** 17, (9), 2386-2394.

12. Lu, Z. H.; Chen, Z. H.; Dahn, J. R., *Chemistry of Materials* **2003,** 15, (16), 3214-3220.

13. Ohzuku, T.; Makimura, Y., *Chemistry Letters* **2001**, (8), 744-745.

14. Makimura, Y.; Ohzuku, T. 2003; 2003; pp 156-160.

15. Arachi, Y.; Kobayashi, H.; Emura, S.; Nakata, Y.; Tanaka, M.; Asai, T., *Chemistry Letters* **2003,** 32, (1), 60-61.

16. Vitins, G.; West, K., *Journal of the Electrochemical Society* **1997,** 144, (8), 2587-2592.

17. Shao-Horn, Y.; Hackney, S. A.; Armstrong, A. R.; Bruce, P. G.; Gitzendanner, R.; Johnson, C. S.; Thackeray, M. M., *Journal of the Electrochemical Society* **1999,** 146, (7), 2404-2412.

18. Reed, J.; Ceder, G.; Van der Ven, A., *Electrochemical and Solid State Letters* **2001,** 4, (6), A78-A81.

19. Kobayashi, H.; Sakaebe, H.; Kageyama, H.; Tatsumi, K.; Arachi, Y.; Kamiyama, T., *Journal of Materials Chemistry* **2003,** 13, (3), 590-595.

20. Strobel, P.; Lambertandron, B., *Journal of Solid State Chemistry* **1988,** 75, (1), 90-98.

21. Massarotti, V.; Bini, M.; Capsoni, D.; Altomare, A.; Moliterni, A. G. G., *Journal of Applied Crystallography* **1997,** 30, 123-127.

22. Van der Ven, A.; Aydinol, M. K.; Ceder, G.; Kresse, G.; Hafner, J., *Physical Review B* **1998,** 58, (6), 2975-2987.

23. Shao-Horn, Y.; Levasseur, S.; Weill, F.; Delmas, C., *Journal of the Electrochemical Society* **2003,** 150, (3), A366-A373.

24. Delmas, C.; Menetrier, M.; Croguennec, L.; Levasseur, S.; Peres, J. P.; Pouillerie, C.; Prado, G.; Fournes, L.; Weill, F., *International Journal of Inorganic Materials* **1999,** 1, (1), 11-19.

25. Pan, C. J.; Lee, Y. J.; Ammundsen, B.; Grey, C. P., *Chemistry of Materials* **2002,** 14, (5), 2289-2299.

26. Lee, Y. J.; Grey, C. P., *Journal of Physical Chemistry B* **2002,** 106, (14), 3576-3582.

27. Breger, J.; Jiang, M.; Dupre, N.; Meng, Y. S.; Shao-Horn, Y.; Ceder, G.; Grey, C. P., *Journal of Solid State Chemistry* **2005,** 178, (9), 2575-2585.

Chapter 3

1. Lu, Z. H.; Beaulieu, L. Y.; Donaberger, R. A.; Thomas, C. L.; Dahn, J. R., *Journal of the Electrochemical Society* 2002, 149, (6), A778-A791.

2. Breger, J.; Dupre, N.; Chupas, P. J.; Lee, P. L.; Proffen, T.; Parise, J. B.; Grey, C. P., *Journal of the American Chemical Society* 2005, 127, (20), 7529-7537.

3. Massarotti, V.; Bini, M.; Capsoni, D.; Altomare, A.; Moliterni, A. G. G., *Journal of Applied Crystallography* 1997, 30, 123-127.

4. Strobel, P.; Lambertandron, B., *Journal of Solid State Chemistry* 1988, 75, (1), 90-98.

5. Meng, Y. S.; Ceder, G.; Grey, C. P.; Yoon, W. S.; Shao-Horn, Y., *Electrochemical and Solid State Letters* 2004, 7, (6), A155-A158.

6. Meng, Y. S.; Ceder, G.; Grey, C. P.; Yoon, W. S.; Jiang, M.; Breger, J.; Shao-Horn, Y., *Chemistry of Materials* 2005, 17, (9), 2386-2394.

7. Jansen, M.; Hoppe, R., *Zeitschrift Fur Anorganische Und Allgemeine Chemie* 1973, 397, (3), 279-289.

8. Riou, A.; Lecerf, A.; Gerault, Y.; Cudennec, Y., *Materials Research Bulletin* 1992, 27, (3), 269-275.

9. Lang, G., *Zeitschrift Fur Anorganische Und Allgemeine Chemie* 1966, 348, (5-6), 246-&.

10. H. Kobayshi, M. T., M. Shikano, H. Kageyama, R. Kanno,J., *J. Mater. Chem* 2003, 13.

11. Treacy, M. M. J.; Newsam, J. M.; Deem, M. W., *Proceedings of the Royal Society of London Series a-Mathematical Physical and Engineering Sciences* 1991, 433, (1889), 499-520.

12. Ohzuku, T.; Makimura, Y., *Chemistry Letters* 2001, (8), 744-745.

13. Lu, Z. H.; MacNeil, D. D.; Dahn, J. R., *Electrochemical and Solid State Letters* 2001, 4, (12), A200-A203.

14. Yoon, W. S.; Kim, N.; Yang, X. Q.; McBreen, J.; Grey, C. P., *Journal of Power Sources* 2003, 119, 649-653.

15. Lee, Y. J.; Grey, C. P., *Journal of Physical Chemistry B* 2002, 106, (14), 3576-3582.

16. Morgan, K. R.; Collier, S.; Burns, G.; Ooi, K., *Journal of the Chemical Society-Chemical Communications* 1994, (14), 1719-1720.

17. Mustarelli, P.; Massarotti, V.; Bini, M.; Capsoni, D., *Physical Review B* 1997, 55, (18), 12018-12024.

18. Grey, C. P.; Lee, Y. J. 2003; 2003; pp 883-894.

19. Toby, B. H., *Journal of Applied Crystallography* 2001, 34, 210-213.

20. F. Muller, A. P.-o., G. Besson, V.A. Drits,, *Mater. Struct.* 1999, 6, 129.

21. Warren, B. E., *Physical Review* 1941, 59, (9), 693-698.

22. Yang, D.; Frindt, R. F., *Journal of Applied Physics* 1996, 79, (5), 2376-2385.

23. Shi, H.; Reimers, J. N.; Dahn, J. R., *Journal of Applied Crystallography* 1993, 26, 827-836.

24. Thiel, J. P.; Chiang, C. K.; Poeppelmeier, K. R., *Chemistry of Materials* 1993, 5, (3), 297-304.

Chapter 4

1. Abraham, K. M.; Pasquariello, D. M.; Willstaedt, E. M., *Journal of the Electrochemical Society* **1998,** 145, (2), 482-486.

2. Levi, M. D.; Salitra, G.; Markovsky, B.; Teller, H.; Aurbach, D.; Heider, U.; Heider, L., *Journal of the Electrochemical Society* **1999,** 146, (4), 1279-1289.

3. Levasseur, S.; Menetrier, M.; Suard, E.; Delmas, C., *Solid State Ionics* **2000,** 128, (1-4), 11-24.

4. Rougier, A.; Gravereau, P.; Delmas, C., *Journal of the Electrochemical Society* **1996,** 143, (4), 1168-1175.

5. Spahr, M. E.; Novak, P.; Schnyder, B.; Haas, O.; Nesper, R., *Journal of the Electrochemical Society* **1998,** 145, (4), 1113-1121.

6. Yoshio, M.; Todorov, Y.; Yamato, K.; Noguchi, H.; Itoh, J.; Masaki, O.; Mouri, T., *Journal of Power Sources* **1998,** 74, (1), 46-53.

7. Rossen, E.; Jones, C. D. W.; Dahn, J. R., *Solid State Ionics* **1992,** 57, (3-4), 311-318.

8. Ohzuku, T.; Makimura, Y., *Chemistry Letters* **2001**, (8), 744-745.

9. Joeng, J. W.; Kang, S. G., *Journal of Power Sources* **2003,** 123, (1), 75-78.

10. Kim, J.; Amine, K., *Journal of Power Sources* **2002,** 104, (1), 33-39.

11. Lu, Z. H.; MacNeil, D. D.; Dahn, J. R., *Electrochemical and Solid State Letters* **2001,** 4, (12), A200-A203.

12. Makimura, Y.; Ohzuku, T. 2003; 2003; pp 156-160.

13. Yoon, W. S.; Paik, Y.; Yang, X. Q.; Balasubramanian, M.; McBreen, J.; Grey, C. P., *Electrochemical and Solid State Letters* **2002,** 5, (11), A263-A266.

14. Ohzuku, T.; Makimura, Y., *Chemistry Letters* **2001**, (7), 642-643.

15. Lu, Z. H.; Dahn, J. R., *Journal of the Electrochemical Society* **2002,** 149, (7), A815-A822.

16. Mustarelli, P.; Massarotti, V.; Bini, M.; Capsoni, D., *Physical Review B* **1997,** 55, (18), 12018-12024.

17. Breger, J.; Dupre, N.; Chupas, P. J.; Lee, P. L.; Proffen, T.; Parise, J. B.; Grey, C. P., *Journal of the American Chemical Society* **2005,** 127, (20), 7529-7537.

Chapter 5

1. Lu, Z. H.; Beaulieu, L. Y.; Donaberger, R. A.; Thomas, C. L.; Dahn, J. R., *Journal of the Electrochemical Society* **2002,** 149, (6), A778-A791.

2. Lu, Z. H.; Dahn, J. R., *Journal of the Electrochemical Society* **2002,** 149, (7), A815-A822.

3. Lu, Z. H.; MacNeil, D. D.; Dahn, J. R., *Electrochemical and Solid State Letters* **2001,** 4, (12), A200-A203.

4. Robertson, A. D.; Bruce, P. G., *Electrochemical and Solid State Letters* **2004,** 7, (9), A294-A298.

5. Armstrong, A. R.; Holzapfel, M.; Novak, P.; Johnson, C. S.; Kang, S. H.; Thackeray, M. M.; Bruce, P. G., *Journal of the American Chemical Society* **2006,** 128, (26), 8694-8698.

6. Balasubramanian, M.; Sun, X.; Yang, X. Q.; McBreen, J., *Journal of Power Sources* **2001,** 92, (1-2), 1-8.

7. Lee, P. L.; Shu, D. M.; Ramanathan, M.; Preissner, C.; Wang, J.; Beno, M. A.; Von Dreele, R. B.; Ribaud, L.; Kurtz, C.; Antao, S. M.; Jiao, X.; Toby, B. H., *Journal of Synchrotron Radiation* **2008,** 15, 427-432.

8. Lee, Y. J.; Grey, C. P., *Journal of Physical Chemistry B* **2002,** 106, (14), 3576-3582.

9. Weppner, W.; Huggins, R. A., *Journal of the Electrochemical Society* **1977,** 124, (3), C135-C135.

10. Weppner, W.; Huggins, R. A., *Journal of the Electrochemical Society* **1979,** 126, (8), C305-C305.

11. Amarilla, J. M.; Tedjar, F.; Poinsignon, C., *Electrochimica Acta* **1994,** 39, (15), 2321-2331.

12. Chabre, Y.; Pannetier, J., *Progress in Solid State Chemistry* **1995,** 23, (1), 1-130.

13. Lu, Z. H.; Chen, Z. H.; Dahn, J. R., *Chemistry of Materials* **2003,** 15, (16), 3214-3220.

14. Rietveld, H. M., *Journal of Applied Crystallography* **1969,** 2, 65-&.

15. Breger, J.; Meng, Y. S.; Hinuma, Y.; Kumar, S.; Kang, K.; Shao-Horn, Y.; Ceder, G.; Grey, C. P., *Chemistry of Materials* **2006,** 18, (20), 4768-4781.

16. Breger, J.; Kang, K.; Cabana, J.; Ceder, G.; Grey, C. P., *Journal of Materials Chemistry* **2007,** 17, (30), 3167-3174.

17. Kang, K. S.; Meng, Y. S.; Breger, J.; Grey, C. P.; Ceder, G., *Science* **2006,** 311, (5763), 977-980.

18. Breger, J.; Dupre, N.; Chupas, P. J.; Lee, P. L.; Proffen, T.; Parise, J. B.; Grey, C. P., *Journal of the American Chemical Society* **2005,** 127, (20), 7529-7537.

19. Yoon, W. S.; Kim, N.; Yang, X. Q.; McBreen, J.; Grey, C. P., *Journal of Power Sources* **2003,** 119, 649-653.

20. Meyer, B. M.; Leifer, N.; Sakamoto, S.; Greenbaum, S. G.; Grey, C. P., *Electrochemical and Solid State Letters* **2005,** 8, (3), A145-A148.

21. Yoon, W. S.; Paik, Y.; Yang, X. Q.; Balasubramanian, M.; McBreen, J.; Grey, C. P., *Electrochemical and Solid State Letters* **2002,** 5, (11), A263-A266.

22. Yoon, W. S.; Grey, C. P.; Balasubramanian, M.; Yang, X. Q.; McBreen, J., *Chemistry of Materials* **2003,** 15, (16), 3161-3169.

23. Balasubramanian, M.; McBreen, J.; Davidson, I. J.; Whitfield, P. S.; Kargina, I., *Journal of the Electrochemical Society* **2002,** 149, (2), A176-A184.

24. Lei, C. H.; Bareno, J.; Wen, J. G.; Petrov, I.; Kang, S. H.; Abraham, D. P., *Journal of Power Sources* **2008,** 178, (1), 422-433.

25. La Mantia, F.; Rosciano, F.; Tran, N.; Novak, P. 2008; Springer: 2008; pp 893-896.

Chapter 6

1. Tarascon, J. M.; Armand, M., *Nature* **2001,** 414, (6861), 359-367.

2. Mizushima, K.; Jones, P. C.; Wiseman, P. J.; Goodenough, J. B., *Materials Research Bulletin* **1980,** 15, (6), 783-789.

3. Poizot, P.; Laruelle, S.; Grugeon, S.; Dupont, L.; Tarascon, J. M., *Nature* **2000,** 407, (6803), 496-499.

4. Li, H.; Richter, G.; Maier, J., *Advanced Materials* **2003,** 15, (9), 736-739.

5. Li, H.; Balaya, P.; Maier, J., *Journal of the Electrochemical Society* **2004,** 151, (11), A1878-A1885.

6. Badway, F.; Cosandey, F.; Pereira, N.; Amatucci, G. G., *Journal of the Electrochemical Society* **2003,** 150, (10), A1318-A1327.

7. Badway, F.; Pereira, N.; Cosandey, F.; Amatucci, G. G., *Journal of the Electrochemical Society* **2003,** 150, (9), A1209-A1218.

8. H. Arai, S. O., Y. Sakurai, J. Yamaki, *Journal of Power Sources* **1997,** 68.

9. Cosandey, F.; Al-Sharab, J. F.; Badway, F.; Amatucci, G. G.; Stadelmann, P., *Microscopy and Microanalysis* **2007,** 13, (2), 87-95.

10. Roert E. Doe, K. A. P., Y. Shirley Meng, Gerbrand Ceder, *in preparation* **2008**.

11. Grey, C. P.; Dupre, N., *Chemical Reviews* **2004,** 104, (10), 4493-4512.

12. Breger, J.; Dupre, N.; Chupas, P. J.; Lee, P. L.; Proffen, T.; Parise, J. B.; Grey, C. P., *Journal of the American Chemical Society* **2005,** 127, (20), 7529-7537.

13. Lee, P. L.; Shu, D. M.; Ramanathan, M.; Preissner, C.; Wang, J.; Beno, M. A.; Von Dreele, R. B.; Ribaud, L.; Kurtz, C.; Antao, S. M.; Jiao, X.; Toby, B. H., *Journal of Synchrotron Radiation* **2008,** 15, 427-432.

14. Lee, Y. J.; Grey, C. P., *Journal of Physical Chemistry B* **2002,** 106, (14), 3576-3582.

15. Chupas, P. J.; Qiu, X. Y.; Hanson, J. C.; Lee, P. L.; Grey, C. P.; Billinge, S. J. L., *Journal of Applied Crystallography* **2003,** 36, 1342-1347.

16. Hinedi, Z. R.; Chang, A. C.; Borchardt, D. B., *Water Research* **1997,** 31, (4), 877-883.

17. West, A. R., *Solid State Chemistry and it's Application*. John Wiley & Son: New York: 1992.

18. Kim, J.; Nielsen, U. G.; Grey, C. P., *Journal of the American Chemical Society* **2008,** 130, (4), 1285-1295.

19. Nielsen, U. G.; Paik, Y.; Julmis, K.; Schoonen, M. A. A.; Reeder, R. J.; Grey, C. P., *Journal of Physical Chemistry B* **2005,** 109, (39), 18310-18315.

20. Liao, P.; MacDonald, B. L.; Dunlap, R. A.; Dahn, J. R., *Chemistry of Materials* **2008,** 20, (2), 454-461.

21. Meyer, B. M.; Leifer, N.; Sakamoto, S.; Greenbaum, S. G.; Grey, C. P., *Electrochemical and Solid State Letters* **2005,** 8, (3), A145-A148.

22. Plakhotnyk, A. V.; Ernst, L.; Schmutzler, R., *Journal of Fluorine Chemistry* **2005,** 126, (1), 27-31.

23. Shachar, G.; Shaked, H.; Makovsky, J., *Physical Review B* **1972,** 6, (5), 1968-&.

24. Breger, J.; Kang, K.; Cabana, J.; Ceder, G.; Grey, C. P., *Journal of Materials Chemistry* **2007,** 17, (30), 3167-3174.

25. Roert E. Doe, K. A. P., Y. Shirley Meng, Gerbrand Ceder, *in preparation* **2008**.

Chapter 7

1. Dahn, J. R.; Zheng, T.; Liu, Y. H.; Xue, J. S., *Science* **1995,** 270, (5236), 590-593.

2. Megahed, S.; Scrosati, B., *Journal of Power Sources* **1994,** 51, (1-2), 79-104.

3. Courtney, I. A.; Dahn, J. R., *Journal of the Electrochemical Society* **1997,** 144, (9), 2943-2948.

4. Courtney, I. A.; Dahn, J. R., *Journal of the Electrochemical Society* **1997,** 144, (6), 2045-2052.

5. Idota, Y.; Kubota, T.; Matsufuji, A.; Maekawa, Y.; Miyasaka, T., *Science* **1997,** 276, (5317), 1395-1397.

6. Li, H.; Balaya, P.; Maier, J., *Journal of the Electrochemical Society* **2004,** 151, (11), A1878-A1885.

7. Li, H.; Richter, G.; Maier, J., *Advanced Materials* **2003,** 15, (9), 736-739.

8. Badway, F.; Mansour, A. N.; Pereira, N.; Al-Sharab, J. F.; Cosandey, F.; Plitz, I.; Amatucci, G. G., *Chemistry of Materials* **2007,** 19, (17), 4129-4141.

9. Gabano, J. P.; Gerbier, G.; Jammet, J.; Dechenau.V, *Journal of the Electrochemical Society* **1972,** 119, (4), 459-&.

10. Okamoto, K.; Kawai, S., *Japanese Journal of Applied Physics* **1973,** 12, (8), 1130-1138.

11. Etienne, A., *Journal of the Electrochemical Society* **1970,** 117, (7), 870-&.

12. Chung, J. S.; Sohn, H. J., *Journal of Power Sources* **2002,** 108, (1-2), 226-231.

13. Debart, A.; Dupont, L.; Patrice, R.; Tarascon, J. M., *Solid State Sciences* **2006,** 8, (6), 640-651.

14. Grugeon, S.; Laruelle, S.; Herrera-Urbina, R.; Dupont, L.; Poizot, P.; Tarascon, J. M., *Journal of the Electrochemical Society* **2001,** 148, (4), A285-A292.

15. Ikeda, H.; Narukawa, S., *Journal of Power Sources* **1983,** 9, (3-4), 329-334.

16. Matsuda, Y.; Teraji, K.; Takasu, Y., *Denki Kagaku* **1976,** 44, (5), 363-364.

17. Novak, P., *Electrochimica Acta* **1985,** 30, (12), 1687-1692.

18. Lee, P. L.; Shu, D. M.; Ramanathan, M.; Preissner, C.; Wang, J.; Beno, M. A.; Von Dreele, R. B.; Ribaud, L.; Kurtz, C.; Antao, S. M.; Jiao, X.; Toby, B. H., *Journal of Synchrotron Radiation* **2008,** 15, 427-432.

19. Lee, Y. J.; Grey, C. P., *Journal of Physical Chemistry B* **2002,** 106, (14), 3576-3582.

20. Hinedi, Z. R.; Chang, A. C.; Borchardt, D. B., *Water Research* **1997,** 31, (4), 877-883.

21. Liu, H. M.; Sullivan, R. M.; Hanson, J. C.; Grey, C. P.; Martin, J. D., *Journal of the American Chemical Society* **2001,** 123, (31), 7564-7573.

22. Gullion, T., *Chemical Physics Letters* **1995,** 246, (3), 325-330.

23. West, A. R., *Solid State Chemistry and it's Application*. John Wiley & Son: New York: 1992.

24. Plakhotnyk, A. V.; Ernst, L.; Schmutzler, R., *Journal of Fluorine Chemistry* **2005,** 126, (1), 27-31.

25. Pattrick, R. A. D.; Mosselmans, J. F. W.; Charnock, J. M.; England, K. E. R.; Helz, G. R.; Garner, C. D.; Vaughan, D. J., *Geochimica Et Cosmochimica Acta* **1997,** 61, (10), 2023-2036.

26. Ba, Y.; Kao, H. M.; Grey, G. P.; Chopin, L.; Gullion, T., *Journal of Magnetic Resonance* **1998,** 133, (1), 104-114.